AN EXPERIMENTAL INVESTIGATION OF AN AIRFOIL PITCHING AT MODERATE TO HIGH RATES TO LARGE ANGLES OF ATTACK

by

GARY M. GRAHAM, M.S. in M.E.

A DISSERTATION

IN

MECHANICAL ENGINEERING

Submitted to the Graduate Faculty
of Texas Tech University in
Partial Fulfillment of
the Requirements for
the Degree of

DOCTOR OF PHILOSOPHY

December 1985

AC
801
T3
1985
No.55
cop.2

ACKNOWLEDGMENTS

The author wishes to thank Dr. J. H. Strickland for his support throughout this research project. In addition, the author is grateful to the AFOSR (contract #F49620-82-C-0035) and Sandia National Laboratories (contract #21-3574) for their support.

TABLE OF CONTENTS

Page

ACKNOWLEDGMENTS ii

ABSTRACT v

LIST OF FIGURES vi

NOMENCLATURE ix

CHAPTER

I. INTRODUCTION 1

1.1 Background 1
1.2 Previous Related Research 5

II. EXPERIMENTAL INVESTIGATION OF DYNAMIC STALL 9

2.1 Experimental Objectives 9
2.2 Test Facility 9
2.3 Flow Visualization 13
2.4 Pressure Distributions and Integrated Forces 17
2.5 Strain Gage Measurements 23

III. DISCUSSION OF RESULTS 29

3.1 Aerodynamic Loads 29
3.2 Flow Visualization Data 33
3.3 Pressure Distributions 44
3.4 Empirical Correlations 49

IV. ANALYTICAL METHODS AND RESULTS 65

4.1 Discussion of Analytical Model 65
4.2 Analytical Results 72

V. CLOSURE 89

5.1 Summary of Experimental Investigation 89
5.2 Summary of Analytical Model 89
5.3 Conclusions 91
5.4 Recommendations 93

Page

REFERENCES 95

APPENDIX

A. UNCERTAINTY ANALYSIS 99
B. PRESSURE DISTRIBUTIONS 104
C. AERODYNAMIC FORCES 149
D. SOFTWARE LISTINGS 162

ABSTRACT

An experimental investigation of the variation in aerodynamic performance of a NACA 0015 airfoil over a range of constant pitching rates was performed in the Texas Tech tow-tank facility. The test results consist of flow visualization data, surface pressure measurements, and load cell data, and encompass a wide range of non-dimensional pitching rates $\left(K = \frac{\dot{\alpha} c}{2U_\infty}\right)$ varying from 0.1 to 1.0 at angles of attack from 0° to 90°. The test Reynolds number was 100,000. These data have yielded several interesting physical correlations associated with large-scale pitch rate motions. Included in these are simple trigonometric correlations for the lift and drag forces and an extension of the Gormont model for the inception of leading edge separation. Very large lift and drag coefficients on the order of 10 have been generated. These large forces, produced by unsteady effects, may perhaps be exploited in the supermaneuverability concept for fighter aircraft.

LIST OF FIGURES

Page

1. Comparison of Minimum Time Maneuvers 3
2. Lift Coefficient Trends for a Pitching Airfoil as a Function of Pitching Rate 4
3. Schematic of General Test Setup 11
4. Schematic of Drive Mechanism 12
5. Constant Pitching Rate Angle of Attack Data 14
6. Typical Flow Visualization Results for K = 0.19 15
7. Schematic of Experimental Arrangement for Flow Visualization 16
8. Schematic of Pressure Measurement Test Setup 19
9. Typical Pressure Distribution for K = .088 20
10. Typical Lift Coefficient Data for K = .088 24
11. Typical Drag Coefficient Data for K = .088 25
12. Schematic for Load Cell Measurements 26
13. Low Pitch Rate Lift and Drag 30
14. High Pitch Rate Lift and Drag 31
15. Effective Nose Angle of Attack as a Function of Geometric Angle of Attack 32
16. Flow Visualization and Pressure Data for K = .088 34
17. Flow Visualization and Pressure Data for K = 0.19 36
18. Flow Visualization and Pressure Data for K = 0.29 38
19. Flow Visualization and Pressure Data for K = 0.51 41
20. Flow Visualization and Pressure Data for K = 0.71 42
21. Flow Visualization and Pressure Data for K = 0.99 43

Page

22. Pressure Distributions for K = 0.51 45

23. Time History of the Intersection of Topside and Underside Pressure Distributions 47

24. Maximum Pressure Coefficients 48

25. Maximum Lift and Drag Coefficients 51

26. Angle of Attack at Maximum Lift and Drag 52

27. Maximum Normal Force Coefficient 54

28. Comparison of Lift and Drag Force Data with Simple Trigonometric Correlations 55

29. Coefficients for Lift and Drag Force Correlations 56

30. Lift Force Correlation for Low Pitch Rates 57

31. Drag Force Correlation for Low Pitch Rates 58

32. Lift Force Correlation for High Pitch Rates 60

33. Drag Force Correlation for High Pitch Rates 61

34. Gormont Correlation for Leading Edge Separation 63

35. Analytical Representation of Airfoil and Wake 66

36. Vortex Core Approximation 70

37. Effect of Leading Edge Vortex Strength on the Lift Coefficient for K = 0.19 74

38. Effect of Leading Edge Vortex Strength on the Drag Coefficient for K = 0.19 75

39. Analytical Lift Force Results for K = 0.088 76

40. Analytical Drag Force Results for K = 0.088 77

41. Analytical Lift Force Results for K = 0.19 78

42. Analytical Drag Force Results for K = 0.19 79

43. Analytical Lift Force Results for K = 0.29 80

Page

44. Analytical Drag Force Results for K = 0.29 81

45. Analytical Lift Force Results for K = 0.51 82

46. Analytical Drag Force Results for K = 0.51 83

47. Analytical Lift Force Results for K = 0.71 84

48. Analytical Drag Force Results for K = 0.71 85

49. Analytical Lift Force Results for K = 0.99 86

50. Analytical Drag Force Results for K = 0.99 87

NOMENCLATURE

A_D	Coefficient for Drag Force Correlation
A_L	Coefficient for Lift Force Correlation
A_{ji}	Coefficient Expressing the Downwash Influence of the i^{th} Bound Vortex Upon the j^{th} Control Point
AR	Airfoil Aspect Ratio
AR_{eff}	Effective Airfoil Aspect Ratio
b	Airfoil Span
B^k_{ji}	Coefficient Expressing the Downwash Influence of the i^{th} Wake Vortex Upon the j^{th} Control Point at k^{th} Time-Step
c	Airfoil Chordlength
C_D	Drag Coefficient
C^+_D	Normalized Drag Coefficient
C_{Di}	Induced Drag
C_L	Lift Coefficient
C^+_L	Normalized Lift Coefficient
C_p	Pressure Coefficient
C_{jn}	Coefficient Expressing the Downwash Influence of Leading Edge Separation Vortex Upon the j^{th} Control Point
C_{jT}	Coefficient Expressing the Downwash Influence of Nascent Trailing Edge Vortex Upon the j^{th} Control Point
C_1	Load Cell Normal Force Calibration Constant
C_2	Load Cell Tangential Force Calibration Constant
D	Drag Force
$\vec{e}_n$	Surface Normal Unit Vector
$\vec{e}_s$	Surface Tangent Unit Vector
E_1	Load Cell Normal Force Bridge Output

E_2	Load Cell Tangential Force Bridge Output
F	Complex Potential
F_c	Centripetal Force
F_n	Normal Force Per Unit Length
F_n^+	Non-dimensional Normal Force
F_t	Tangential Force Per Unit Length
F_t^+	Non-dimensional Tangential Force
h	Distance from Airfoil Free End to Tow-Tank Floor
HR	Height Ratio
K	Non-dimensional Pitch Rate
m	Mass of Test Blade
M	Complex Momentum
M_x	x-Component of Momentum
M_y	y-Component of Momentum
NB	Number of Bound Vortices
NW^k	Number of Wake Vortices at kth Time-Step
P	Airfoil Surface Pressure
P_a	Ambient Pressure
P_∞	Freestream Pressure
R	Distance from Pitching Point to Airfoil Center of Mass
R_{core}	Vortex Core Diameter
U	Velocity
U_{Mj}^k	Downwash at jth Control Point Due to Airfoil Motion at kth Time-Step
t	Airfoil Thickness
Δt	Real Time Step

Δt^*	Non-dimensional Time Step
$\vec{U}_r$	Relative Velocity Between Airfoil Surface and Freestream
U_∞	Freestream Velocity
x	Chordwise Distance from Airfoil Leading Edge
z	Complex Variable $(x + iy)$
α	Geometric Angle of Attack
α_N	Effective Angle of Attack at Airfoil Leading Edge
$\Delta\alpha_{stall}$	Stall Delay Angle
$\dot{\alpha}$	Airfoil Pitching Rate
Γ^k_{Bi}	Strength of i^{th} Bound Vortex at k^{th} Time-Step
Γ^k_N	Strength of Leading Edge Separation Vortex at k^{th} Time-Step
Γ^k_T	Strength of Nascent Trailing Edge Vortex at k^{th} Time-Step
Γ_{Wi}	Strength of i^{th} Wake Vortex
ϕ	Velocity Potential
ρ	Fluid Density
ξ	Airfoil Pitching Point in Percent Chord

CHAPTER I

INTRODUCTION

1.1 Background

The ability to predict unsteady fluid behavior is important in many engineering devices including helicopter rotors [1], rotating turbomachinery [2], and vertical axis wind turbines [3]. In association with these machines, there has been considerable investigation of the phenomenon of aerodynamic stall on pitching airfoils as reviewed in references [4-5].

The onset of dynamic stall gives rise to transient airfoil loads which are larger than their static counterparts. This dynamic augmentation of forces is large enough to reduce the fatigue life of helicopter rotor mechanical components. In addition, vertical axis wind turbines operating near regulation windspeed experience dynamic stall and consequently produce significantly higher power than at most normal operating windspeeds. This dynamic overshoot in the power versus windspeed curve has an unfavorable impact upon the economics of turbine, drive train and generator matching. In attempts to solve these problems, much of the research into dynamic stall has been undertaken with the intent of ultimately limiting the aerodynamic loads. Recently, interest has been aroused in the possible exploitation of the highly energetic nature of this flow such as in the concept of supermaneuverability of fighter aircraft as discussed by Herbst [6].

Herbst defines supermaneuverability as "the capability of a fighter aircraft to execute tactical maneuvers with controlled side slipping and at angles of attack beyond maximum static lift." Post stall turns (PST) are a type of supermaneuverability which give a fighter aircraft with PST capability a decided advantage over an aircraft without PST features. Flight simulations [6] have indicated that an aircraft with PST capabilities will have an exchange ratio of weapons of 2:1 with an equal aircraft without PST ability. A typical tactical encounter between an aircraft with supermaneuverability and a conventional aircraft is shown in Figure 1. As illustrated in this figure the aircraft with PST capability is able to execute a sharper turn giving the pilot an uncontested first-shot opportunity. In addition, the aircraft with PST ability is in a position to deliver weapons for a longer period of time.

This type of rapidly pitching, high angle of attack motion gives rise to a complex flow field and unsteady loads which are difficult to predict analytically. The idealized effects of increasing the non-dimensional pitching rate K on the lift coefficient are shown in Figure 2. Here the non-dimensional pitch rate K is defined by

$$K = \frac{\dot{\alpha} c}{2U_\infty} \tag{1}$$

where $\dot{\alpha}$ is the angular velocity, c is the airfoil chord, and U_∞ is the undisturbed freestream velocity. It should be noted that experimental data are shown only at the lower values of K. As will be pointed out in a subsequent section, the experimental data deviate considerably from this analysis at high K values. The analytical prediction is based on a

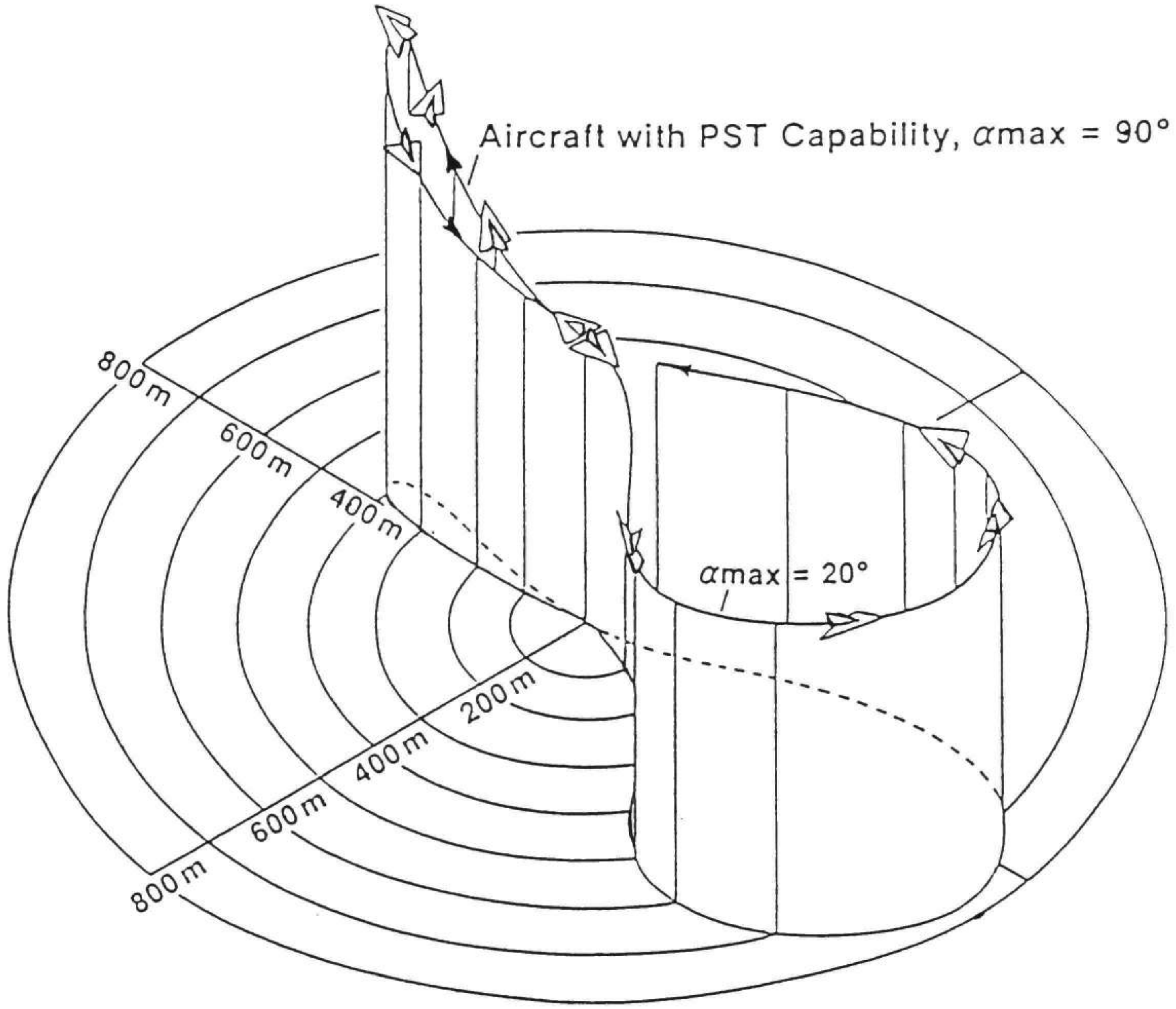
Aircraft with PST Capability, αmax = 90°
αmax = 20°
800 m
600 m
400 m
200 m
400 m
600 m
800 m

Figure 1. Comparison of Minimum Time Maneuvers [6]

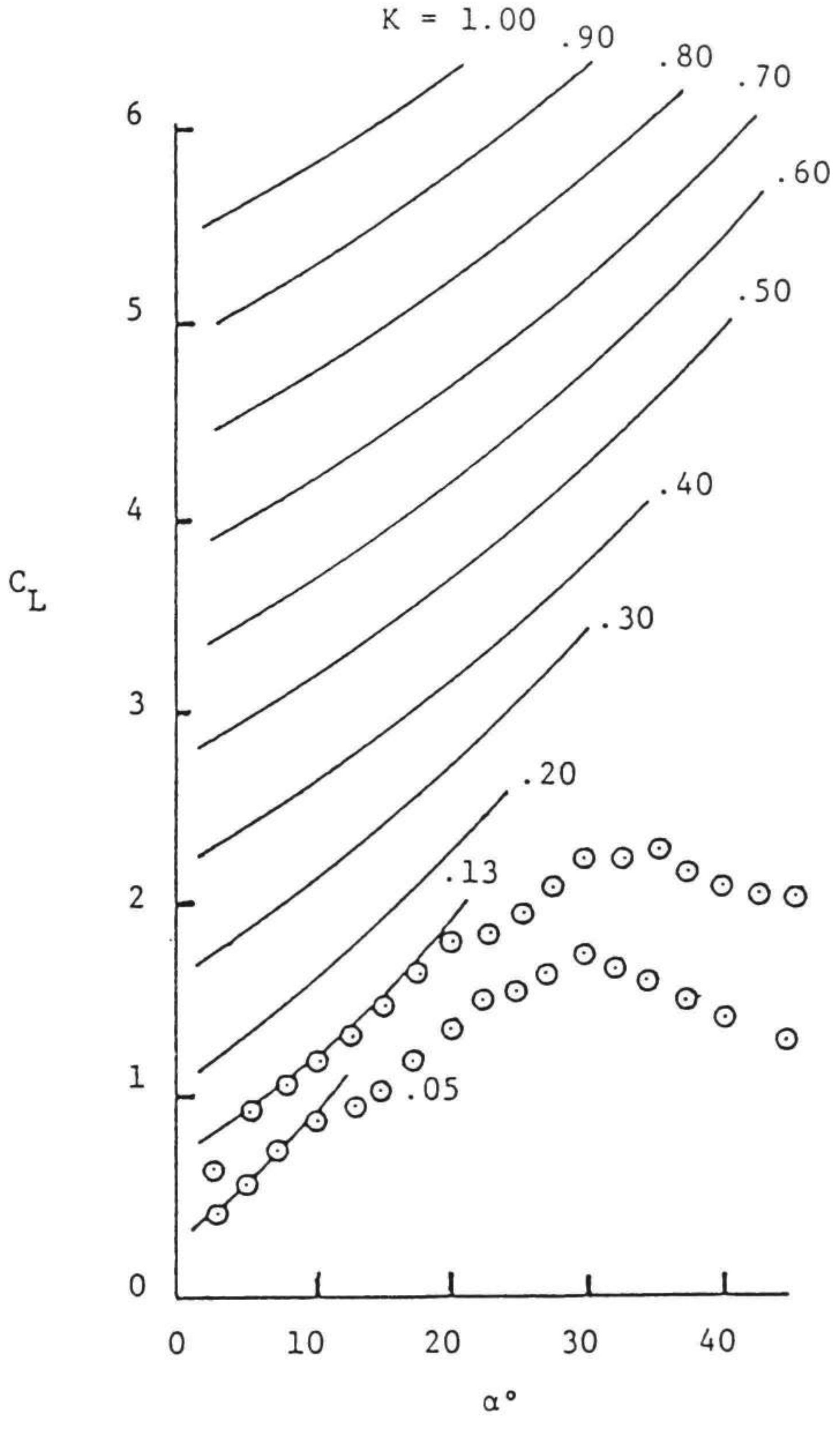

Figure 2. Lift Coefficient Trends for a Pitching Airfoil as a Function of Pitching Rate (O - Francis, et al. [29], - inviscid solution [7])

simple analysis for constant $\dot{\alpha}$ at substall angles of attack [7] but is helpful in visualizing the lift coefficient trends. It is the purpose of this dissertation to present the results of an experimental investigation designed to assess the variation in aerodynamic performance of a NACA 0015 airfoil with rate of pitch in the moderate to high range ($.1 < K < 1$). The results consist of flow visualization data, surface pressure distributions and integrated forces, and strain gage measurements for angles of attack from 0° to 90°.

1.2 Previous Related Research

A number of approaches have been taken with regard to the prediction of unsteady stalled airfoils. In general, these approaches range from empirical models [8-11] to models based on the Navier-Stokes equations [12-13]. The empirical models are generally applicable to small sinusoidal pitch oscillations about some relatively low angle of attack. The Navier-Stokes solutions consume enormous amounts of computer time and are usually limited to low Reynolds number solutions. Most of these works are only applicable to two-dimensional airfoils. There have been several boundary layer codes developed which can be used to predict some of the behavior associated with unsteady stall [14-16]. There have also been models of the potential flow behavior related to the shedding of leading edge vorticity typified by the work of Ham [17]. More recently Katz [18] simulated the unsteady separated flow over a thin cambered airfoil. The models of both Ham and Katz require empirical information regarding the appearance and position of the separation point. Presently there are at least two groups of investigators who are developing analytical techniques based on panel representations of the airfoil surfaces and discrete vortex representations of the separated wake surfaces [19-20]. To date, however, none of these analytical methods has been proven to be totally satisfactory for predicting the lift and drag on arbitrary airfoil sections undergoing arbitrary airfoil motions with the potential occurrence of dynamic stall. Part of this lack of credibility is rooted in the fact that experimental data pertaining to dynamic stall are reasonably limited. Not only does this lack of data disallow rigorous checks of particular analytical methods but, in addition, may be hiding a certain amount of the "physics" of the problem which should be included in the less sophisticated approaches.

Most of the experimental data obtained for unsteady separated flow airfoils are for oscillating airfoils undergoing relatively small sinusoidal pitch oscillations (± 1 to ± 10°) about a relatively low mean angle of attack (0° to 15°) as typified by the experiments reported by McCroskey and Philippe [21], McAlister and Carr [22], Martin et al. [23], Robinson and Luettges [24], Liiva and Davenport [25], and Rainey [26]. The type of data obtained in these studies include flow visualization, hot-film and hot-wire data, and surface pressure distributions. In addition, dynamic stall on simulated Darrieus rotors, whose flightpath is something of a skewed small-amplitude sinusoid, has been investigated by Strickland, et al. [27] and Oler and Strickland [3]. These oscillating airfoil data are, of course, applicable to many of the fluid devices studied in the past and represent a large portion of the foundation upon which the present understanding of dynamic stall rests. On the other hand, there are few experimental data available for situations where the airfoil undergoes a rapid change in pitch up to large angles of attack and deep dynamic stall. Applications such as the recently conceived "supermaneuverability" of fighter aircraft require a more thorough understanding of dynamically stalled airfoils at angles of attack which may exceed 45°. In addition, the motion of the airfoil for this application will perhaps be more closely related to a constant $\dot{\alpha}$ motion as opposed to a sinusoidal motion.

A limited amount of experimental data has been obtained for airfoils undergoing constant pitching rate motion up to moderate angles of attack of at least 30°. These works include the study of Harper and Flanigan [28] who obtained force balance data on a small aircraft model pitching up to 30°, and the work of Ham and Garelick [1] who obtained surface pressure measurements on an airfoil pitching up to 30°, and the work of Francis et al. [29] who obtained surface pressure measurements on an airfoil pitching up to 60°. None of these works contains any flow visualization data which are particularly useful in analyzing the fluid dynamics of the deep stall flow. Deekens and Kuebler [30] obtained flow visualization data for a NACA 0015 airfoil and observed the dynamic leading edge separation phenomenon for several low Reynolds numbers ($R < 3 \times 10^4$) and non-dimensional pitching rates up to 0.26. Daley [31] obtained leading edge dynamic stall data for Reynolds numbers up to 3×10^5 and non-dimensional pitching rates up to 0.06. Walker et al. [32] obtained flow visualization data along with some hot-wire data for a NACA 0015 undergoing constant pitch rate motions. These data were obtained for Reynolds numbers of the order of 4.5×10^4 and non-dimensional pitch rates up to 0.30. The further work of Walker and

Helin [33] produced surface pressure distributions on a NACA 0015 experiencing constant pitch rates up to $K = 0.3$ over a range of low Reynolds numbers ($47,500 < Re < 190,000$) up to 60° angle of attack. These studies showed an inverse relationship between the maximum lift force and the Reynolds number for a given constant pitch rate for $45,000 < Re < 95,000$, while for $95,000 < Re < 190,000$ the maximum lift coefficient is relatively insensitive to changes in the Reynolds number.

A principal objective of the present experiment was to extend the availability of constant $\dot{\alpha}$ data to cases of moderate to high non-dimensional pitching rates ($.1 < K < 1$) up to high angles of attack.

CHAPTER II

EXPERIMENTAL INVESTIGATION OF DYNAMIC STALL

2.1 Experimental Objectives

There were four major objectives to be accomplished in the present work. These objectives can be summarized as follows:

- Obtain surface pressure data as a function of airfoil angle of attack α and the non-dimensional pitch rate K. The range of variation will be $0° < \alpha < 90°$ and $0.10 \leq K \leq 1.00$.

- Obtain transient lift and drag coefficients from direct measurements using a strain gage load cell and from integrated surface pressure distributions.

- Obtain high-quality flow visualization data of the large-scale vortical motion associated with the transient flow.

- Obtain correlations with existing data (at the lower K values), seek to correlate data trends for the set of data taken, and compare the experimental results with an analytical method.

2.2 Test Facility

The tests were conducted in the Texas Tech University, Mechanical Engineering Department's tow tank facility. The use of water as a working fluid allowed the high non-dimensional pitch rates to be studied while keeping the actual dynamic parameters of the airfoil motion in the realm of experimental practicality. The fiberglass tow tank has horizontal dimensions of 16 ft by 32 ft with a water depth of 4 ft. The large width of the tow tank eliminates blockage effects which are sometimes a problem in high angle of attack studies. As depicted in Figure 3 the airfoil is mounted on a carriage which provides both translational and pitching motion to the airfoil. The carriage slides along a pair of fixed rails which are supported along the 32 ft length of the tow tank by a steel structural member. Instrumentation signals from the moving carriage housing are transmitted to a fixed frame of reference via electrical cables suspended from the laboratory ceiling with elastic tubing.

The carriage motion as well as the rotary motion is imparted by a roller chain system. The rigging associated with this system is shown in Figure 4. A motor mounted on one end of the rail is used to drive a roller chain loop which is connected to a second loop via a spur gear set. The linear speed of the carriage is the average of the tangential speeds of the two roller chain loops. The rotational speed is proportional to the difference between the roller chain loops tangential speeds. The non-dimensional pitching rate can be expressed as

$$K = \frac{c}{2r}\left(\frac{r_2 - r_1}{r_2 + r_1}\right) \tag{2}$$

The value of K can be changed using spur gear sets with various diameter ratios. The motion of the carriage is controlled via a three position remote control switch. The carriage can be stopped or started in either direction by the control switch except at the ends of travel where limit switches stop the motion in one direction. In addition, a pitch delay

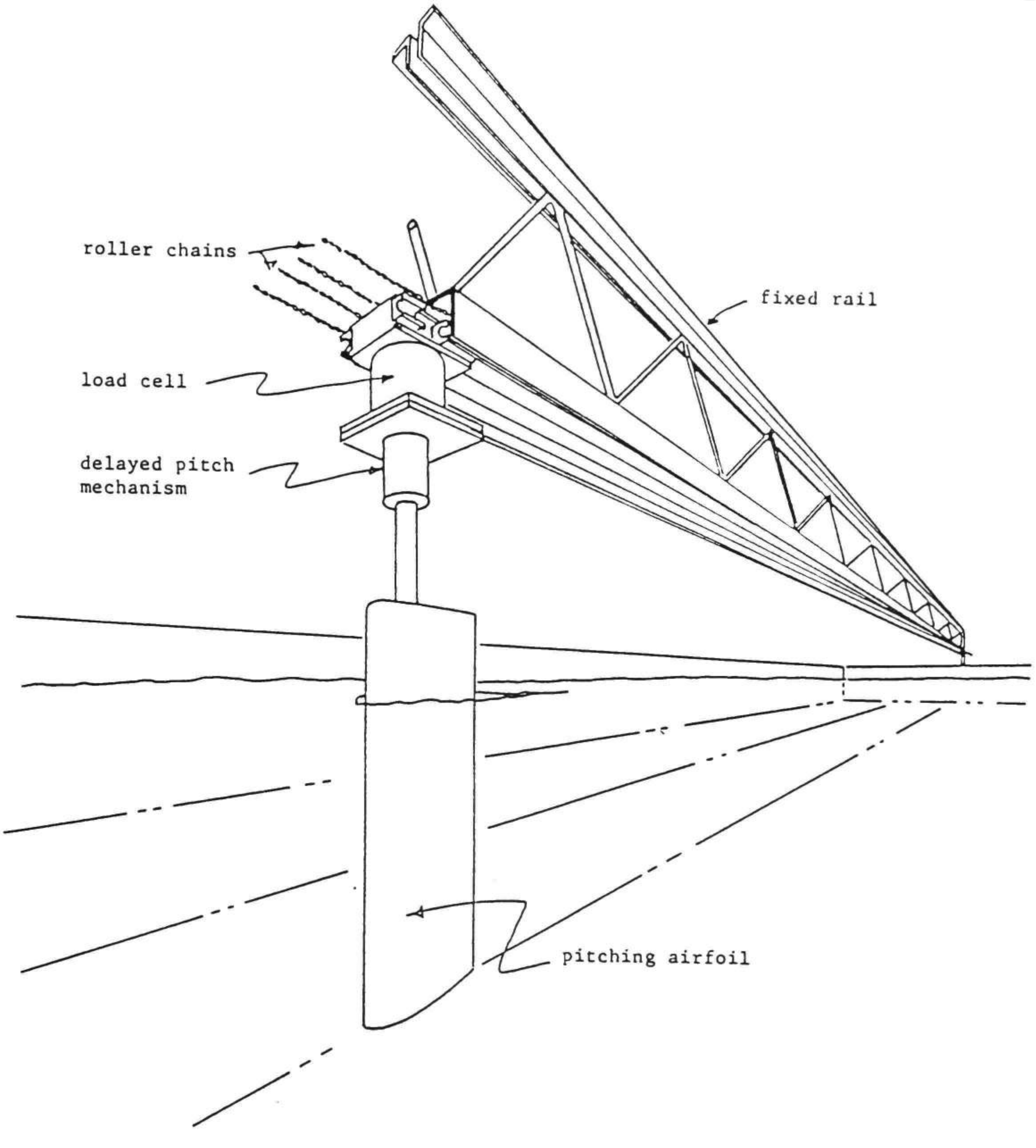
roller chains
fixed rail
load cell
delayed pitch mechanism
pitching airfoil

Figure 3. Schematic of General Test Setup

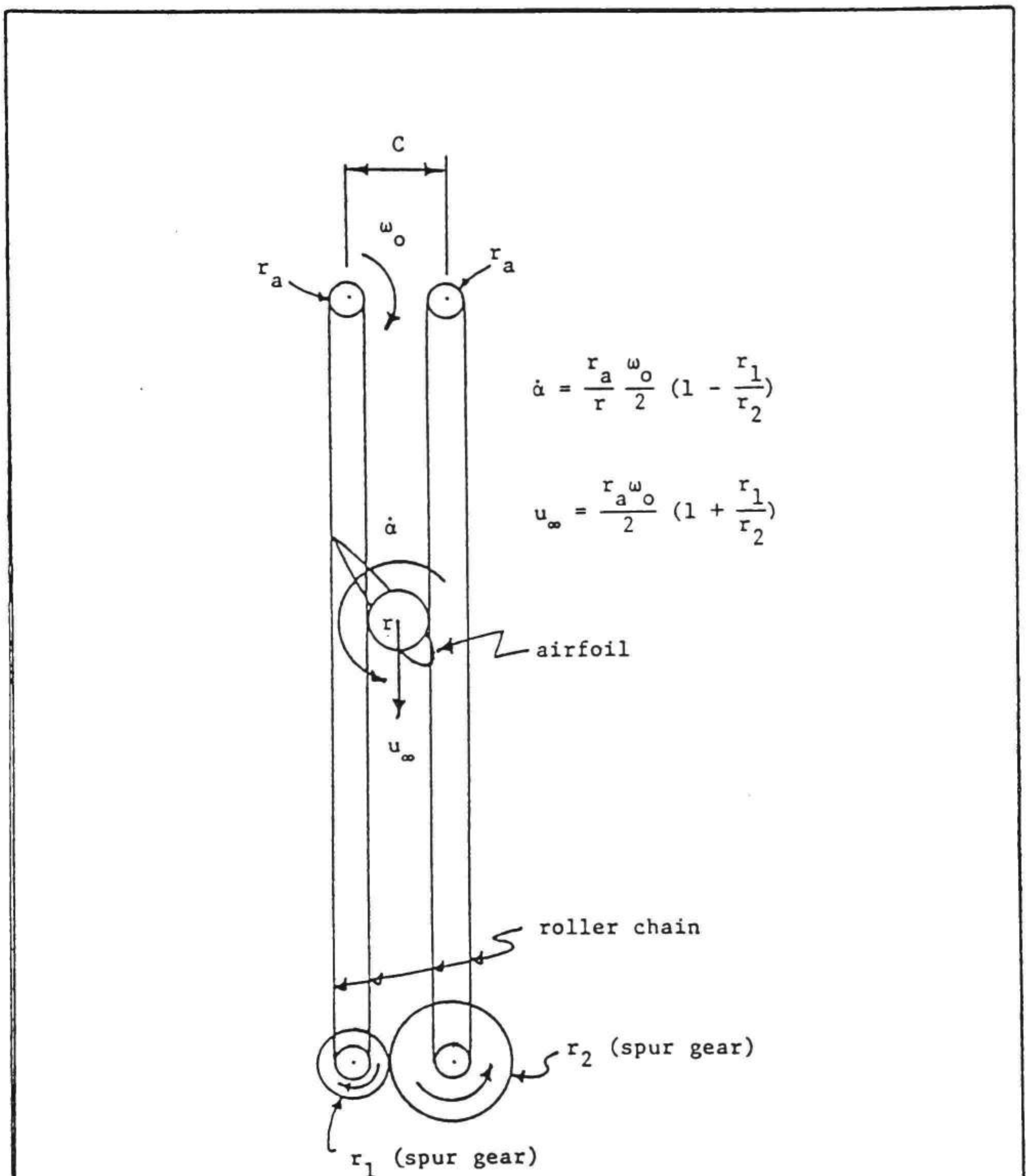
c
ω_o
r_a
r_a
$\dot{\alpha} = \frac{r_a}{r}\frac{\omega_o}{2}(1 - \frac{r_1}{r_2})$
$u_\infty = \frac{r_a \omega_o}{2}(1 + \frac{r_1}{r_2})$
$\dot{\alpha}$
r
airfoil
u_∞
roller chain
r_2 (spur gear)
r_1 (spur gear)

Figure 4. Schematic of Drive Mechanism

mechanism was employed which allows the airfoil to move about three chord lengths before the pitching motion begins.

In the present experiment all measurements were performed on a NACA 0015 airfoil ($c = 14$ in) pitching about its quarter chord over a range of pitching rates ($.1 < K < 1$). The Reynolds number was held constant at 1×10^5. A plot of angle of attack versus time for the six pitching rates considered is shown in Figure 5.

The data acquisition process was automated using a Hewlett-Packard 9835A micro-computer, and a HP6940B equipped with a HP69336A high-speed A/D converter and HP69422A high-speed scanner. This system is capable of sampling rates up to 20 kHz.

2.3 Flow Visualization

Flow visualization data were obtained on a NACA 0015 airfoil pitching about its quarter chord at non-dimensional pitching rates of .088, .19, .29, .51, .71, and .99. The photographs shown in Figure 6 are representative of the results for the cases of moderate ($K = .19$) pitching rate. In general, the flow visualization data were particularly useful in analyzing leading edge stall inception and deep-stall events.

A schematic of the flow visualization experiment arrangement is shown in Figure 7. The flow was marked by use of a hydrogen bubble wire placed about one-half chord upstream of the airfoil. McAlister and Carr [22] have successfully used this technique to visualize dynamic stall processes on airfoils oscillating in a water tunnel. The bubble wire in this study was a "ladder" type probe of the kind discussed in reference

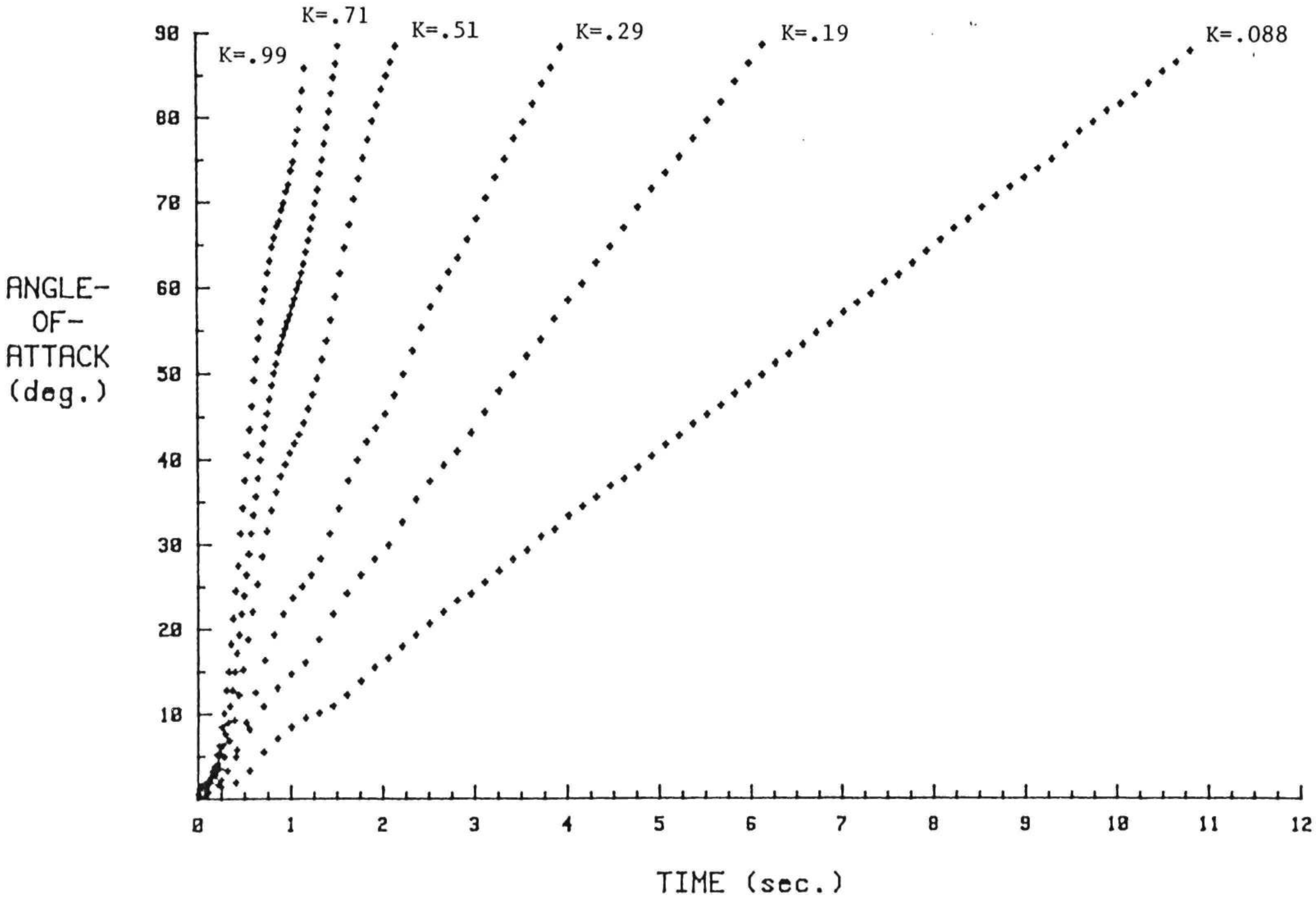

Figure 5. Constant Pitching Rate Angle of Attack Data

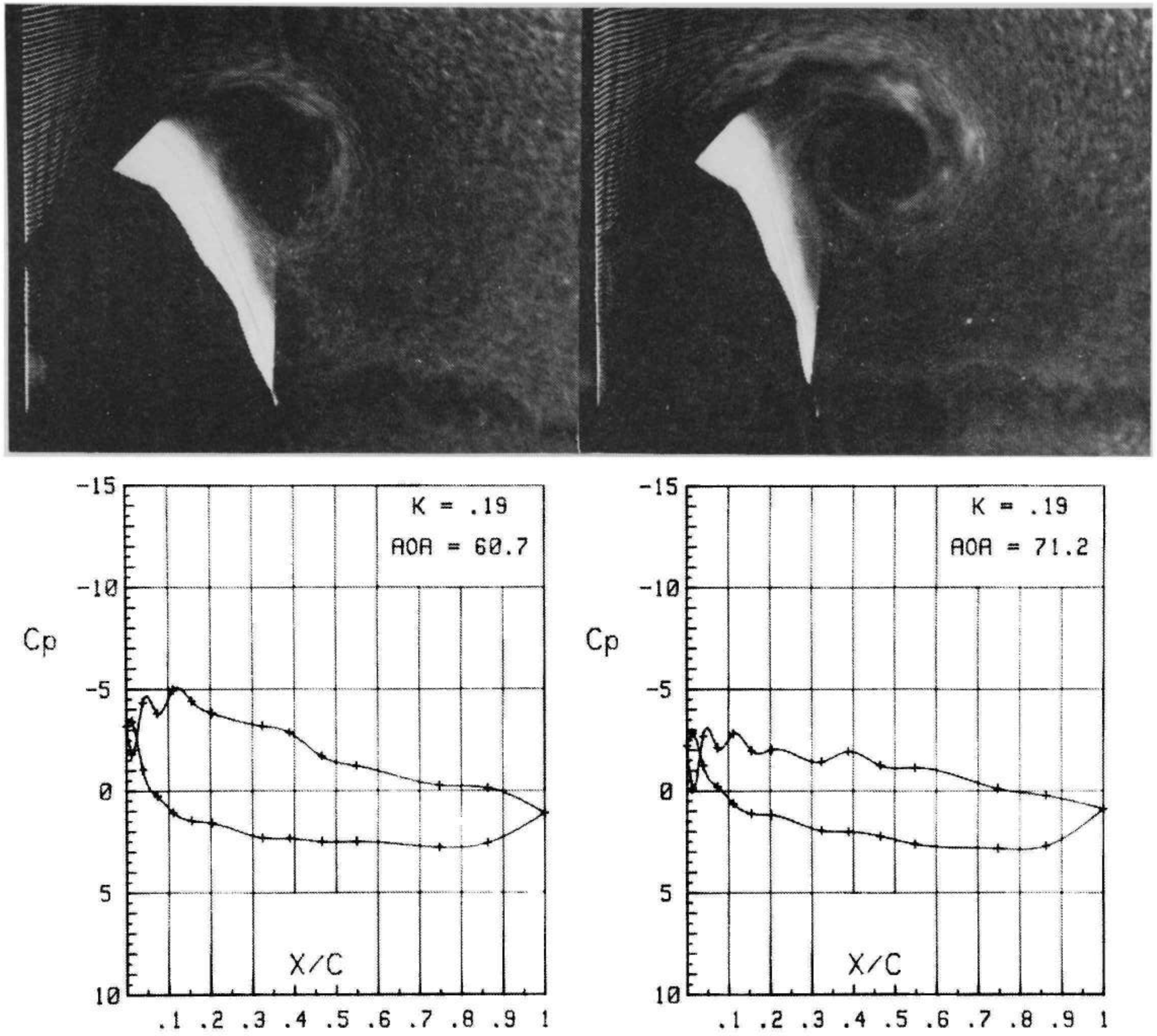

Figure 6. Typical Flow Visualization Results for K = 0.19

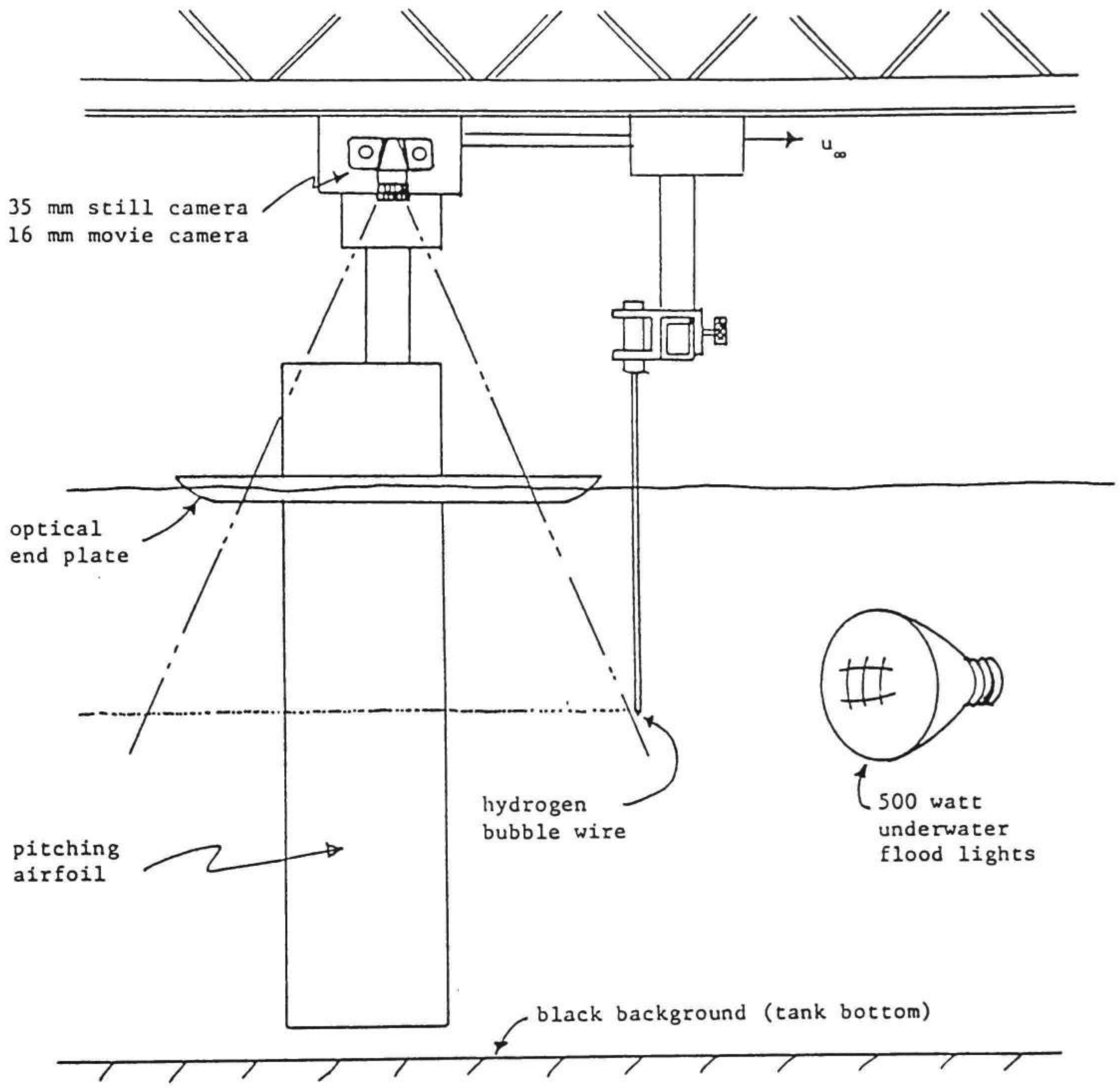
u_∞
35 mm still camera
16 mm movie camera
optical end plate
hydrogen bubble wire
500 watt underwater flood lights
pitching airfoil
black background (tank bottom)

Figure 7. Schematic of Experimental Arrangement for Flow Visualization

[34]. In addition, approximately 18 lbs. of anhydrous sodium sulfate was added to the tank water to increase the rate of hydrogen production.

The flow was photographed using both a 35-mm Olympus camera and a Zenith VM6000 video camera mounted to the moving carriage. The 35-mm camera was triggered at preselected angles of attack by the HP9835 data acquisition system which monitors the signal from an angular position transducer mounted on the pitch axis shaft. The flow was illuminated by eight 500 watt underwater flood lights. For the hydrogen bubble experiments, the normally white bottom of the tow tank was covered with a black plastic panel within the camera field of view.

2.4 Pressure Distributions and Integrated Forces

Surface pressure measurements were made on a NACA 0015 airfoil at the locations shown in Table 1. A schematic of the test model is shown in Figure 8. The pressure ports were connected to diaphram pressure transducers (Validyne DP45-18) via copper tubing which was inserted through the hollow core of the blade. At each port location the tubing was cemented in place then ground flush with the airfoil contour. The time response of the model has been shown to be completely adequate [35]. Each transducer signal was modulated (Validyne CD-18) and introduced into the HP data acquisition system.

Typical pressure distributions for the case of K = .088 are shown in Figure 9. Also shown in Figure 9 are the data of Walker and Helin [33]. Here the pressure coefficient is defined as

$$C_p = \frac{P - P_a}{\frac{1}{2}\rho U_\infty^2} \qquad (3)$$

TABLE 1

PRESSURE PORT LOCATION COORDINATES

Port #	x/c	y/c
1	0	0
2	.013	.024
3	.039	.040
4	.075	.052
5	.113	.061
6	.156	.068
7	.207	.072
8	.322	.075
9	.388	.073
10	.463	.069
11	.551	.062
12	.745	.040
13	.864	.024
14	1.0	.001

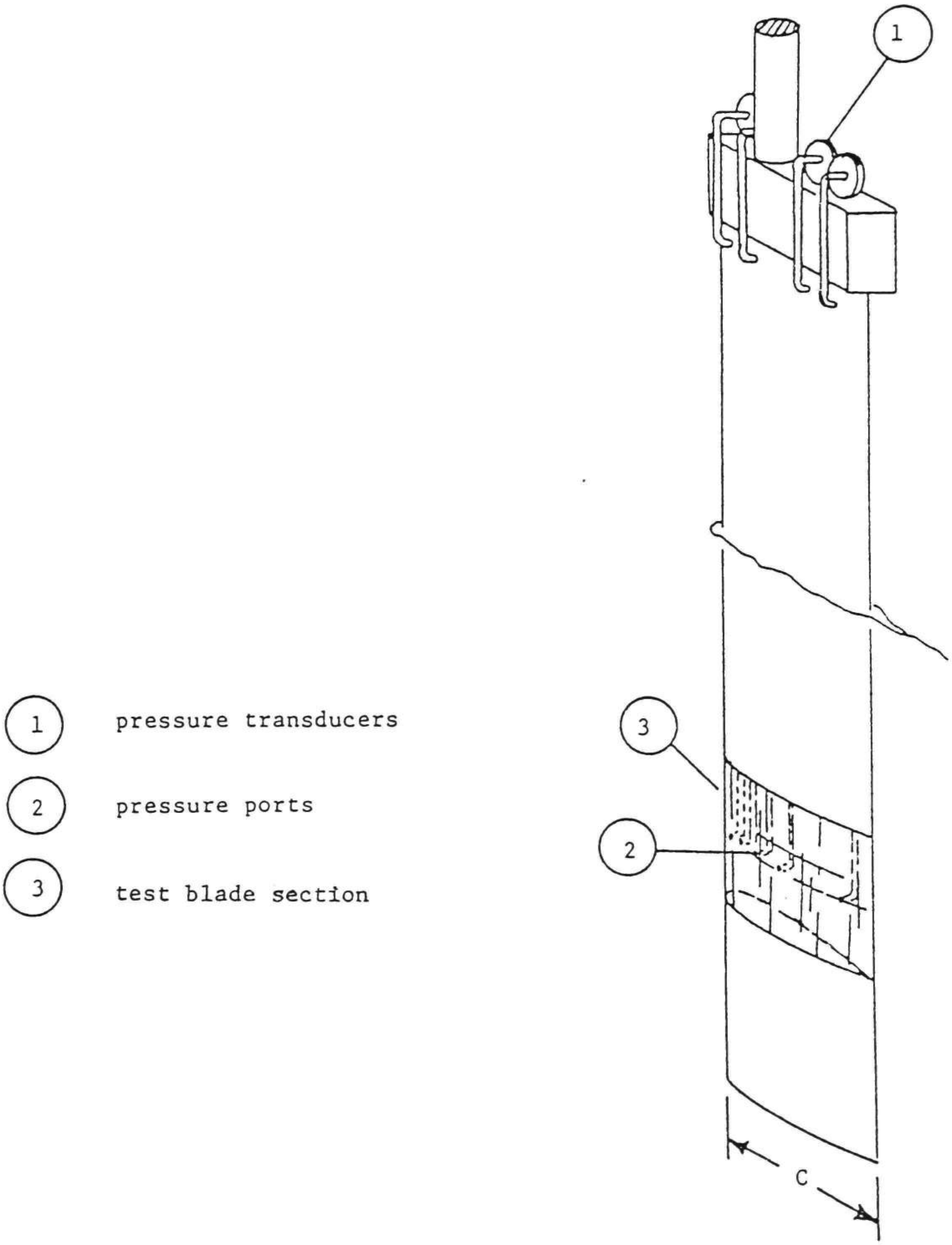
①
②
③
C
① pressure transducers
② pressure ports
③ test blade section

Figure 8. Schematic of Pressure Measurement Test Setup

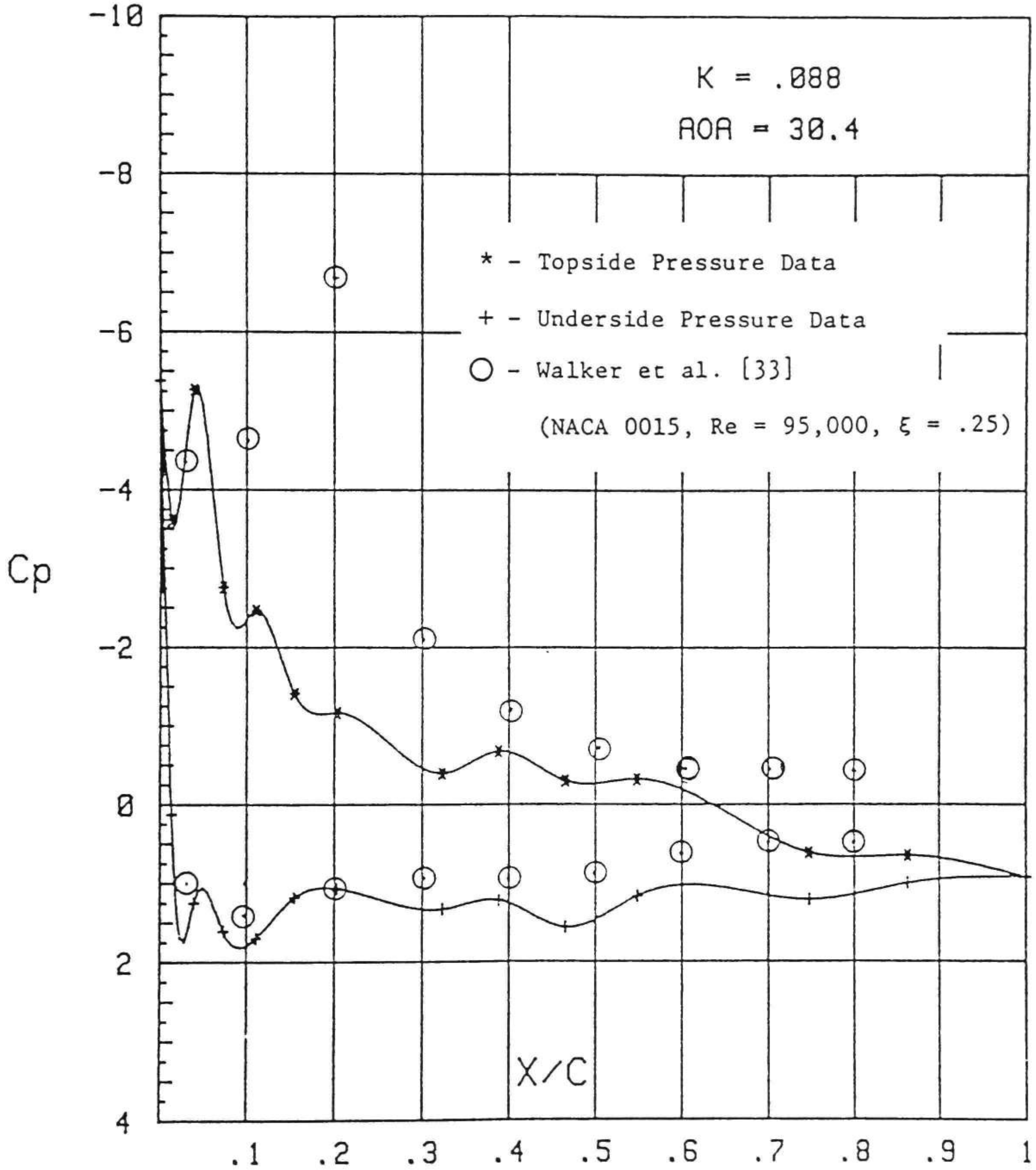

Figure 9. Typical Pressure Distribution for K = .088
a) $\alpha = 30.4°$

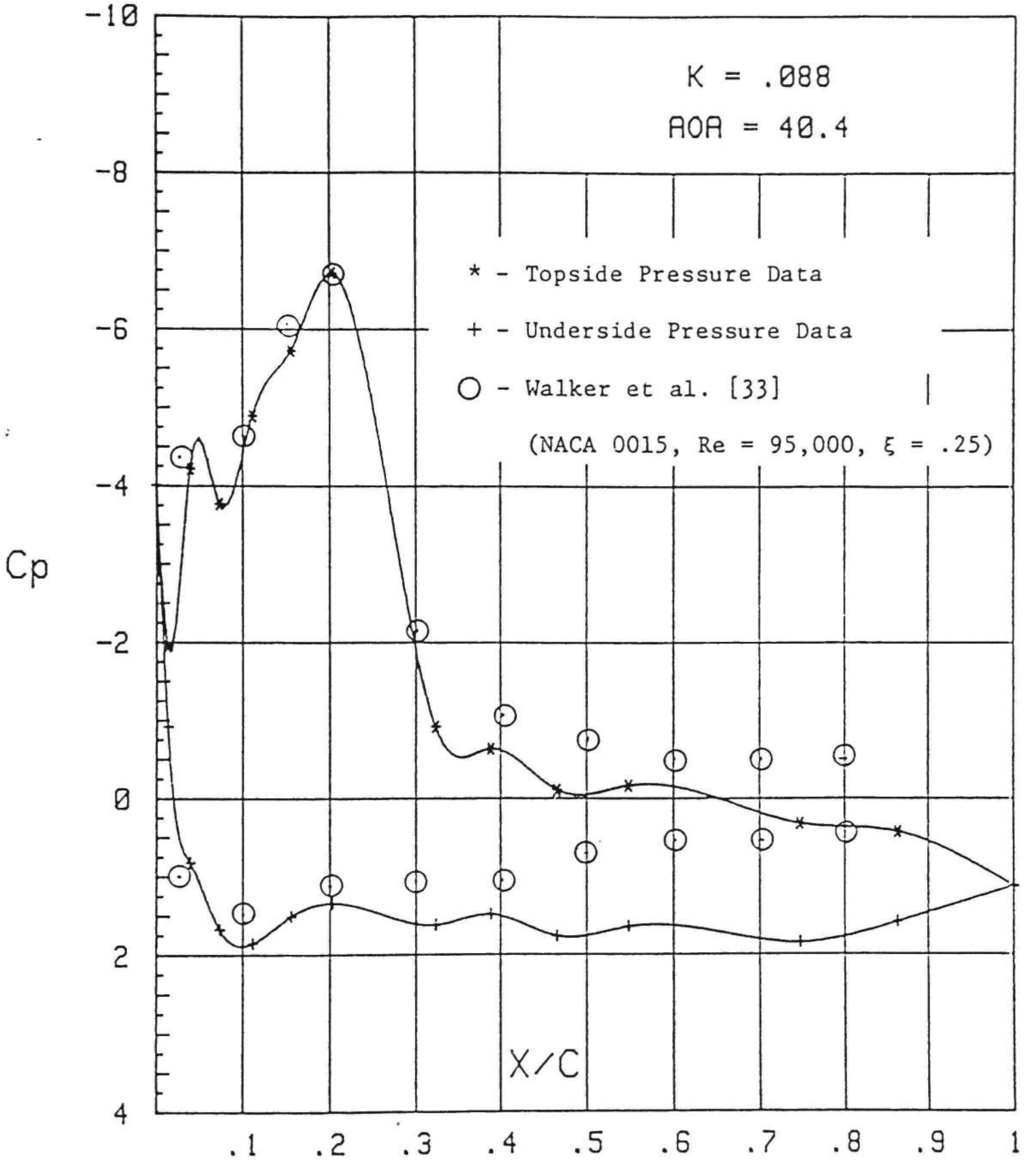

Figure 9. Continued
b) $\alpha = 40.4°$

where P_a is the atmospheric pressure. The Validyne demodulator unit used in the tests is capable of simultaneously conditioning seven signals. Therefore, acquiring 27 data points for each distribution required four experimental runs. In addition, each test was performed twice to determine the repeatability of the data. The discrepancies from run to run were found to be minor. It is interesting to note the similarity between the pressure distribution of Walker and Helin for an angle of attack of 30° and the distribution for an angle of attack of 40° measured in these tests as seen in Figure 9.

The normal and tangential forces may be obtained by integrating the pressure distribution over the chord and thickness, respectively. The integration was carried out by assuming that the pressure between the most aft pressure port and the trailing edge remained constant at the value registered at that port. This assumption is reasonable since near the trailing edge the pressure drops abruptly to the value at the trailing edge. The lift and drag coefficients may be then computed using

$$\begin{aligned} C_\ell &= F_n^+ \cos\alpha + F_t^+ \sin\alpha \\ C_d &= F_n^+ \sin\alpha - F_t^+ \cos\alpha \end{aligned} \tag{4}$$

Here F_n^+ and F_t^+ are the non-dimensional normal and tangential forces defined as

$$\begin{aligned} F_n^+ &= \frac{F_n}{\frac{1}{2}\rho U_\infty^2 c} \\ F_t^+ &= \frac{F_t}{\frac{1}{2}\rho U_\infty^2 c} \end{aligned} \tag{5}$$

where F_n and F_t are the normal force and tangential force per unit span.

Integrated lift and drag data for a non-dimensional pitching rate of K = .088 are shown in Figures 10 and 11, respectively. As can be seen, the dynamic forces are approximately three times larger than the static loads for a NACA 0015 (the maximum lift and drag coefficients in the static case are approximately one). For the higher pitching rates, the integrated lift force is negative at small angles of attack as can be seen in the lift force plots presented in Appendix C. The reason for this is not completely understood at present, but may be associated with an inertial effect on the water standing in the pressure lines or in the pressure transducer diaphrams which moved with the airfoil. Also shown in Figure 10 are the data of Francis et al. [29] and Walker and Helin [33]. As pointed out previously, there seems to be a discrepancy of about 10° angle of attack between the present data and that of Walker and Helin. As seen in Figure 10 the lift force of Walker and Helin begins to decline approximately 10° sooner than the lift force measured here.

2.5 Strain Gage Measurements

Measurements of normal and tangential forces were performed on a NACA 0015 airfoil for the six pitching rates previously noted. Two repetitive runs were made to determine the repeatability of the data.

As indicated in Figure 12 the two forces were measured using strain gages located on a load cell mounted at the quarter chord. Each bridge was arranged so that it was only sensitive to the desired force. The

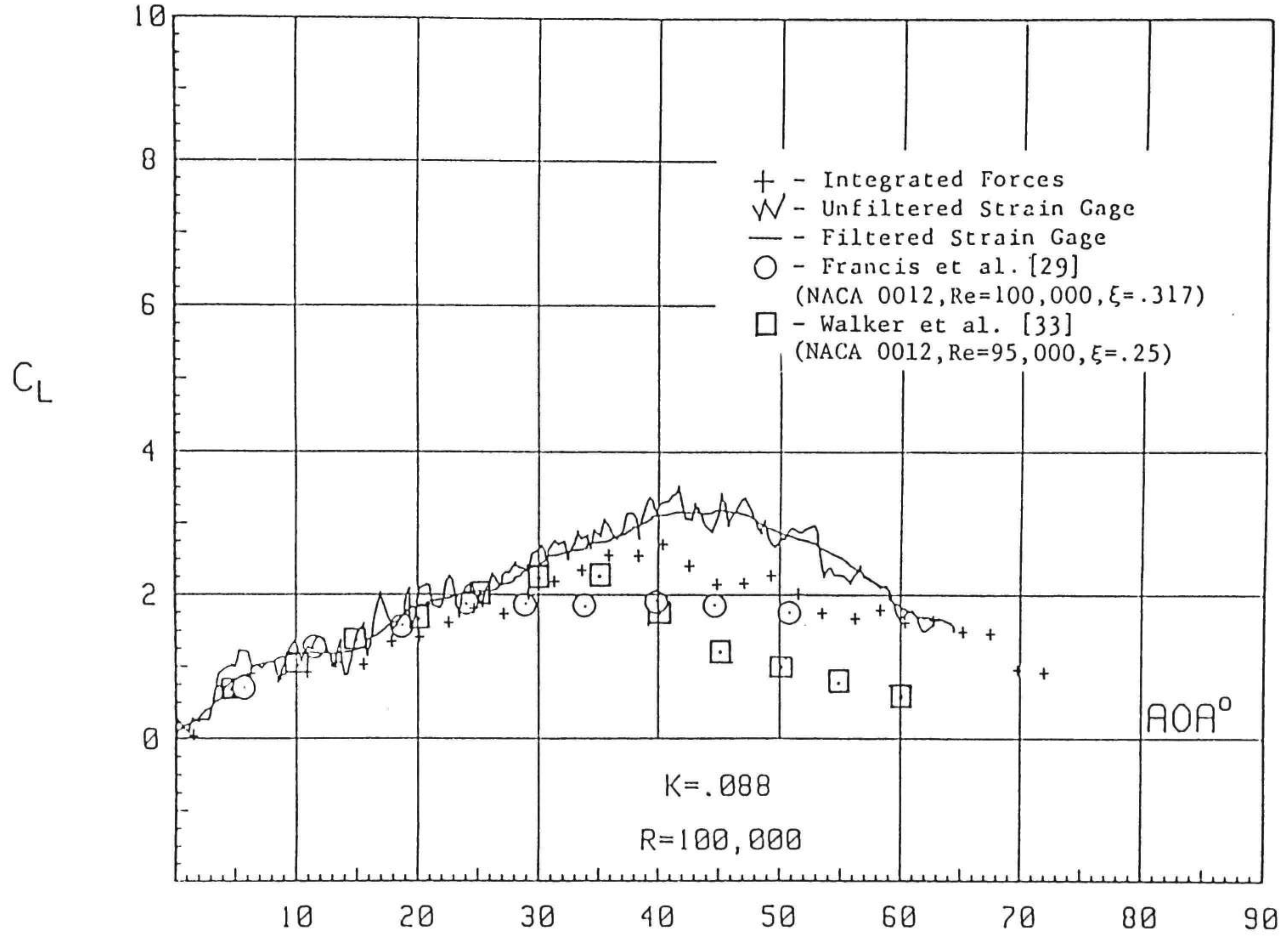

Figure 10. Typical Lift Coefficient Data for K = .088

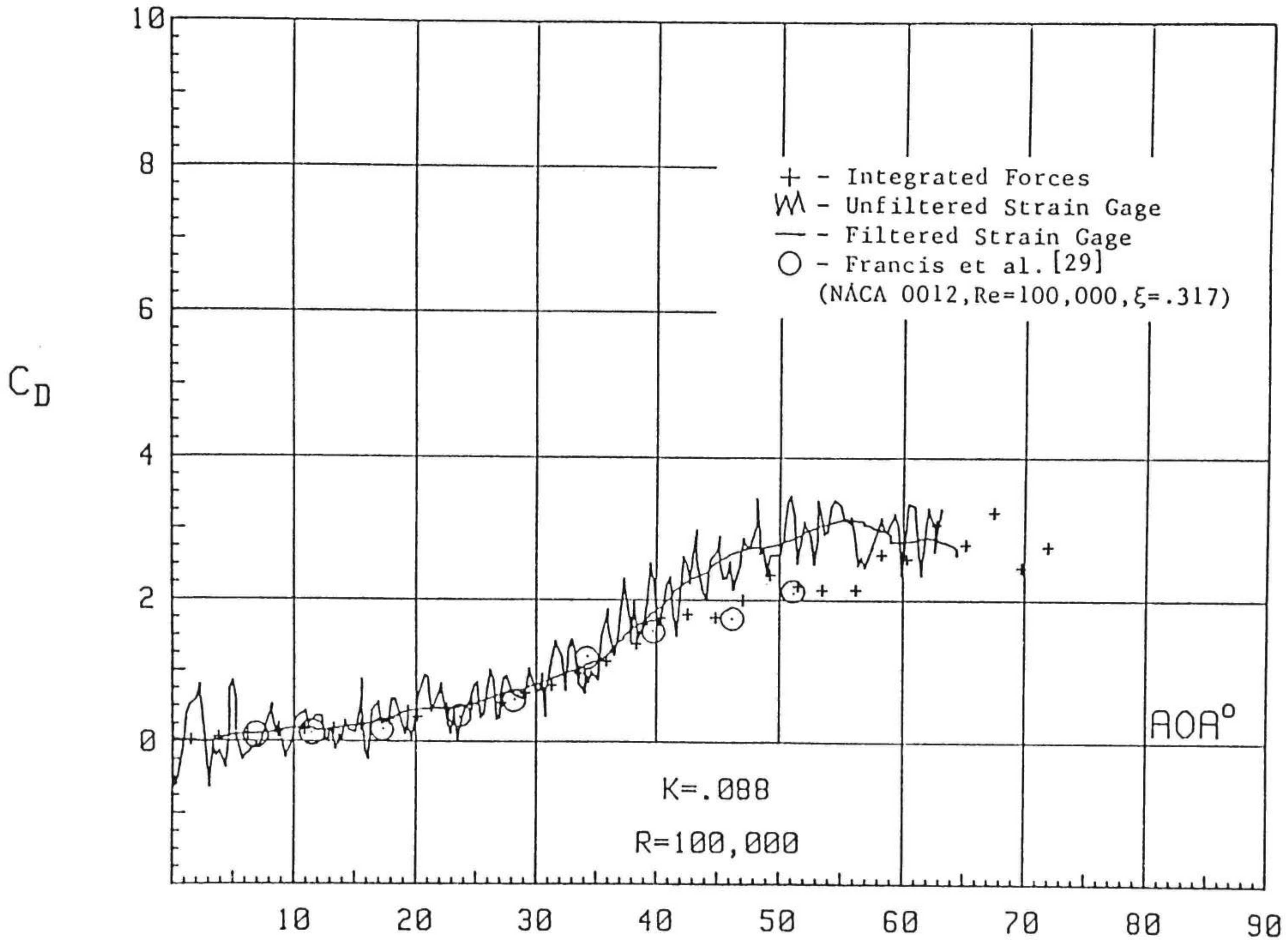

Figure 11. Typical Drag Coefficient Data for K = .088

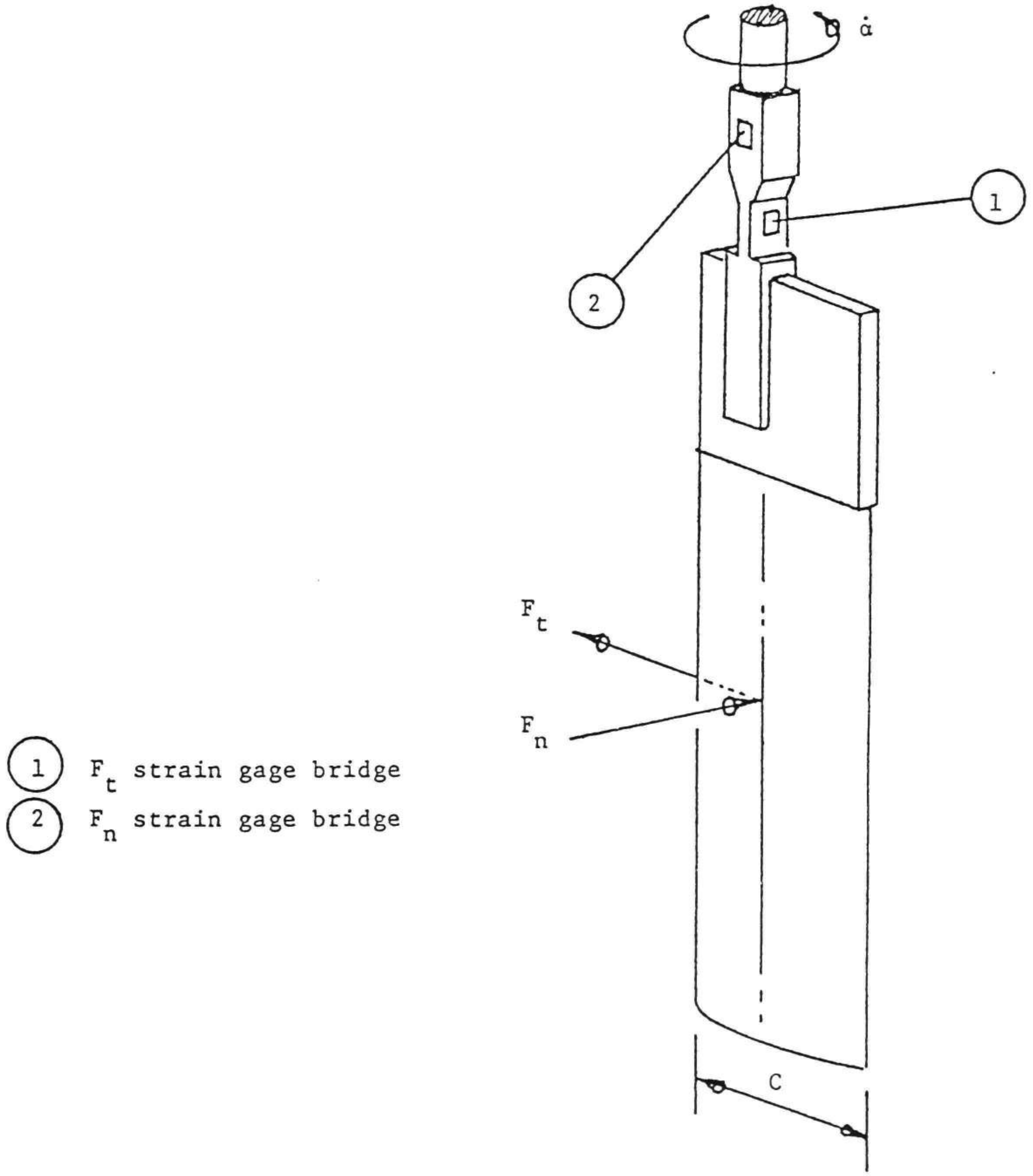
$\dot{\alpha}$
1
2
F_t
F_n
C
① F_t strain gage bridge
② F_n strain gage bridge

Figure 12. Schematic for Load Cell Measurements

instrumentation consisted of four 350 ohm strain gages connected in a Wheatstone bridge configuration, a 15 vdc Calex power supply, a Calex model 176 amplifier, and a Krohnite model 3343 low pass filter. A 15 vdc signal was applied across the bridge. The output voltage was amplified approximately 1000 times to increase the signal level into the desired voltage range (0 V to 10 V). In addition to recording the "raw" output signal, the output from each bridge was passed through a filter to low pass the signal below a cutoff frequency of 1.5 Hz. This was done in order to eliminate extraneous mechanical noise at about 2 Hz. Finally, the signal was introduced into the data acquisition system and stored on magnetic tape.

The output voltages from the strain gage bridges E_1 and E_2 are related to the blade forces by

$$\begin{aligned} F_n &= C_1 E_1 \\ F_t &= C_2 E_2 \end{aligned} \tag{6}$$

where C_1 and C_2 are calibration constants. It should be noted that E_2 includes the effect of the centrifugal force given by

$$F_c = mR\dot{\alpha}^2 \tag{7}$$

where m is the mass of the blade and R is the distance from the quarter chord to the center of mass of the airfoil. While this effect is relatively small it was nevertheless subtracted from the equation for F_t.

The lift and drag coefficients were computed using equations (4) and (5) discussed in section 2.4. The drag force results were corrected for finite aspect ratio effects. The induced drag [36] is given by

$$C_{Di} = \frac{C_L^2}{\pi AR}\left(\frac{1}{1 + \frac{1}{4} HR}\right) = \frac{C_L^2}{\pi AR_{eff}}$$

$$AR_{eff} = AR\left(1 + \frac{1}{4} HR\right) \tag{8}$$

$$AR = b/c$$

$$HR = b/h$$

where b is the airfoil span and h is the distance from the free end of the airfoil to the bottom of the tank (b = 80 in., h = 1 in.). The effective aspect ratio of the blade was approximately 120, and therefore these corrections tend to be small. Typical filtered and unfiltered strain gage data are shown in Figures 10 and 11.

CHAPTER III

DISCUSSION OF RESULTS

3.1 Aerodynamic Loads

Lift and drag coefficients obtained from strain gage measurements for the three lowest pitch rates are given in Figure 13 while those for the three highest rates are given in Figure 14. These data are also given in Appendix C along with lift coefficients obtained from integral surface pressure measurements.

In order to aid in the understanding of the lift curve shapes (especially at low geometric angles of attack), Figure 15 is given which presents the relationship between the geometric angle of attack and the angle of attack at the nose of the airfoil. In general, the relative angle of attack at the airfoil leading edge is reduced due to the upward motion of the leading edge. The plots in Figure 15 are based on pitching about the quarter chord point on the airfoil.

At the lowest pitching rates (Figure 13) the lift curves can be characterized by an initial rapid increase in lift up until about a 10° to 15° geometric angle of attack. At this point the lift curve slope is decreased somewhat. This change in slope is associated with the onset of stall. The lift curve slopes continue to increase until a maximum is reached in the neighborhood of 40° - 45° geometric angle of attack. The maximum lift is a function of the non-dimensional pitch rate K and increases with increasing K. The drag coefficients are relatively similar at the lowest pitching rates out to geometric angles of attack of the order of 50°. After this point there is a tendency for the curves

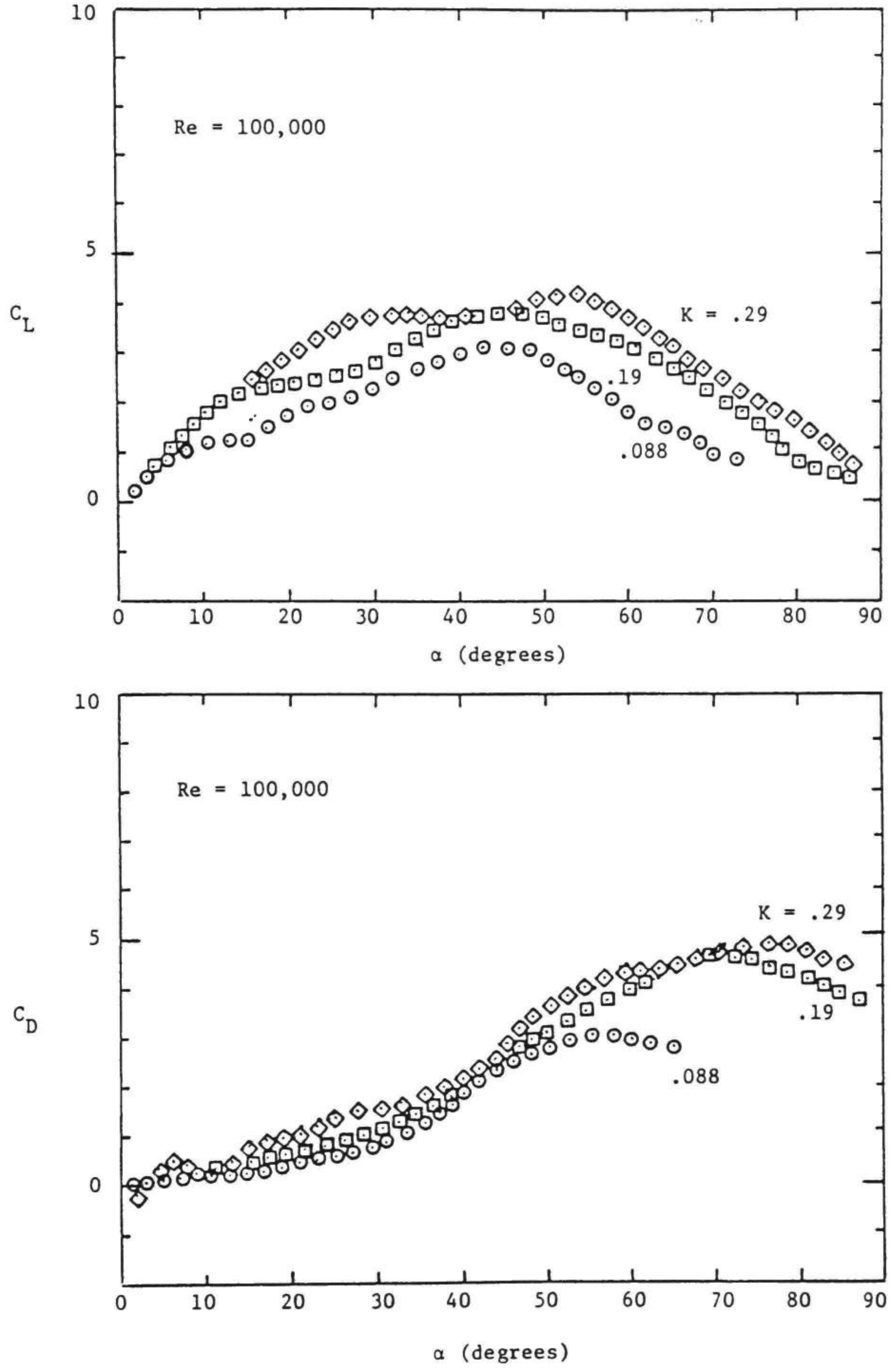

Figure 13. Low Pitch Rate Lift and Drag

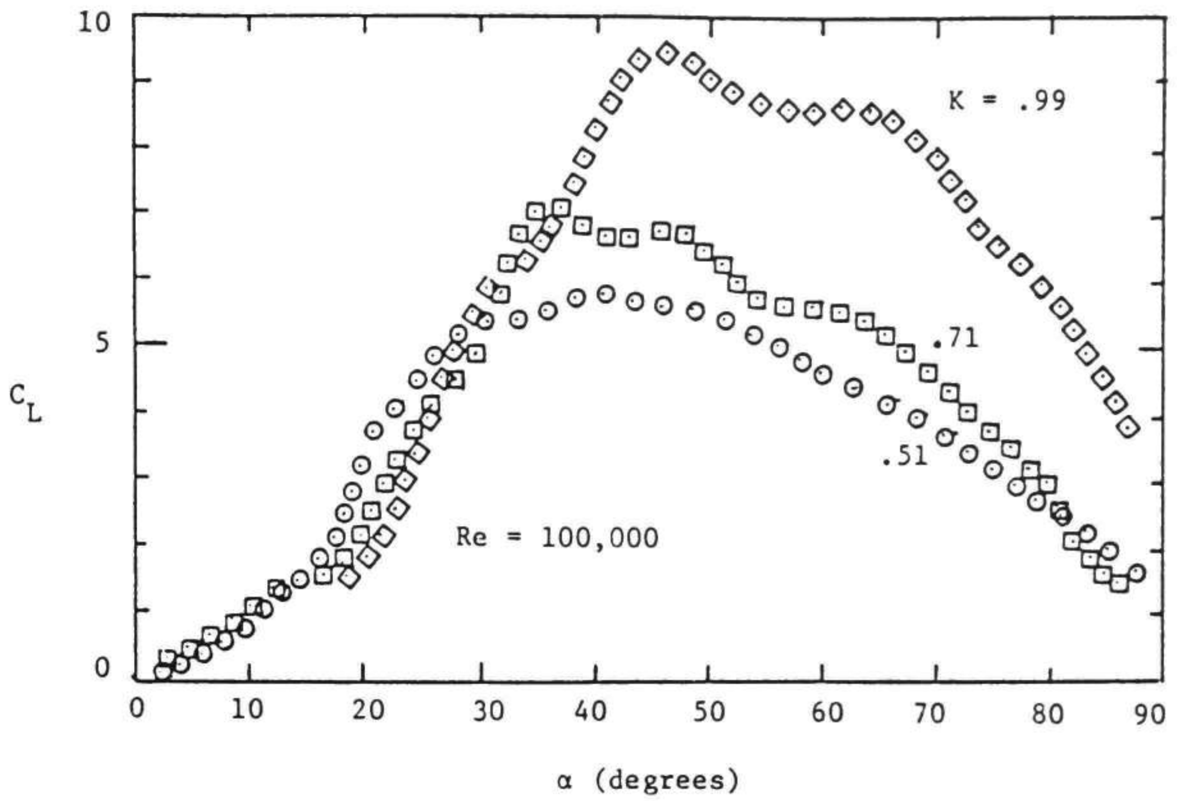

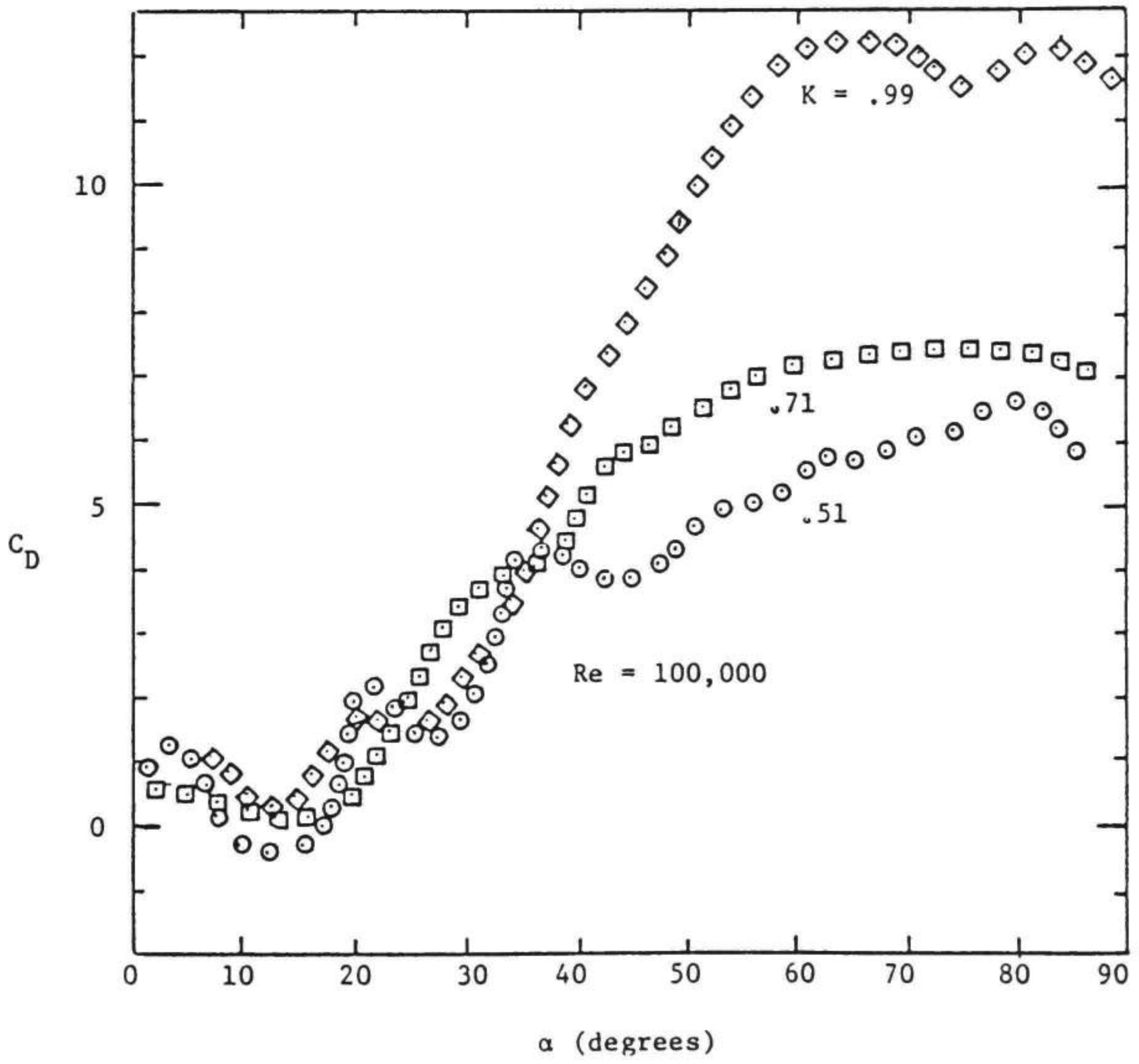

Figure 14. High Pitch Rate Lift and Drag

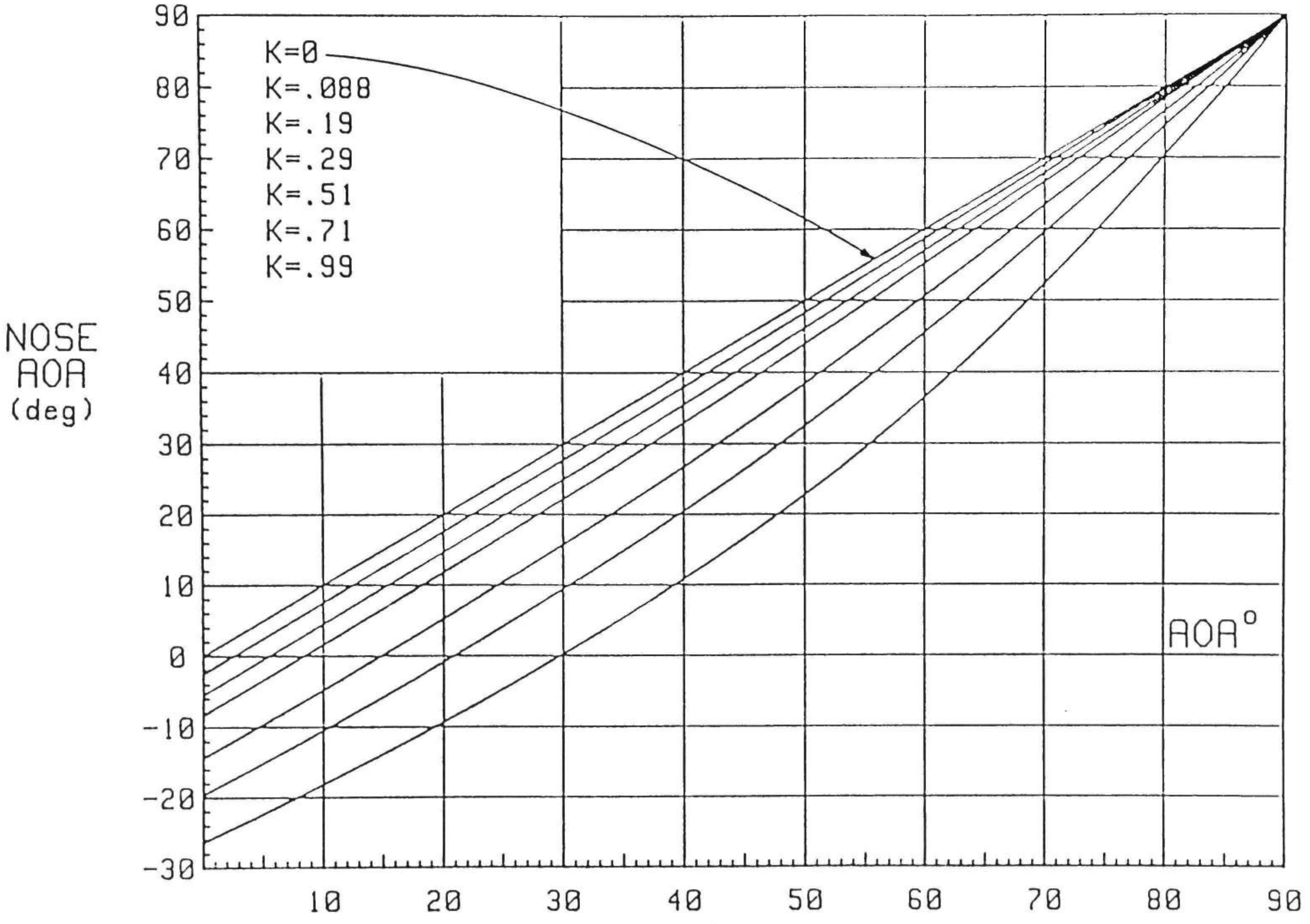

Figure 15. Effective Nose Angle of Attack as a Function of Geometric Angle of Attack

at the larger K values to continue to rise while those at the lower values flatten out.

At the high pitching rates (Figure 14) the lift curves display an initial slope which is less than the initial slopes for the low pitch rates. Referring to Figure 15 it is interesting to note that for a geometric angle of attack of 0° the nose angle of attack is less than -10° for each of the high pitch rate cases. This indicates that there may be a separated region near the nose on the underside (the suction side is the topside) causing a decrease in the lift curve slope. The large negative effective nose angles of attack give rise to a region of negative pressure near the leading edge on the underside and a region of positive pressure on the topside which effectively reduces the lift. This is discussed in more detail in Section 3.3. At geometric angles of attack between 15° to 20° where the nose angle of attack decreases below 10° the lift curve slope becomes steeper. Finally, at effective angles of attack of the order of 10° (geometric angles of 25° to 40°) the airfoil stalls again and the lift curve flattens and decays. The drag coefficients are similar at low angles of attack but depart dramatically from each other after the second stall occurs as may be seen in Figure 15.

3.2 Flow Visualization Data

The flow visualization results for the pitching rates of .088, .19, and .29 are shown in Figures 16-18. Also shown in these figures are the corresponding pressure distributions which will be discussed in the next section.

It may be seen that the flow at the three lowest pitch rates considered display similar features. The stall phenomenon is characterized

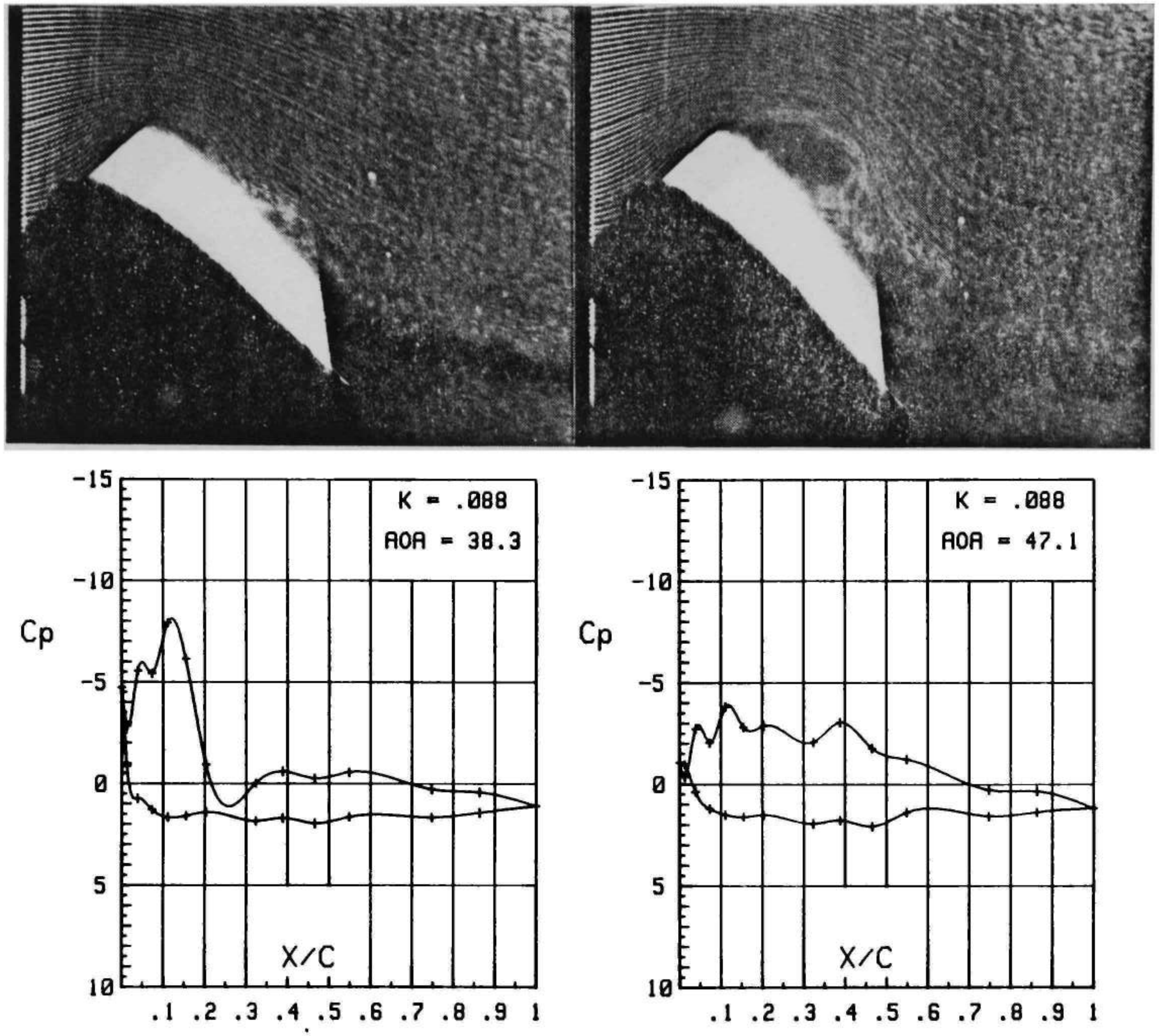

Figure 16. Flow Visualization and Pressure Data for K = 0.088

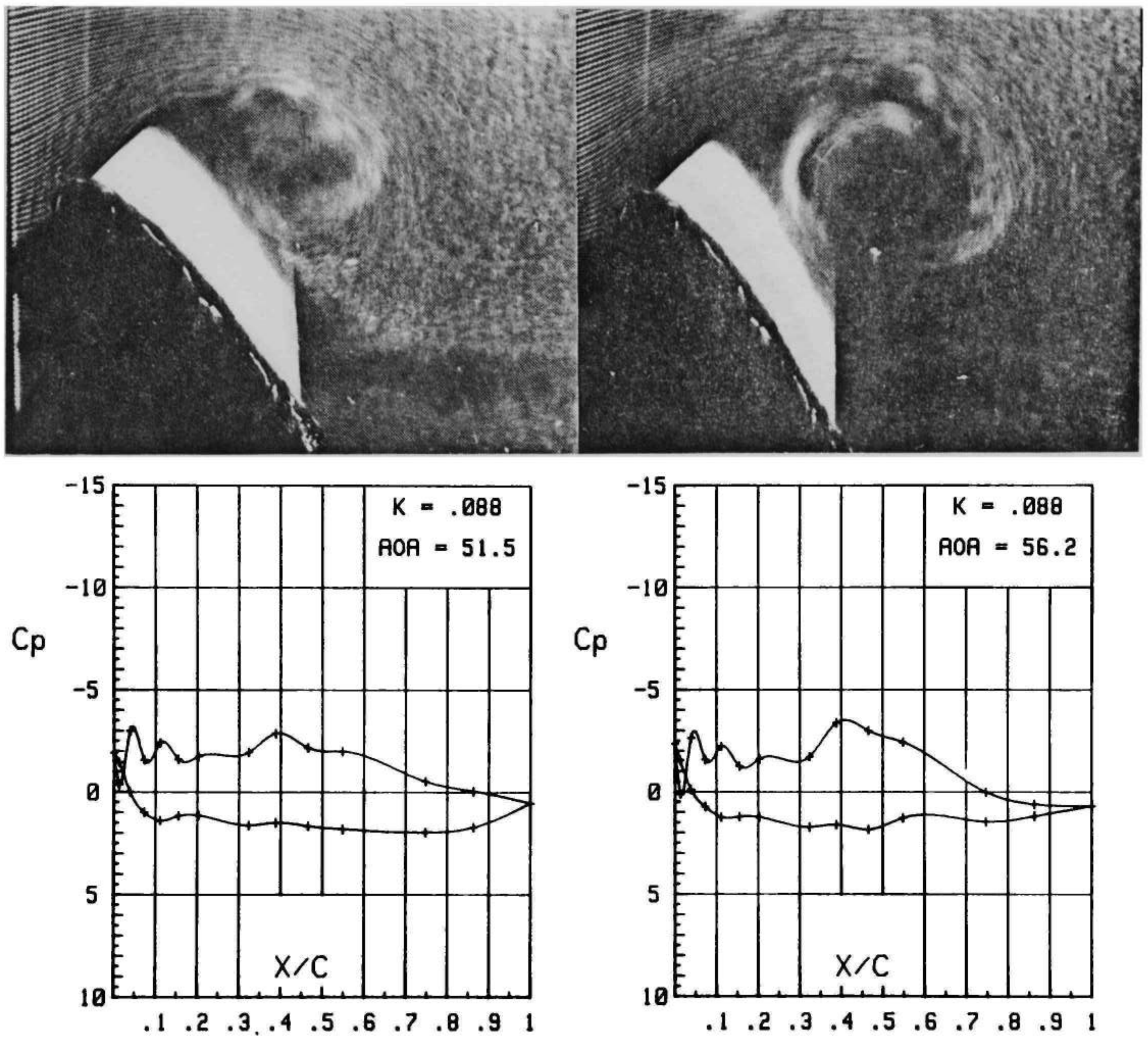

Figure 16. Continued

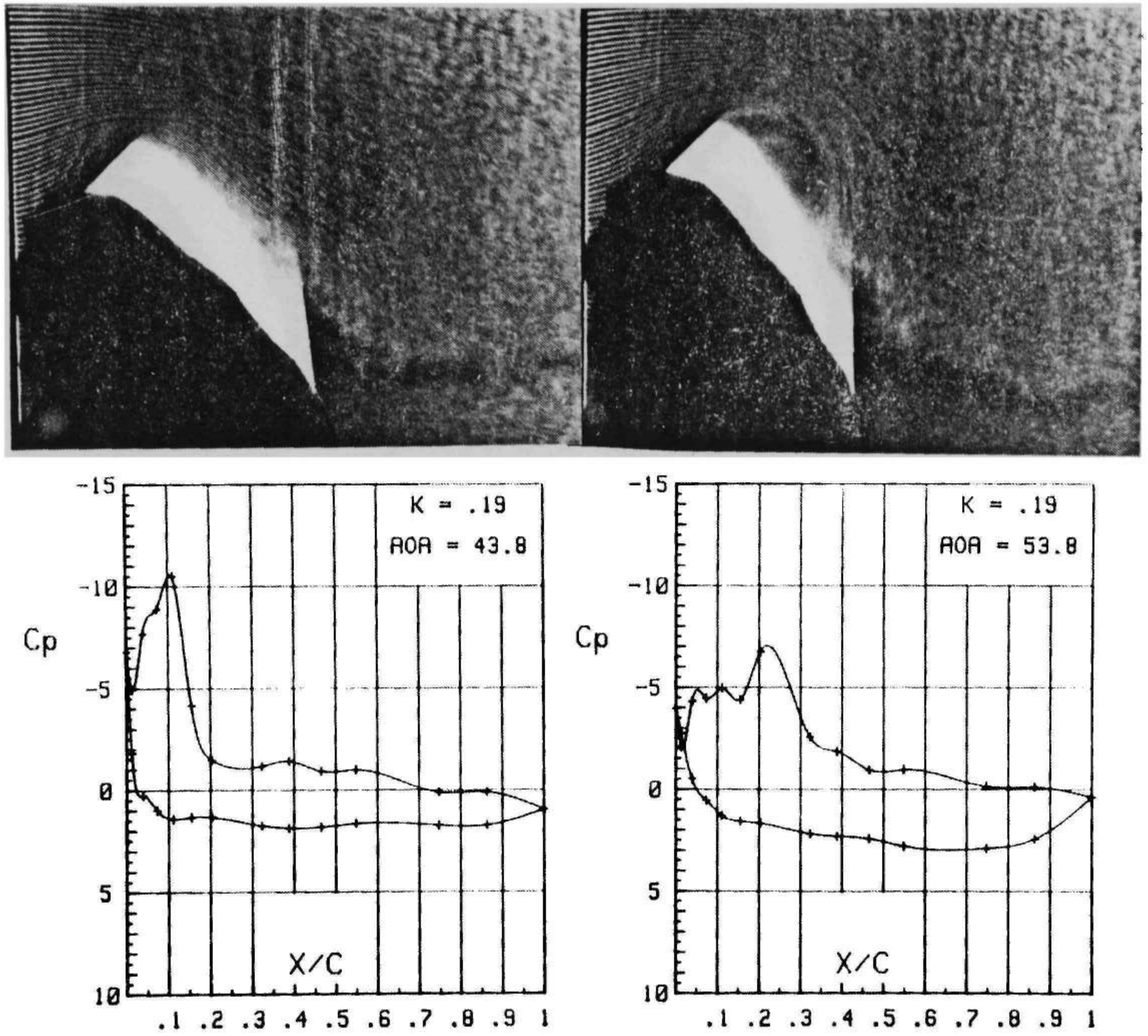

Figure 17. Flow Visualization and Pressure Data for K = 0.19

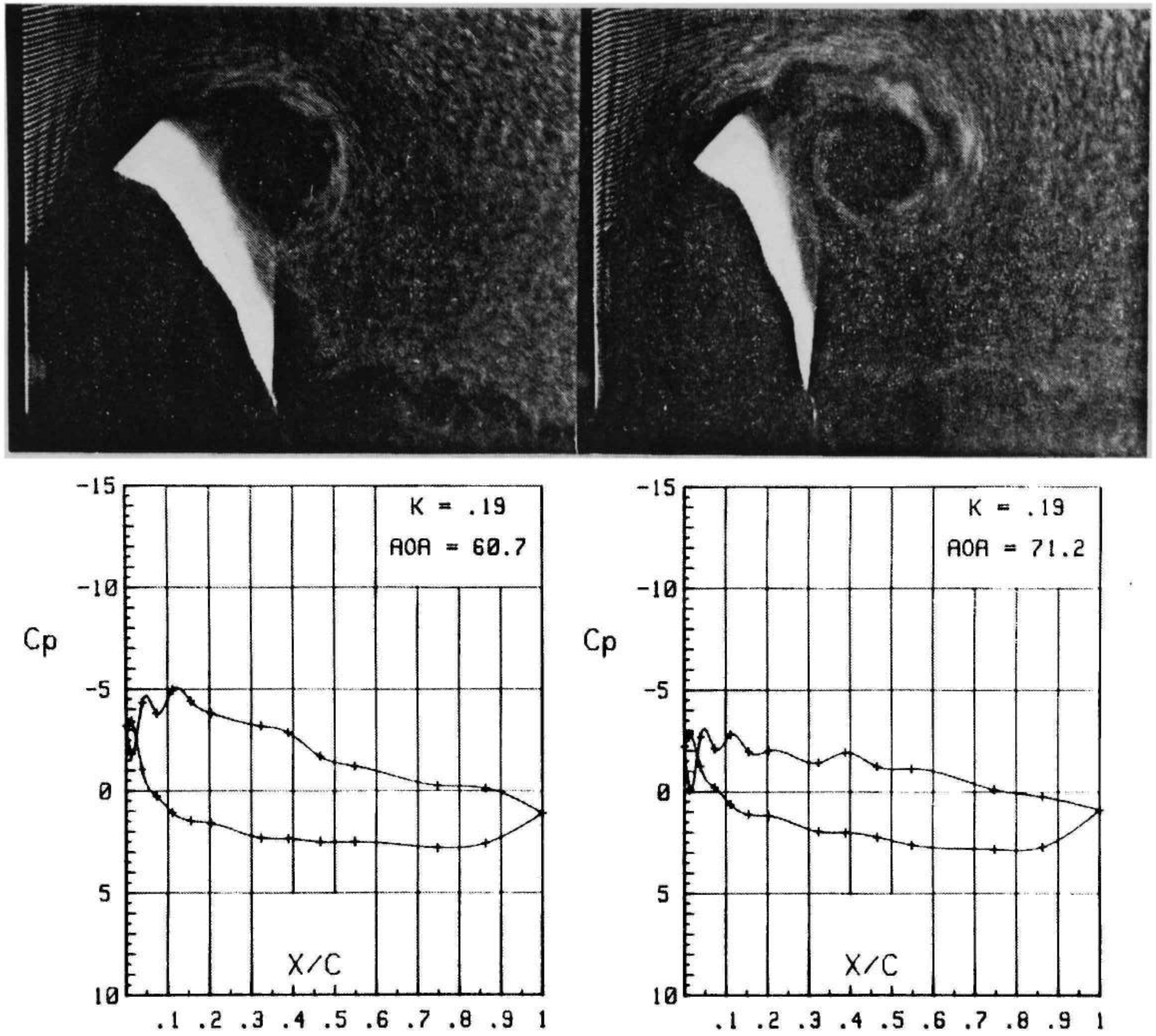

Figure 17. Continued

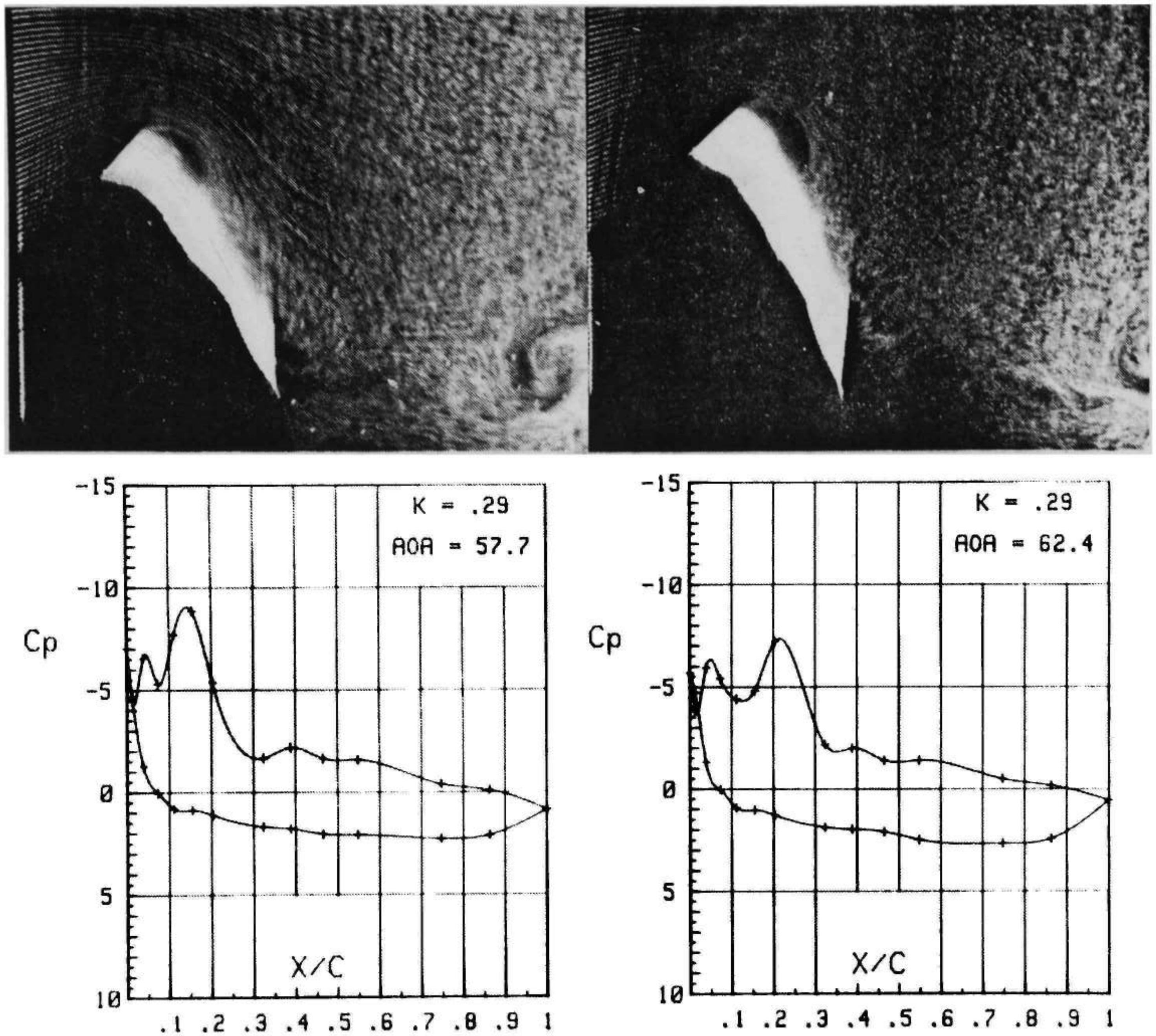

Figure 18. Flow Visualization and Pressure Data for K = 0.29

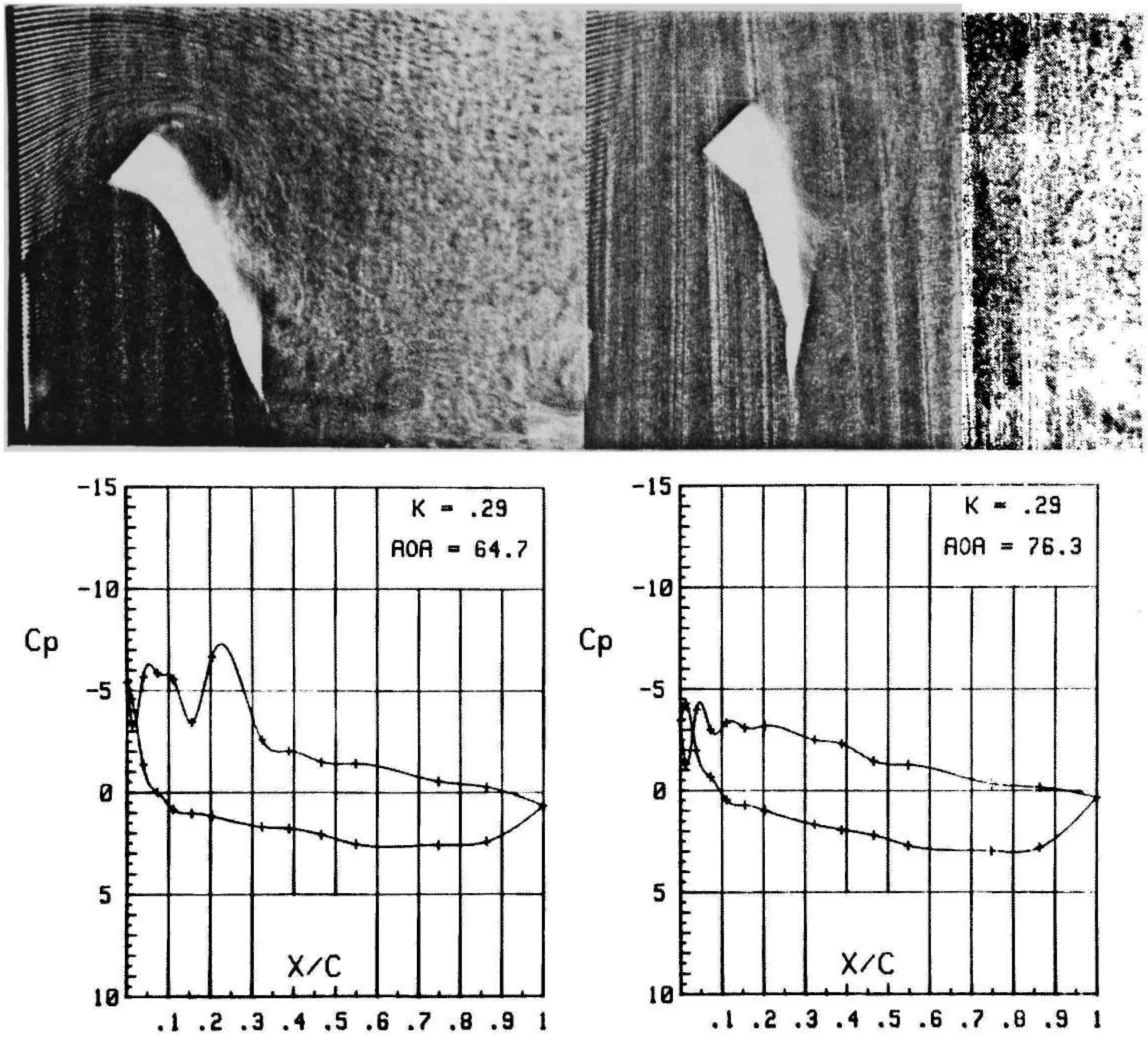

Figure 18. Continued

by the appearance of a separation bubble near the leading edge as can be clearly seen in the photograph for K = .29 at an angle of attack of 57.7° in Figure 18. As the angle of attack increases, vorticity is continuously shed from the leading edge and accumulates into the large "dynamic stall" vortex which may be seen for K = .19, α = 71.2° in Figure 17. Further inspection of the photographs indicate that the angle of attack at which the flow begins to separate increases with increasing pitching rate. For example, in the case where K = .088 the flow separates from the leading edge at an angle of attack around 38° whereas in the case where K = .29 separation does not occur until about 55°. This is not surprising since the effective angle of attack at the nose decreases with increasing pitch rate as pointed out in the previous section.

Another interesting feature of the stall phenomenon is the appearance of a secondary vortex on the rearward portion of the airfoil as may be seen in the visualizations for K = 0.088, α = 47.1° in Figure 16 and K = 0.29, α = 64.7° in Figure 18. Binary vortical structures such as these have been noted in other visualization studies [32]. This secondary vortex is not as energetic as the primary vortex and seems to become engulfed by the primary vortex as the airfoil enters the deep stall regime.

The flow visualizations for the non-dimensional pitching rates of .51, .71, and .99 are shown in Figures 19-21. Again, it is seen that increasing the pitching rate delays leading edge separation on the top-side of the airfoil. For instance, the photograph for K = 0.51, α = 82.4° in Figure 19 clearly shows a separated region while in the case

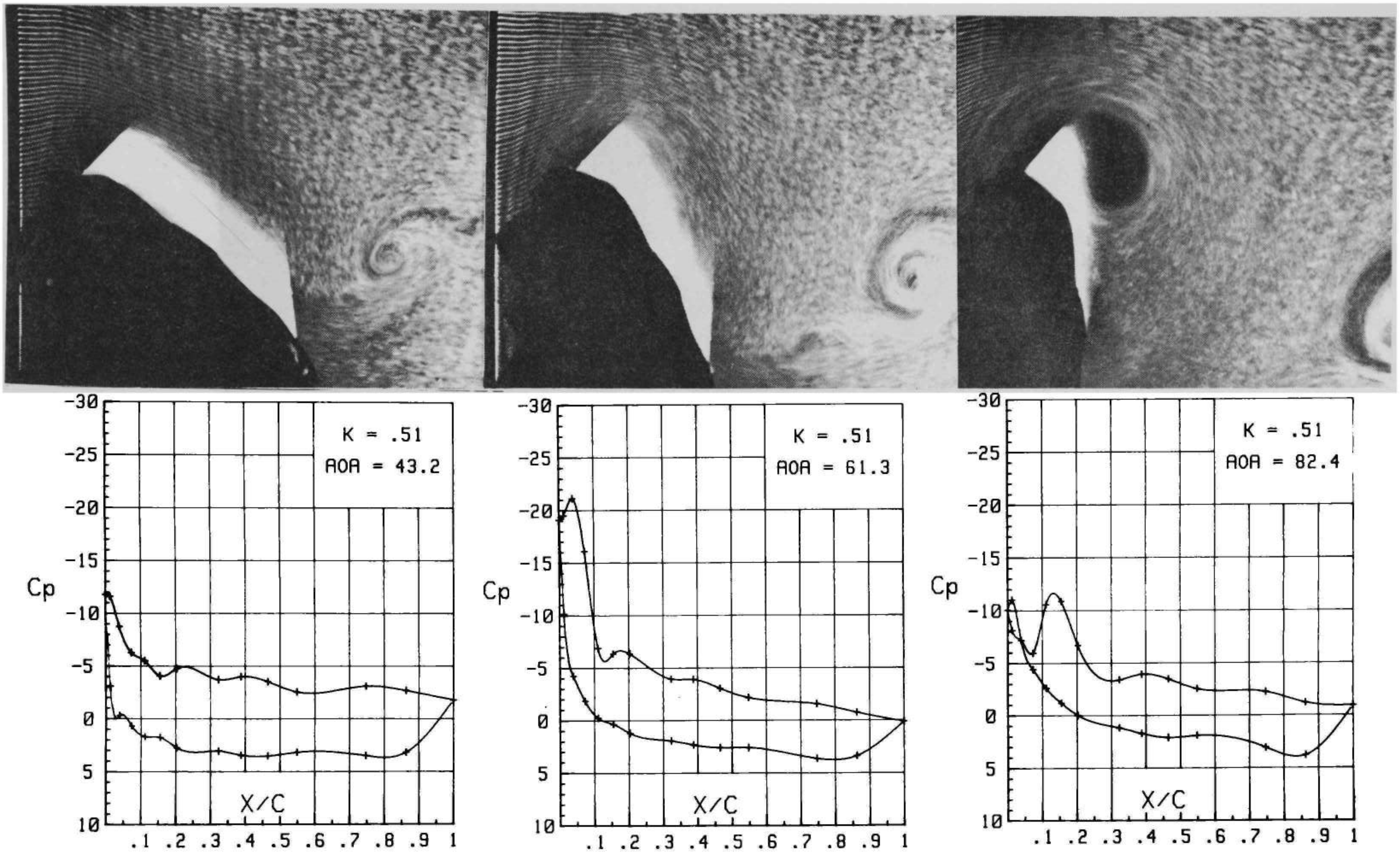

Figure 19. Flow Visualization and Pressure Data for K = 0.51

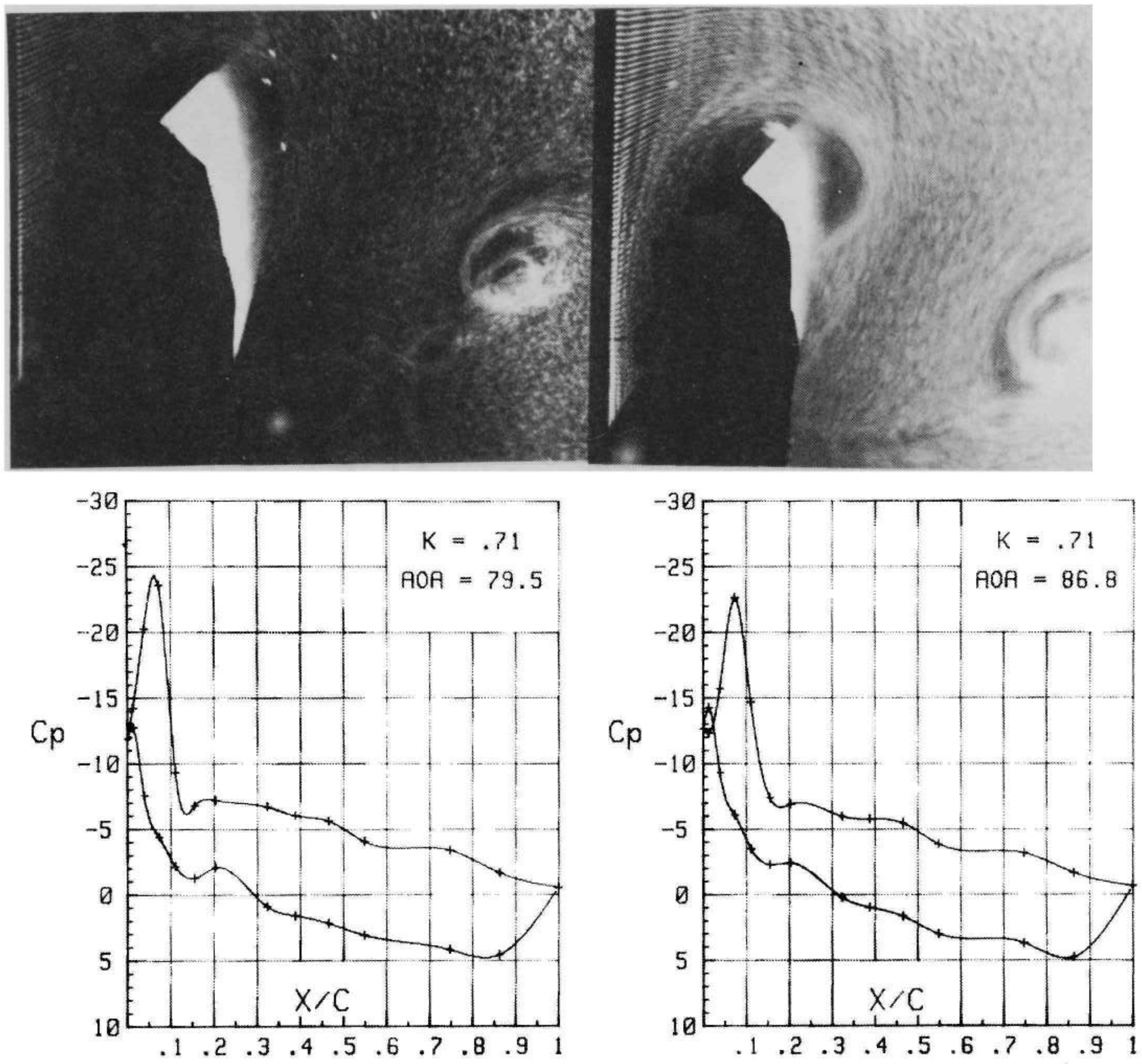

Figure 20. Flow Visualization and Pressure Data for K = 0.71

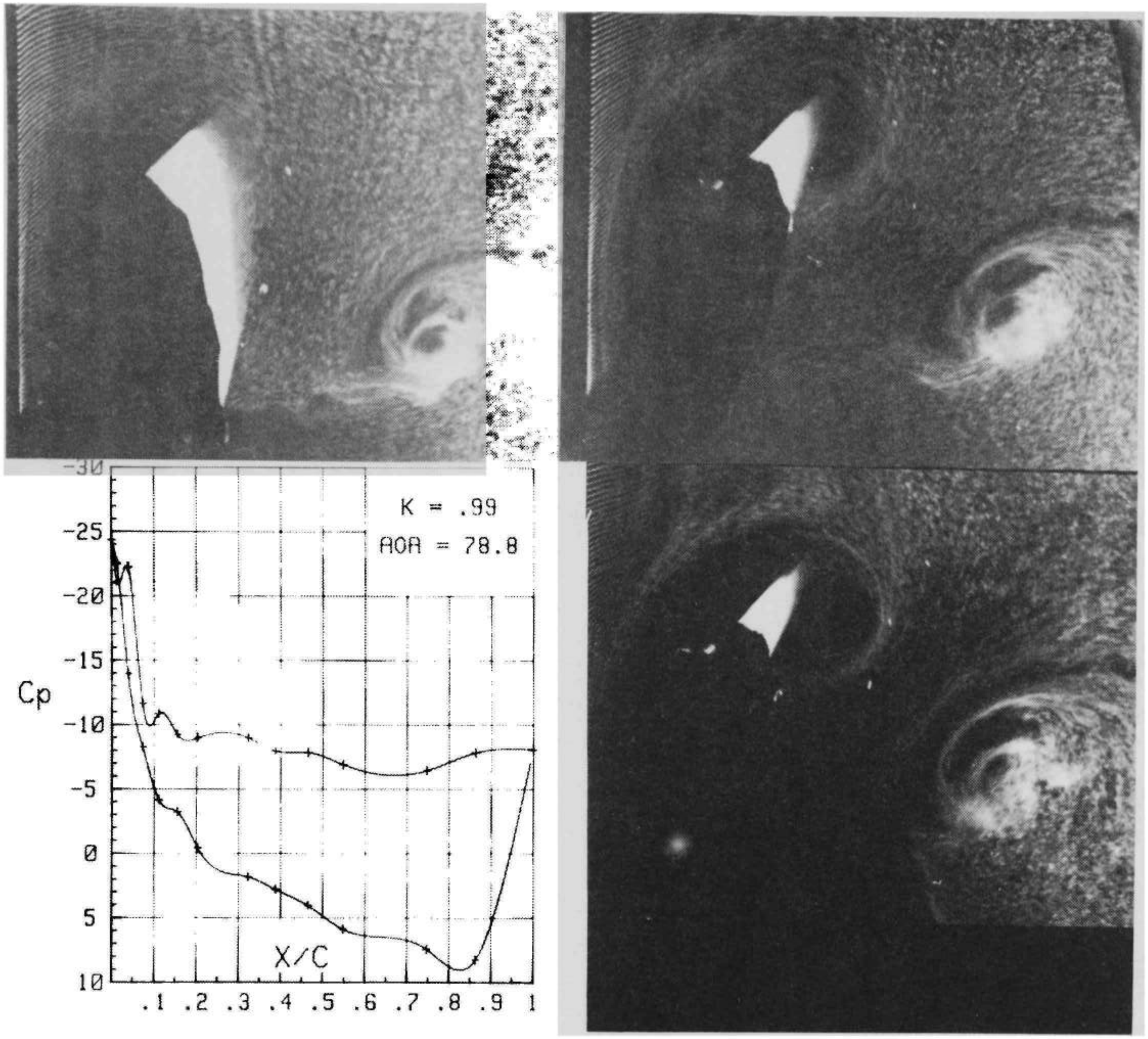

Figure 21. Flow Visualization and Pressure Data for K = 0.99

of $K = 0.99$, $\alpha = 78.8°$ in Figure 21 the flow has not yet separated from the leading edge. The flow on the underside of the airfoil, however, appears to be different in the high pitch rate cases ($K > .5$) than in the moderate cases ($.1 < K < .5$). Inspection of the flow visualization data for the case of $K = .71$, $\alpha = 86.8°$ in Figure 20 reveals a zone adjacent to the underside of the airfoil which appears to be separated. This effect is more pronounced in the case of $K = 0.99$.

In addition to the vortical activity very near the airfoil, the "starting" vortex shed from the trailing edge when the pitching motion begins appears to be very energetic, particularly in the high pitch rate cases. This vortex may be an important consideration [37] for aircraft in close proximity or in wake traversal following the completion of a post-stall maneuver.

3.3 Pressure Distributions

Pressure distributions corresponding to the flow visualization photographs are also shown in Figures 16-21. Throughout this section, the reader may wish to refer to the more complete set of data given in Appendix B.

As pointed out in Section 3.1, the negative effective angles of attack at the airfoil leading edge give rise to a region of negative pressure on the airfoil underside and a region of positive pressure on the topside. As seen in Figure 22 for a non-dimensional pitch rate of 0.51, this results in a crossing of the underside and topside distributions. As the angle of attack increases the intersection point moves toward the leading edge and eventually disappears. The location of this point of intersection as a function of the non-dimensional time is shown

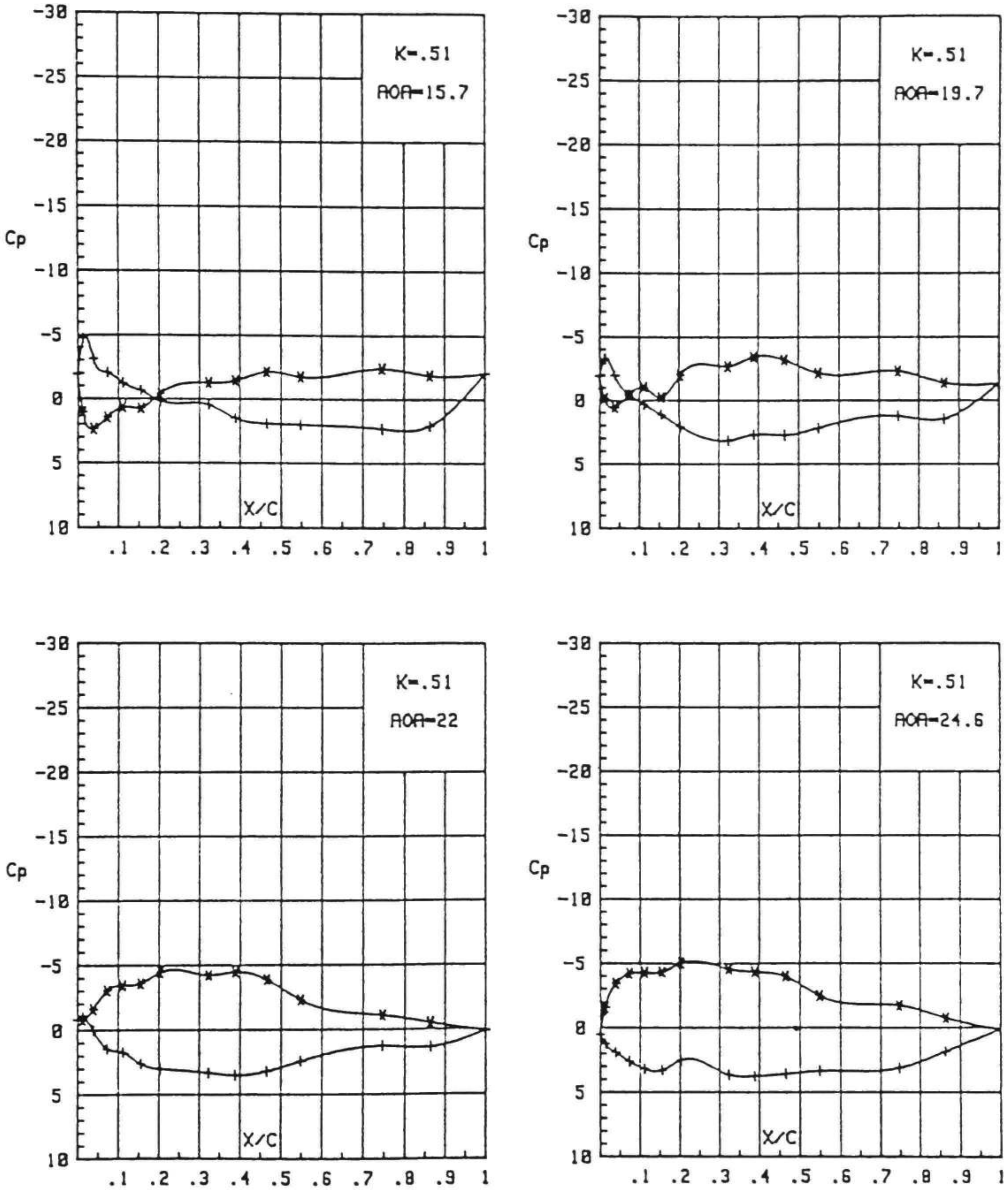

Figure 22. Pressure Distributions for K = 0.51

in Figure 23. As may be seen, the upper and lower distributions initially intersect at about the mid-chord. This point moves forward as time increases and reaches the nose at a non-dimensional time of about 0.38. A complete understanding of the physics of this phenomenon has not been reached at the present time; however, it may be associated with the variation in local effective angle of attack along the airfoil chord.

Following this event, the geometry of the pressure distributions more closely resembles that for steady flow. Prior to separation, there is a gradual build-up of suction on the topside of the airfoil as the angle of attack increases giving rise to a well-defined peak at about the 5 percent chord point. The magnitude of this peak is much larger than that for the static case. For instance, at a non-dimensional pitching rate of $K = 0.29$ pressure coefficients on the order of -15 were recorded while in the static case the magnitude of this peak is on the order of -3 for a NACA 0015 airfoil [29]. As seen in Figure 24, the variation of the maximum value of the suction peak pressure with non-dimensional pitching rate is approximately linear for $K < 0.5$. Also shown in this figure are the maximum positive pressures measured on the underside of the airfoil.

The onset of dynamic stall is accompanied by a loss of suction very near the leading edge while the suction peak moves to about the 10 percent chord. This may be seen in the figures for $K = 0.088$, $\alpha = 38.3°$ in Figure 16, $K = 0.19$, $\alpha = 43.8°$ in Figure 17, and $K = 0.29$, $\alpha = 57.7°$ in Figure 18. This effect is evident in the data of Walker and Helin [33] also. This is noticeable in the higher pitching rate studies

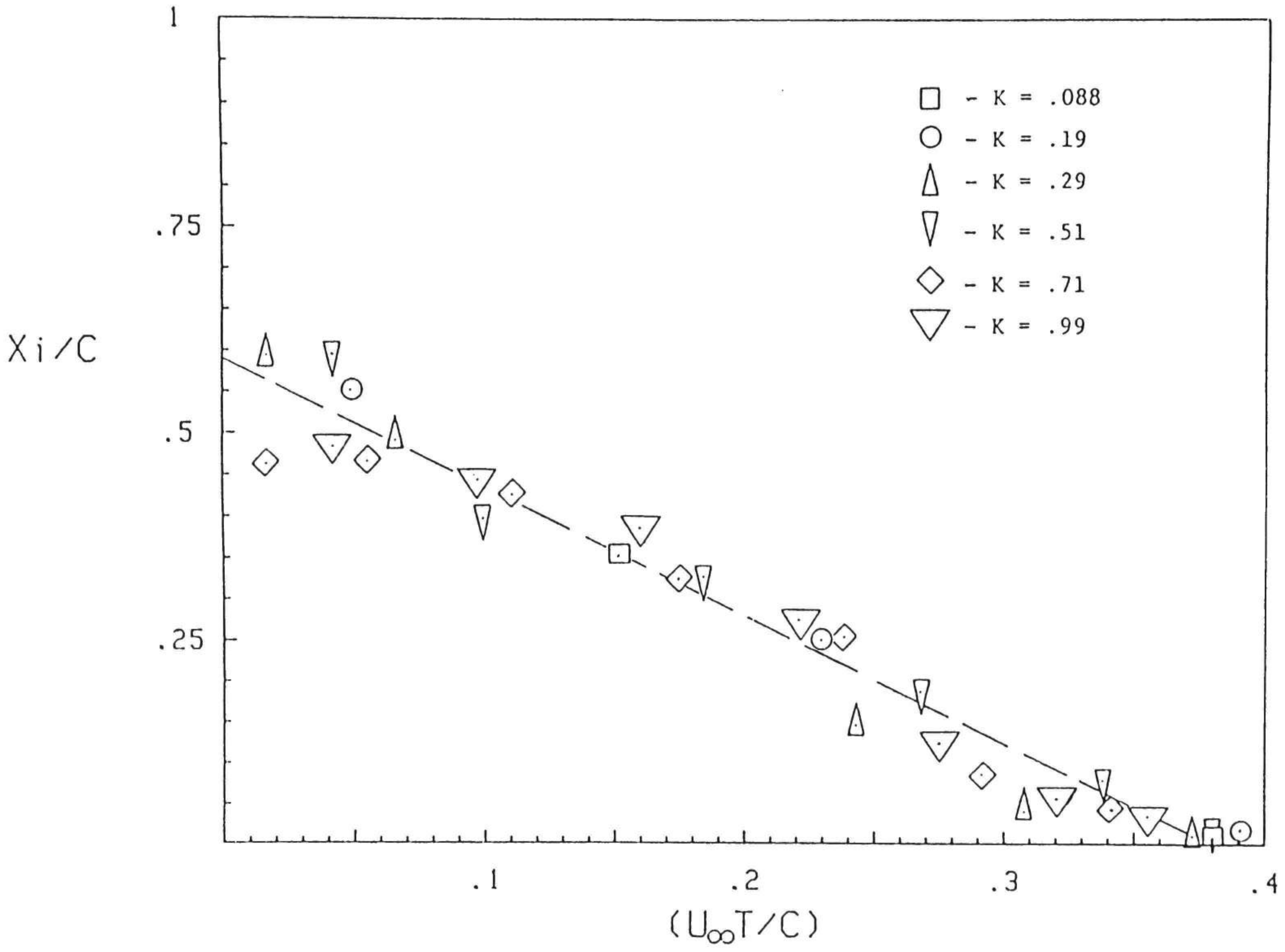

Figure 23. Time History of the Intersection of Topside and Underside Pressure Distributions

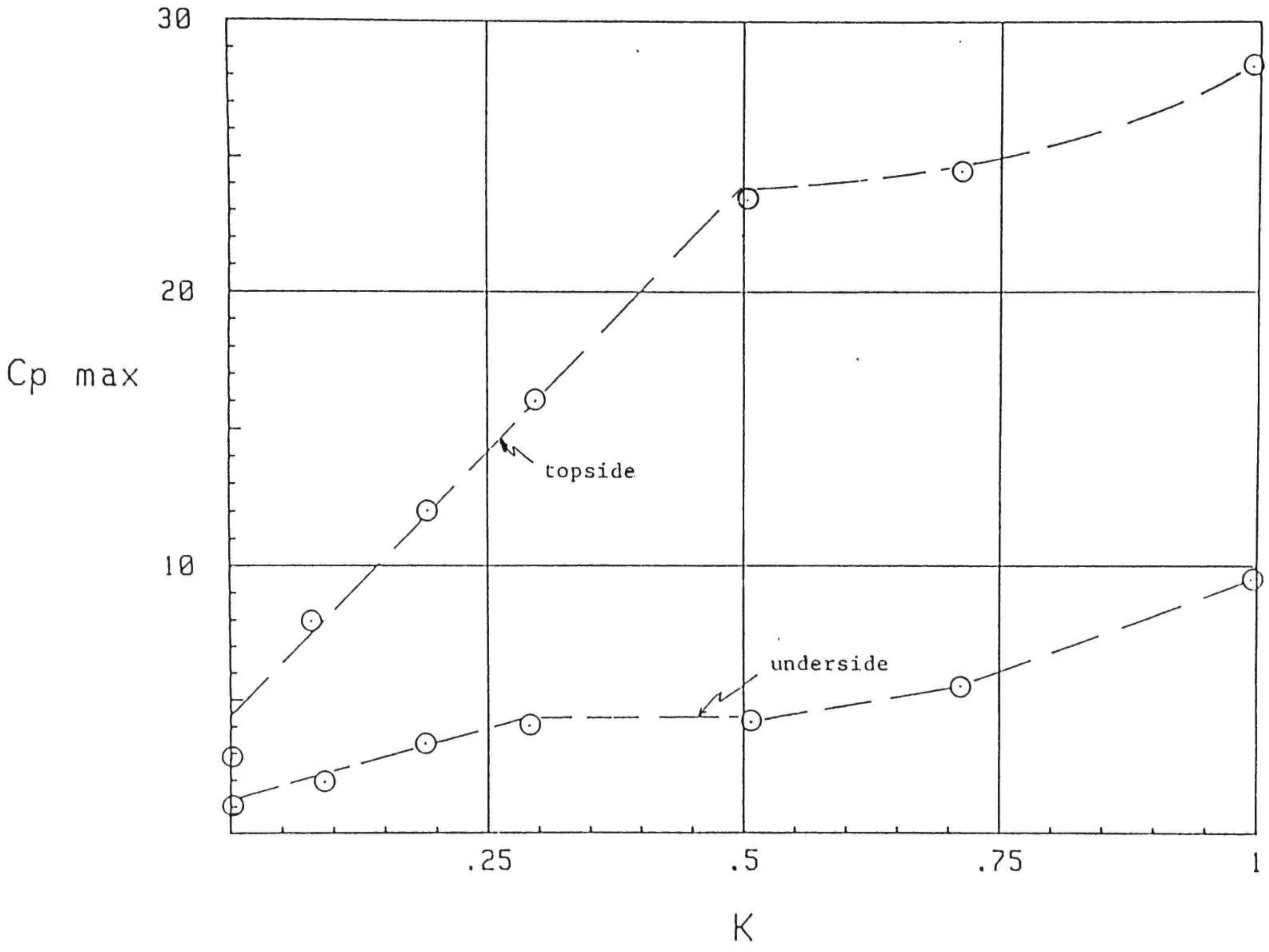

Figure 24. Maximum Pressure Coefficients

as well. It will be shown in the next section that this loss of suction is indicative of leading edge separation as becomes apparent when correlating the pressure distributions with the flow visualization data. Also in these figures, it is interesting to note the very large adverse pressure gradient on the downstream side of the suction peak.

As the dynamic stall vortex grows the pressure distribution on the topside of the airfoil assumes a flatter shape with localized peaks corresponding to regions of energetic activity. For example, inspection of the pressure distribution for $K = .088$, $\alpha = 56.2°$ in Figure 16 indicates a disturbance at about the 40 percent chord point. Comparing this with the adjoining photograph reveals the cause of this disturbance as the passage of the dynamic stall vortex. Similar comparisons can be made between other photographs and corresponding pressure distributions.

At least two observations can be made with regard to the pressure distribution on the underside of airfoil. The first observation is the considerable extent and magnitude of a region of negative pressure near the airfoil leading edge, particularly in the high pitching rate studies. The effect of this, of course, is to reduce the normal force. The second observation is the very large positive pressures over the aft portion of the airfoil, the magnitude of which grows with increasing pitching rate, as shown in Figure 24.

3.4 Empirical Correlations

As indicated previously, the shapes of the lift and drag curves, as a function of angle of attack, are different for low to moderate pitch rates as compared with those for high pitch rates (K > 0.5) particularly at low geometric angles of attack. The differences may be traced to the large negative effective angles of attack at the airfoil leading edge in the high pitch rate cases. Therefore, in the following discussion it may at times be appropriate to form two different correlations for the two pitch rate ranges.

In Figure 25 the maximum lift and drag coefficients are plotted as a function of the non-dimensional pitch rate parameter K. As can be seen from this figure, the resulting plots are essentially straight lines given by

$$\begin{aligned} C_{LMAX} &\simeq 1.75 + 8.35\ K \\ C_{DMAX} &\simeq 2.20 + 8.80\ K \end{aligned} \tag{9}$$

Equation 9 represents the maximum lift and drag coefficients achieved as the NACA 0015 airfoil pitches up from 0° to 90° at a constant non-dimensional pitch rate $\left(K = \frac{\dot{\alpha} c}{2U_\infty}\right)$.

In Figure 26 plots are given for the geometric angles of attack at which the maximum lift and drag coefficients occur. As can be noted from Figure 26(a) there is a definite change in trend as a value of K = 0.3 is approached. The lift curve at K = 0.3 displays maximum values in two places. It is also interesting to note that the curve in Figure 26(a) follows a plot of an 11° nose angle of attack for K > 0.3. The static stall angle of attack for the NACA 0015 airfoil at Re = 100,000 is

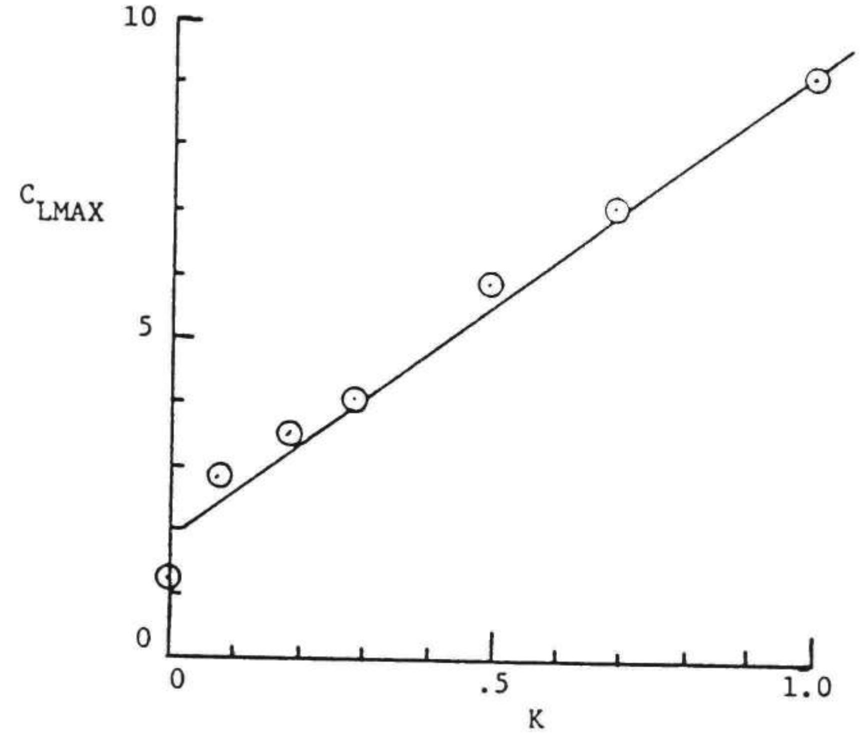

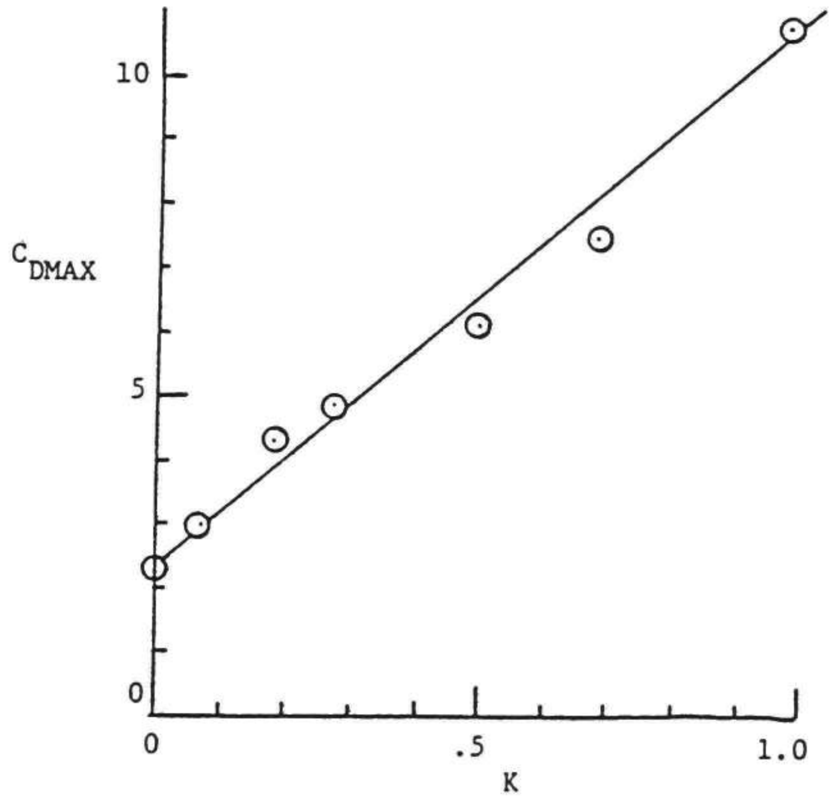

Figure 25. Maximum Lift and Drag Coefficients

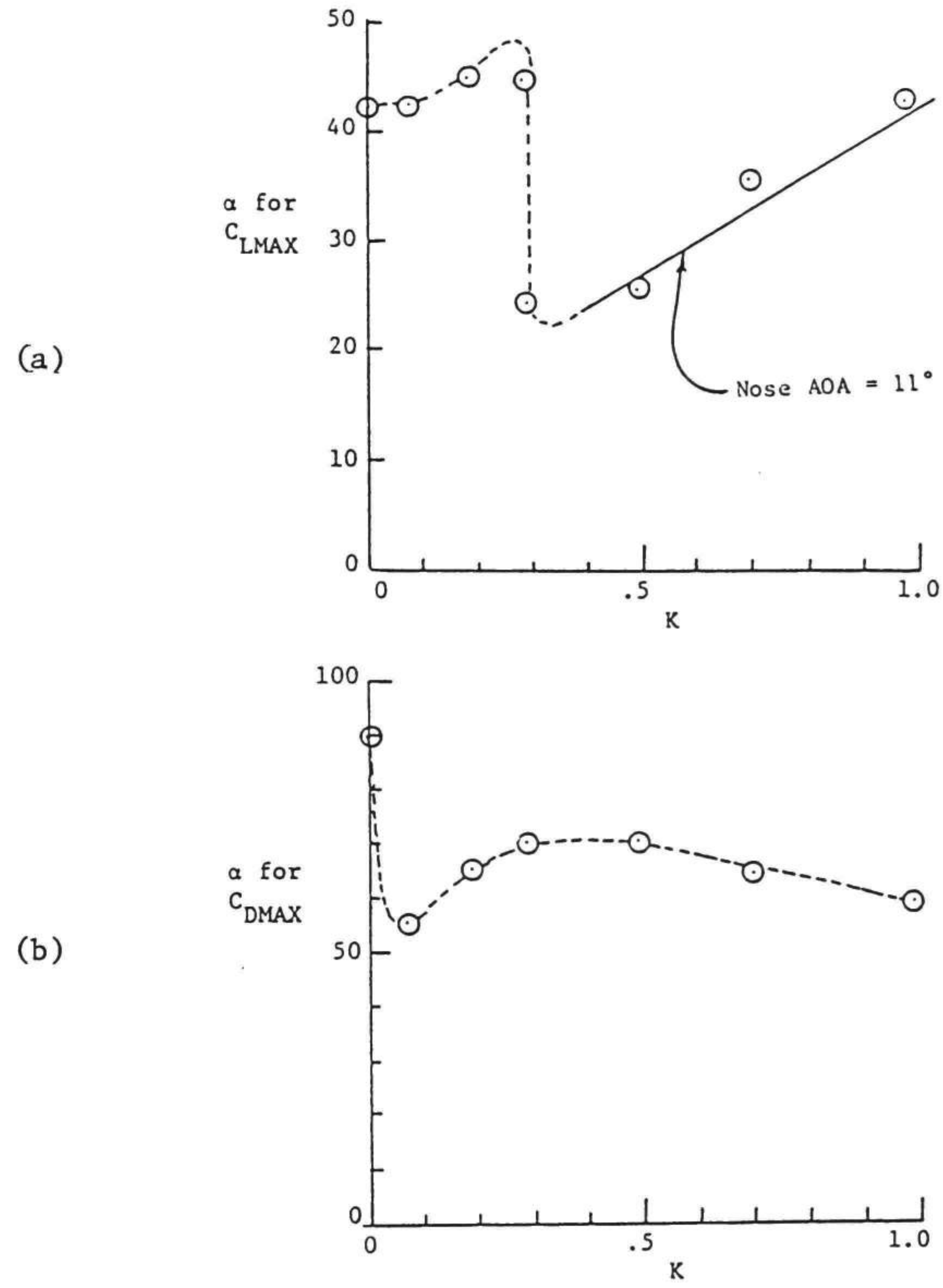

Figure 26. Angle of Attack at Maximum Lift and Drag

approximately 11°. The maximum drag occurs over a broad range of angles of attack which are, in general, greater than 60° as indicated in Figure 26(b).

The maximum normal force curve is given in Figure 27. Unlike the lift and drag curves, there is a distinct shift in the curve between the high and low pitching rates. The data can be correlated by

$$\begin{aligned} F^{+}_{n\ MAX} &= 2.2 + 19.0\ K \text{ for } K < 0.3 \\ F^{+}_{n\ MAX} &= 13.0\ K \text{ for } K > 0.3 \end{aligned} \qquad (10)$$

Depicted in Figure 28 are aerodynamic force data (from load cell measurements) for non-dimensional pitch rates of 0.0, 0.19, and 0.71. The smooth solid curves indicate that the lift and drag forces vary approximately according to simple trigonometric functions given by

$$\begin{aligned} C_L &= 2A_L \sin\alpha \cos\alpha \\ C_D &= A_D \sin^2\alpha \end{aligned} \qquad (11)$$

The variation of the coefficients A_L and A_D with non-dimensional pitch rate may be seen in Figure 29. These values were computed using a least-squares curve fit method. The relations for the solid lines are given by

$$\begin{aligned} A_L &= 7.1K + 2.25 \quad (0.1 < K < 1.0) \\ A_D &= 8.05K + 3.25 \quad (0.1 < K < 0.7) \end{aligned} \qquad (12)$$

Shown in Figures 30-31 are the lift and drag force data from load cell measurements for the three lowest pitch rates and the static case. The

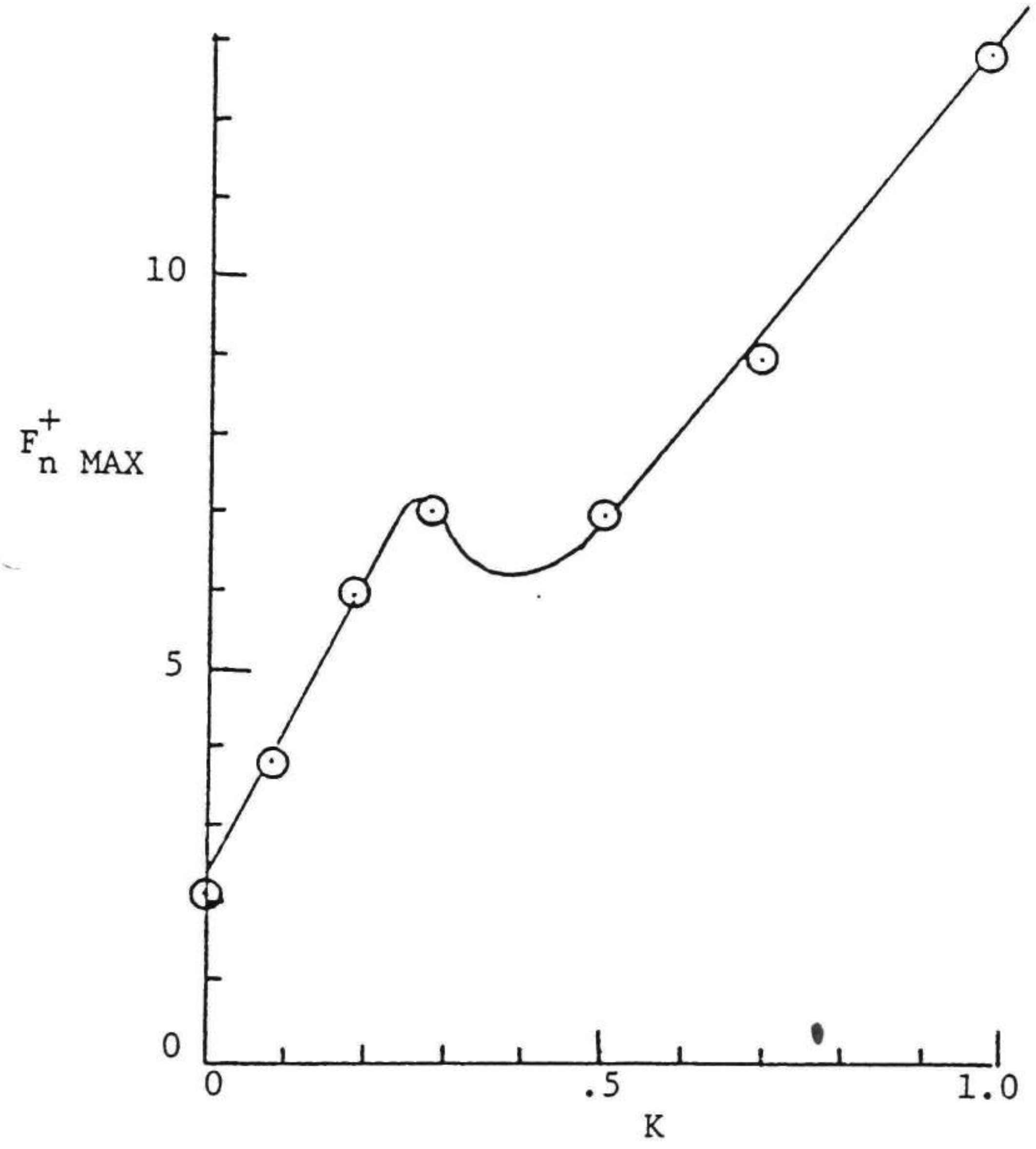

Figure 27. Maximum Normal Force Coefficient

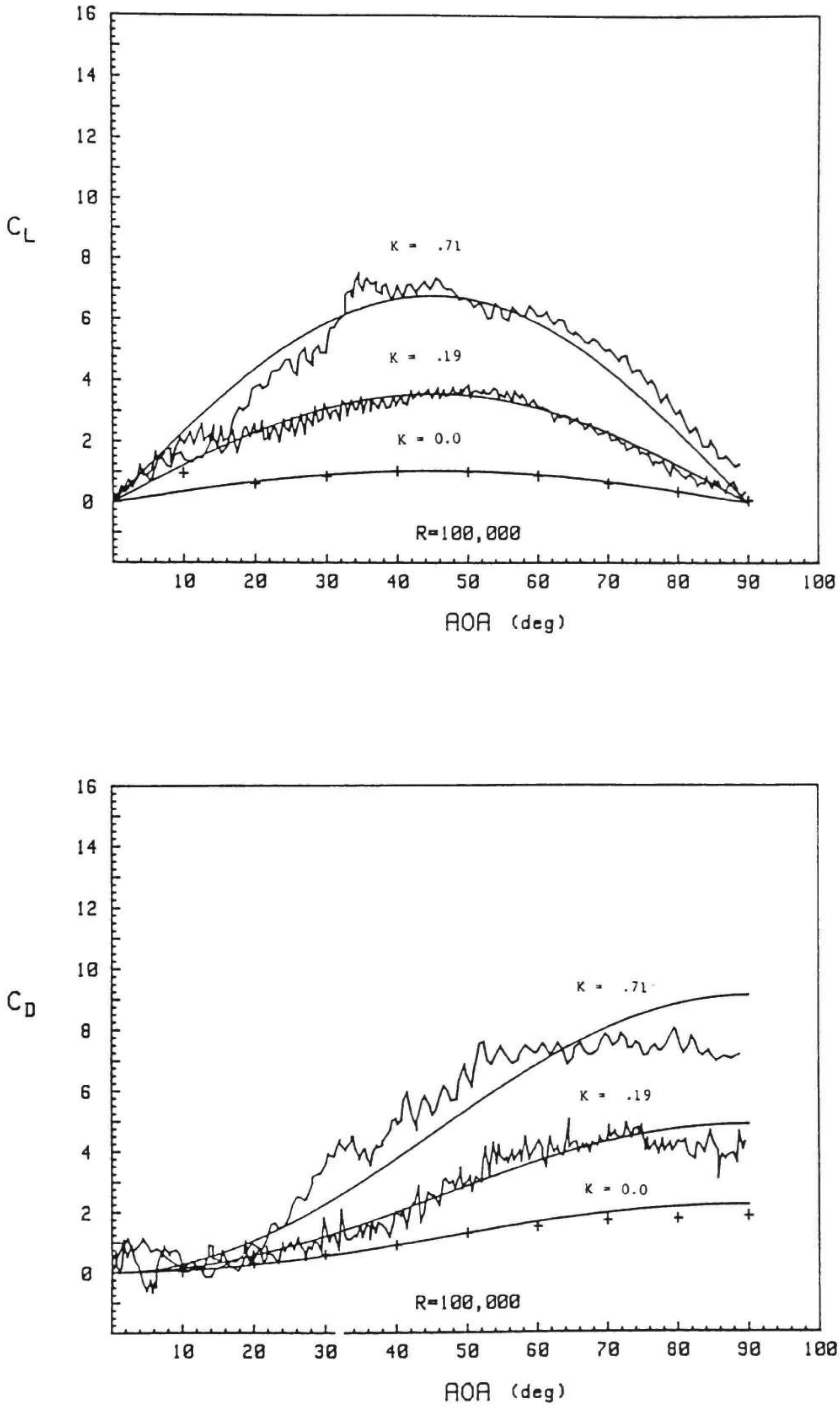

Figure 28. Comparison of Lift and Drag Force Data with Simple Trigonometric Correlations

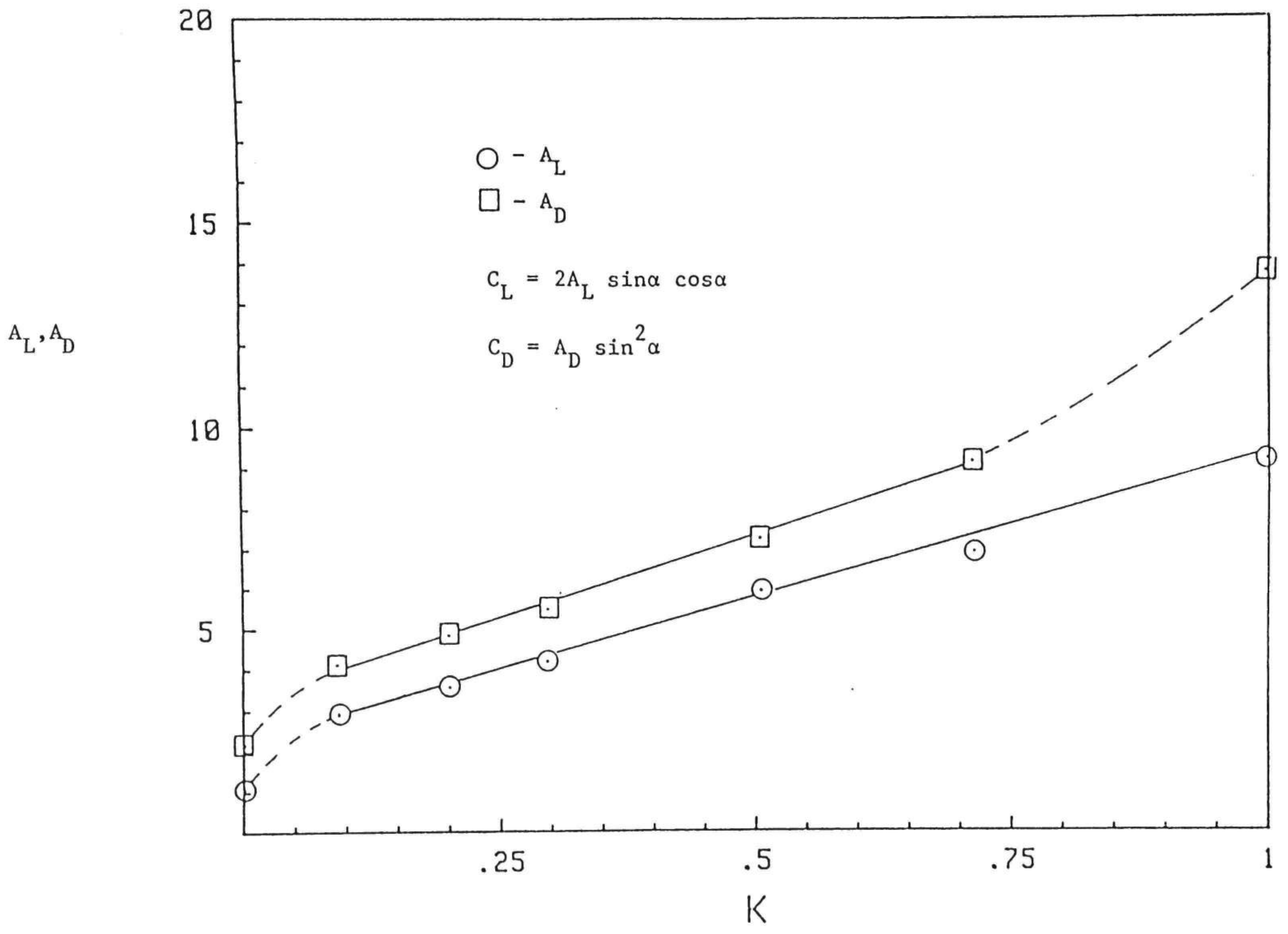

Figure 29. Coefficients for Lift and Drag Force Correlations

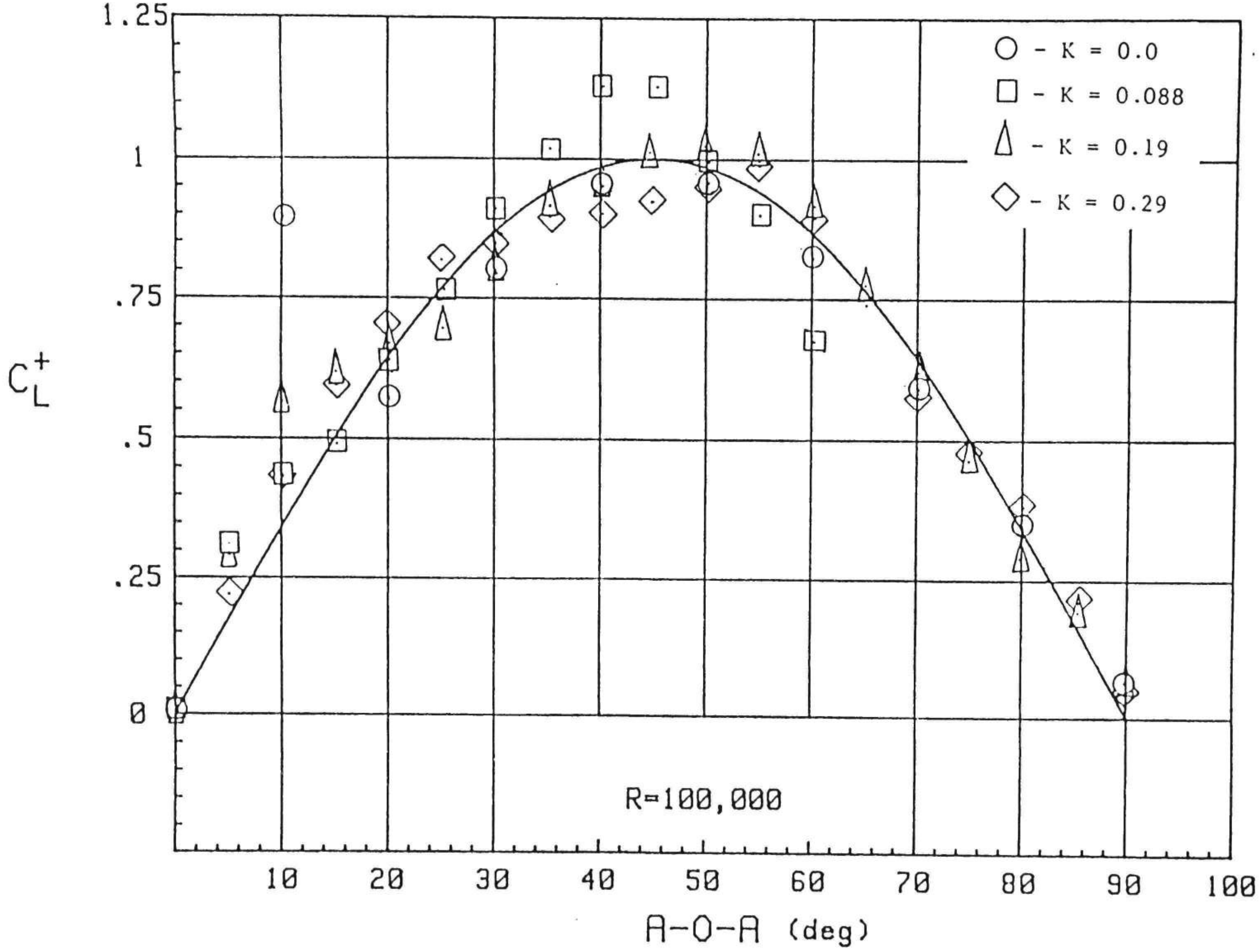

Figure 30. Lift Force Correlation for Low Pitch Rates

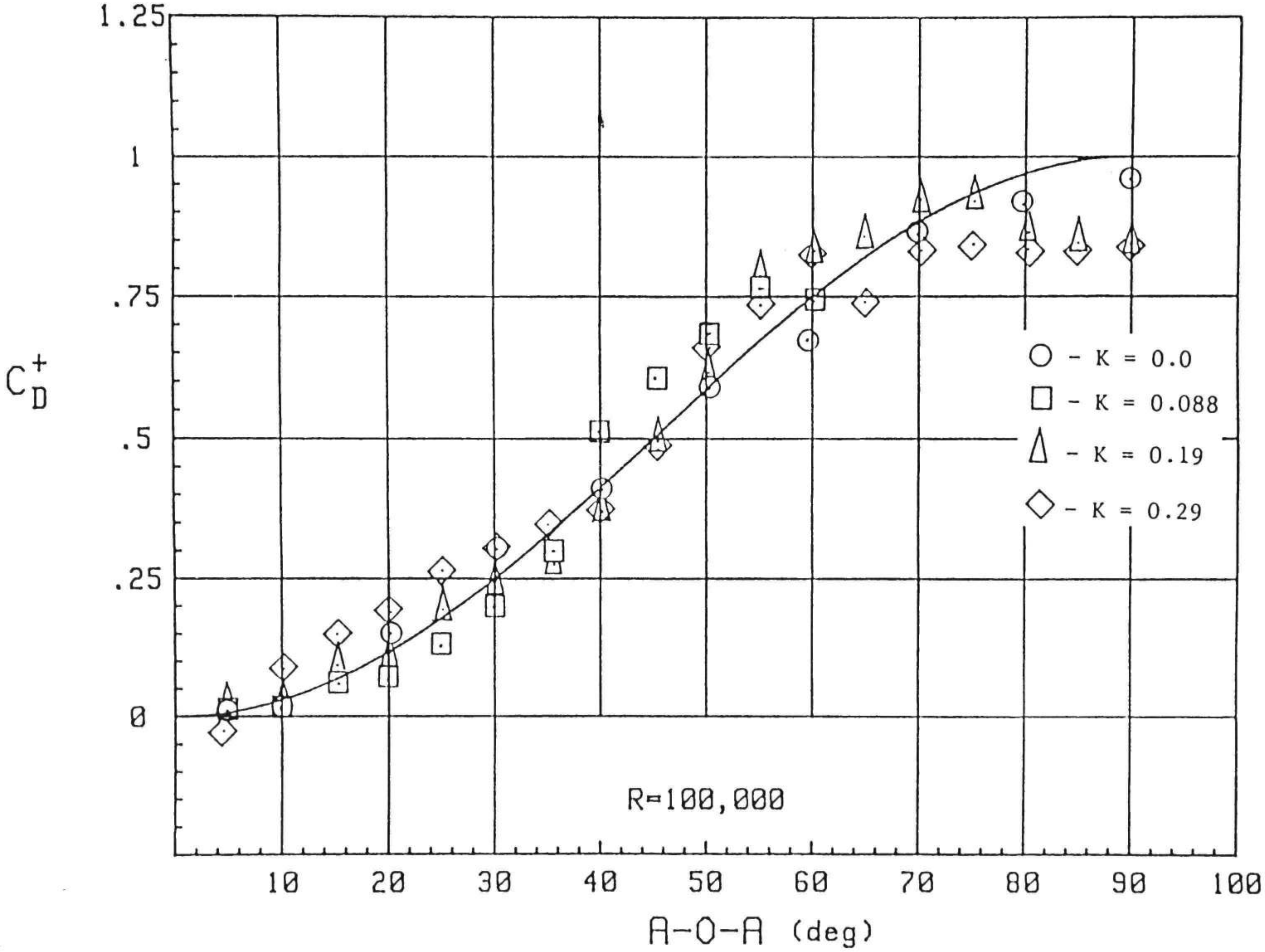

Figure 31. Drag Force Correlation for Low Pitch Rates

data for the three highest pitch rates are shown in Figures 32-33. These data have been normalized as follows

$$\begin{aligned} C_L^+(\alpha) &= C_L(\alpha)/A_L \\ C_D^+(\alpha) &= C_D(\alpha)/A_D \end{aligned} \tag{13}$$

As may be seen in Figures 30 and 31, the agreement between the low to moderate pitch rates (as well as the static case) and the simple trigonometric correlations is reasonably good over a wide range of angles of attack. The correlations begin to break down, particularly for the lift force, at the higher pitch rates as may be seen in Figures 32 and 33. There are undoubtedly other types of correlating functions which might be applied over subintervals of angles of attack which would be more accurate than the simple trigonometric ones presented here.

In addition to obtaining correlations involving aerodynamic force data, the flow visualization data and surface pressure distributions were analyzed to detect the inception of leading edge separation. A significant loss of suction at the pressure tap nearest the leading edge on the topside of the airfoil was taken to be indicative of separation. For instance, referring to pressure distributions for $K = 0.088$ and $\alpha = 35.8$ presented in Appendix B, the value of the pressure coefficient at the topside pressure port located at the $x/c = 0.013$ is approximately -6. This value drops to -3 at $\alpha = 38.3°$. This is in close agreement with the flow visualization data. This effect is not as obvious in the high pitch rate cases, and for the case of $K = 0.99$ was impossible to detect.

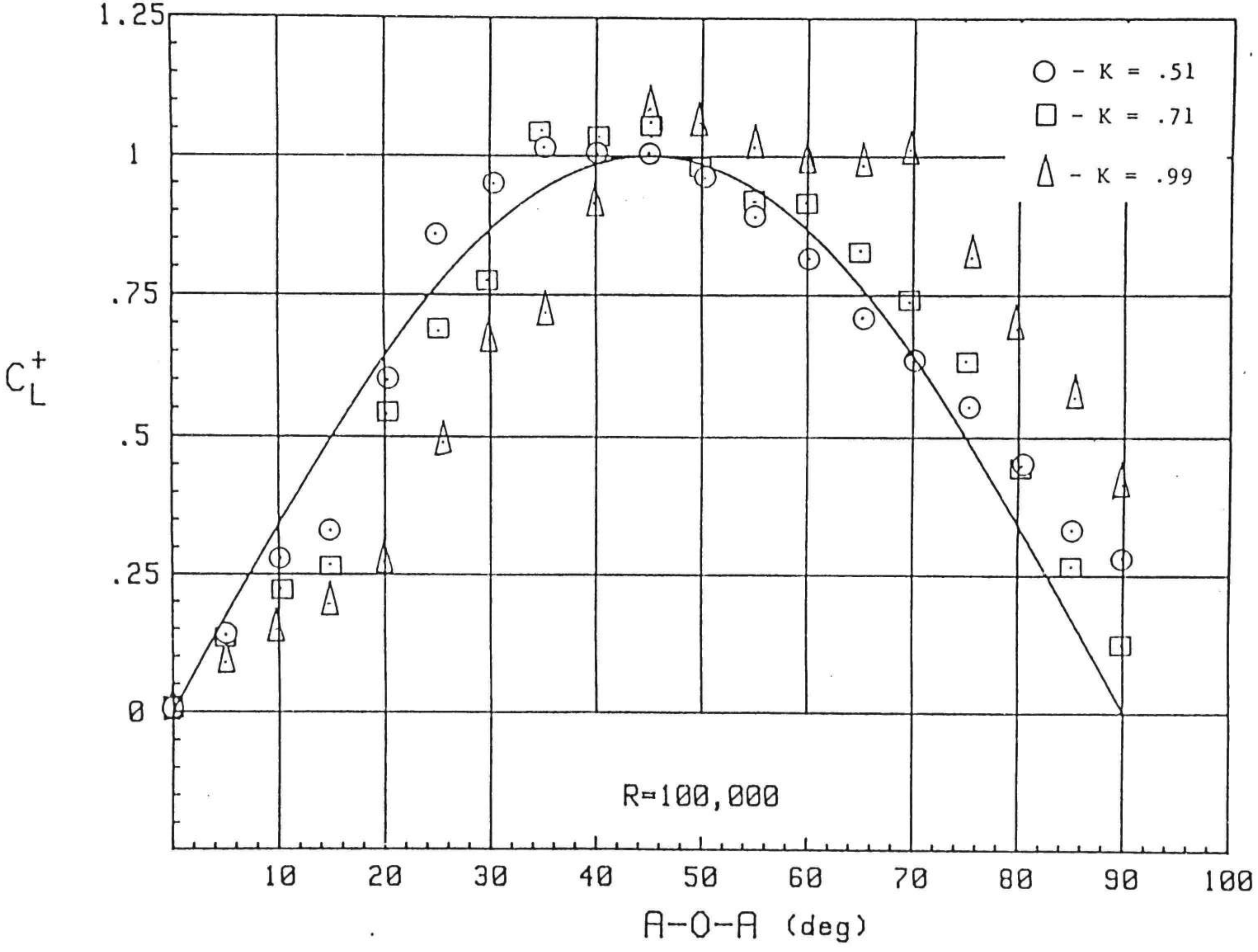

Figure 32. Lift Force Correlation for High Pitch Rates

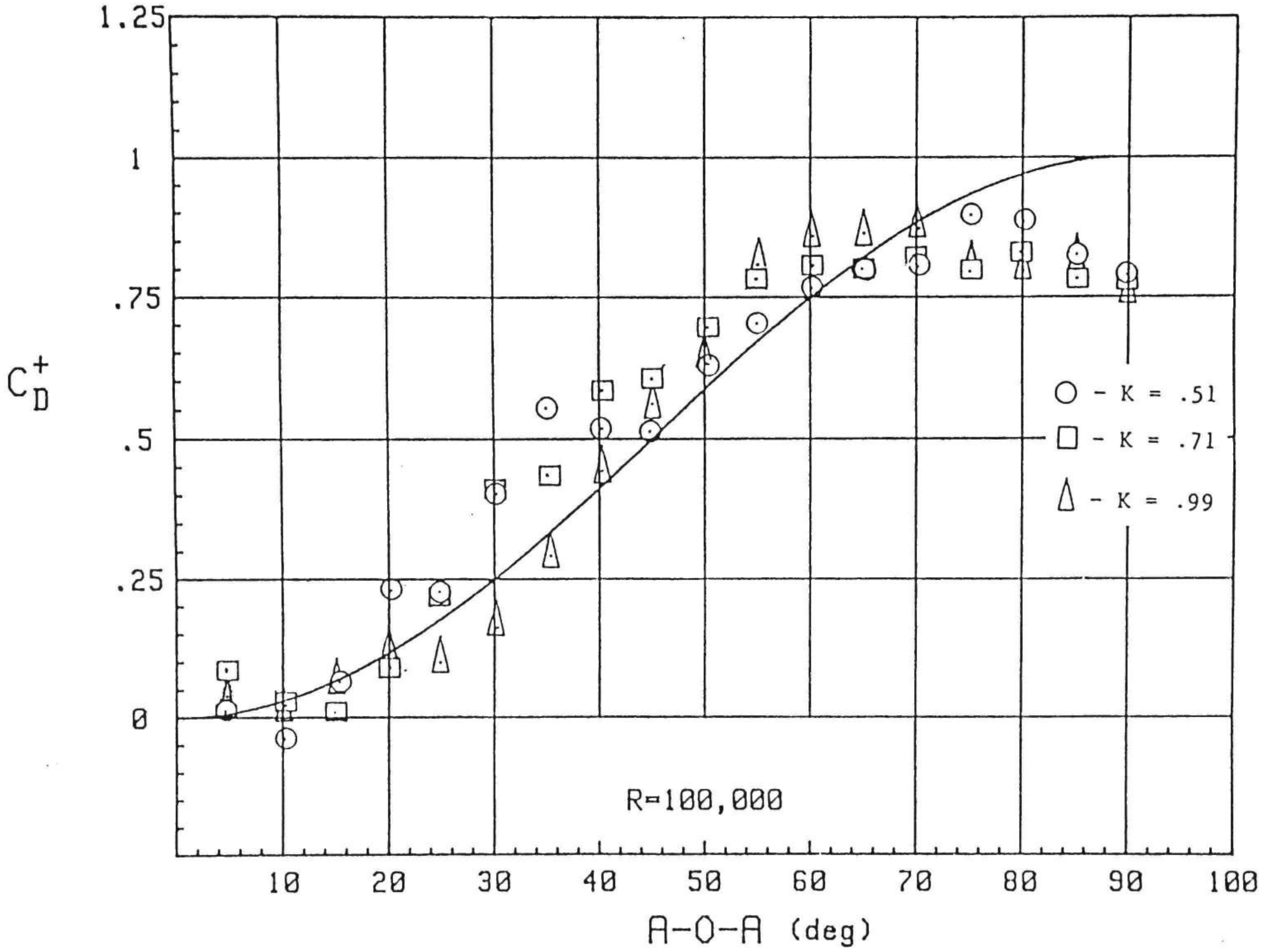

Figure 33. Drag Force Correlation for High Pitch Rates

An existing correlation for the onset of leading edge separation due to Gormont [9], which is based upon oscillating airfoil data, was extended to encompass the wide range of pitching rates considered in this study, the results of which are presented in Figure 34. The Gormont model is applicable to airfoils operating over a wide range of Mach numbers and contains a correlation for various airfoil maximum thickness ratios. The Gormont model for low Mach number "moment stall" is given by

$$\Delta\alpha_{stall} = K_1\gamma\left(\left| \frac{C\dot{\alpha}}{2U_\infty} \right| \right)^{1/2} S_{\dot{\alpha}}$$

$$\gamma = 1.0 - 2.5\,(\,.06 - t/c) \tag{11}$$

$$K_1 = \frac{3}{4} + \frac{1}{4} S_{\dot{\alpha}}$$

$$S_{\dot{\alpha}} = \text{sign of } \dot{\alpha}$$

where γ and K_1 are empirical constants and $\Delta\alpha_{stall}$ is the difference between the effective angle of attack (α_N) at the leading edge for which separation occurs in the dynamic case and the static stall angle, i.e.,

$$\Delta\alpha_{stall} = \alpha_{N\text{ dyn. stall}} - \alpha_{\text{static stall}} \tag{12}$$

The effective angle of attack and the geometric angle of attack are related by

$$\tan\alpha_N = \tan\alpha - \frac{2\xi K}{\cos\alpha}$$

$$K = \frac{\dot{\alpha} c}{2U_\infty} \tag{13}$$

ξ = pivot point location
(fraction of chord from nose)

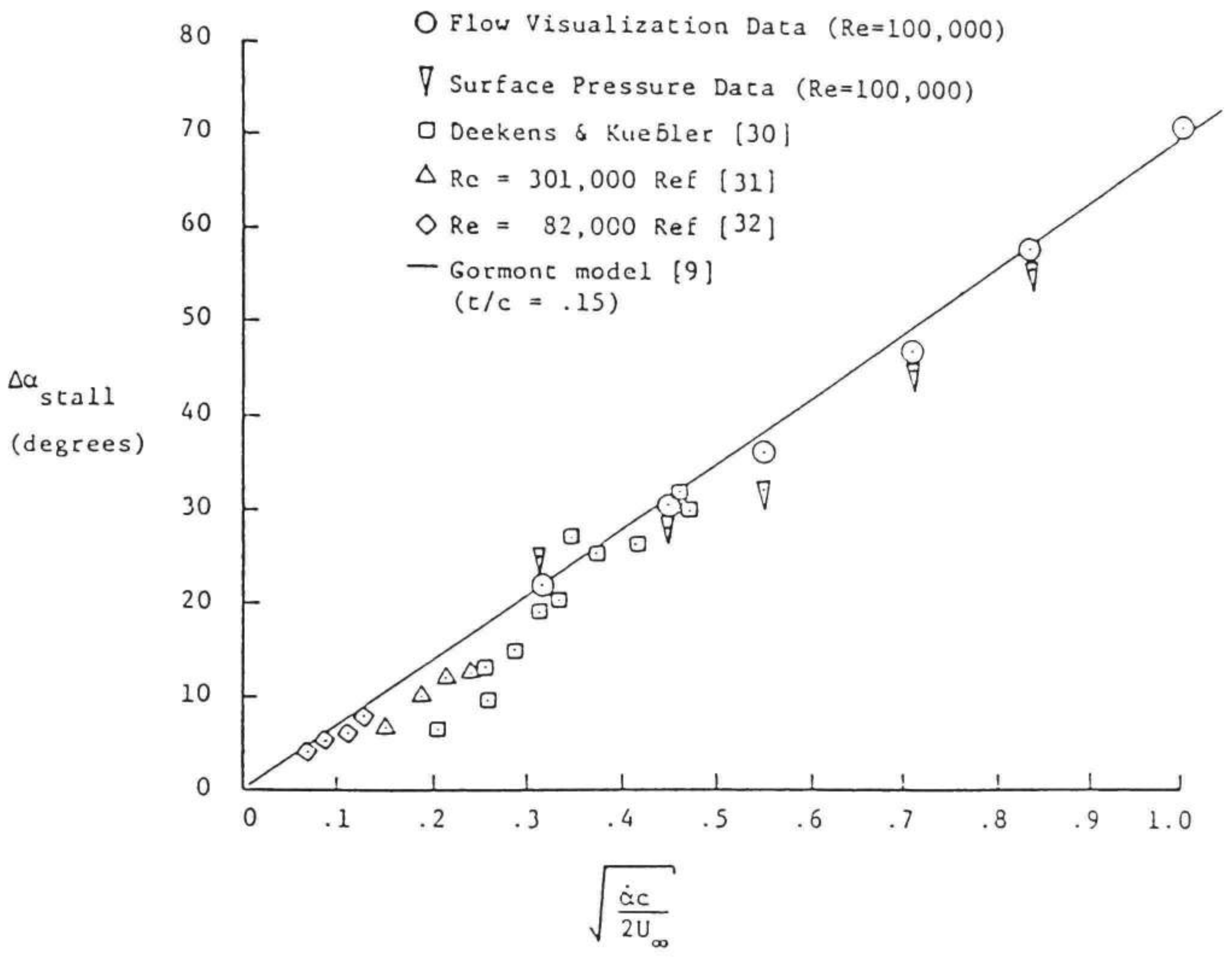

Figure 34. Gormont Correlation for Leading Edge Separation

It should be noted that the Gormont model also includes a correlation for "lift stall" which occurs subsequent to moment stall. The occurrence of moment stall is, however, the appropriate indication of boundary layer separation since it represents the *first* major disturbance of the potential flow by the boundary layers. It should also be noted that all of the cases presented in Figure 34 represent the onset of stall and thus it remains to be seen whether the Gormont correlation is also valid for the cessation of stall for the constant pitch rate situation.

CHAPTER IV

ANALYTICAL METHODS AND RESULTS

4.1 Discussion of Analytical Model

A two-dimensional discrete vortex method was used to model the airfoil body and free wake. As shown in Figure 35, the body was represented by a flat plate divided into a number of panels with a discrete bound vortex and control point on each panel. The strengths of the bound vortices can be uniquely determined by forcing the fluid velocity at the control points to be tangent to the airfoil surface. At a particular control point j, at a time step k, the surface tangency condition may be represented by

$$\sum_{i=1}^{NB} A_{ji} \Gamma_{Bi}^{k} + \sum_{i=1}^{NW^{k}} B_{ji}^{k} \Gamma_{Wi} + U_{Mj}^{k} + U_{\infty} \sin\alpha^{k}$$

$$+ C_{jT} \Gamma_{T}^{k} + C_{jN} \Gamma_{N}^{k} = 0 \qquad (14)$$

where NB is the number of bound vortices and NW^k is the number of free wake vortices. In equation (14) the first term is the downwash due to the bound vorticity, the second term is the downwash due to the wake, the third term is the downwash due to the body motion (pitching, etc.), the fourth term is the downwash due to the freestream, the fifth term is the downwash due to a nascent vortex at the trailing edge, and the sixth term is the downwash due to a separation vortex at the leading edge. The presence of a superscript k on any term above indicates that the value may change with time. The influence coefficients appearing in front of the vortex strengths may be computed using the Biot-Savart law [36] and geometric considerations.

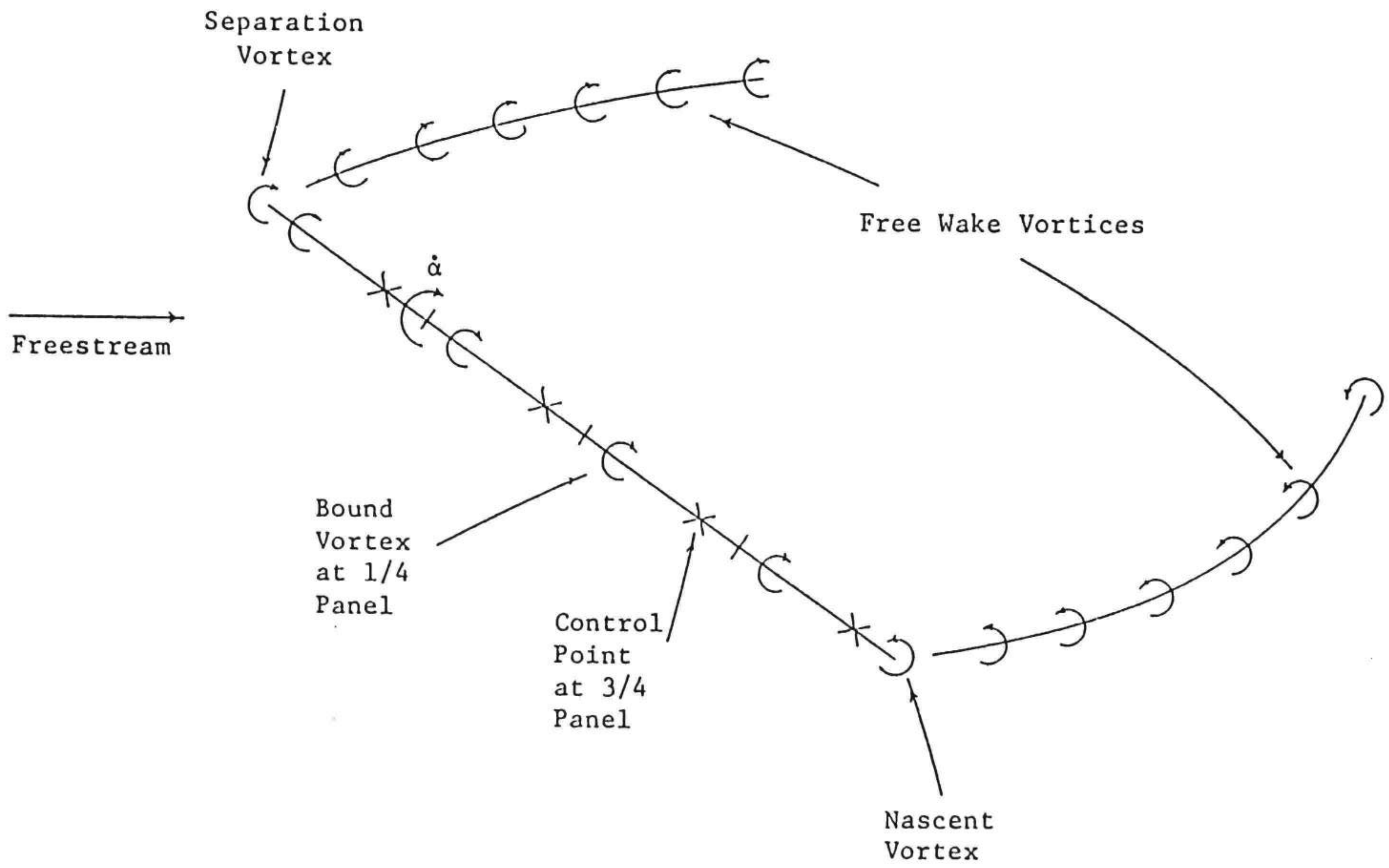
Separation Vortex
Free Wake Vortices
$\dot{\alpha}$
Freestream
Bound Vortex at 1/4 Panel
Control Point at 3/4 Panel
Nascent Vortex

Figure 35. Analytical Representation of Airfoil and Wake

There are NB+2 unknowns in equation (14); namely, the bound vortex strengths, the nascent vortex strength (Γ_T^k), and the separation vortex strength (Γ_N^k). In this analysis, the quantity Γ_N^k is treated as an input parameter after leading edge separation occurs and is simply equal to zero prior to separation. The angle of attack at which separation occurs is given by the empirical correlation of Gormont which is discussed in section 3.4. The strengths of the free wake vortices are known from previous time steps since each of these, at one time, was either a nascent trailing edge vortex or a leading edge separation vortex. The free wake vortices are assumed to remain constant in strength throughout time. The strength of the trailing edge nascent vortex is related to the bound vorticity through Kelvin's theorem which requires that the total vorticity in the flow remain constant and is given by

$$\Gamma_T^k = -\sum_{i=1}^{NB}\left(\Gamma_{Bi}^k - \Gamma_{Bi}^{k-1}\right) - \Gamma_N^k \tag{15}$$

Substituting this into equation (14) yields

$$\sum_{i=1}^{NB}\left(A_{ji} - C_{jT}\right)\Gamma_{Bi}^k + \sum_{i=1}^{NB} C_{jT}\,\Gamma_{Bi}^{k-1} + \sum_{i=1}^{NW^k} B_{ji}^k\,\Gamma_{Wi} + U_{Mj}^k$$

$$+ U_\infty \sin\alpha^k + \left(C_{jN} - C_{jT}\right)\Gamma_N^k = 0 \tag{16}$$

An equation of the form of equation (16) may be written for each control point resulting in a system of NB linear equations in the NB unknowns $\Gamma_{B1}^k, \Gamma_{B2}^k \ldots \Gamma_{BNB}^k$. This may be expressed in matrix notation as

$$[D]\{\Gamma_B\}^k = \{E\}^k \tag{17}$$

where $D_{ji} = (A_{ji} - C_{jT})$ $\qquad j = 1,2,\ldots NB,\ i = 1,2,\ldots NB$

$$E_j = -\left[\sum_{i=1}^{NB} C_{jT} \Gamma_{Bi}^{k-1} + \sum_{i=1}^{NW^k} B_{ji}^{k} \Gamma_{Wi} + U_{Mj}^{k} + U_\infty \sin\alpha^k + \left(C_{jN} - C_{jT} \right) \Gamma_N^k \right]$$

$$j = 1,2,\ldots NB$$

The unknown bound vortex strengths may then be computed using

$$\left\{\Gamma_B\right\}^k = [D]^{-1} \left\{E\right\}^k \tag{18}$$

noting that the matrix [D] is not a function of time and, therefore, need be inverted only once. Having determined the bound vortex strengths from equation (18), the nascent vortex strength may be computed using equation (15).

At this point in the computations the strength of each vortex in the flow has been determined. The induced velocity at any point in the flow due to all vortices, bound and free, may be calculated using the Biot-Savart law and the known geometry of the flow field. In this fashion the free wake elements are convected downstream at their respective local velocities. In other words, the motion of the wake vortices in Figure 35 is obtained by superimposing the perturbation velocities produced by other wake vortices and the bound vortices on the freestream velocity. In addition, the nascent vortex and separation vortex are released to the free wake with velocities equal to those of the induced velocities at the trailing edge and leading edge, respectively, superimposed on the freestream velocity. As they are released a new separation vortex and nascent vortex appear on the leading and trailing edges, respectively. It should be pointed out that the Biot-Savart law for the velocity induced by a vortex is an inverse relation which becomes infinite as the center of a vortex is approached. This is a departure from physical reality and, therefore, a vortex core approximation was applied. As illustrated in Figure 36, the core approximation limits the velocity a vortex induces at points in close proximity to the vortex. The best agreement between the analysis and the data was obtained for a core diameter of three-eighths of the length of an individual panel on the body.

Forces on the airfoil can be obtained by integrating the surface pressure forces around the airfoil. The pressure distribution is given by the unsteady Bernoulli equation

$$P = P_\infty - \rho\left[\frac{\partial \phi^*}{\partial t} + \frac{1}{2}\left(\nabla \phi^*\right)^2\right] \tag{19}$$

where ϕ^* is the velocity potential in some fixed reference frame. Following the development of Oler [3], the unsteady Bernoulli equation may be written in terms of a reference frame fixed in the lifting surface as

$$P = P_\infty - \rho\left[\frac{\partial \phi}{\partial t} + \frac{\partial \phi}{\partial s}\left(\vec{U}_r \cdot \vec{e}_s\right) - \frac{1}{2}\left(\vec{U}_r \cdot \vec{e}_n\right)^2 + \frac{1}{2}\left(\frac{\partial \phi}{\partial s}\right)^2\right] \tag{20}$$

where ϕ is the velocity potential in the airfoil frame of reference, $\vec{U}_r$ is the relative velocity between the airfoil surface and the freestream, s is the coordinate along the airfoil surface, and n is the coordinate perpendicular to the surface.

An alternate method to calculate the forces on the airfoil is to use a momentum approach. It can be shown [39] that the complex momentum associated with a two-dimensional potential flow can be given by

$$M_x + i\, M_y = -\, i \oint F dz \tag{21}$$

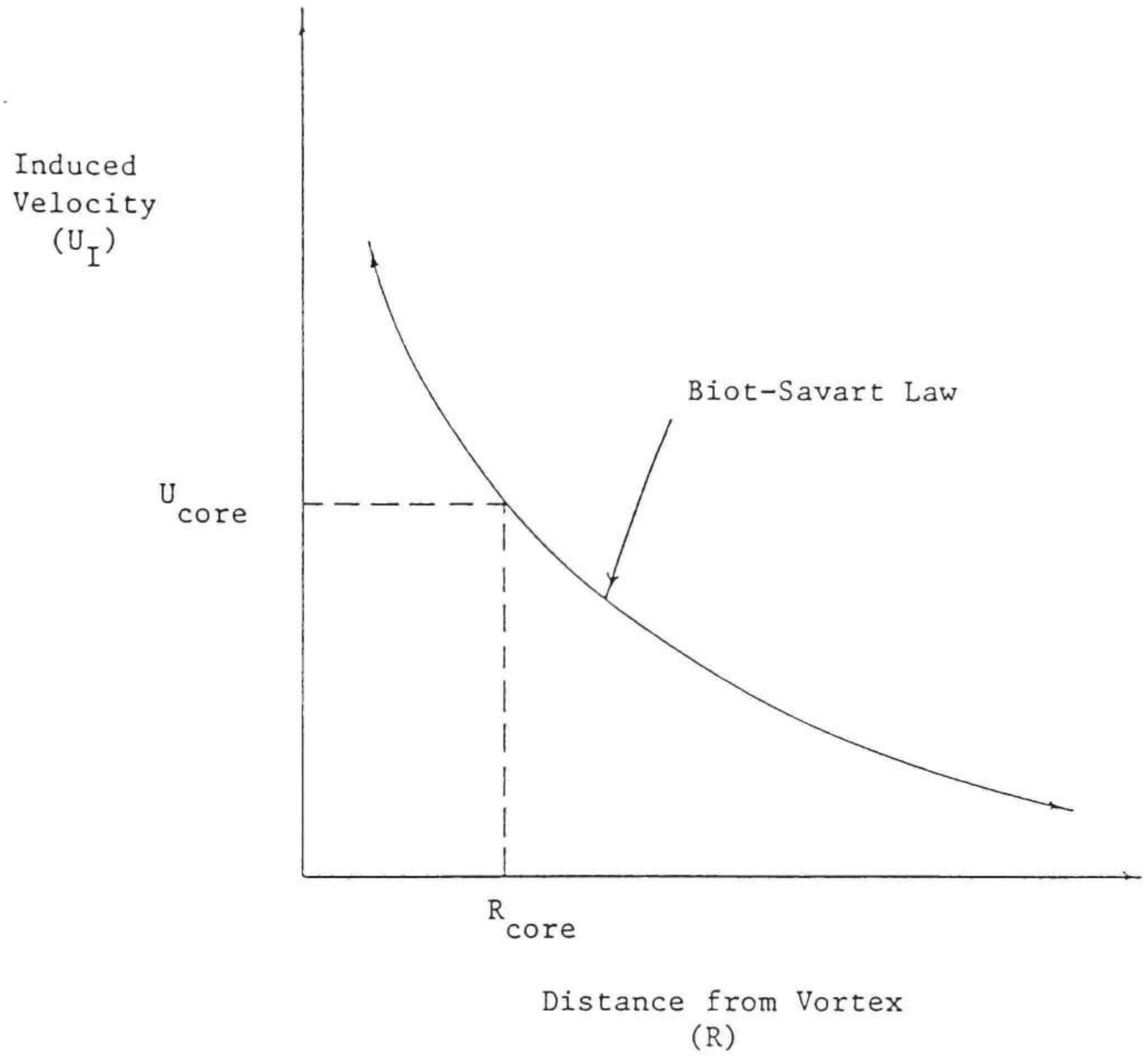

$$U_I(R) = \frac{\Gamma}{2\pi|R|} \qquad \text{for } R > R_{core}$$

$$U_I(R) = \frac{\Gamma}{2\pi|R_{core}|} \qquad \text{for } R < R_{core}$$

Figure 36. Vortex Core Approximation

where M_x and M_y are the momentum in the x and y directions, F is the complex potential and $Z = x + iy$. This equation holds for cases where the following line integral relationships are valid for the flow

$$\oint_{C_\infty} \phi\, dy = 0, \oint_{C_\infty} \phi\, dx = 0 \tag{22}$$

Here ϕ is the velocity potential and C_∞ is a curve at infinity.

For a system of n discrete vortices the complex potential can be written as

$$F = \sum_n i \frac{\Gamma_n}{2\pi} \ell n(Z-Z_n) \tag{23}$$

where Γ_n is the circulation strength of the nth vortex in the clockwise direction. Using equation (23) in equation (21) the complex momentum M can be written as

$$M = \sum_n i\rho\Gamma_n(Z_\infty - Z_n) \tag{24}$$

Since the complex force on the system is equal to the time derivative of the complex momentum, then the lift and drag forces associated with a body (system of bound and wake vortices) moving in an unbounded still fluid are given by

$$\begin{aligned} L &= -\rho\sum_n\left(\Gamma_n u_n + \frac{\partial\Gamma_n}{\partial t} x_n\right) \\ D &= \rho\sum_n\left(\Gamma_n v_n + \frac{\partial\Gamma_n}{\partial t} y_n\right) \end{aligned} \tag{25}$$

A listing of the software for this model is presented in Appendix D.

In the following section, the results of this analysis are presented along with some results of a model developed by Im [40]. Im's Advanced Dynamic Airfoil Model in Two-Dimensions (ADAM2) uses combined vortex and source panels to represent the airfoil and wake. The source and vortex strengths are determined by enforcing a set of kinematic conditions in the flow. The wake shedding is governed by a dynamic free surface condition and the characteristics of the flow near the boundary layer separation points. Separation is predicted using a momentum integral boundary layer analysis. Wake convection is governed by the induced velocity field superimposed upon the freestream.

4.2 Analytical Results

As noted in the previous section, the strengths of the separation vortices shed from the airfoil leading edge are treated as input parameters in the unsteady model. An empirical relationship which seems to express the shedding rate is given by

$$\Gamma_N^k = - \left(C_N \, K \sin\alpha^k \right) \Delta t^* \tag{26}$$

where C_N is a constant, K is the non-dimensional pitch rate, and Δt^* is the non-dimensional time step defined as

$$\Delta t^* = \frac{\Delta t U_\infty}{c} \tag{27}$$

The change in the geometric angle of attack and the non-dimensional time step are related by

$$\Delta\alpha = 2K\Delta t^* \tag{28}$$

In the present analysis the change in angle of attack, $\Delta\alpha$, was held constant at 2 degrees or 0.0349 radius for each pitching rate considered. The effect of increasing or decreasing the constant C_N on the lift and drag force calculations may be seen in Figures 37 and 38, respectively, for the illustrative case of K = 0.19. The best agreement between the analysis and the present experimental data was achieved for a value of $C_N = 15.0$.

The analytical lift and drag force results for the three lowest pitch rates considered in this study are shown in Figures 39-44. These results are for a body divided into four panels. Also shown in Figures 39-44 are the results of the analytical model (ADAM2) developed by Im [40]. For these cases the agreement between the experimental lift force and the analysis is relatively good up to high angles of attack. The drag force calculations agree favorably at the low angles of attack. However, at high angles of attack, the present analysis predicts drag forces much smaller than the experimental results. The agreement could be improved somewhat by increasing the constant C_N; however, this would alter the lift force calculations and result in larger discrepancies between the analytical lift and the experimental lift data. The drag force results of ADAM2 are seen to be in slightly better agreement than the present analysis at the higher angles of attack.

The analytical lift and drag force results for the non-dimensional pitch rates of K = .51, .71, and .99 are shown in Figures 45-50. In these cases the predicted lift forces are seen to be far in excess of the experimental results. The rapid increase in the analytical lift force at low angles of attack is due to the very large upwash on the

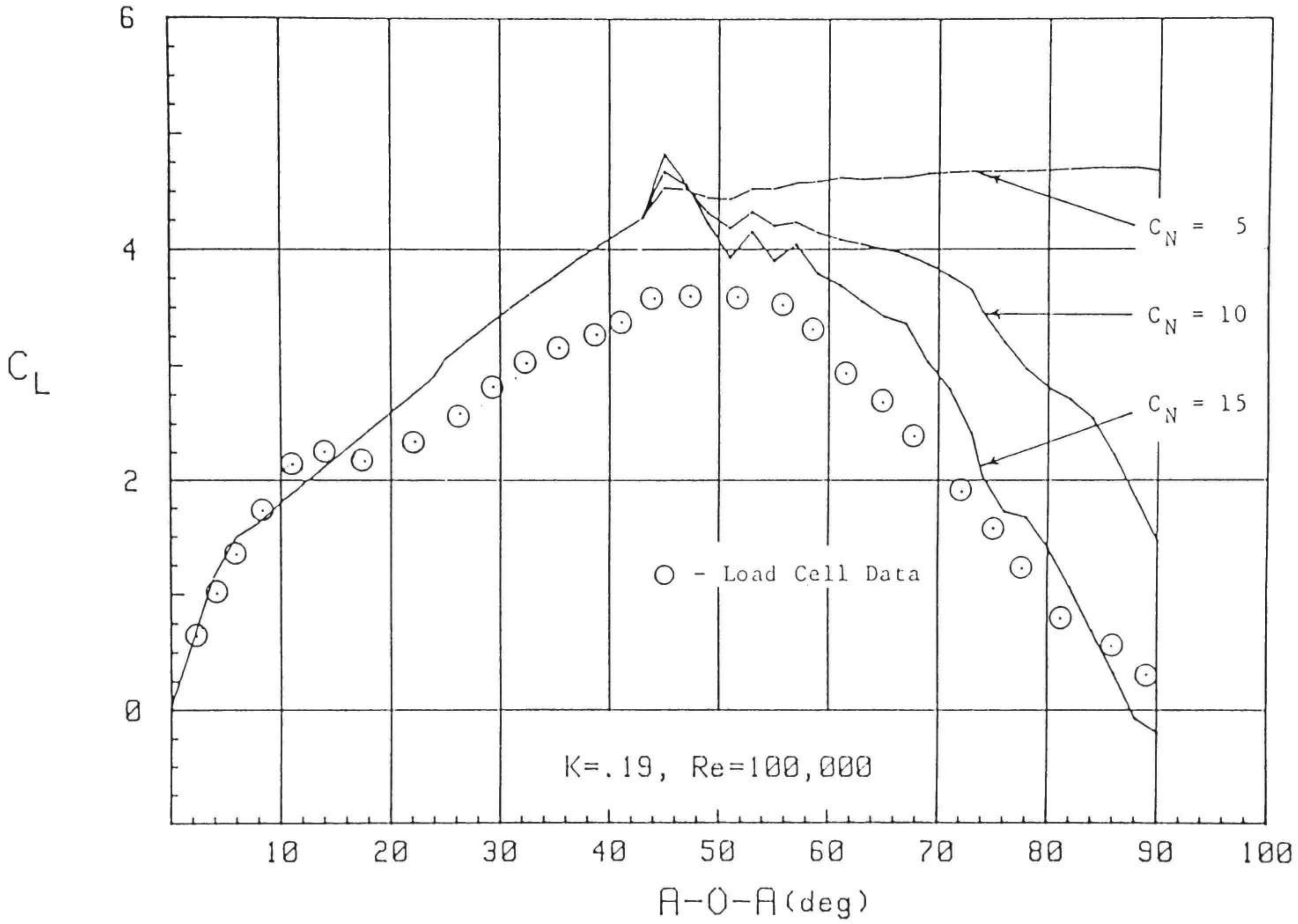

Figure 37. Effect of Leading Edge Vortex Strength on the Lift Coefficient for K = 0.19

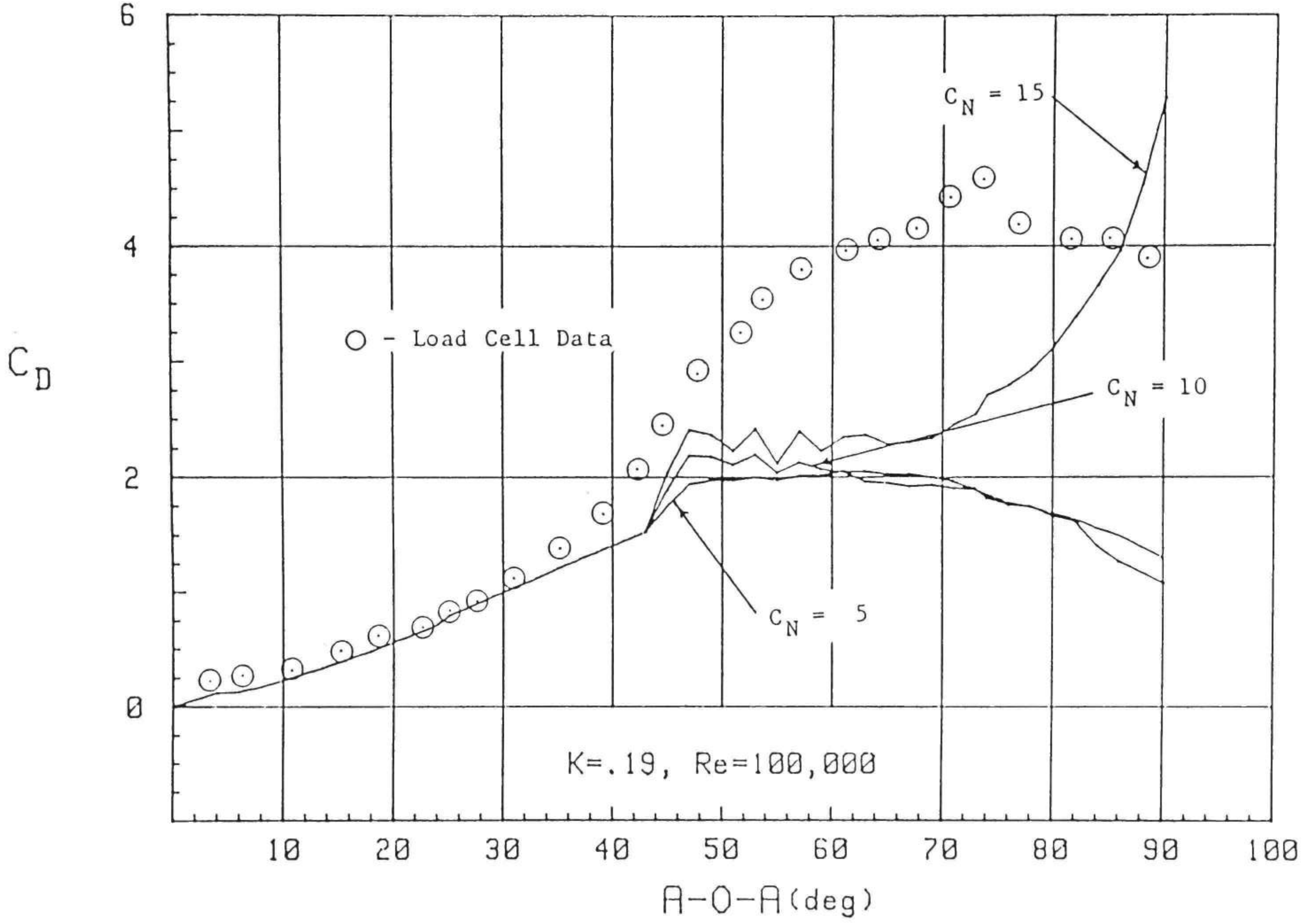

Figure 38. Effect of Leading Edge Vortex Strength on the Drag Coefficient for K = 0.19

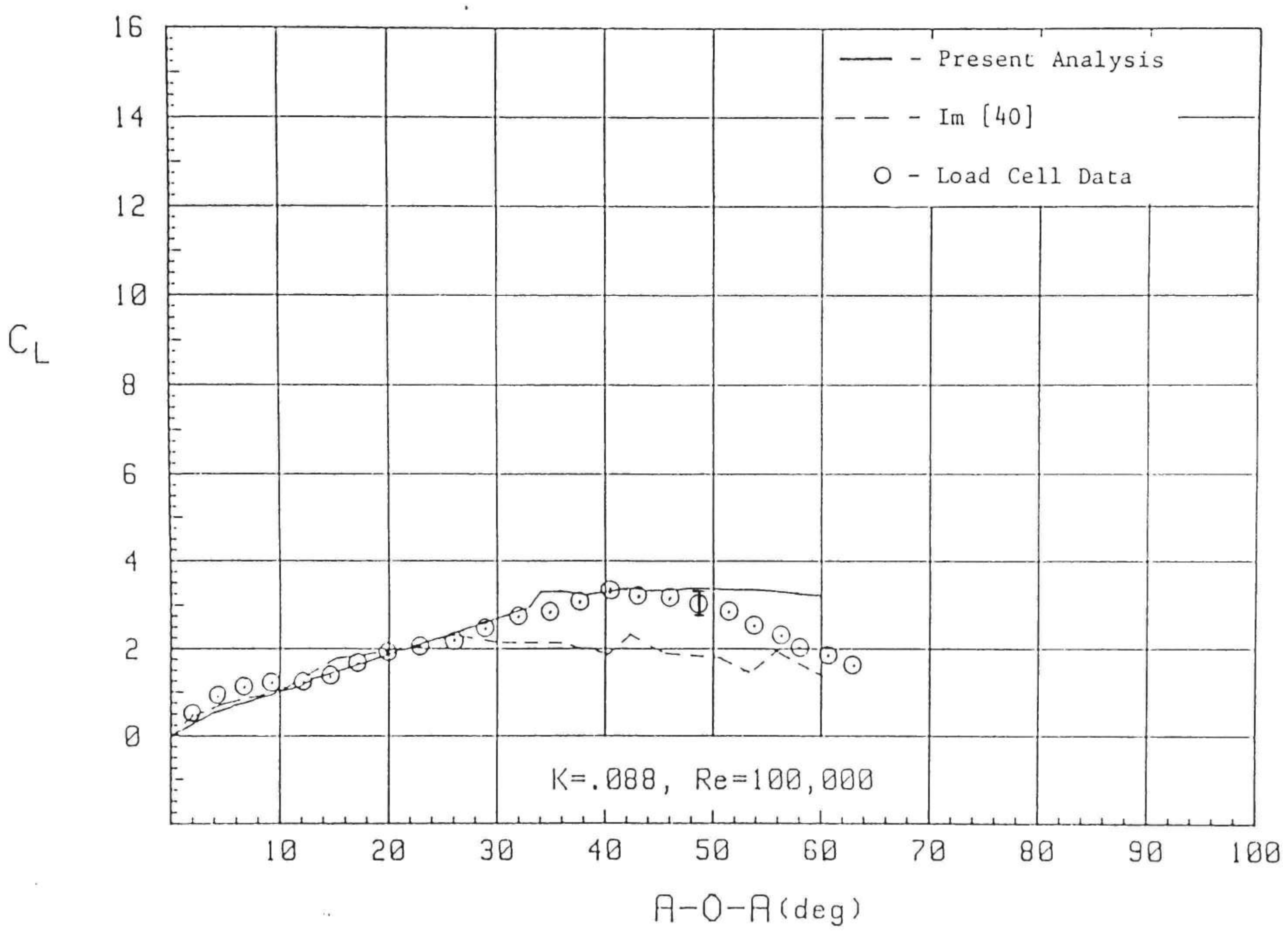

Figure 39. Analytical Lift Force Results for K = 0.088

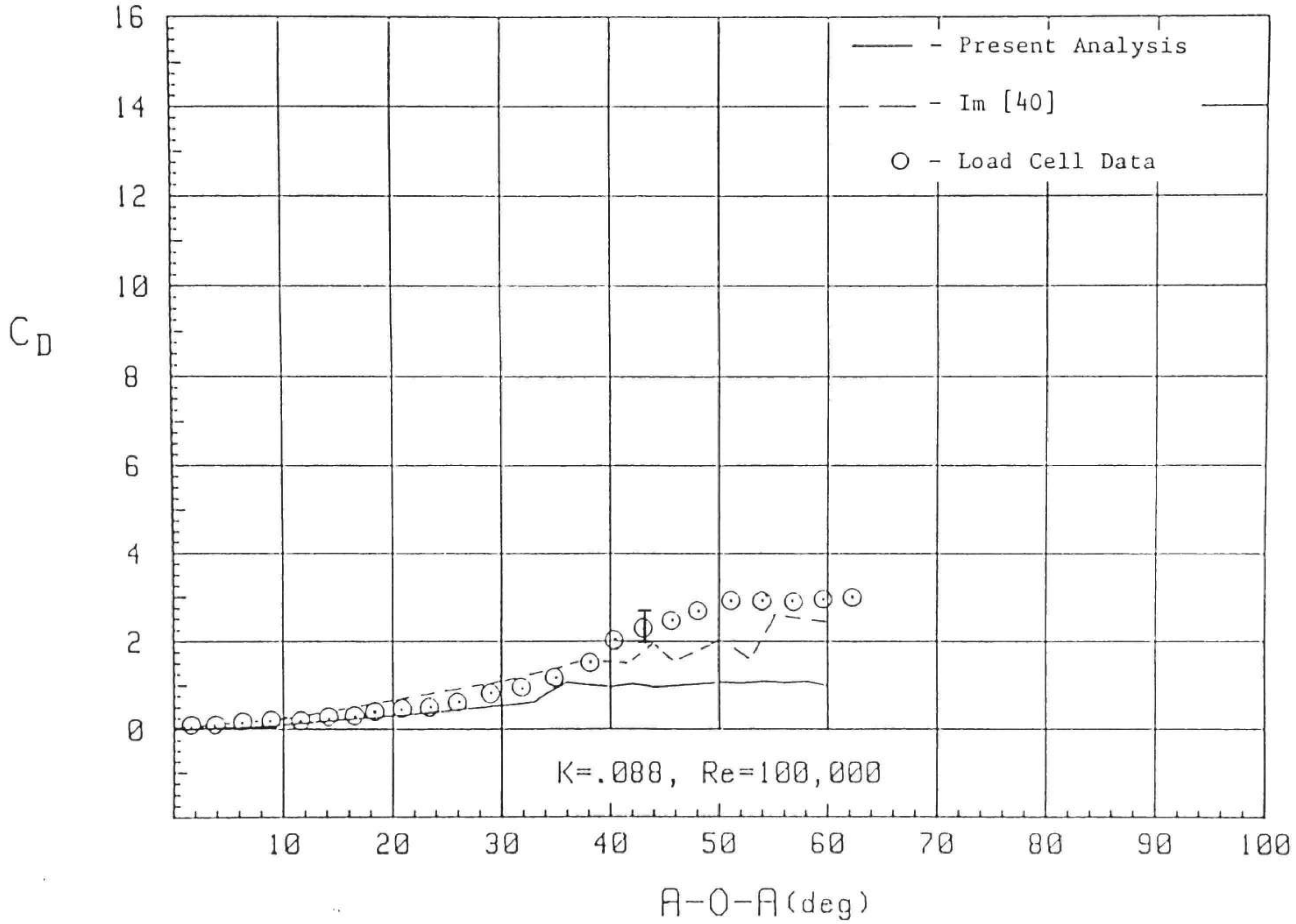

Figure 40. Analytical Drag Force Results for K = 0.088

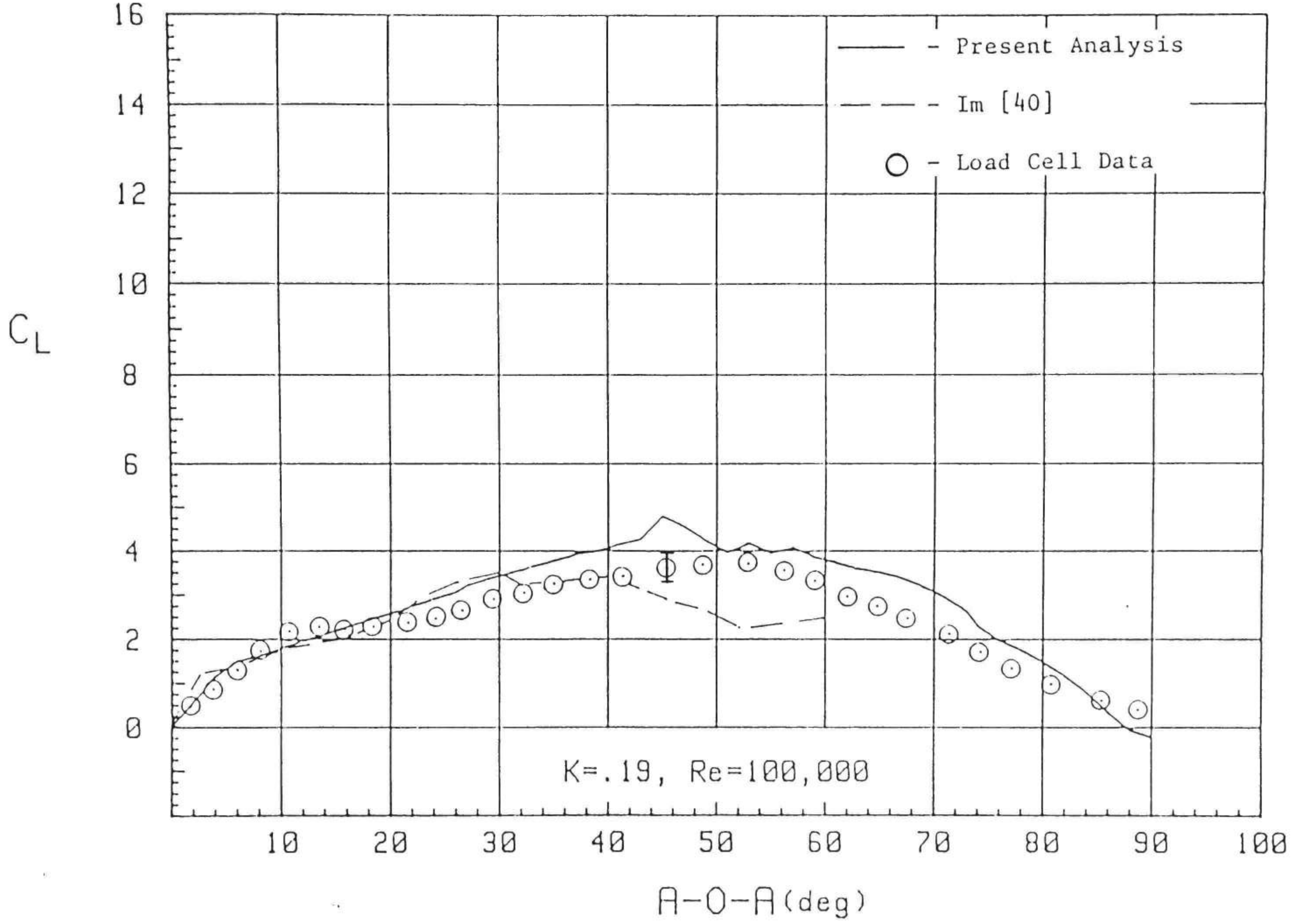

Figure 41. Analytical Lift Force Results for K = 0.19

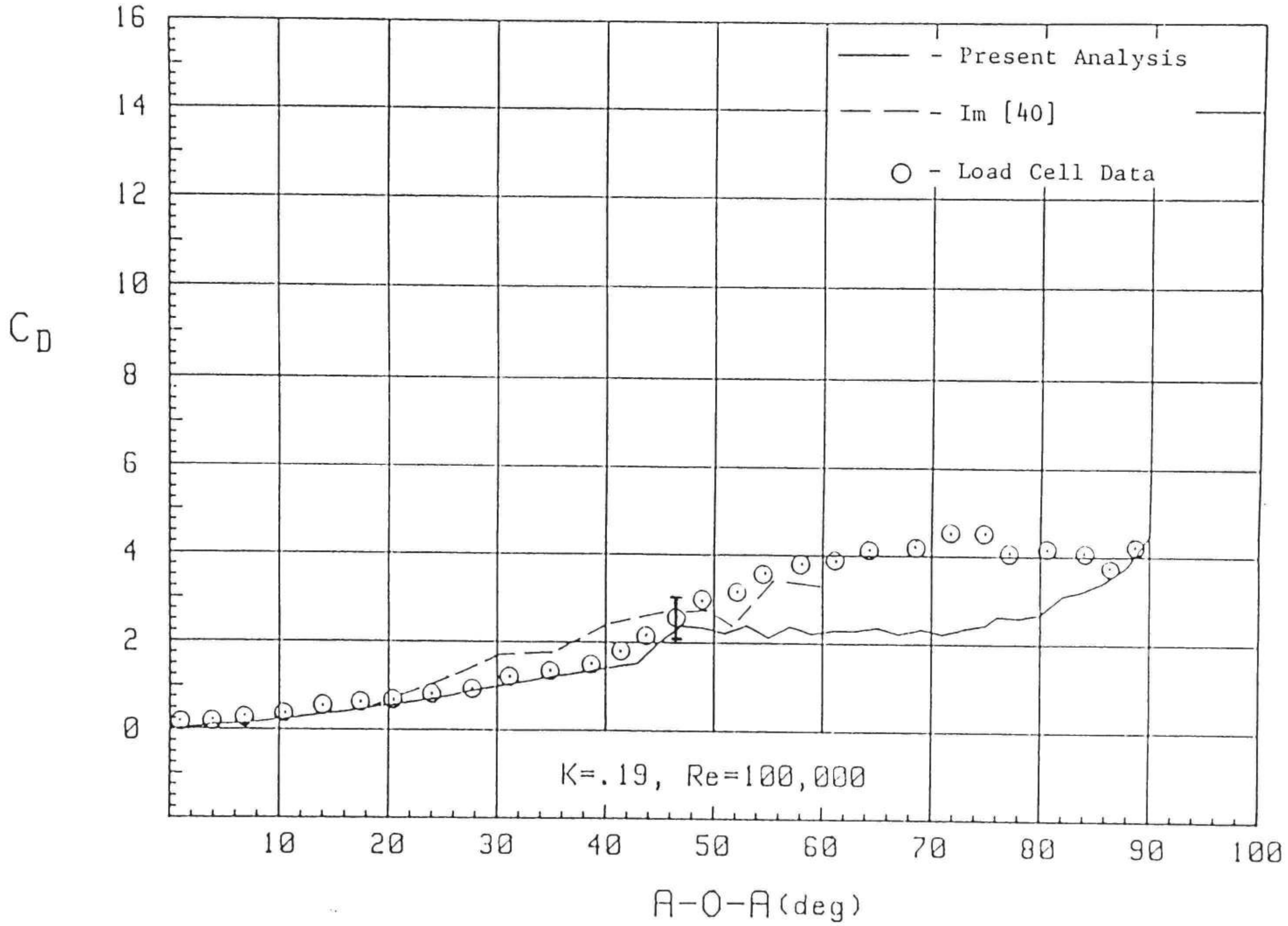

Figure 42. Analytical Drag Force Results for K = 0.19

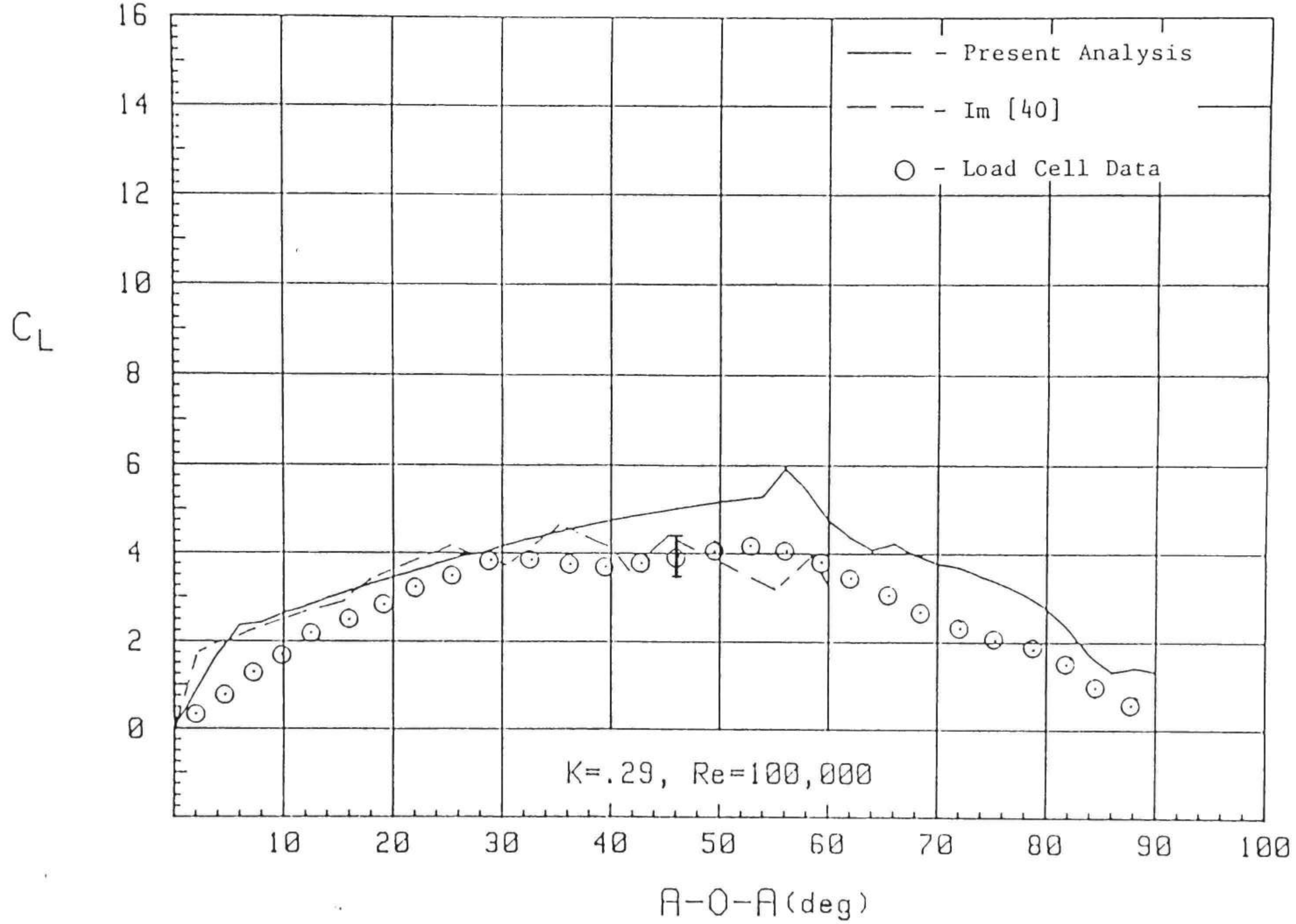

Figure 43. Analytical Lift Force Results for K = 0.29

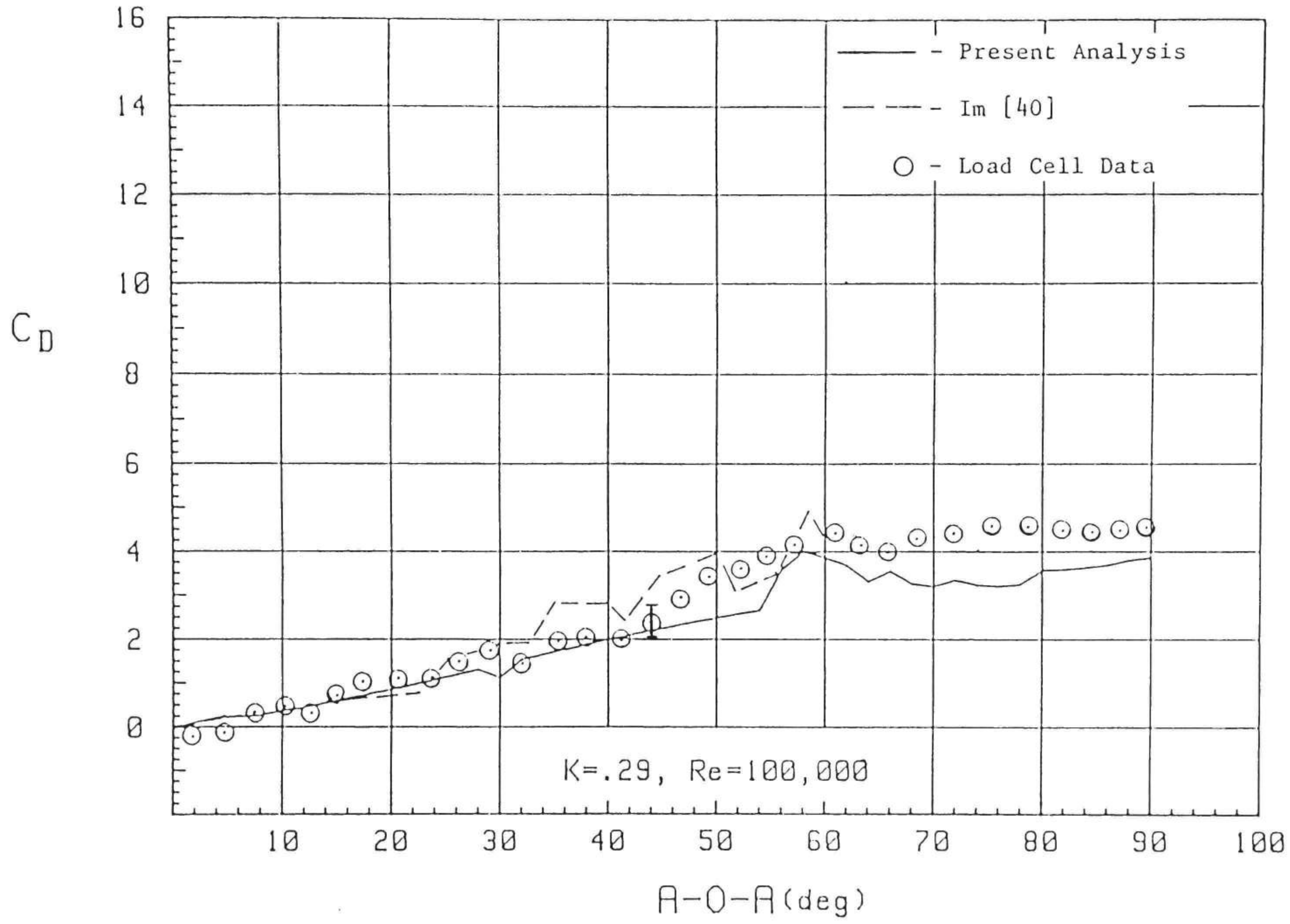

Figure 44. Analytical Drag Force Results for K = 0.29

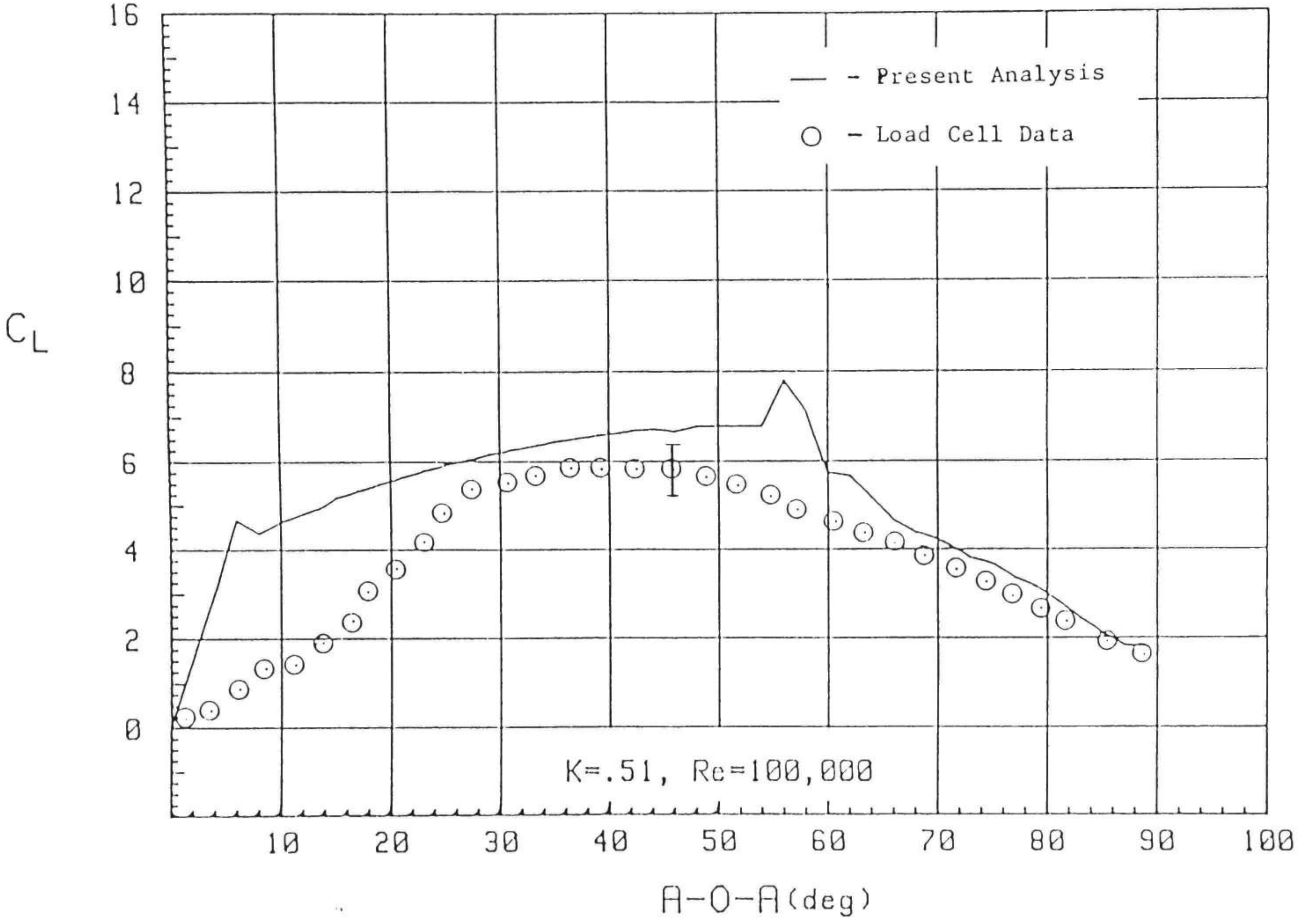

Figure 45. Analytical Lift Force Results for K = 0.51

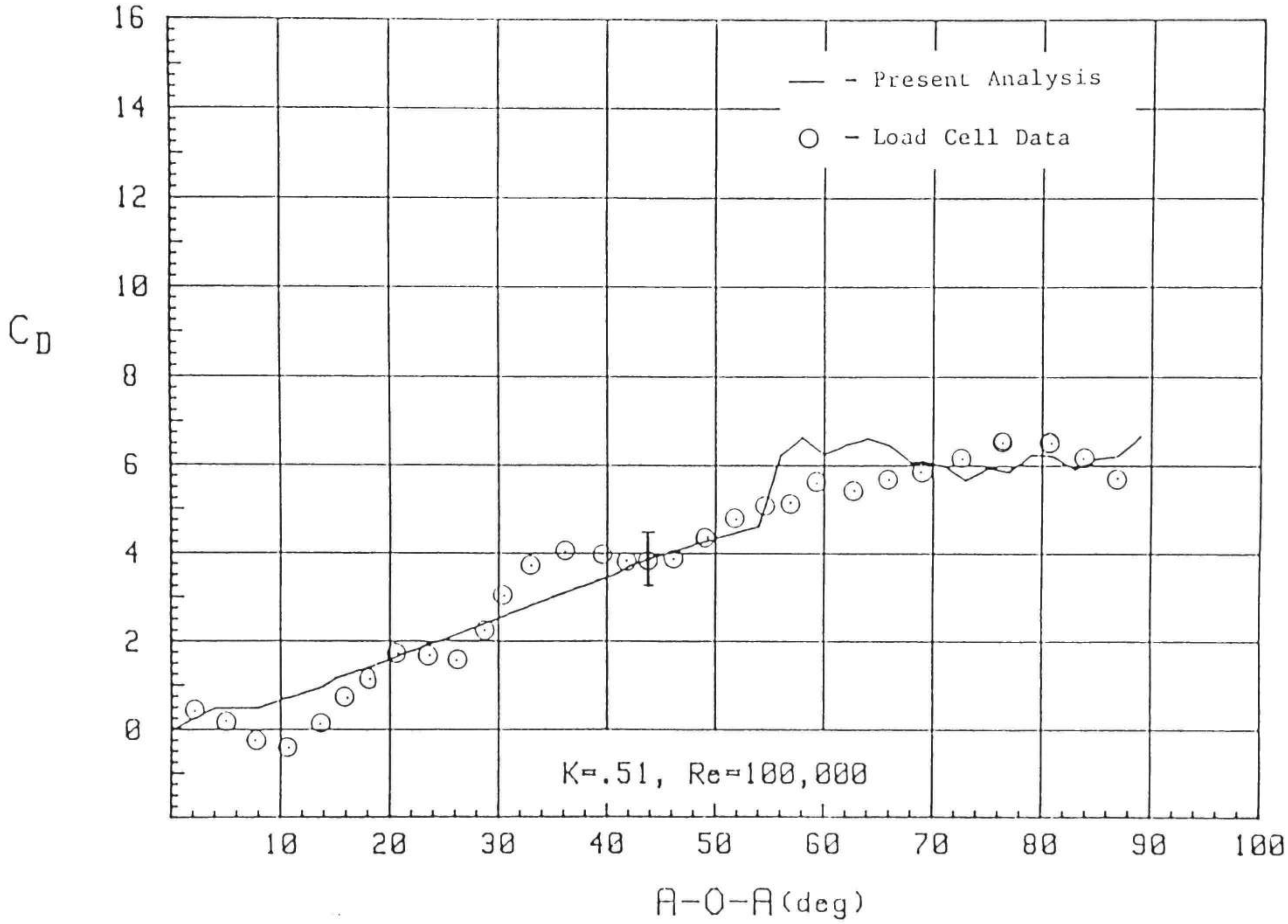

Figure 46. Analytical Drag Force Results for K = 0.51

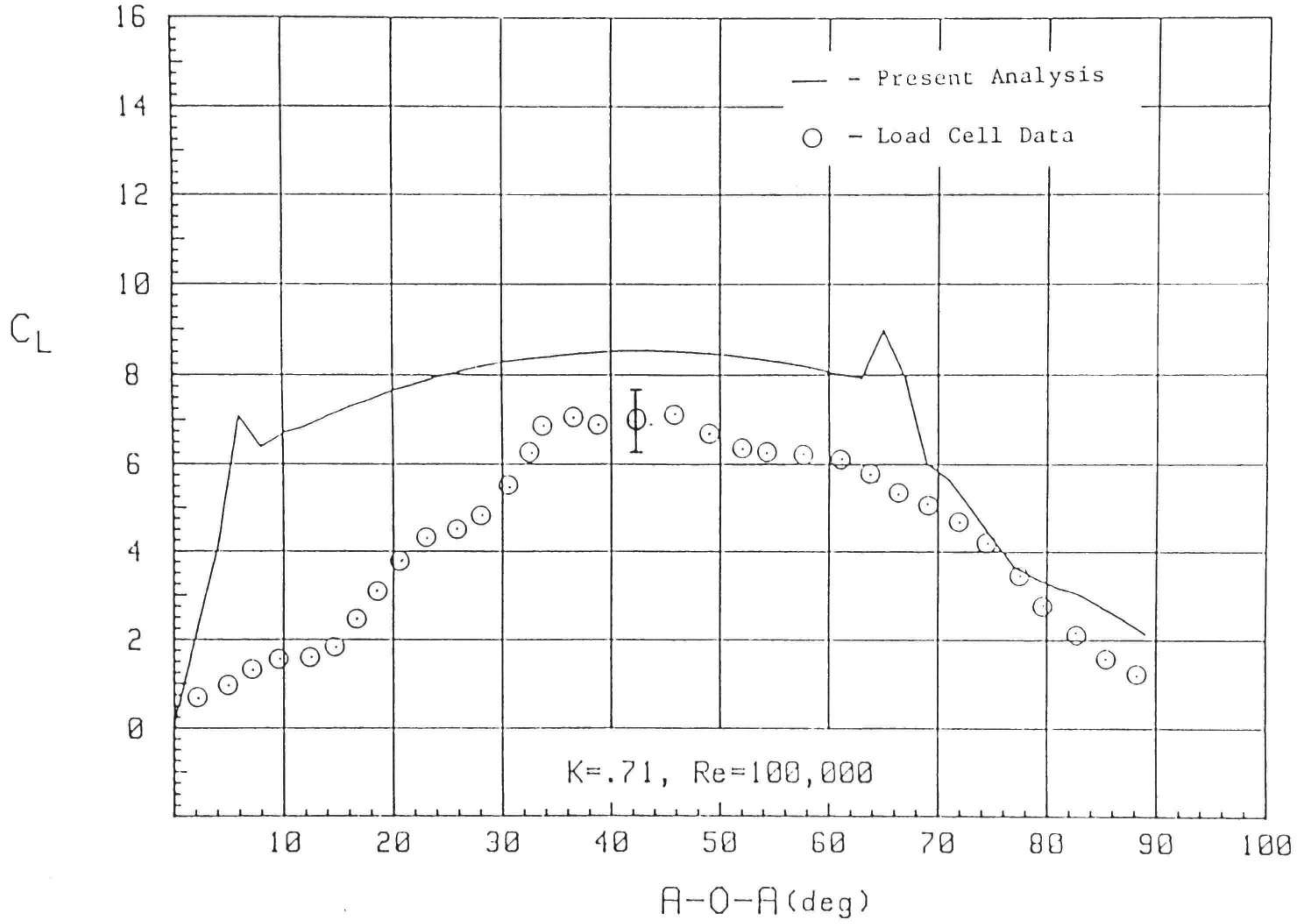

Figure 47. Analytical Lift Force Results for K = 0.71

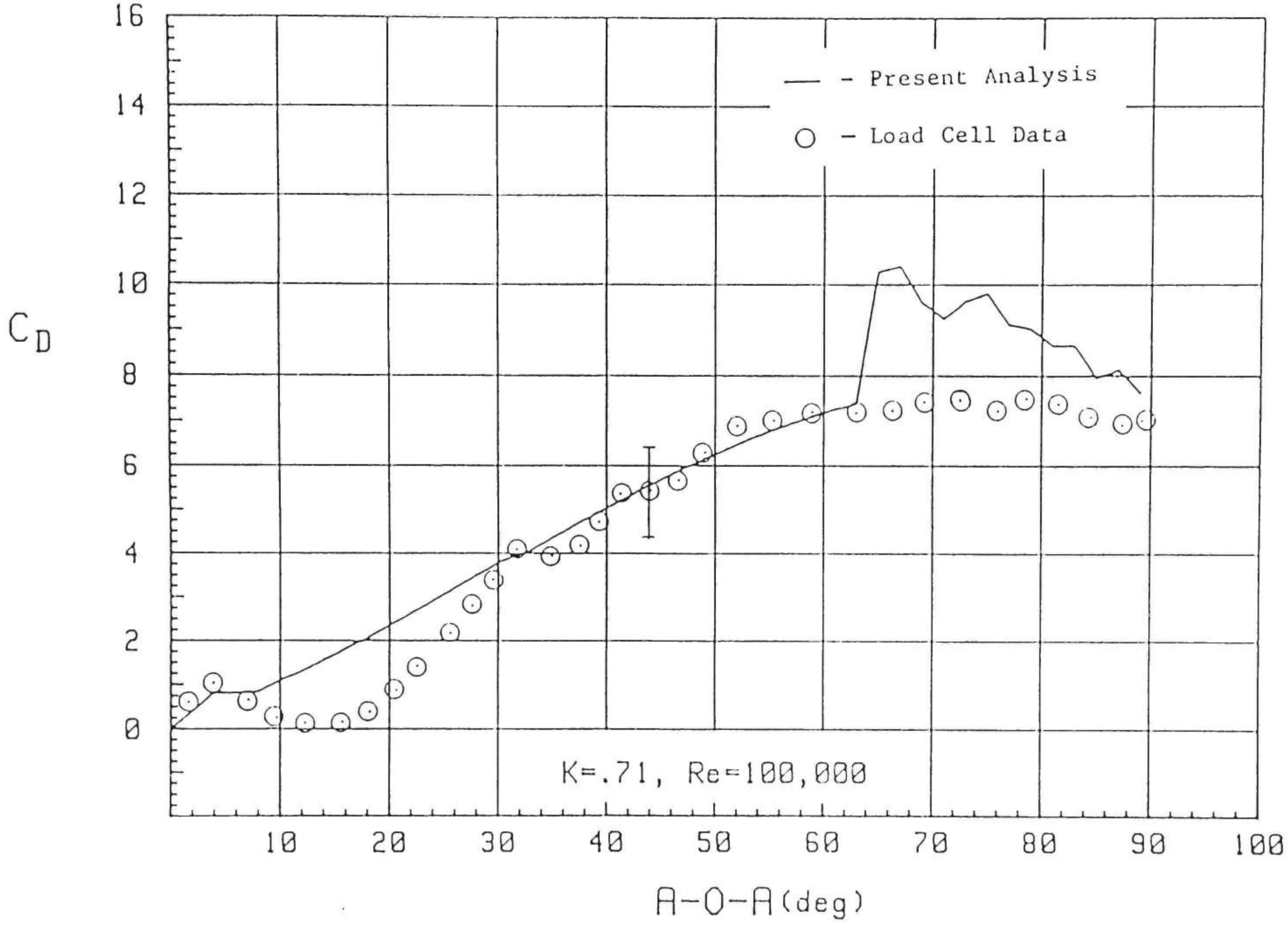

Figure 48. Analytical Drag Force Results for K = 0.71

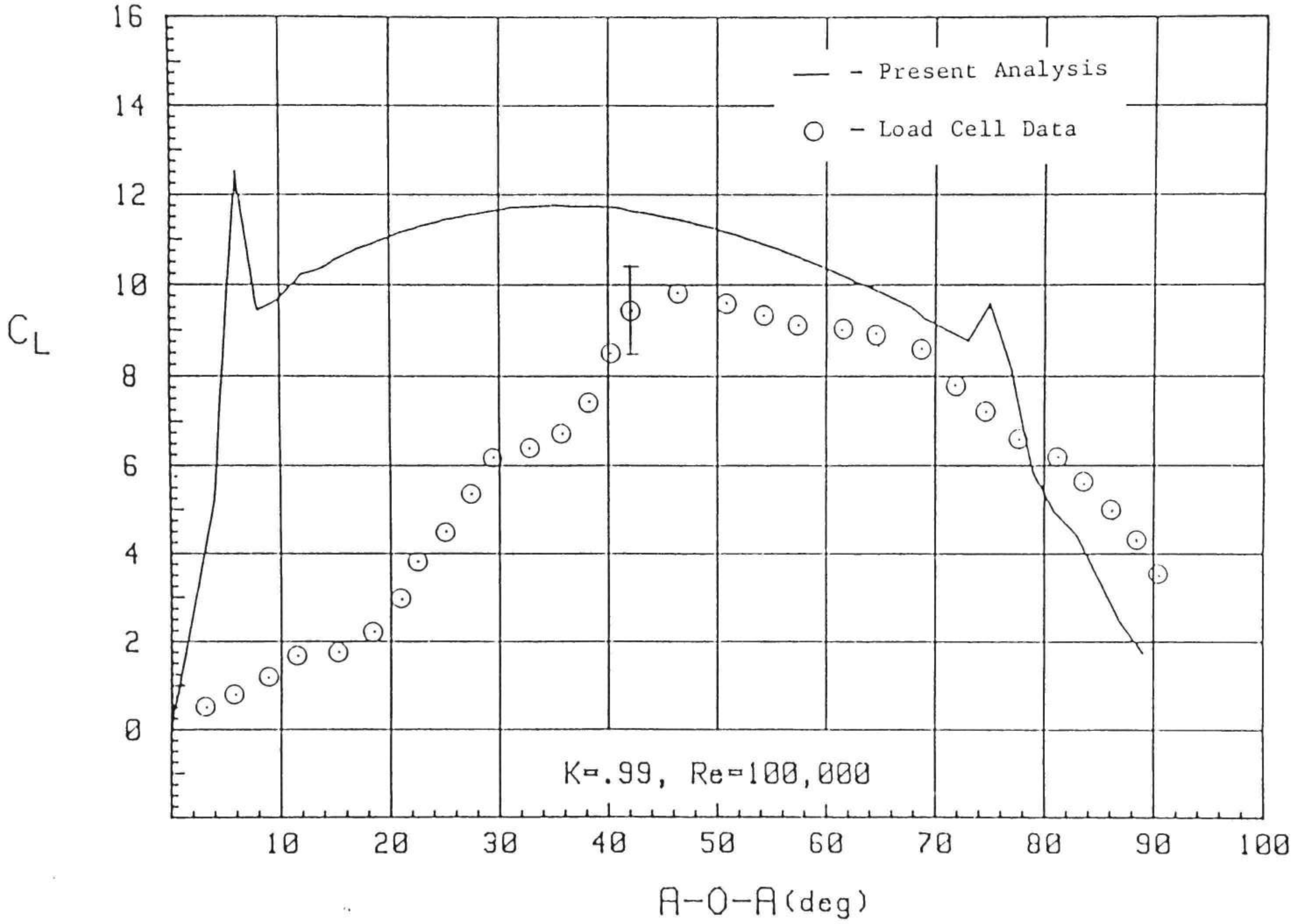

Figure 49. Analytical Lift Force Results for K = 0.99

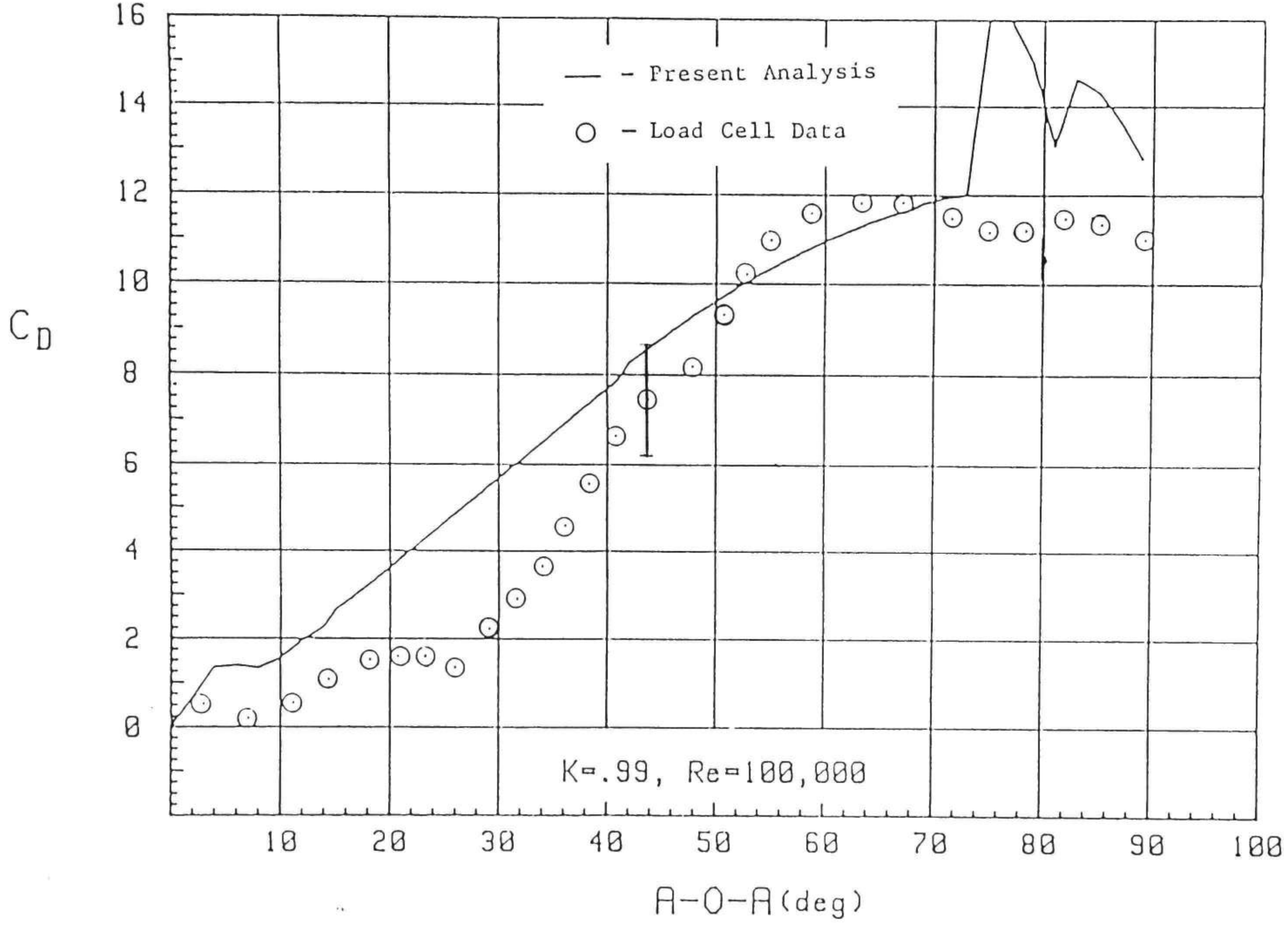

Figure 50. Analytical Drag Force Results for K = 0.99

airfoil caused by the airfoil pitching motion. Since the calculations proceed by enforcing a surface tangency condition, this large upwash forces the bound vorticity to grow rapidly, resulting in the large lift force results. As the maximum lift force is approached the agreement between the analysis and measurement improves. However, it must be concluded that the present analysis is inadequate for predicting lift forces in the high pitch rate flows. The model of Im in its present form is also inadequate for these cases, as it becomes unstable at high pitch rates.

The drag force calculations for the high pitch rate cases are seen to agree favorably with the experimental data for K = .51. For K = .71 and .99 the analytical drag forces are larger than the experimental results at low angles of attack as may be seen in Figures 48 and 50. This may be partially attributed to mechanical oscillations in the experimental model which significantly affected the tangential force measurements, and thus the drag force results at low angles of attack. In addition, the agreement between the analysis and measurements is seen to be poor at post-stall angles of attack.

CHAPTER V

CLOSURE

5.1 Summary of Experimental Investigation

The primary objective of the experimental study was to observe the variations in aerodynamic performance of a NACA 0015 airfoil with rate of pitch over a range of non-dimensional pitching rates which may be characterized as moderate to high ($.1 < K < 1$). Much of the data presented herein pertains directly to the phenomenon of aerodynamic stall which naturally occurs at the high angles of attack (up to 90°) considered in these tests. The data, which were obtained in the Texas Tech tow-tank facility, consist of aerodynamic loads, surface pressure distributions, and flow visualizations for a NACA 0015 airfoil pitching about its quarter chord at a Reynolds number of 1×10^5.

Analysis of the data resulted in empirical correlations for the maximum aerodynamic forces and simple trigonometric relations expressing the variation of lift and drag with pitch rate and angle of attack. In addition, an existing correlation due to Gormont [9] for leading edge separation on oscillating airfoils was extended [38] to encompass the wide range of pitching rates considered in this study. These correlations are discussed in detail in Section 3.4.

5.2 Summary of Analytical Model

A two-dimensional discrete vortex method was used in which the airfoil is modeled as a flat plate divided into a number of panels, each panel consisting of a bound vortex and a control point. The strengths of the bound vortices are determined by the solution of a system of linear equations resulting from imposing a surface tangency condition at each control point.

The wake is modeled as a series of discrete vortices shed from the airfoil leading and trailing edges. The strength of the "separation" vortices shed from the leading edge is left as an input parameter after separation occurs and is equal to zero prior to separation. The angle of attack at which separation occurs is given by an extension of the Gormont model. The strengths of the vortices shed from the trailing edge are computed through application of Kelvin's theorem; which requires that the total vorticity in the flow remain constant. As a vortex leaves the trailing edge it is replaced by a nascent vortex centered on the trailing edge. The effects of the vortex at the leading edge and the nascent vortex at the trailing edge are included in the surface tangency calculations. In the analysis, the wake elements are allowed to convect downstream at their respective local velocities which are given by the superposition of the perturbation velocities of all other wake vortices and the velocity induced by the bound vorticity upon the freestream velocity.

The aerodynamic lift and drag forces are computed using a momentum approach. In this method, the complex momentum associated with a two-dimensional potential flow is related to an integral of the complex potential, which is readily written for a system of discrete vortices. The complex force on the system is obtained by forming the time derivative of the complex momentum.

5.3 Conclusions

The experimental data obtained in this study indicate a direct relation between the aerodynamic airfoil loads and the airfoil pitching rate. The maximum lift and drag coefficients an airfoil achieves over the range of angles of attack from 0° to 90° increase with increasing pitch rate for $0 < K < 1$, at a Reynolds number of 10^5. Lift and drag coefficients on the order of 10 and 12, respectively, were observed at the highest pitch rate considered here. This augmentation of the forces is naturally related to the unsteady behavior of the fluid.

The lift force in the high pitch rate case ($K = .5$) develops slower than that in the low to moderate range. This may be associated with the negative effective angles of attack at the nose for low geometric angles of attack due to the rapid nose-up motion of the airfoil. In the high pitch rate cases this effective angle exceeds the static stall angle; suggesting the possibility of underside separation near the leading edge. This, however, has not yet been substantiated by experimental data. In addition, the large negative effective angles of attack give rise to a region of negative pressure, near the nose on the airfoil underside and a region of positive pressure on the airfoil topside. The effect of this is to reduce the lift force. This is a possible explanation for the observed tendency of the lift to develop slower in the high pitch rate flows.

In the low to moderate pitch rate range, the observed mechanisms of dynamic stall are similar to those reported by other investigators. The stall phenomenon is characterized by flow detachment at the leading edge and by the formation of a large dynamic stall vortex over the airfoil topside. This is accompanied by a loss of suction pressure near the leading edge and a flattening of the pressure distribution over the airfoil topside. The angle of attack at which leading edge separation occurs is delayed with increasing pitch rate.

In the high pitch rate flows, the tendency for the flow to separate at the leading edge is heavily suppressed by the pitching motion of the airfoil. Even at angles of attack approaching 90°, the detached region on the airfoil topside resembles a separation bubble rather than a fully developed dynamic stall vortex. This gives rise to very large suction peaks in the pressure distribution which remain up to high angles of attack. As in the moderate pitch rate cases, the effect of increasing the pitch rate is to delay leading edge separation.

Within the limitations of the analytical model summarized in Section 5.2, it was found that the lift force and the strength of the vorticity shed from the leading edge at post-stall angles of attack are inversely related, while the drag force and the strength of the leading edge vorticity are directly related. The results of the study indicate that the lift force is more sensitive than the drag force to variations in this strength. As noted previously, the strength of the vorticity shed from the leading edge is an input parameter in the analysis. The result of the variation in this parameter which led to the closest agreement with the experimental data is discussed in Section 4.2.

The analytical lift force results were found to be in fair agreement with the experimental data for non-dimensional pitch rates below 0.3 up to large angles of attack. The drag force calculations for these cases was found to be in good agreement with the empirical data for low angles of attack. For post-stall angles of attack, however, the analytical drag predictions are much lower than the experimental results.

In the high pitch rate studies, the analytical lift force develops much more rapidly than the experimental lift. This is associated with the large upwash due to the airfoil pitching motion, which forces the bound vorticity to grow rapidly in order to satisfy the surface tangency condition. In light of this, the present analysis appears to be inadequate for predicting the high pitch rate lift coefficients, if the experimental data are to be believed. The analytical drag force results for the high pitch rate cases are in fair agreement with the experimental results for moderate angles of attack. However, at the low angles of attack the analysis yields drag forces larger than the empirical data. This discrepancy may be partially attributed to large-scale oscillations of the test model in the chordwise directions at low angles of attack, which introduces experimental error in the tangential force which is the dominant component of the drag force.

5.4 Recommendations

Several logical extensions of the present experimental work exist. A few of these are listed below.

- In the present experiment, the airfoil began pitching-up from an angle of attack of zero degrees. It would be interesting to study the behavior of the aerodynamic loads for the case where the original angle of attack is, say, ten degrees.

- The execution of a post stall maneuver would involve an unsteady flow separation and reattachment sequence. The study presented herein considers unsteady flow separation. An investigation could be undertaken to study the aerodynamics of the unsteady flow reattachment. It would be of interest to see if the Gormont model could be extended to these cases.

REFERENCES

1. Ham, N. D. and Young, M. I., "Torsional Oscillations of Helicopter Blades Due to Stall," J. Aircraft, Vol. 3, No. 3, pp. 218-224, May-June 1966.

2. Horlock, J. H., Greitzer, E. M. and Henderson, R. E., "The Response of Turbomachine Blades to Low Frequency Inlet Distortions," J. Engineering Power, p. 195, April 1977.

3. Oler, J. W. and Strickland, J. H., "Dynamic Stall Regulation of the Darrieus Turbine," Sandia Laboratory Report on Contract No. 74-1218.

4. McCroskey, W. J., "Recent Developments in Dynamic Stall," Proceedings of a Symposium on Unsteady Aerodynamics, University of Arizona, Vol. 1, pp. 1-33, 1975.

5. McCroskey, W. J., "Some Current Research in Unsteady Fluid Dynamics - The 1976 Freeman Scholar Lecture," J. Fluids Engineering, Vol. 99, No. 1, pp. 8-38, 1977.

6. Herbst, W., "Supermaneuverability," Proceedings of the Workshop on Unsteady Separated Flow, USAF Academy, August 10-11, 1983 (in press).

7. Strickland, J. H., "Dynamic Stall: A Study of the Constant Pitching Rate Case," USAF Summer Faculty Research Program 1983 Report (in press).

8. Ericsson, L. E. and Reding, J. P., "Dynamic Stall Analysis in Light of Recent Numerical and Experimental Results," J. Aircraft, Vol. 13, pp. 248-255, 1976.

9. Gormont, R. E., "A Mathematical Model of Unsteady Aerodynamics and Radial Flow for Application to Helicopter Rotors," U.S. Army AMRDL Technical Report 72-67, 1973.

10. Carta, F. O., "Unsteady Normal Force on an Airfoil in a Periodically Stalled Inlet Flow," J. Aircraft, Vol. 4, pp. 416-421, 1967.

11. Johnson, W., "The Effect of Dynamic Stall on the Response and Airloading of Helicopter Rotor Blades," J. Am. Hel. Soc., Vol. 14, pp. 68-79, 1969.

12. Mehta, U., "Dynamic Stall of an Oscillating Airfoil," AGARD Fluid Dynamics Panel Symposium, Ottawa, Paper No. 23, September 1977.

13. Hodge, J. K., Stone, A. L., and Miller, T. E., "Numerical Solution for Airfoils Near Stall in Optimized Boundary-Fitted Curvilinear Coordinates," AIAA Journal, Vol. 17, pp. 458-464, 1979.

14. Nash, J. F., Carr, L. W., and Singleton, R. E., "Unsteady Turbulent Boundary Layers in Two-Dimensional Incompressible Flow," AIAA Journal, Vol. 13, pp. 167-173, 1975.

15. Dwyer, H. A. and McCroskey, W. J., "Crossflow and Unsteady Boundary Layer Effects on Rotating Blades," AIAA Journal, Vol. 9, pp. 1498-1505, 1971.

16. Telionis, D. P., "Calculations of Time-Dependent Boundary Layers," Unsteady Aerodynamics, R. B. Kinney (Ed.), Vol. 1, p. 155, 1975.

17. Ham, N. D., "Aerodynamic Loading on a Two-Dimensional Airfoil During Dynamic Stall, AIAA Journal, Vol. 6, pp. 1927-1934, 1968.

18. Katz, J., "A Discrete Vortex Method for the Non-Steady Separated Flow Over an Airfoil," J. Fluid Mech., Vol. 102, pp. 315-328, 1981.

19. Strickland, J. H., Oler, J. W., and Im, B. J., "Preliminary Results from the Unsteady Airfoil Model USTAR2," Proceedings of the Workshop on Unsteady Separated Flow, USAF Academy, August 10-11, 1983 (in press).

20. Dvorak, F. and Maskew, B., "Prediction of Dynamic Stall Characteristics Using Advanced Non-linear Panel Methods," Proceedings of the Workshop on Unsteady Separated Flow, USAF Academy, August 10-11, 1983 (in press).

21. McCroskey, W. J. and Philippe, J. J., "Unsteady Viscous Flow on Oscillating Airfoils," AIAA Journal, Vol. 13, No. 1, pp. 71-79, January 1975.

22. McAlister, K. W. and Carr, L. W., "Water Tunnel Visualizations of Dynamic Stall," J. Fluids Engineering, Vol. 101, pp. 376-380, September 1978.

23. Martin, J. M., Empey, R. W., and McCroskey, W. J., "An Experimental Analysis of Dynamic Stall on an Oscillating Airfoil," J. Am. Hel. Soc., Vol. 19, No. 1, pp. 26-32, January 1973.

24. Robinson, M. C. and Luttges, M. W., "Unsteady Flow Separation and Attachment Induced by Pitching Airfoils," AIAA paper 83-0131, January 1983.

25. Liiva, J. and Davenport, F. J., "Dynamic Stall of Airfoil Sections for High-Speed Rotors," presented at the 24th Annual Forum of the American Helicopter Society, May 1968.

26. Rainey, G. A., "Measurement of Aerodynamic Forces for Various Mean Angles of Attack on an Airfoil Oscillating in Pitch and on Two Finite-Span Wings Oscillating in Bending with Emphasis on Damping in the Stall," NACA TN3643, Washington, D. C., May 1956.

27. Strickland, J. H., Webster, B. T., and Nguyen, T., "A Vortex Model of the Darrieus Turbine: An Analytical and Experimental Study," J. Fluids Engineering, Vol. 101, No. 12, pp. 500-505, 1979.

28. Harper, P. W. and Flanigan, R. E., "The Effect of Rate Change of Angle of Attack on the Maximum Lift of a Small Model," NACA TN2061, 1950.

29. Francis, M. S., Keesee, J. E., and Retelle, J. P., "An Investigation of Airfoil Dynamic Stall With Large Amplitude Motions," USAF/RJSRL Report (in press).

30. Deekens, A. C. and Kuebler, W. R., "A Smoke Tunnel Investigation of Dynamic Separation," Aeronautics Digest, USAF A-TR-79-1, pp. 2-16, February 1979.

31. Daley, D. C., "The Experimental Investigation of Dynamic Stall," Thesis, AFIT/GAE/AA/820-6, Air Force Institute of Technology, WPAFB,OH, 1983.

32. Walker, J., Helin, H., and Strickland, J., "An Experimental Investigation of an Airfoil Undergoing Large Amplitude Pitching Motions," accepted for publication in AIAA J.

33. Walker, J., Helin, H., and Chou, D., "Unsteady Surface Pressure Measurements on a Pitching Airfoil," AIAA Shear Flow Conference Paper, AIAA-85-0532, March 12-14, 1985.

34. Schraub, F. A., Kline, S. J., Henry, J., Runstadler, P. W., and Littell, A., "Use of Hydrogen Bubbles for Quantitative Determination of Time Dependent Velocity Fields in Low-Speed Water Flows," J. Basic Engineering, Vol. 87, pp. 429-522, June 1965.

35. Graham, G. M., "Measurement of Instantaneous Pressure Distributions and Blade Forces on an Airfoil Undergoing Cycloidal Motion," M. S. Thesis, Texas Tech University, December 1982.

36. Karamcheti, K., Principles of Ideal Fluid Aerodynamics, Krieger Publishing, p. 550, 1980.

37. Chou, Y. and Huang, M., "Unsteady Flows About a Joukowski Airfoil in the Presence of Moving Vortices," AIAA 21st Aerospace Meeting Paper, AIAA-83-0129, January 10, 1983.

38. Strickland, J. H. and Graham, G. M., "A Dynamic Stall Inception for Airfoils Undergoing Constant Pitch Rate Motions," Technical Note submitted to AIAA for publication in AIAA J., September 1984.

39. Theodorsen, T., "Impulse and Momentum in an Infinite Fluid, Theodore von Karman Anniversary Volume, published by the friends of Theodore von Karman, Pasadena, California, May 1941.

40. Im, B. J., A Numerical Model for Two-Dimensional Unsteady Flow Calculations With a Surface Panel Method, Doctoral Dissertation, Texas Tech University, In Progress.

41. Kline, S. J. and McClintock, F. A., "Describing Uncertainties in Single Sample Experiments," Mech. Eng., Vol. 75, pp. 3-8, 1953.

APPENDIX A

UNCERTAINTY ANALYSIS

The uncertainties in the airfoil dynamic parameters, the aerodynamic forces and the pressure coefficient are computed for a non-dimensional pitching rate of $K = 0.51$ at 45° angle of attack using the method of Kline and McClintock [41]. The uncertainty in a particular variable X is denoted by ΔX.

A.1 Non-dimensional Pitching Rate

The uncertainties in the actual pitch rate, the airfoil chord length and freestream velocity are estimated to be $(\Delta\dot{\alpha}, \Delta c, \Delta U_\infty) \rightarrow (\pm 2°/s, \pm .02 \text{ in}, \pm .04 \text{ ft/s})$. For $K = .51$, $(\dot{\alpha}, c, U_\infty) \rightarrow (50°/s, 14 \text{ in}, 1 \text{ ft/s})$. The uncertainty in the non-dimensional pitch rate is given by

$$\frac{\Delta K}{K} = \pm \left[\left(\frac{\Delta\dot{\alpha}}{\dot{\alpha}}\right)^2 + \left(\frac{\Delta c}{c}\right)^2 + \left(\frac{\Delta U_\infty}{U_\infty}\right)^2\right]^{1/2} \qquad \text{(A.1)}$$

$$= \pm\ 0.057 \ (10 \text{ to } 1)$$

A.2 Strain Gage Measurements

The uncertainty in the bridge output voltage is affected by the uncertainties in the bridge zero adjustment, the electrical noise, and vibrational mechanical noise. These are estimated to be $(\Delta E_o, \Delta E_N, \Delta E_M) \rightarrow (\pm .05V, \pm .05V, \pm .2V)$. For an angle of attack of 45° and a non-dimensional pitch rate of 0.51 the mean output from the normal force and tangential force bridge are $(E_1, E_2) \rightarrow (5.6V, .9V)$, respectively. The uncertainties in these are

$$\frac{\Delta E_1}{E_1} = \pm \left[\left(\frac{\Delta E_o}{E_1}\right)^2 + \left(\frac{\Delta E_N}{E_1}\right)^2 + \left(\frac{\Delta E_M}{E_1}\right)^2 \right]^{1/2} \tag{A.2}$$

$$= \pm\ 0.038\ (5\ \text{to}\ 1)$$

$$\frac{\Delta E_2}{E_2} = \pm \left[\left(\frac{\Delta E_o}{E_2}\right)^2 + \left(\frac{\Delta E_N}{E_2}\right)^2 + \left(\frac{\Delta E_M}{E_2}\right)^2 \right]^{1/2} \tag{A.3}$$

$$= \pm\ 0.236\ (5\ \text{to}\ 1)$$

The uncertainties in the normal and tangential force calibration constants are believed to be $(\Delta C_1, \Delta C_2) \rightarrow (\pm\ .05\ \text{lb}_f/\text{V}, \pm\ .05\ \text{lb}_f/\text{V})$. The mean value of the calibration constants are $(C_1, C_2) \rightarrow (3.676\ \text{lb}_f/\text{V}, 4.852\ \text{lb}_f/\text{V})$. The uncertainties in the normal and tangential forces are

$$\frac{\Delta F_n}{F_n} = \pm \left[\left(\frac{\Delta E_1}{E_1}\right)^2 + \left(\frac{\Delta C_1}{C_1}\right)^2 \right] \tag{A.4}$$

$$= \pm\ 0.040\ (5\ \text{to}\ 1)$$

$$\frac{\Delta F_t}{F_t} = \pm \left[\left(\frac{\Delta E_2}{E_2}\right)^2 + \left(\frac{\Delta C_2}{C_2}\right)^2 \right]^{1/2} \tag{A.5}$$

$$= \pm\ 0.236\ (5\ \text{to}\ 1)$$

The uncertainties associated with the fluid density and the active blade length are $(\Delta\rho, \Delta L) \rightarrow (\pm\ 3\ \text{lb}_m/\text{ft}^3, \pm\ 0.2\ \text{in})$. The mean values of the density and blade length are $(\rho, L) \rightarrow (62.31\ \text{lb}_m/\text{ft}^3, 38\ \text{in})$. The uncertainties in the non-dimensional normal and tangential forces are given by

$$\frac{\Delta F_n^+}{F_n^+} = \pm \left[\left(\frac{\Delta F_n}{F_n}\right)^2 + \left(\frac{\Delta \rho}{\rho}\right)^2 + \left(\frac{\Delta L}{L}\right)^2 + \left(\frac{\Delta C}{C}\right)^2 + \left(\frac{2\Delta U_\infty}{U_\infty}\right)^2 \right]^{1/2} \qquad (A.6)$$

$= \pm\ 0.102$ (5 to 1)

$$\frac{\Delta F_t^+}{F_t^+} = \pm \left[\left(\frac{\Delta F_t}{F_t}\right)^2 + \left(\frac{\Delta \rho}{\rho}\right)^2 + \left(\frac{\Delta L}{L}\right)^2 + \left(\frac{\Delta C}{C}\right)^2 + \left(\frac{2\Delta U_\infty}{U_\infty}\right)^2 \right]^{1/2} \qquad (A.7)$$

$= \pm\ 0.254$ (5 to 1)

The uncertainties in lift and drag coefficients are given by

$$T_1 = \Delta F_n^+ \cos\alpha$$

$$T_2 = \Delta F_t^+ \sin\alpha$$

$$T_3 = [-F_n^+ \sin\alpha + F_t^+ \cos\alpha]\Delta\alpha$$

$$\frac{\Delta C_L}{C_L} = \frac{[T_1^2 + T_2^2 + T_3^2]^{1/2}}{F_n^+ \cos\alpha + F_t^+ \sin\alpha} \qquad (A.8)$$

$$T_1 = \Delta F_n^+ \sin\alpha$$

$$T_2 = \Delta F_t \cos\alpha$$

$$T_3 = [F_n^+ \cos\alpha + F_t^+ \sin\alpha]\Delta\alpha$$

$$\frac{\Delta C_D}{C_D} = \frac{[T_1^2 + T_2^2 + T_3^2]^{1/2}}{F_n^+ \sin\alpha - F_t^+ \cos\alpha} \qquad (A.9)$$

Using the results of equations A.6 and A.7, the mean values $(F_n^+, F_t^+, \alpha) \rightarrow (6.9, 1.4, 45°)$ and an uncertainty in the angle of attack of $(\Delta\alpha) \rightarrow (\pm 1.5°)$ yields

$$\frac{\Delta C_L}{C_L} = \pm 0.097 \; (5 \text{ to } 1)$$

$$\frac{\Delta C_D}{C_D} = \pm 0.149 \; (5 \text{ to } 1)$$

A.3 Pressure Measurements

The uncertainty in the pressure measurements is estimated to be $(\Delta P) \rightarrow (\pm .15 \text{ in } H_2O)$. The uncertainty in the pressure coefficient is given by

$$\frac{\Delta C_P}{C_P} = \left[\left(\frac{\Delta P}{P}\right)^2 + \left(\frac{\Delta \rho}{\rho}\right)^2 + \left(\frac{2\Delta U_\infty}{U_\infty}\right)^2 \right]^{1/2} \qquad \text{(A.10)}$$

For an angle of attack of 45°, and a non-dimensional pitch rate of 0.51, an average pressure reading over the upper and lower surfaces is $(P) \rightarrow (1.0 \text{ in } H_2O)$. The uncertainty in the pressure coefficient is

$$\frac{\Delta C_P}{C_P} = \pm 0.177 \; (5 \text{ to } 1)$$

The uncertainty in the non-dimensional normal force is

$$\frac{\Delta F_n^+}{F_n^+} = \pm \frac{\sqrt{2}\, \Delta C_{Pn\ avg}}{F_n^+} \qquad \text{(A.11)}$$

where $\Delta C_{Pn\ avg}$ is the uncertainty in the average pressure coefficient difference between the upper and lower surfaces. For the case cited

$(C_{Pn\ avg}) \rightarrow (6.0)$ using the results of A.10 and A.11 yields

$$\frac{\Delta F_n^+}{F_n^+} = \pm\ .218\ \text{(5 to 1)}$$

The uncertainty in the non-dimensional tangential force is

$$\frac{\Delta F_t^+}{F_t^+} = \frac{\sqrt{2}\ \Delta C_{Pt\ avg}\left(\frac{t}{c}\right)}{F_t^+} \qquad (A.12)$$

Where $\Delta C_{Pt\ avg}$ is the uncertainty in the pressure coefficient difference in the chordwise direction. Lt $(C_{Pt\ avg}) \rightarrow (10)$. Then, using A.10 and A.12 yields

$$\frac{\Delta F_t^+}{F_t} = 0.268\ \text{(5 to 1)}$$

The uncertainties in the integrated lift and drag force results may be computed using the results of A.11 and A.12 in A.8 and A.10, respectively. This yields

$$\frac{\Delta C_\ell}{C_\ell} = \pm\ 0.187\ \text{(5 to 1)}$$

$$\frac{\Delta C_D}{C_D} = \pm\ 0.284\ \text{(5 to 1)}$$

APPENDIX B

PRESSURE DISTRIBUTIONS

This appendix contains surface pressure distribution data for nondimensional pitch rates of .088, .19, .29, .51, .71, and .99 at a Reynolds number of 1×10^5.

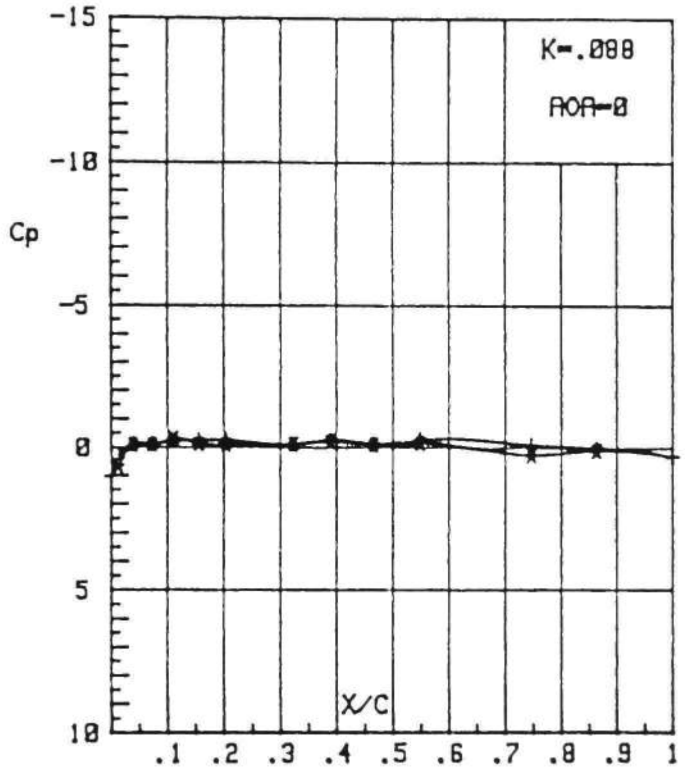
K=.088
AOA=0
-15
-10
Cp
-5
0
5
10
X/C
.1 .2 .3 .4 .5 .6 .7 .8 .9 1

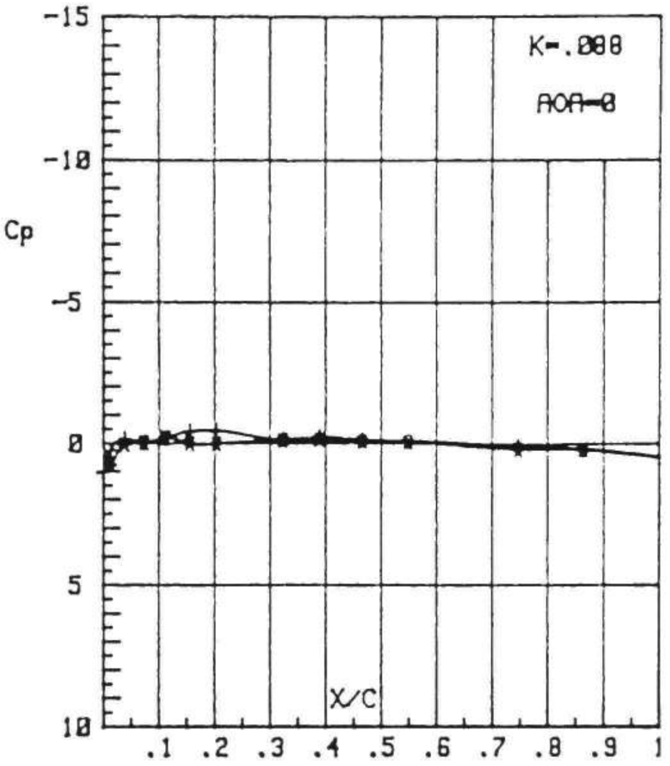
K=.088
AOA=0
-15
-10
Cp
-5
0
5
10
X/C
.1 .2 .3 .4 .5 .6 .7 .8 .9 1

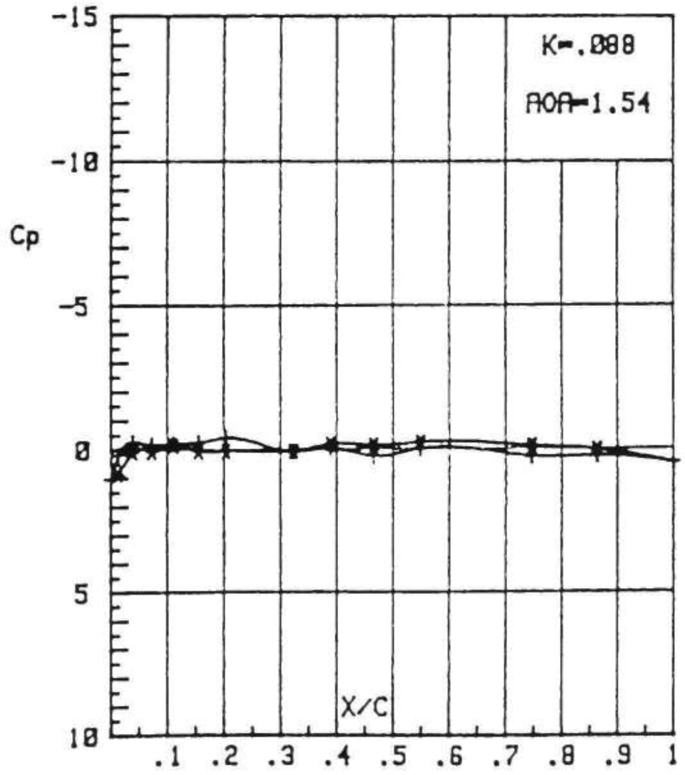
K=.088
AOA=1.54
-15
-10
Cp
-5
0
5
10
X/C
.1 .2 .3 .4 .5 .6 .7 .8 .9 1

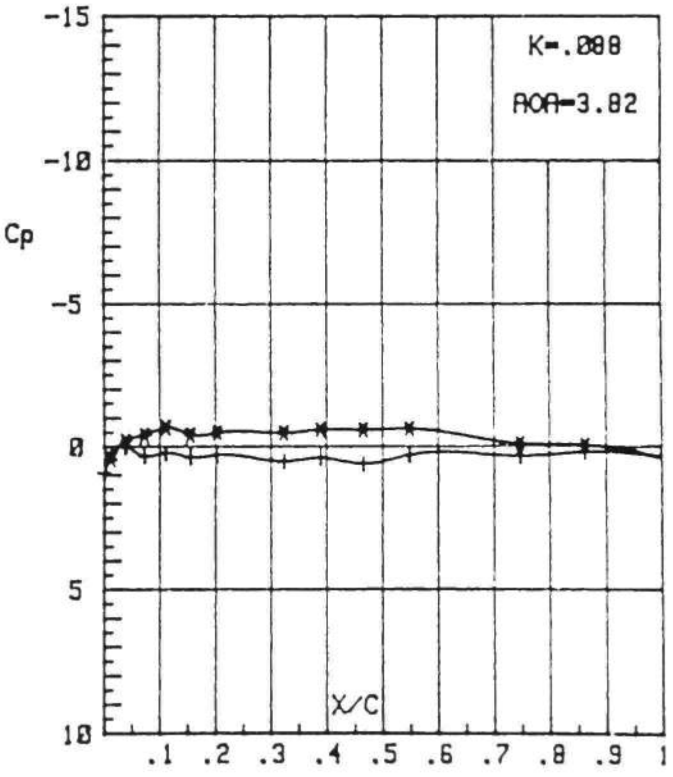
K=.088
AOA=3.82
-15
-10
Cp
-5
0
5
10
X/C
.1 .2 .3 .4 .5 .6 .7 .8 .9 1

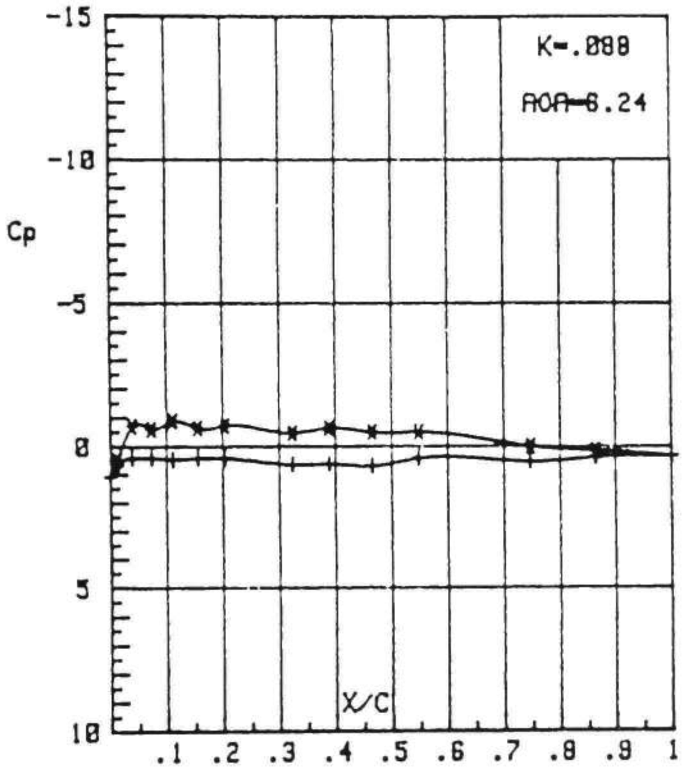
K=.088
AOA=6.24
-15
-10
Cp
-5
0
5
10
X/C
.1
.2
.3
.4
.5
.6
.7
.8
.9
1

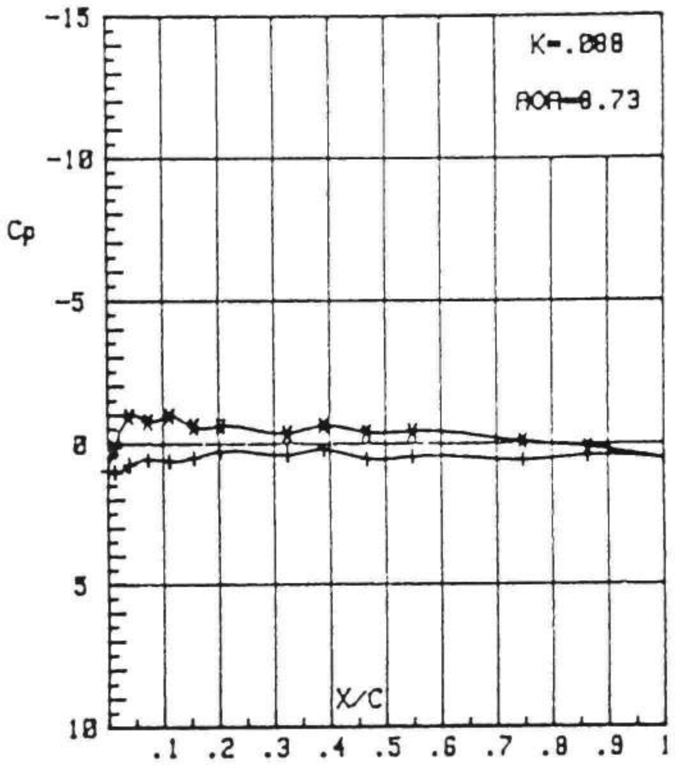
K=.088
AOA=8.73
-15
-10
Cp
-5
0
5
10
X/C
.1
.2
.3
.4
.5
.6
.7
.8
.9
1

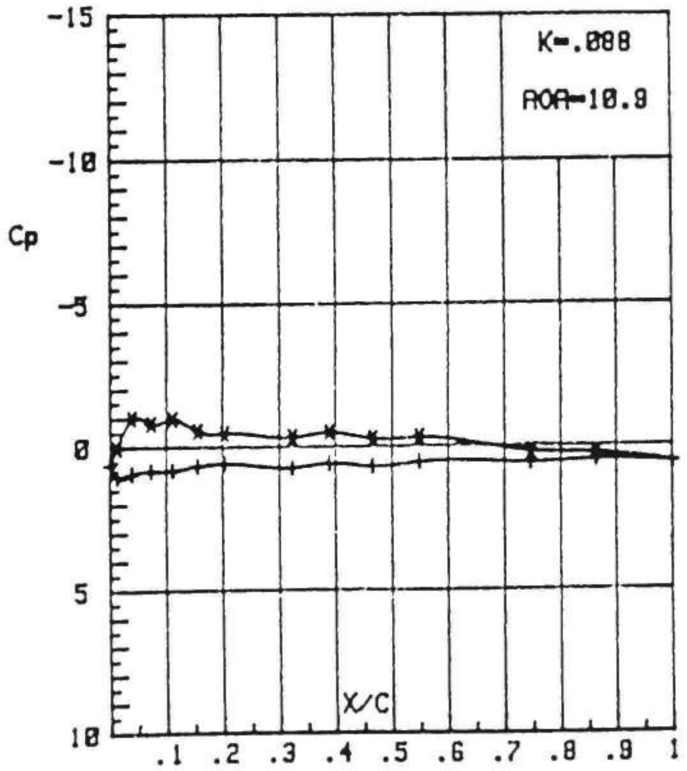
K=.088
AOA=10.8
-15
-10
Cp
-5
0
5
10
X/C
.1
.2
.3
.4
.5
.6
.7
.8
.9
1

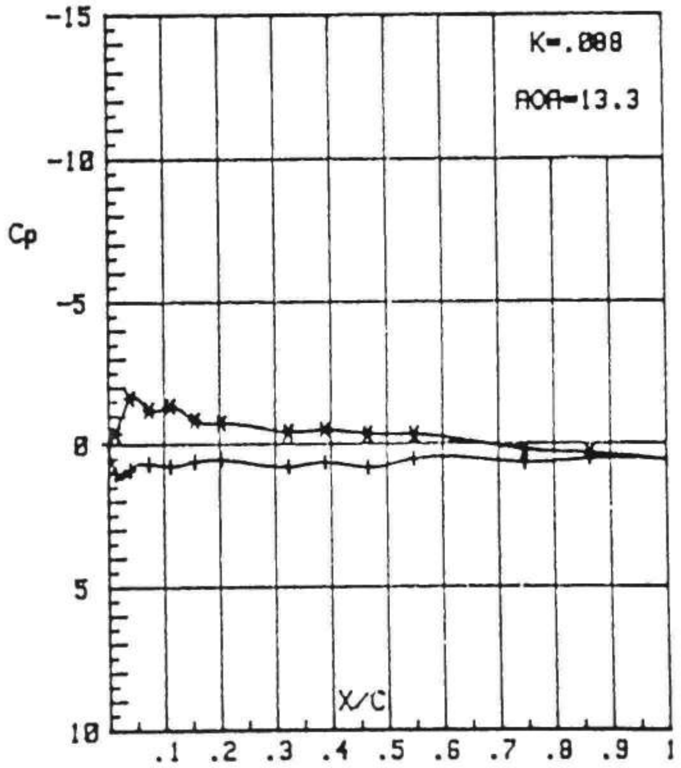
K=.088
AOA=13.3
-15
-10
Cp
-5
0
5
10
X/C
.1
.2
.3
.4
.5
.6
.7
.8
.9
1

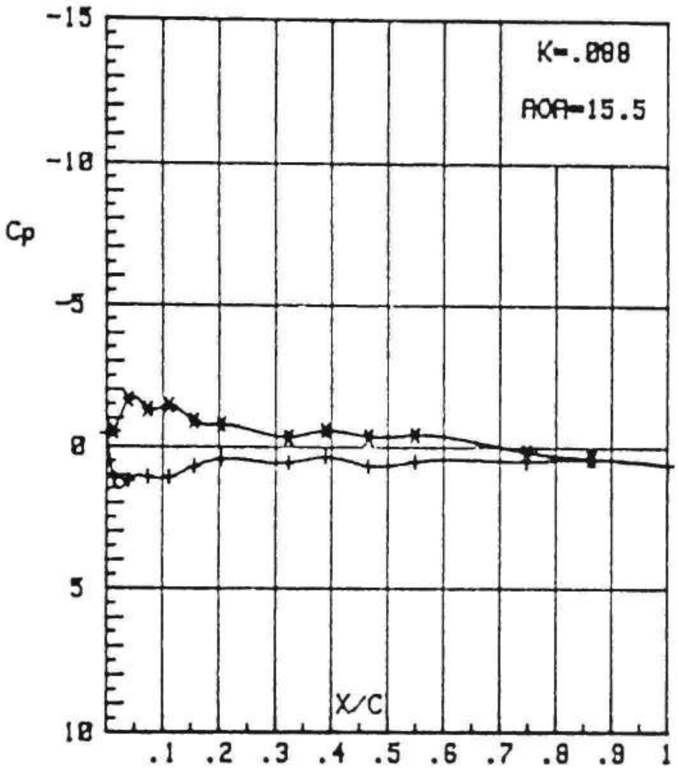
K=.088
AOA=15.5
Cp
-15
-10
-5
0
5
10
X/C
.1
.2
.3
.4
.5
.6
.7
.8
.9
1

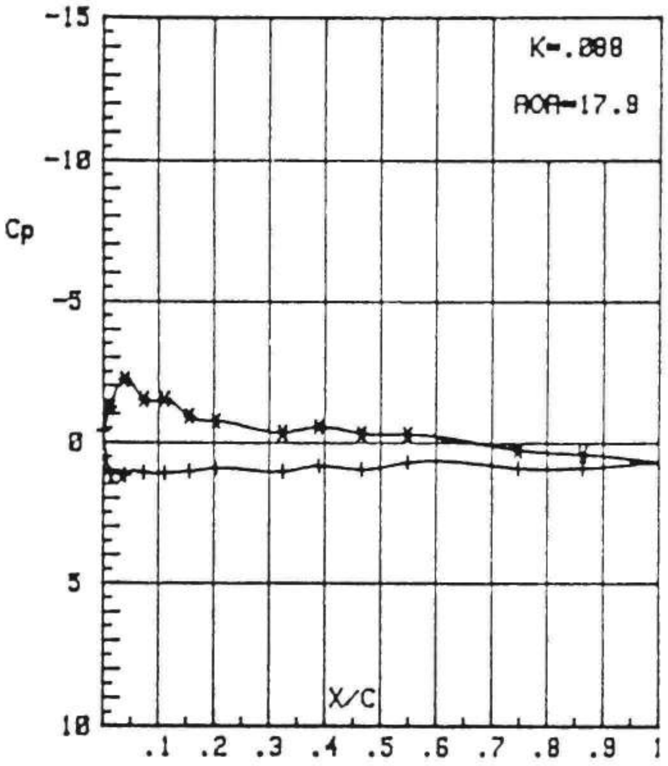
K=.088
AOA=17.9
Cp
-15
-10
-5
0
5
10
X/C
.1
.2
.3
.4
.5
.6
.7
.8
.9
1

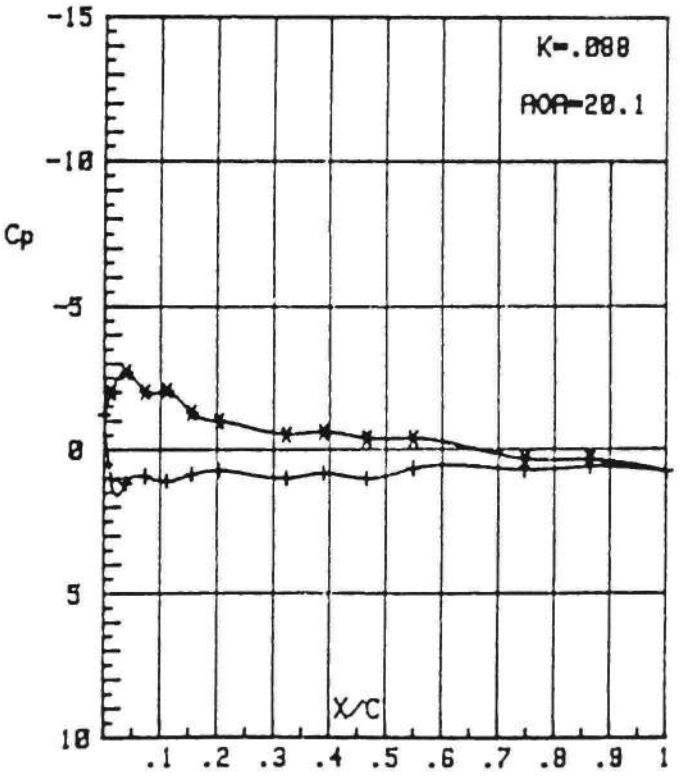
K=.088
AOA=20.1
Cp
-15
-10
-5
0
5
10
X/C
.1
.2
.3
.4
.5
.6
.7
.8
.9
1

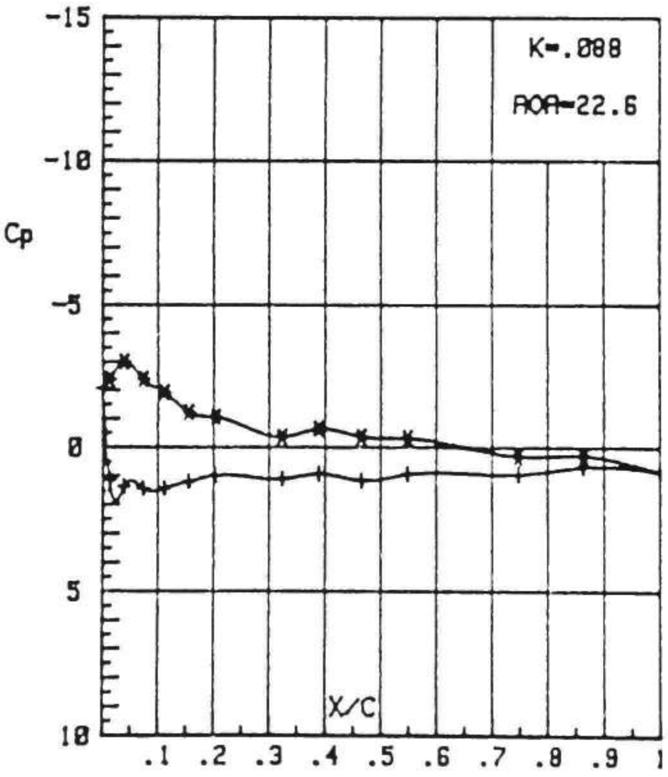
K=.088
AOA=22.6
Cp
-15
-10
-5
0
5
10
X/C
.1
.2
.3
.4
.5
.6
.7
.8
.9
1

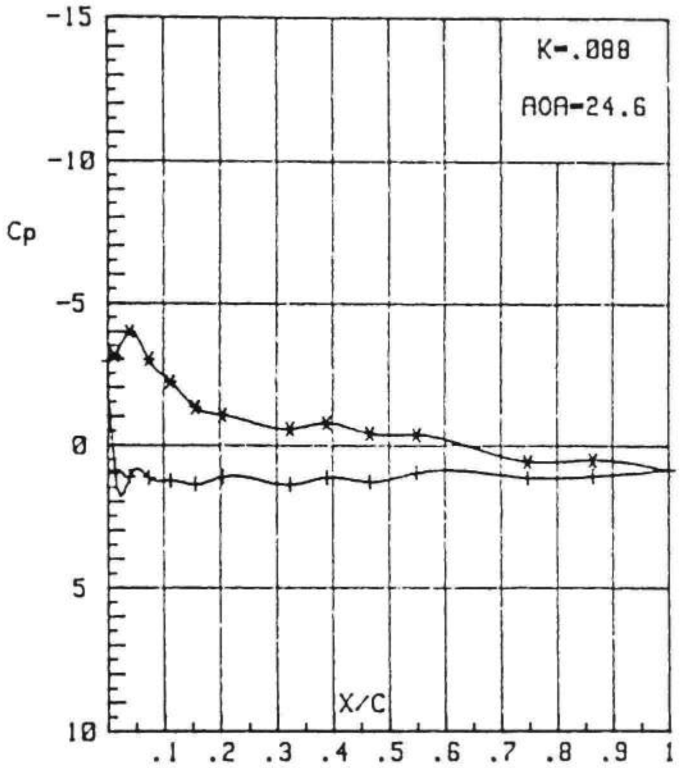
K=.088
AOA=24.6
Cp
-15
-10
-5
0
5
10
X/C
.1
.2
.3
.4
.5
.6
.7
.8
.9
1

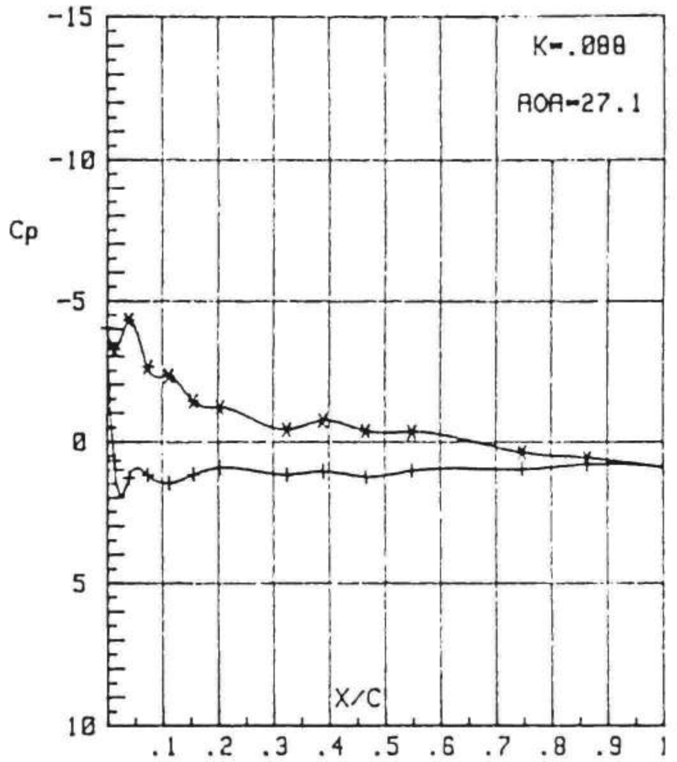
K=.088
AOA=27.1
Cp
-15
-10
-5
0
5
10
X/C
.1
.2
.3
.4
.5
.6
.7
.8
.9
1

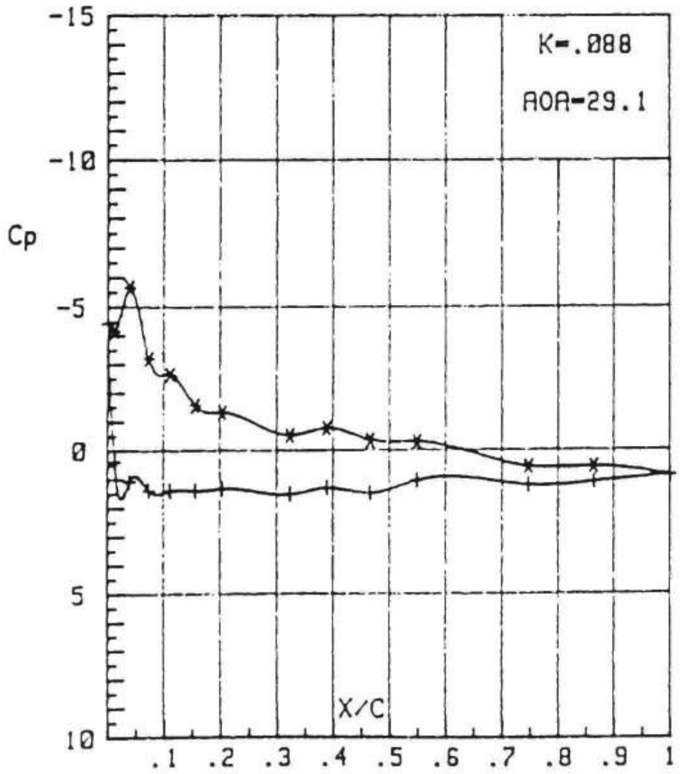
K=.088
AOA=29.1
Cp
-15
-10
-5
0
5
10
X/C
.1
.2
.3
.4
.5
.6
.7
.8
.9
1

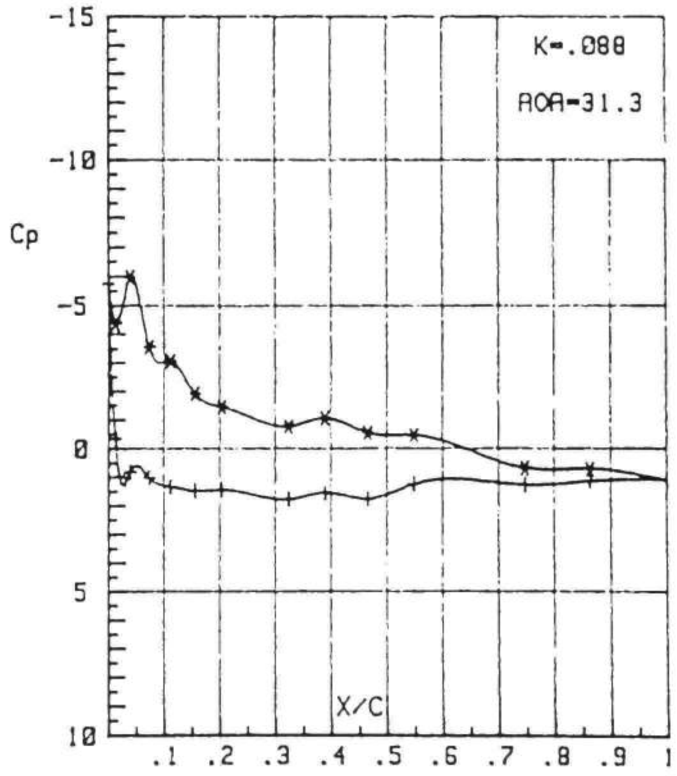
K=.088
AOA=31.3
Cp
-15
-10
-5
0
5
10
X/C
.1
.2
.3
.4
.5
.6
.7
.8
.9
1

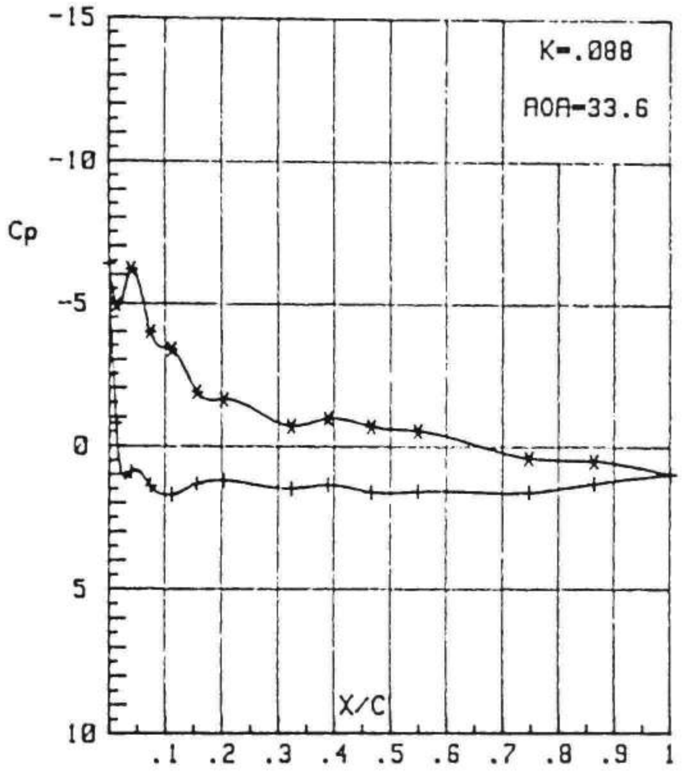
K=.088
AOA=33.6
Cp
-15
-10
-5
0
5
10
X/C
.1
.2
.3
.4
.5
.6
.7
.8
.9
1

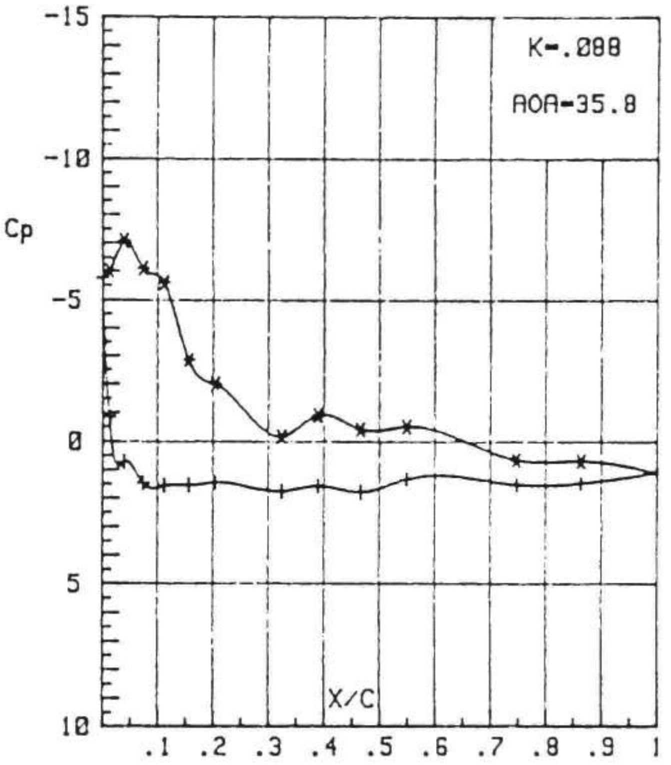
K=.088
AOA=35.8
Cp
-15
-10
-5
0
5
10
X/C
.1
.2
.3
.4
.5
.6
.7
.8
.9
1

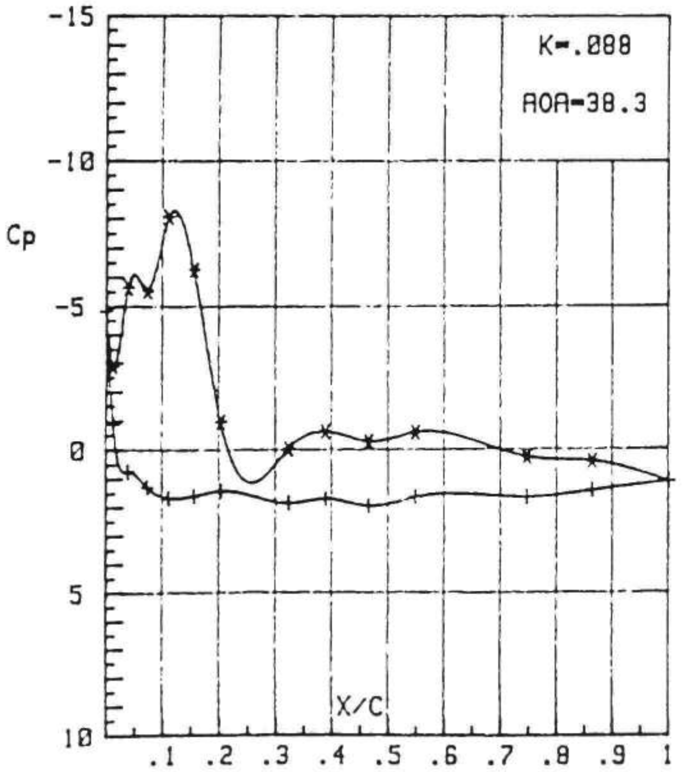
K=.088
AOA=38.3
Cp
-15
-10
-5
0
5
10
X/C
.1
.2
.3
.4
.5
.6
.7
.8
.9
1

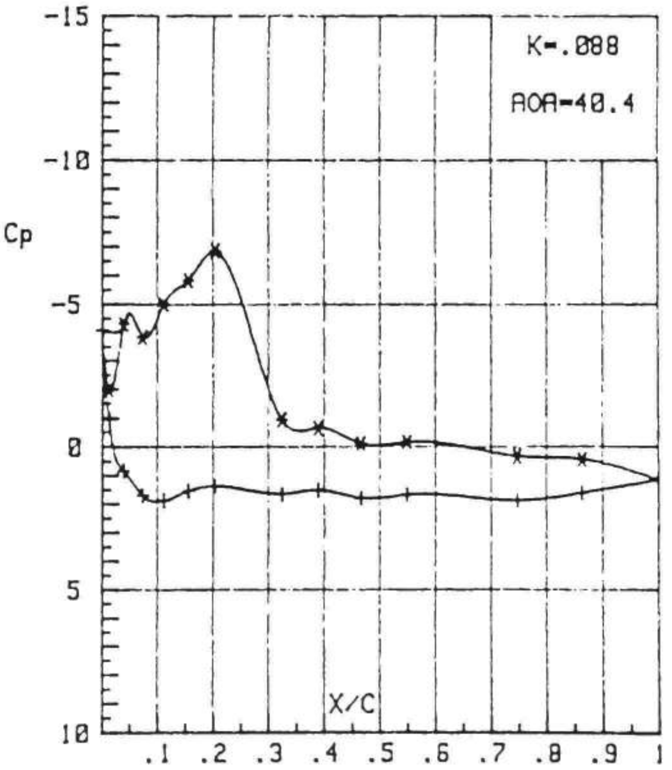
K=.088
AOA=40.4
Cp
-15
-10
-5
0
5
10
X/C
.1
.2
.3
.4
.5
.6
.7
.8
.9
1

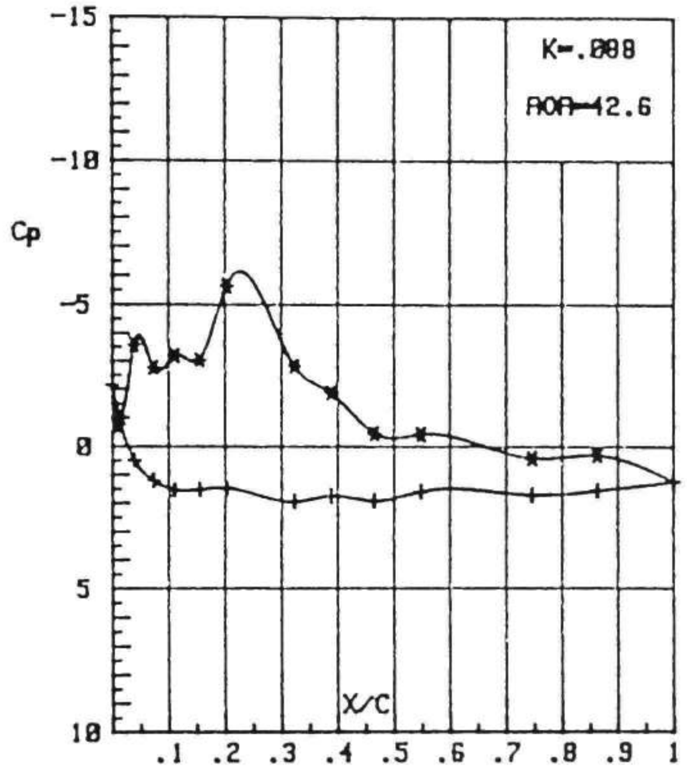
K=.000
AOA=42.6
Cp
-15
-10
-5
0
5
10
X/C
.1
.2
.3
.4
.5
.6
.7
.8
.9
1

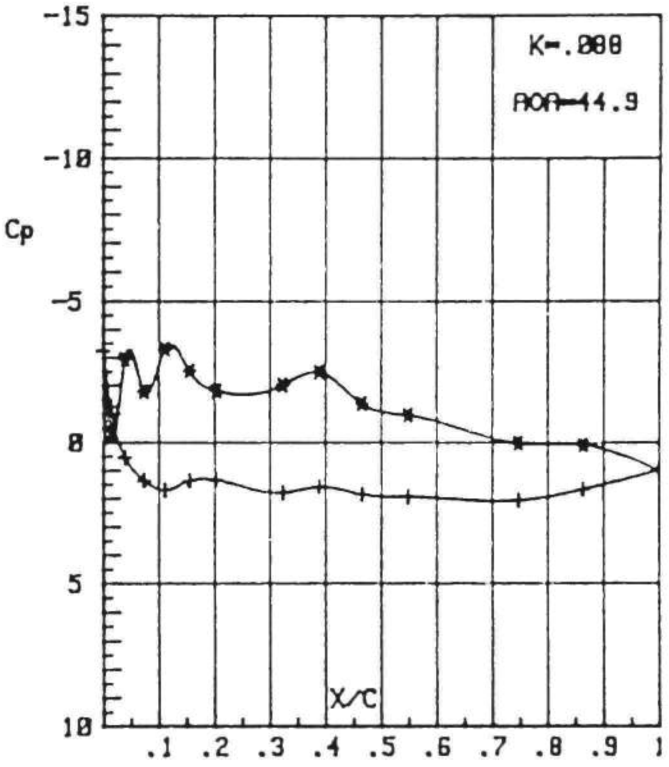
K=.000
AOA=44.9
Cp
-15
-10
-5
0
5
10
X/C
.1
.2
.3
.4
.5
.6
.7
.8
.9
1

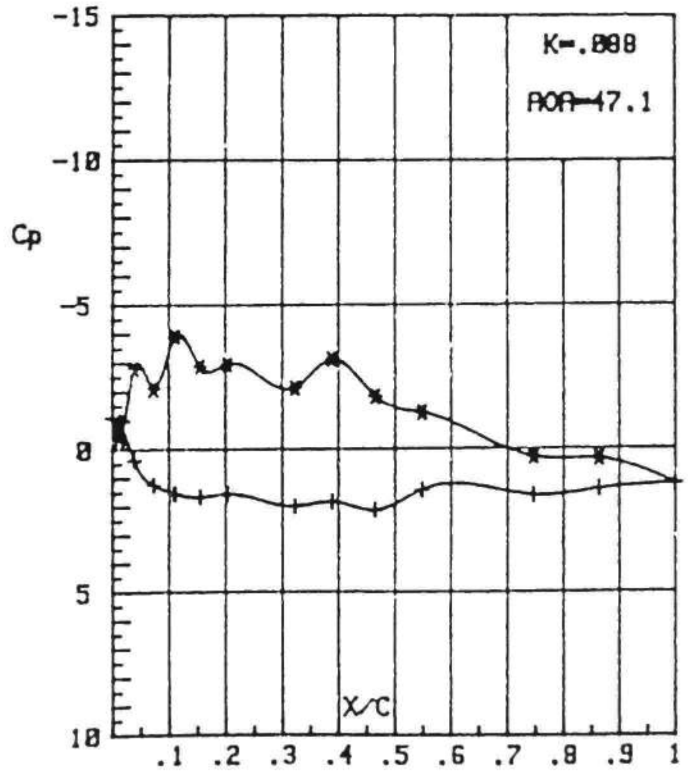
K=.000
AOA=47.1
Cp
-15
-10
-5
0
5
10
X/C
.1
.2
.3
.4
.5
.6
.7
.8
.9
1

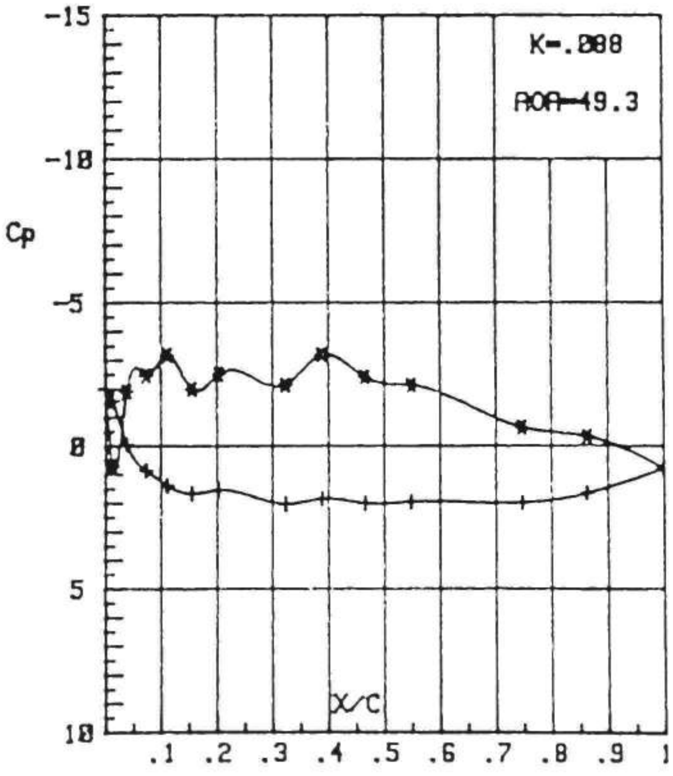
K=.000
AOA=49.3
Cp
-15
-10
-5
0
5
10
X/C
.1
.2
.3
.4
.5
.6
.7
.8
.9
1

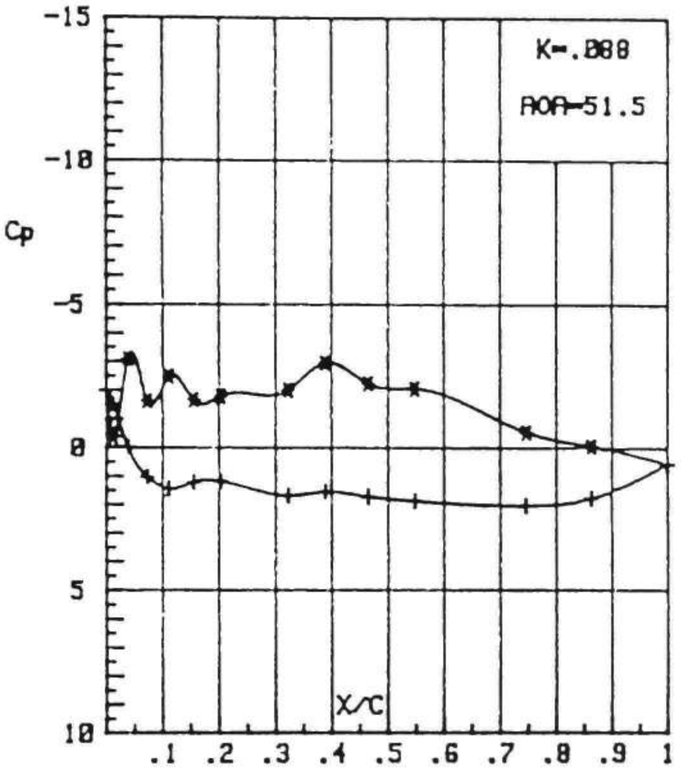
K=.000
AOA=51.5
Cp
-15
-10
-5
0
5
10
X/C
.1
.2
.3
.4
.5
.6
.7
.8
.9
1

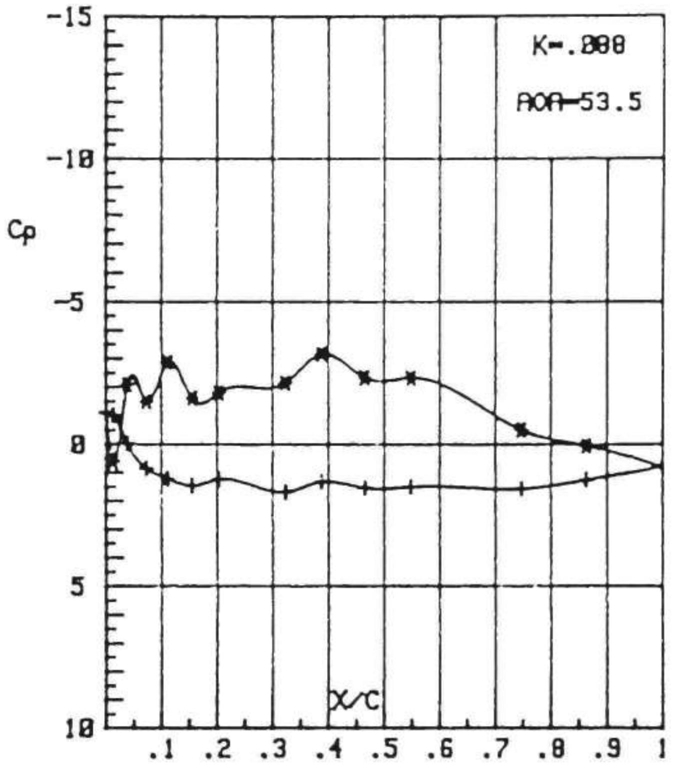
K=.000
AOA=53.5
Cp
-15
-10
-5
0
5
10
X/C
.1
.2
.3
.4
.5
.6
.7
.8
.9
1

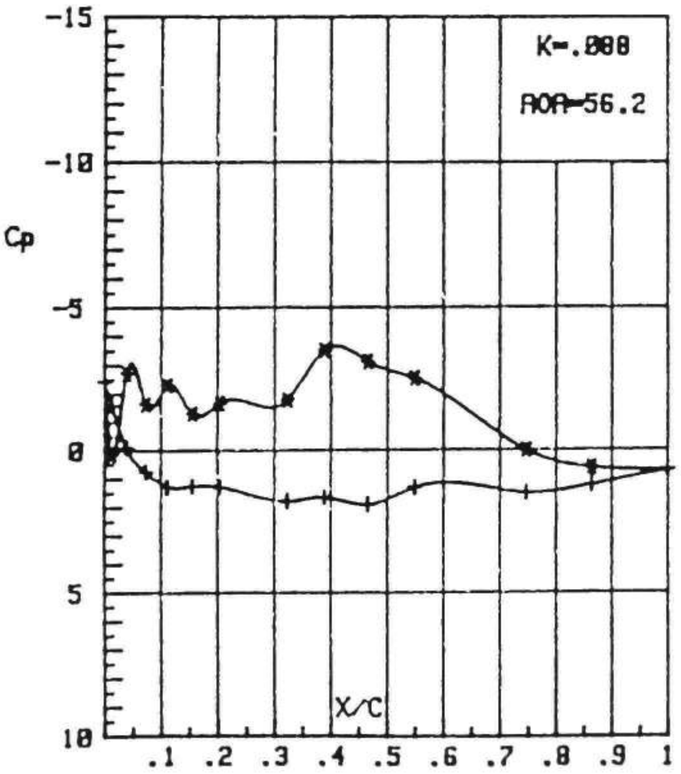
K=.000
AOA=56.2
Cp
-15
-10
-5
0
5
10
X/C
.1
.2
.3
.4
.5
.6
.7
.8
.9
1

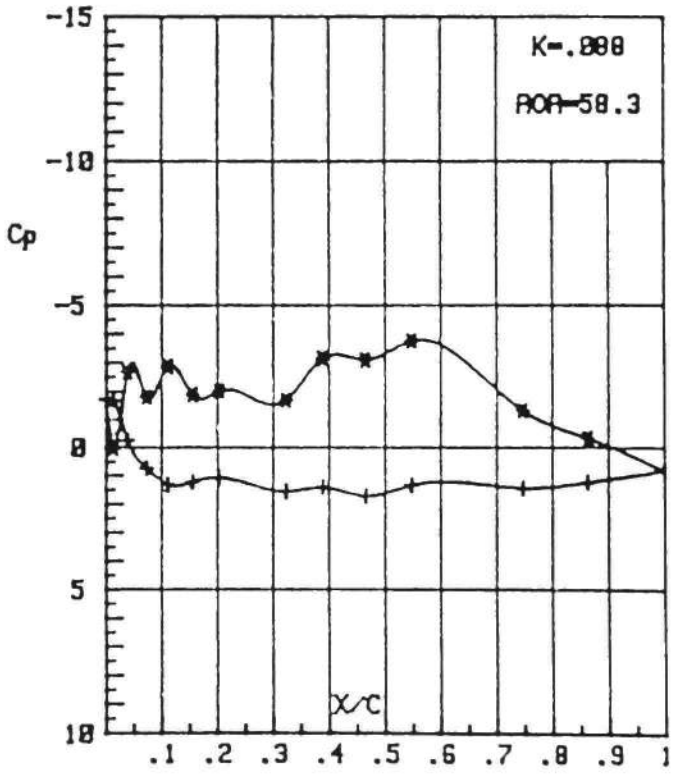
K=.000
AOA=58.3
Cp
-15
-10
-5
0
5
10
X/C
.1
.2
.3
.4
.5
.6
.7
.8
.9
1

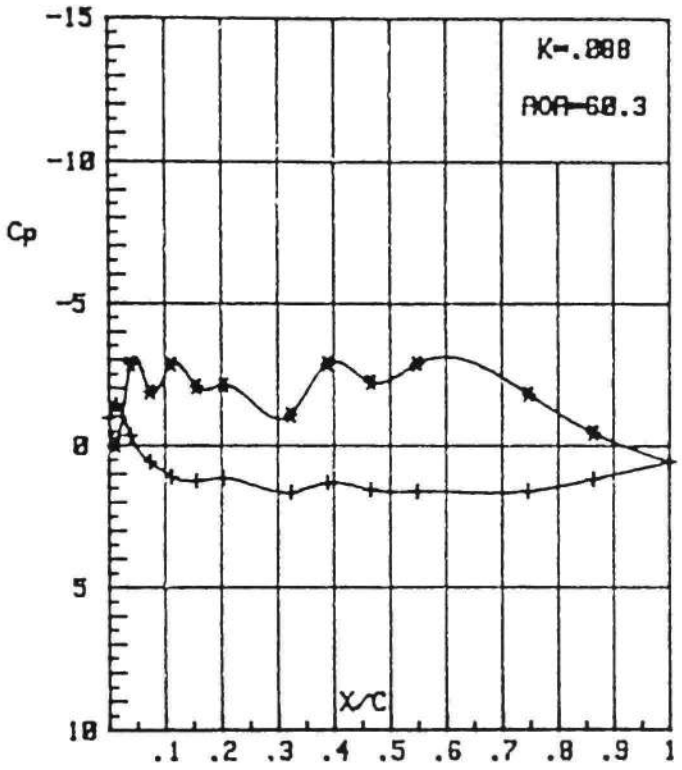
K=.000
AOA=60.3
Cp
-15
-10
-5
0
5
10
X/C
.1
.2
.3
.4
.5
.6
.7
.8
.9
1

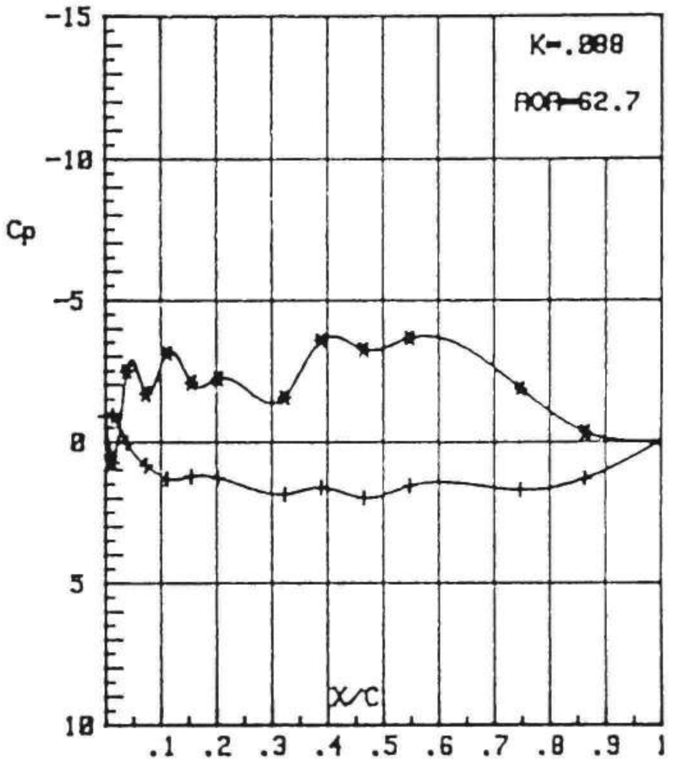
K=.000
AOA=62.7
Cp
-15
-10
-5
0
5
10
X/C
.1
.2
.3
.4
.5
.6
.7
.8
.9
1

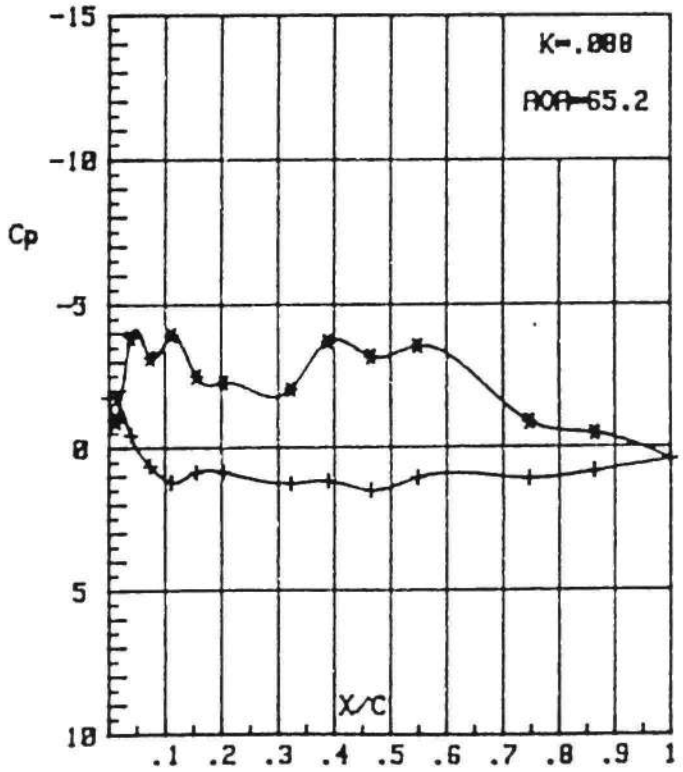
K=.000
AOA=65.2
Cp
-15
-10
-5
0
5
10
X/C
.1
.2
.3
.4
.5
.6
.7
.8
.9
1

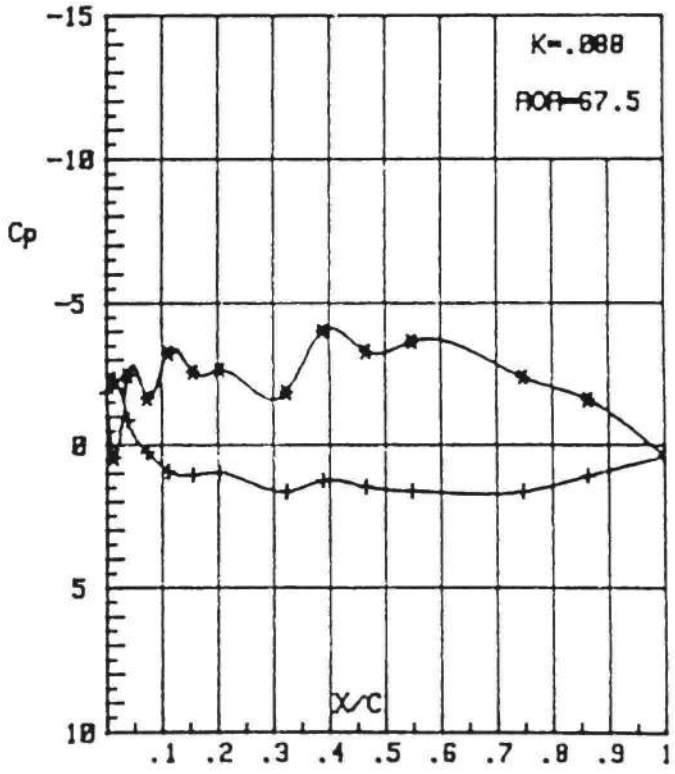
K=.000
AOA=67.5
Cp
-15
-10
-5
0
5
10
X/C
.1
.2
.3
.4
.5
.6
.7
.8
.9
1

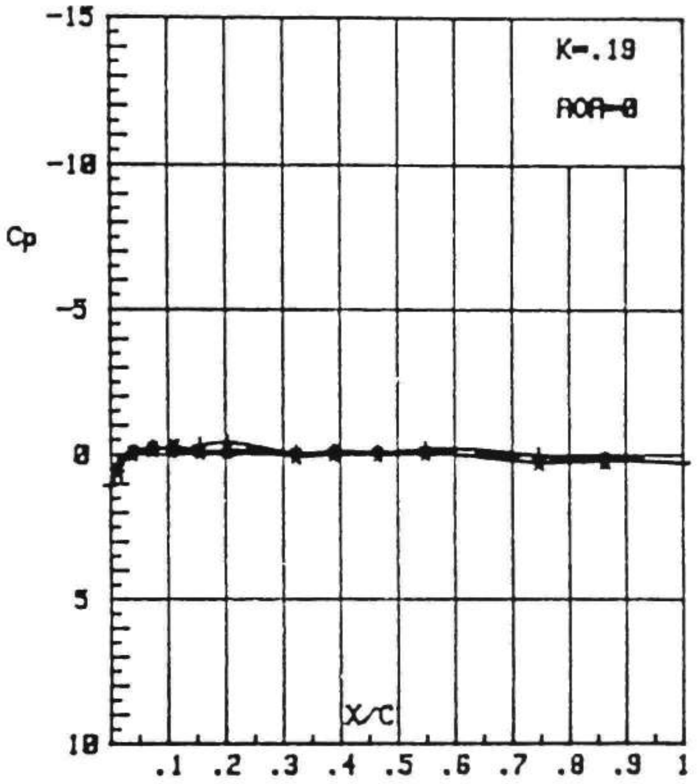
K=.19
AOA=0
Cp
-15
-10
-5
0
5
10
X/C
.1
.2
.3
.4
.5
.6
.7
.8
.9
1

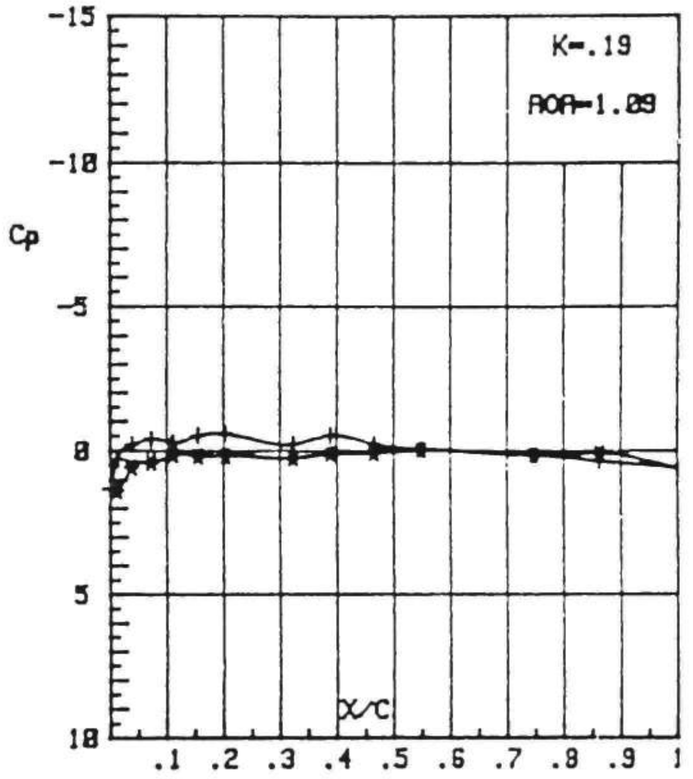
K=.19
AOA=1.09
Cp
-15
-10
-5
0
5
10
X/C
.1
.2
.3
.4
.5
.6
.7
.8
.9
1

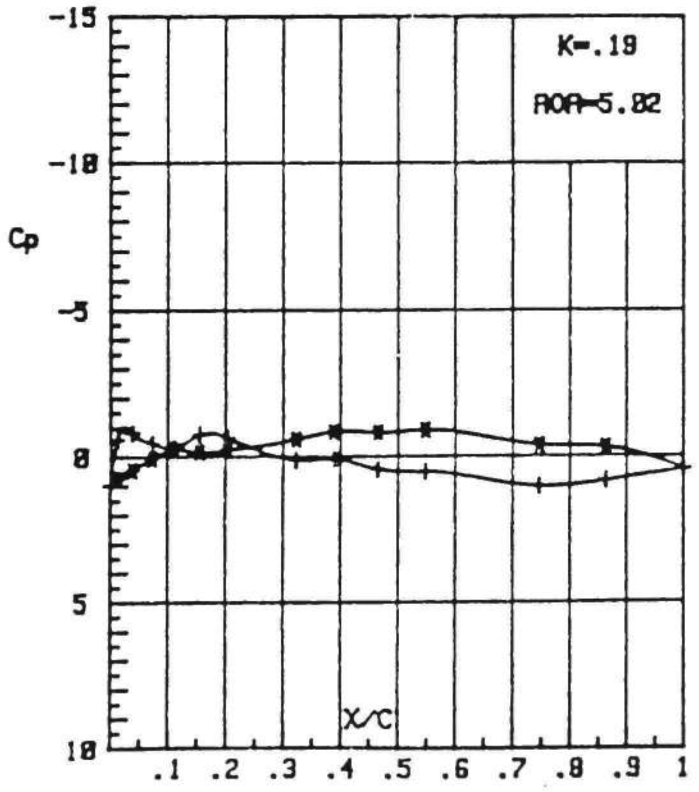
K=.19
AOA=5.02
Cp
-15
-10
-5
0
5
10
X/C
.1
.2
.3
.4
.5
.6
.7
.8
.9
1

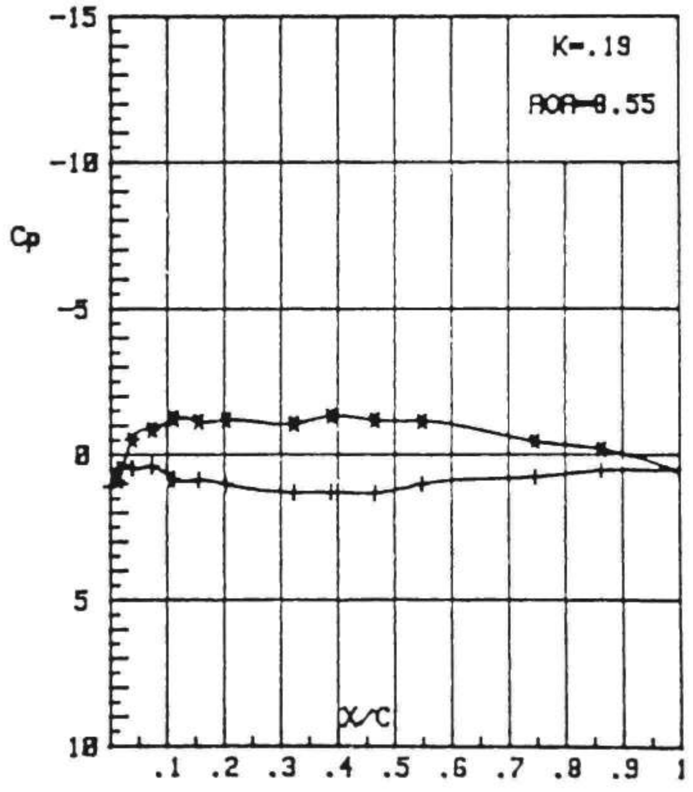
K=.19
AOA=8.55
Cp
-15
-10
-5
0
5
10
X/C
.1
.2
.3
.4
.5
.6
.7
.8
.9
1

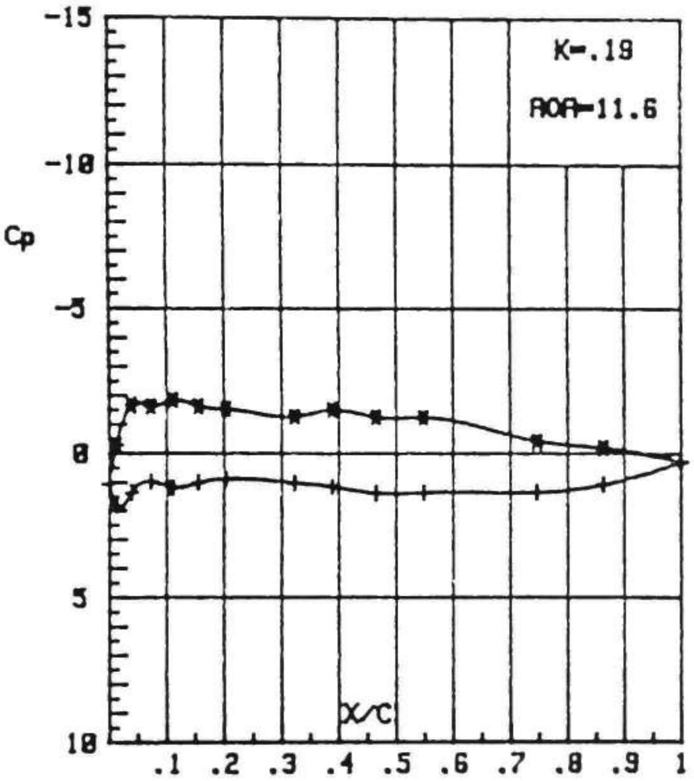
K=.19
AOA=11.6
Cp
-15
-10
-5
0
5
10
X/C
.1
.2
.3
.4
.5
.6
.7
.8
.9
1

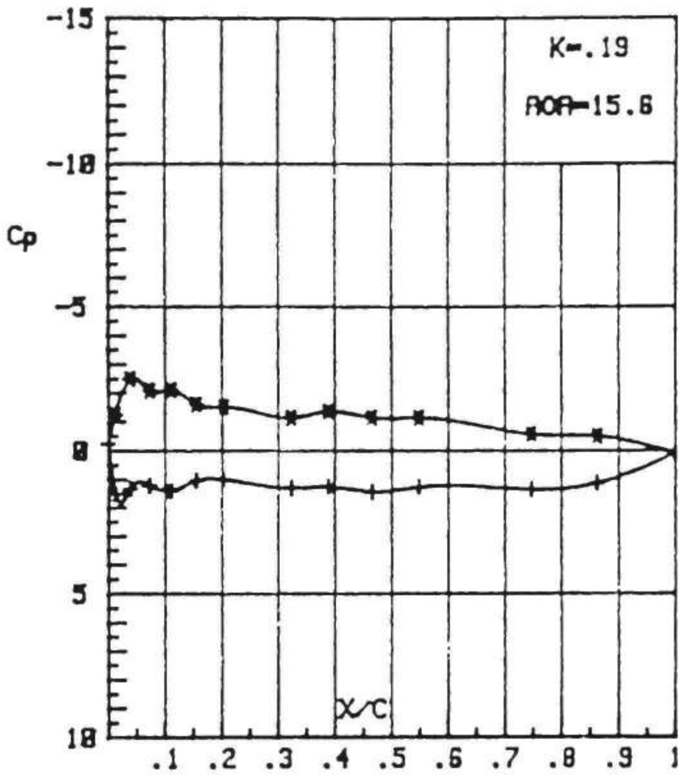
K=.19
AOA=15.6
Cp
-15
-10
-5
0
5
10
X/C
.1
.2
.3
.4
.5
.6
.7
.8
.9
1

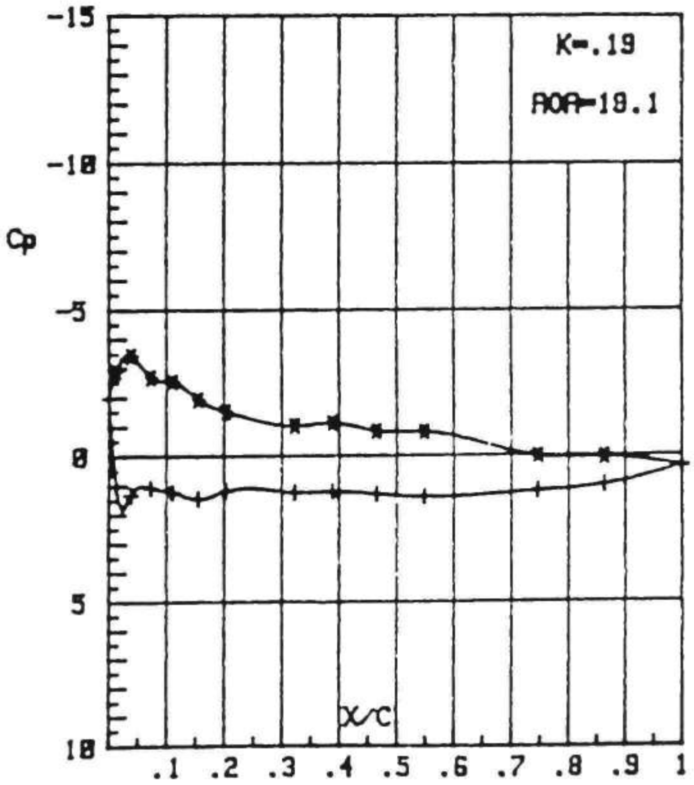
K=.19
AOA=18.1
Cp
-15
-10
-5
0
5
10
X/C
.1
.2
.3
.4
.5
.6
.7
.8
.9
1

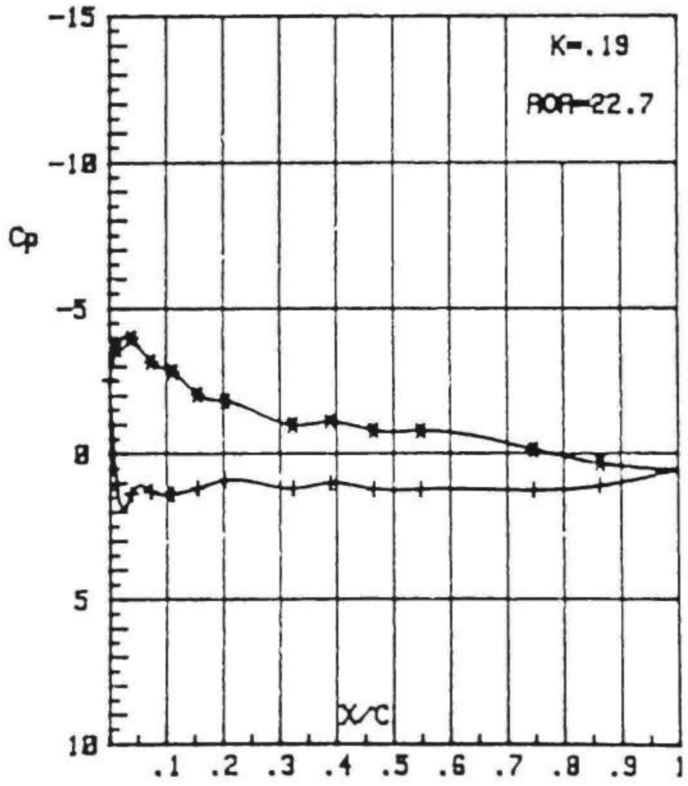
K=.19
AOA=22.7
Cp
-15
-10
-5
0
5
10
X/C
.1
.2
.3
.4
.5
.6
.7
.8
.9
1

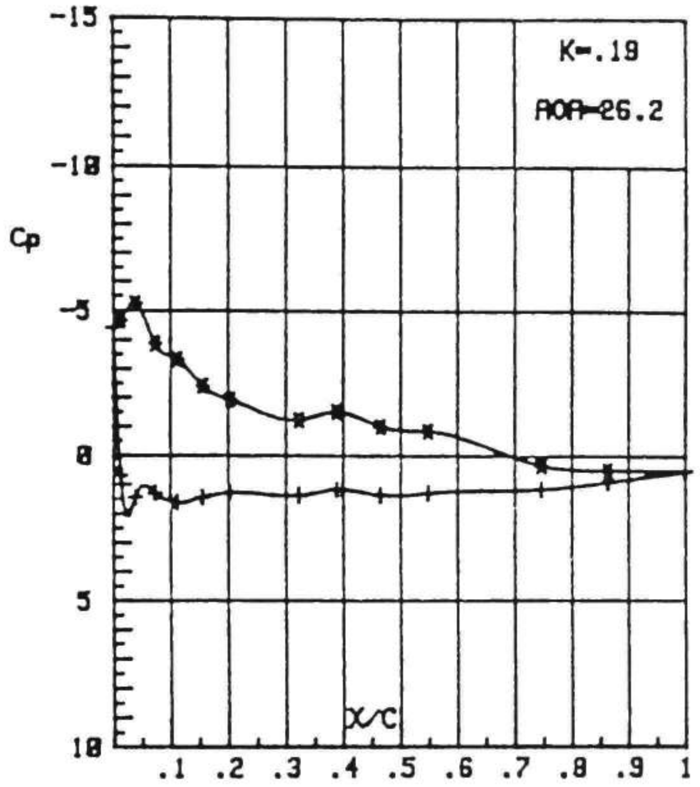
-15
-10
Cp
-5
0
5
10
K=.19
AOA=26.2
X/C
.1
.2
.3
.4
.5
.6
.7
.8
.9
1

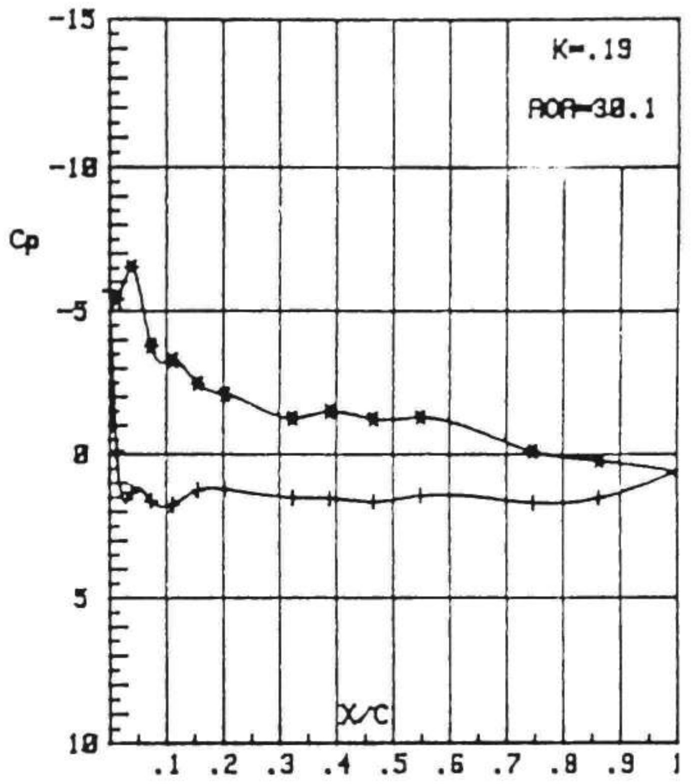
-15
-10
Cp
-5
0
5
10
K=.19
AOA=30.1
X/C
.1
.2
.3
.4
.5
.6
.7
.8
.9
1

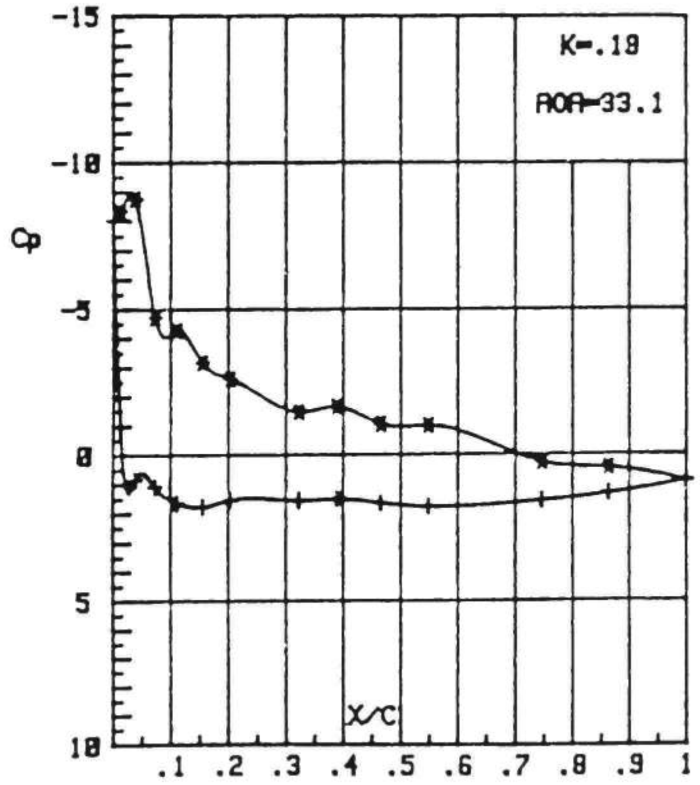
-15
-10
Cp
-5
0
5
10
K=.19
AOA=33.1
X/C
.1
.2
.3
.4
.5
.6
.7
.8
.9
1

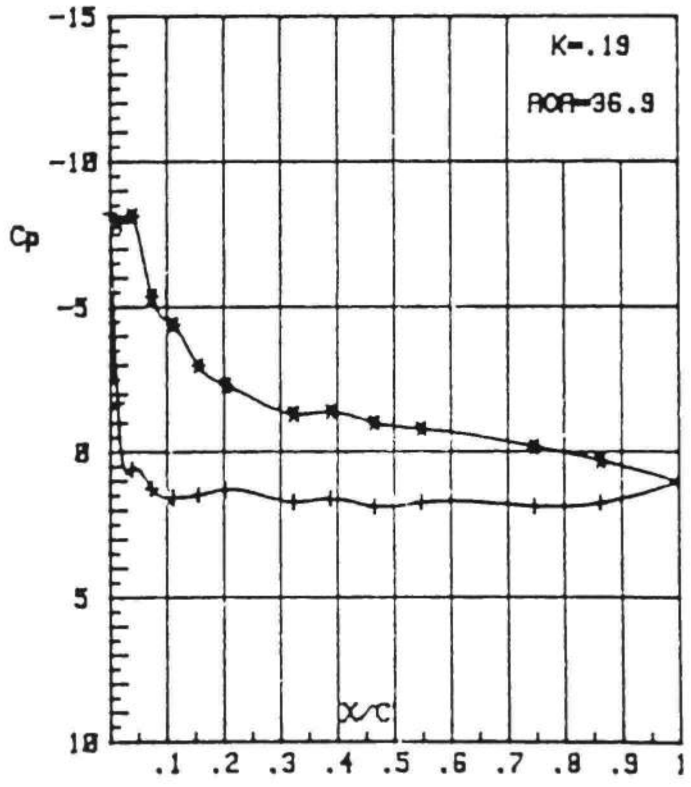
-15
-10
Cp
-5
0
5
10
K=.19
AOA=36.9
X/C
.1
.2
.3
.4
.5
.6
.7
.8
.9
1

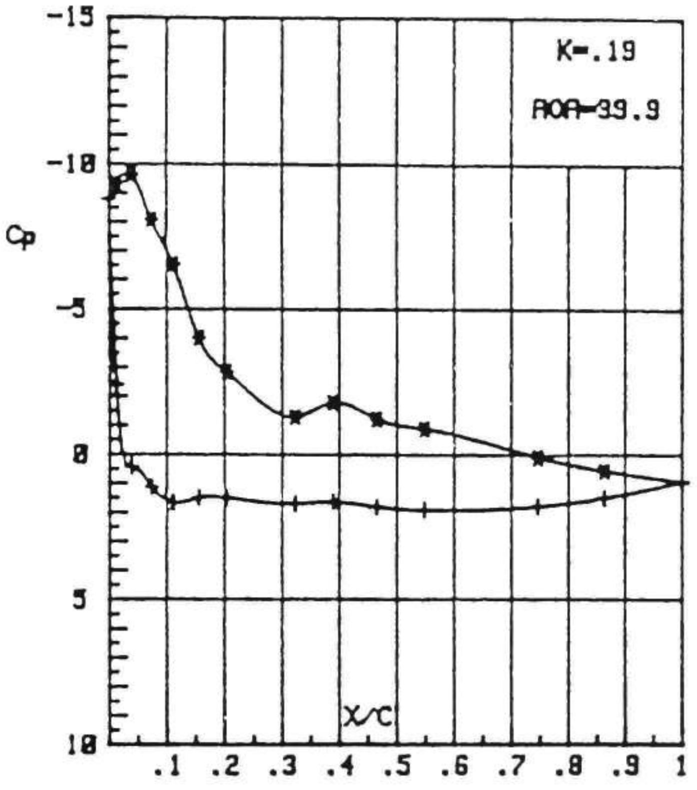
K=.19
AOA=39.9
Cp
-15
-10
-5
0
5
10
X/C
.1
.2
.3
.4
.5
.6
.7
.8
.9
1

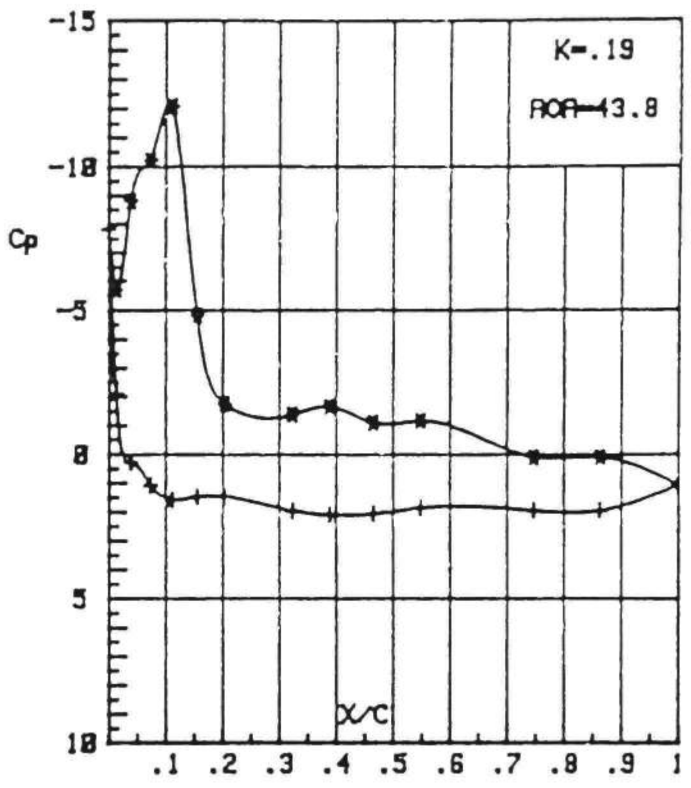
K=.19
AOA=43.8
Cp
-15
-10
-5
0
5
10
X/C
.1
.2
.3
.4
.5
.6
.7
.8
.9
1

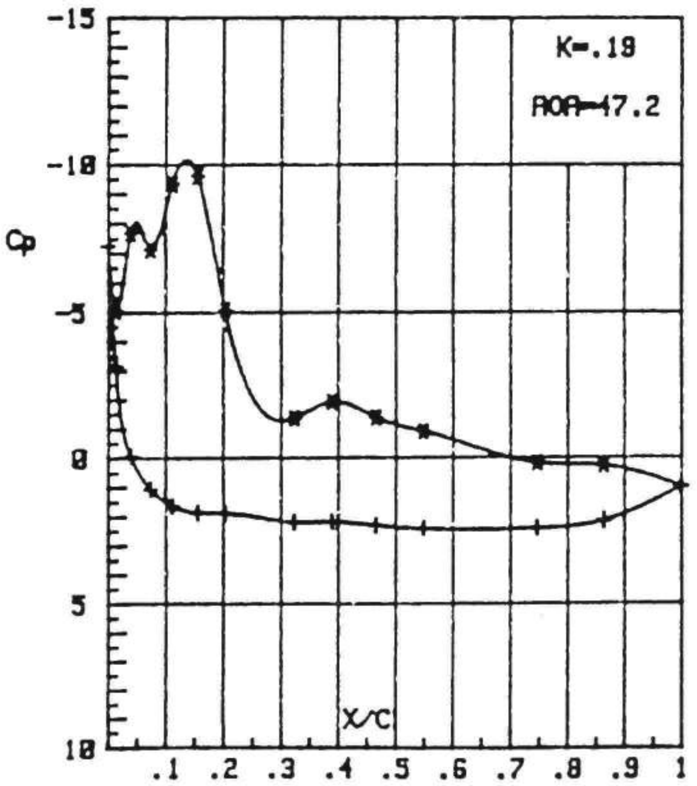
K=.19
AOA=47.2
Cp
-15
-10
-5
0
5
10
X/C
.1
.2
.3
.4
.5
.6
.7
.8
.9
1

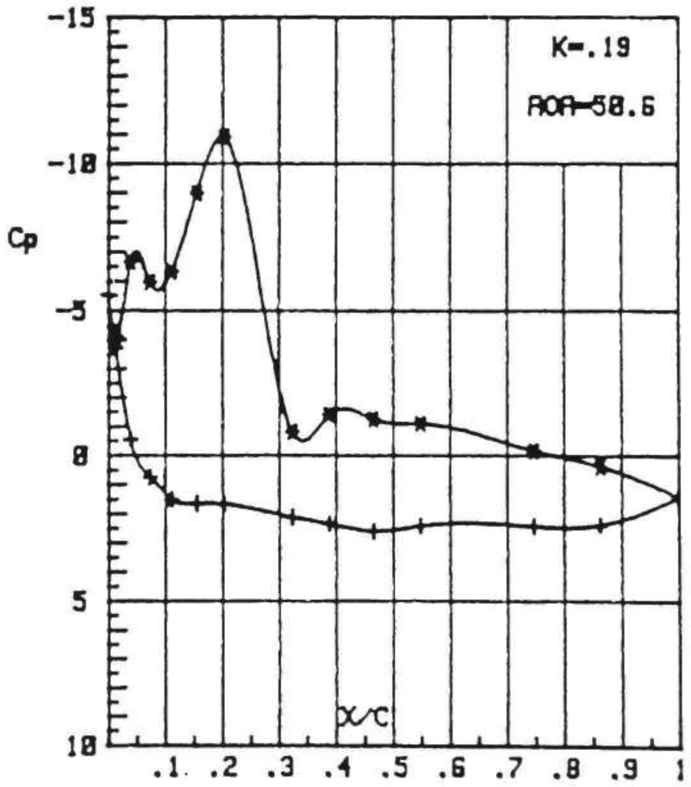
K=.19
AOA=50.6
Cp
-15
-10
-5
0
5
10
X/C
.1
.2
.3
.4
.5
.6
.7
.8
.9
1

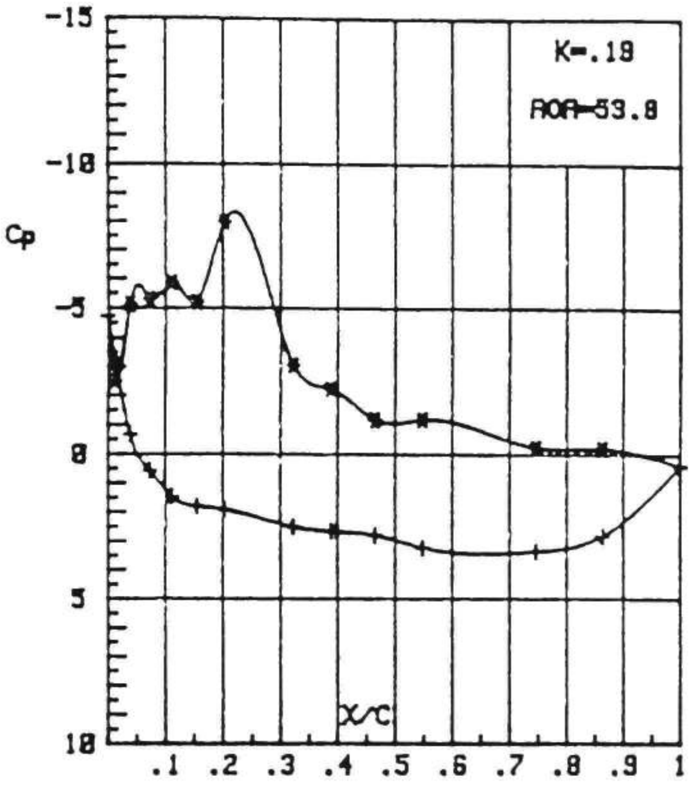
-15
-10
-5
0
5
10
Cp
K=.19
AOA=53.8
X/C
.1
.2
.3
.4
.5
.6
.7
.8
.9
1

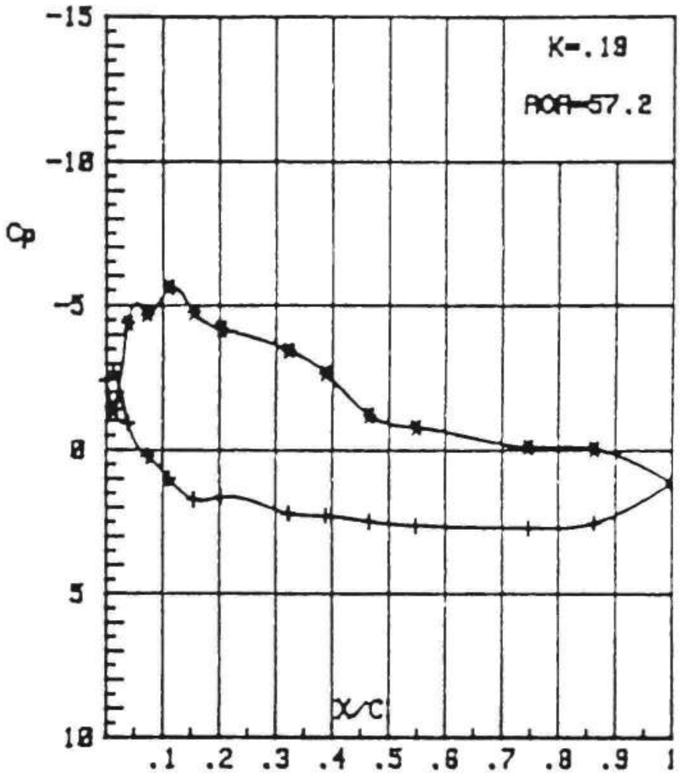
-15
-10
-5
0
5
10
Cp
K=.19
AOA=57.2
X/C
.1
.2
.3
.4
.5
.6
.7
.8
.9
1

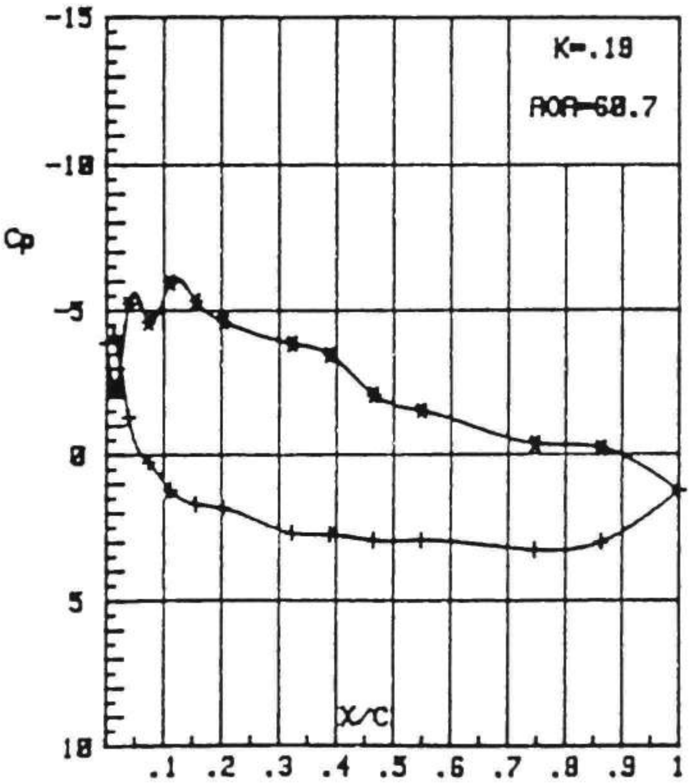
-15
-10
-5
0
5
10
Cp
K=.19
AOA=60.7
X/C
.1
.2
.3
.4
.5
.6
.7
.8
.9
1

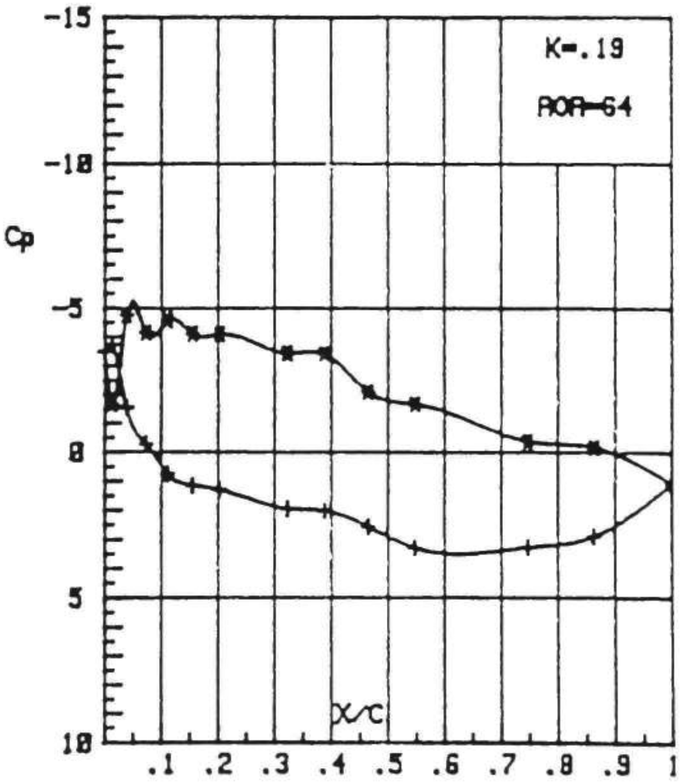
-15
-10
-5
0
5
10
Cp
K=.19
AOA=64
X/C
.1
.2
.3
.4
.5
.6
.7
.8
.9
1

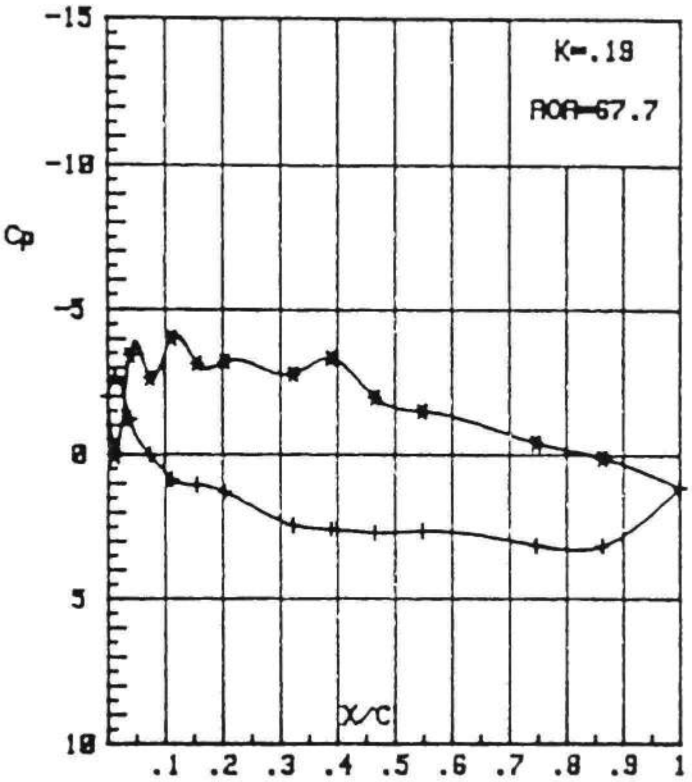
K=.19
AOA=67.7
Cp
-15
-10
-5
0
5
10
X/C
.1
.2
.3
.4
.5
.6
.7
.8
.9
1

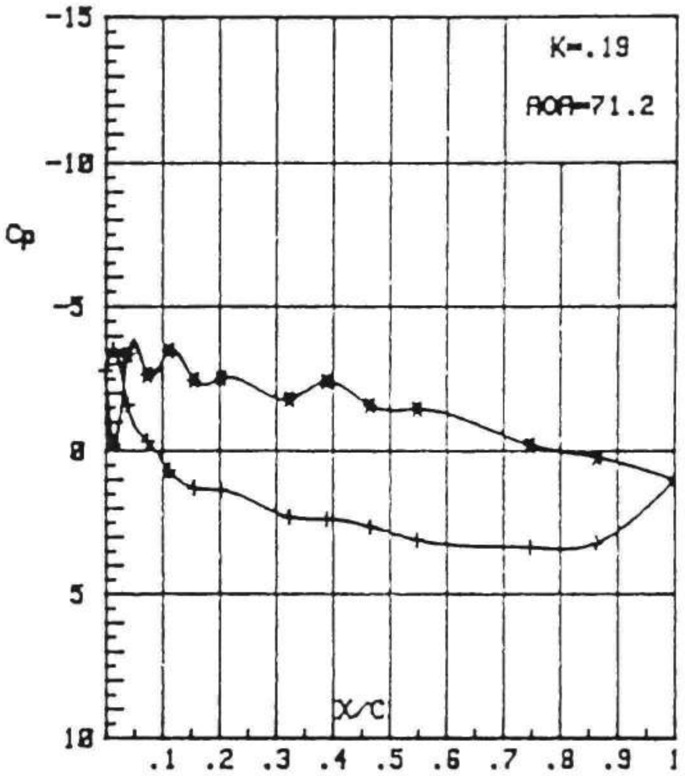
K=.19
AOA=71.2
Cp
-15
-10
-5
0
5
10
X/C
.1
.2
.3
.4
.5
.6
.7
.8
.9
1

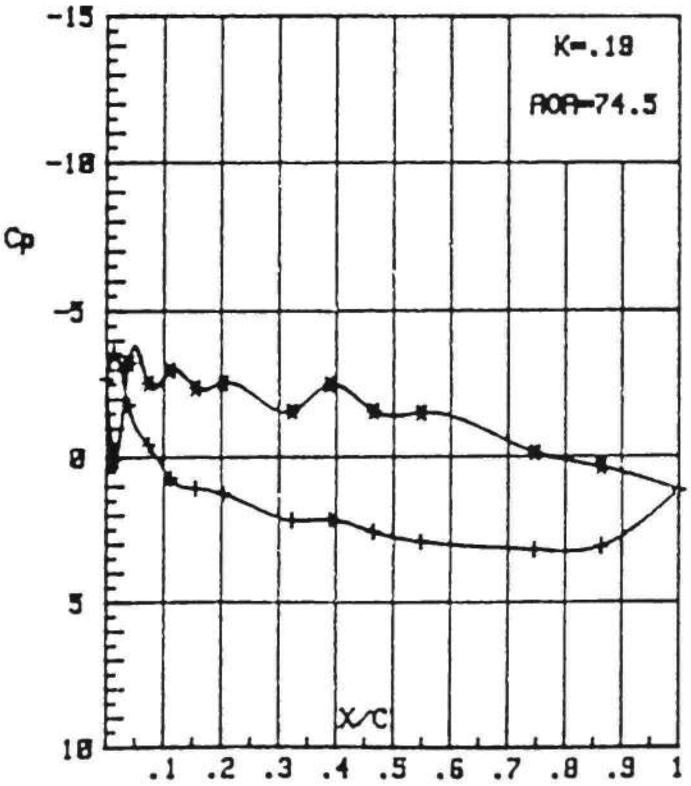
K=.19
AOA=74.5
Cp
-15
-10
-5
0
5
10
X/C
.1
.2
.3
.4
.5
.6
.7
.8
.9
1

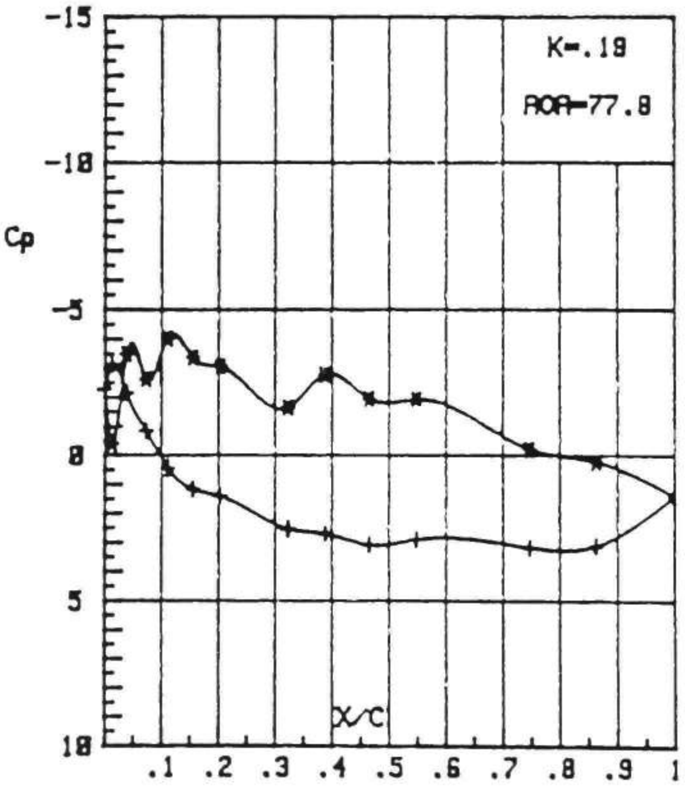
K=.19
AOA=77.8
Cp
-15
-10
-5
0
5
10
X/C
.1
.2
.3
.4
.5
.6
.7
.8
.9
1

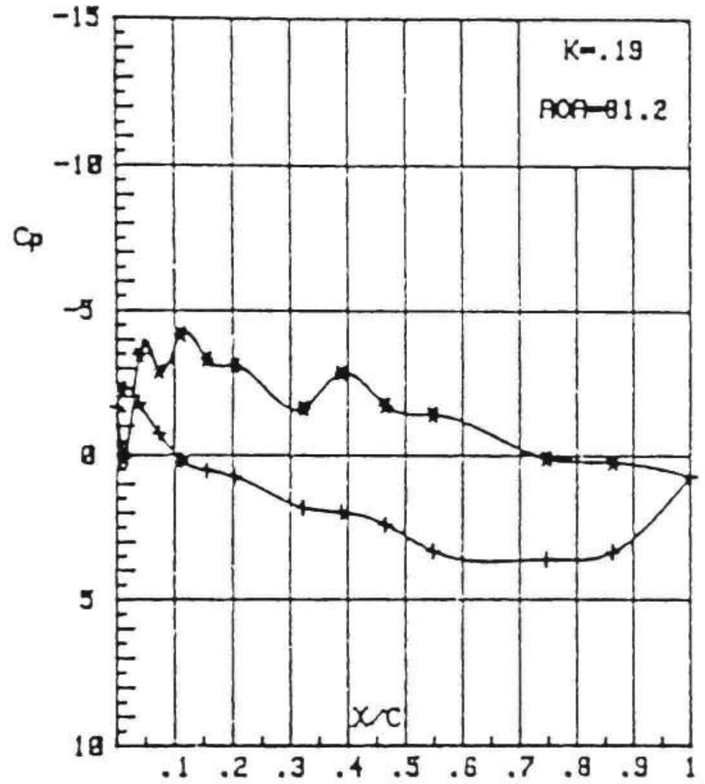
-15
-10
Cp
-5
0
5
10
K=.19
AOA=81.2
X/C
.1
.2
.3
.4
.5
.6
.7
.8
.9
1

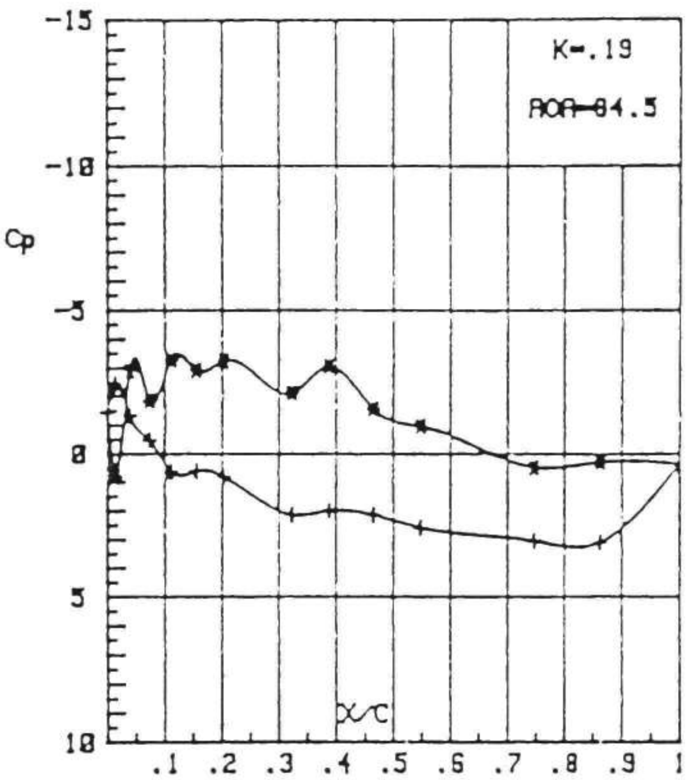
-15
-10
Cp
-5
0
5
10
K=.19
AOA=84.5
X/C
.1
.2
.3
.4
.5
.6
.7
.8
.9
1

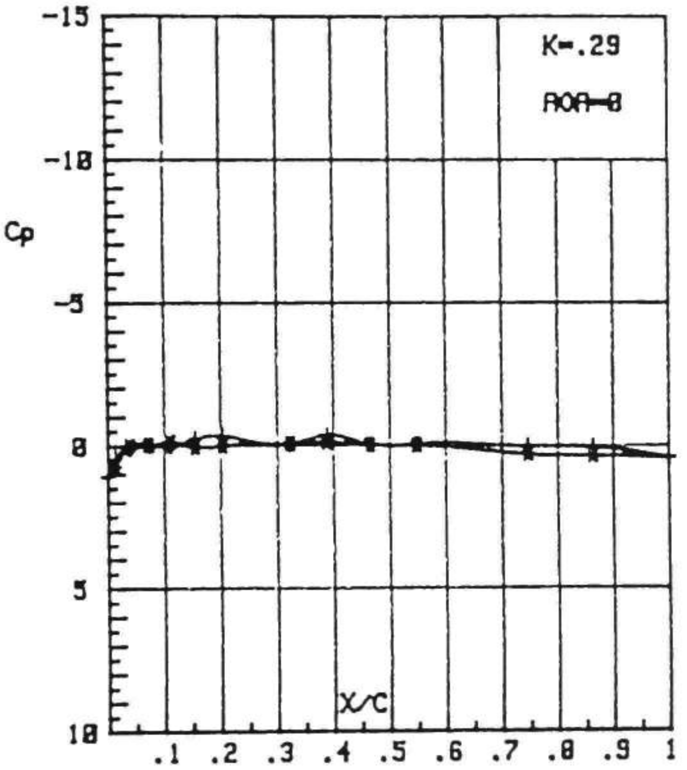
K=.29
AOA=0
Cp
-15
-10
-5
0
5
10
X/C
.1
.2
.3
.4
.5
.6
.7
.8
.9
1

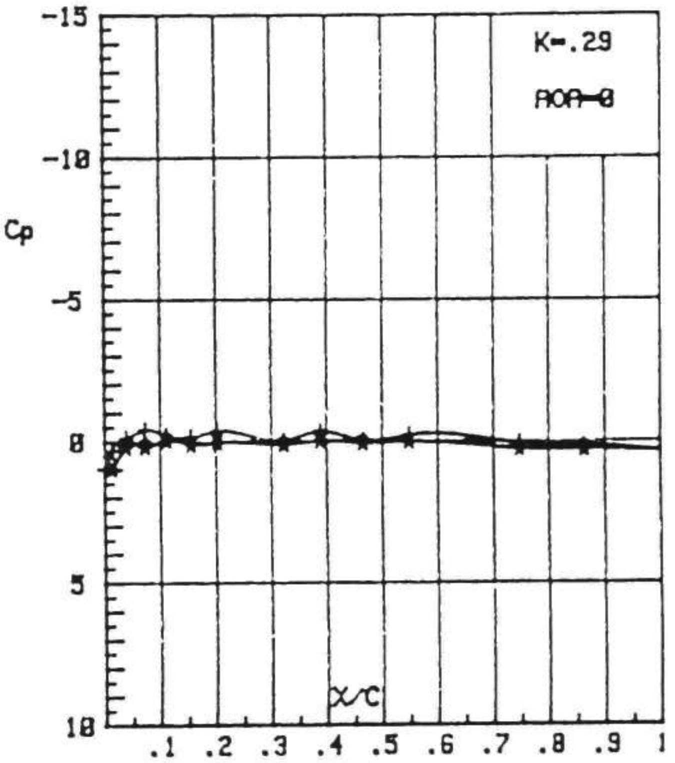
K=.29
AOA=0
Cp
-15
-10
-5
0
5
10
X/C
.1
.2
.3
.4
.5
.6
.7
.8
.9
1

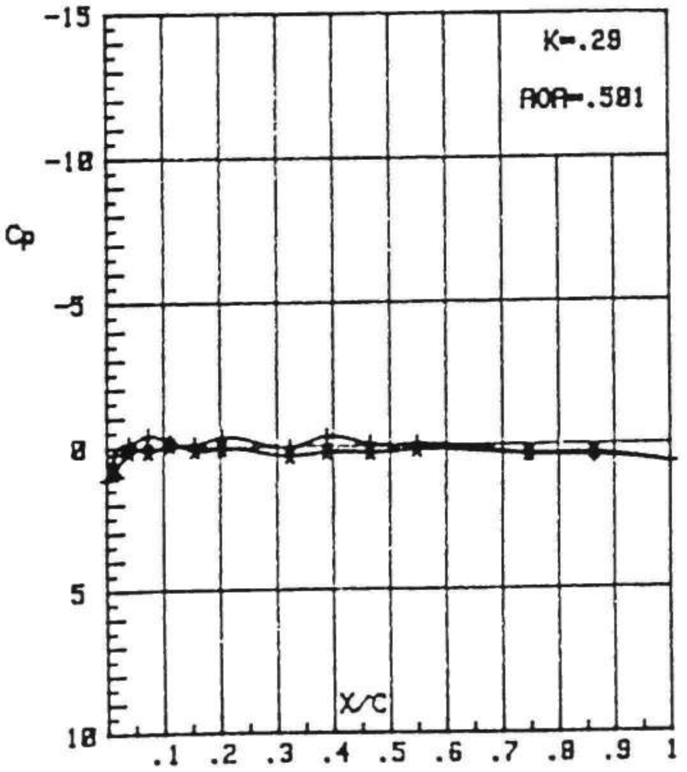
K=.29
AOA=.501
Cp
-15
-10
-5
0
5
10
X/C
.1
.2
.3
.4
.5
.6
.7
.8
.9
1

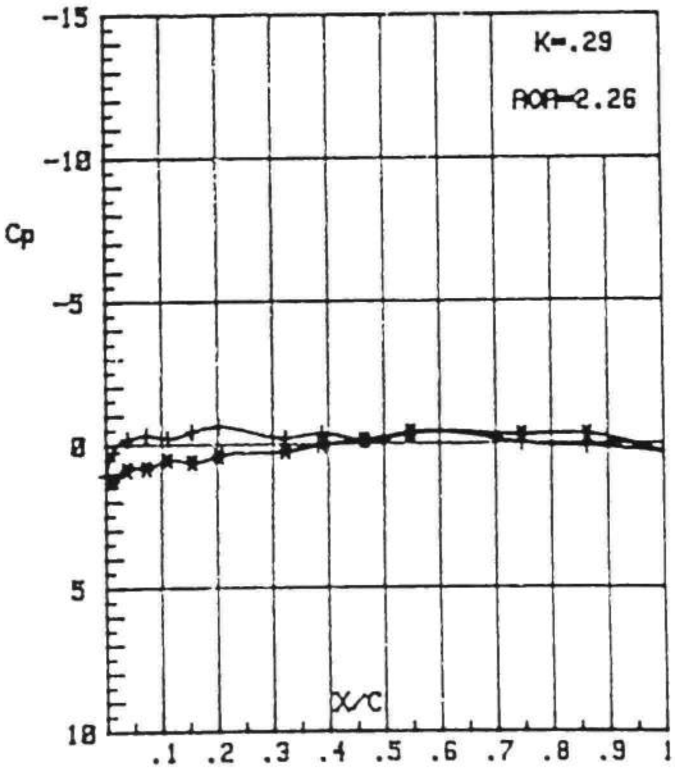
K=.29
AOA=2.26
Cp
-15
-10
-5
0
5
10
X/C
.1
.2
.3
.4
.5
.6
.7
.8
.9
1

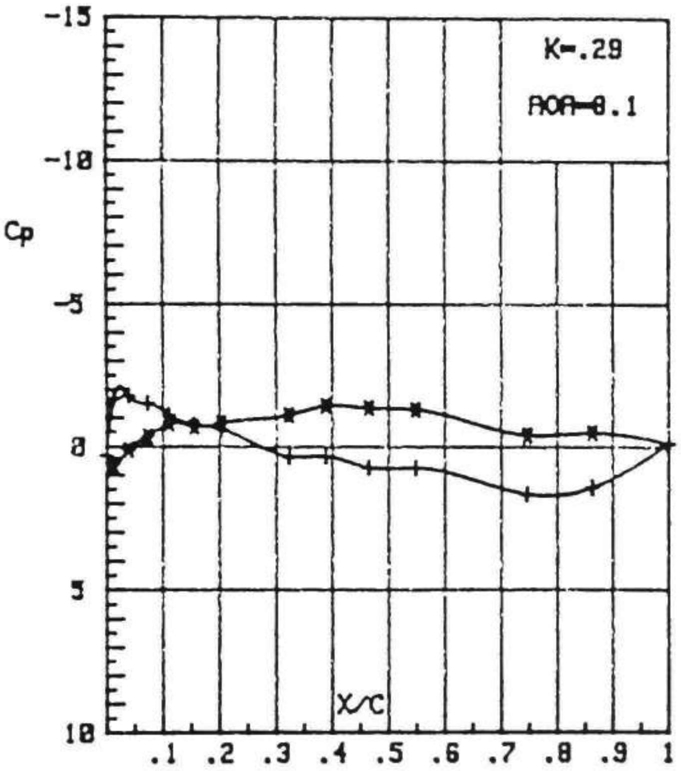
K=.29
AOA=8.1
Cp
-15
-10
-5
0
5
10
X/C
.1
.2
.3
.4
.5
.6
.7
.8
.9
1

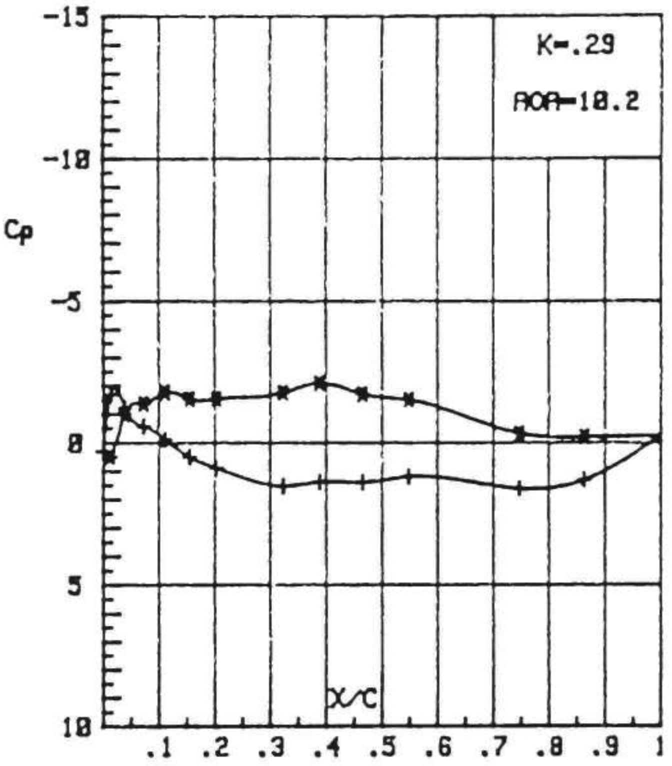
K=.29
AOA=10.2
Cp
-15
-10
-5
0
5
10
X/C
.1
.2
.3
.4
.5
.6
.7
.8
.9
1

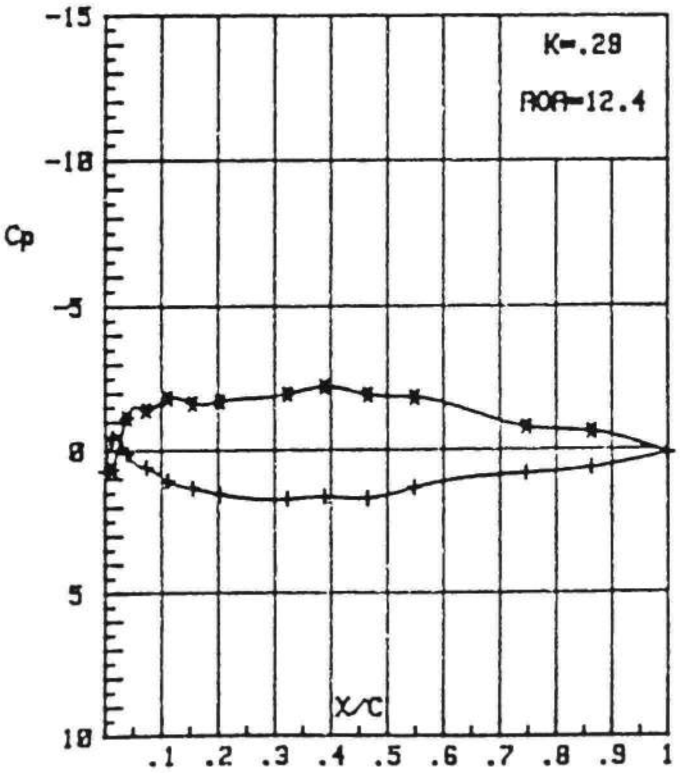
K=.29
AOA=12.4
Cp
-15
-10
-5
0
5
10
X/C
.1
.2
.3
.4
.5
.6
.7
.8
.9
1

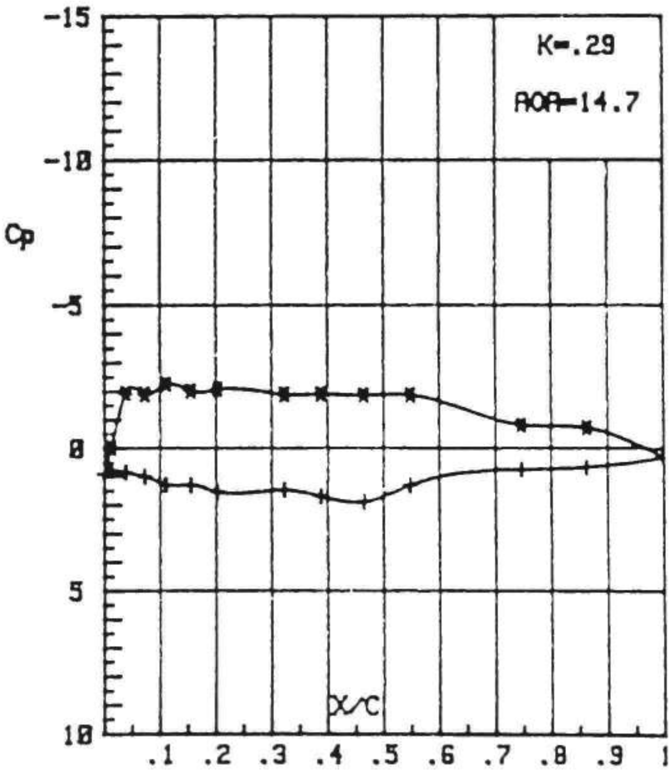
K=.29
AOA=14.7
Cp
-15
-10
-5
0
5
10
X/C
.1
.2
.3
.4
.5
.6
.7
.8
.9
1

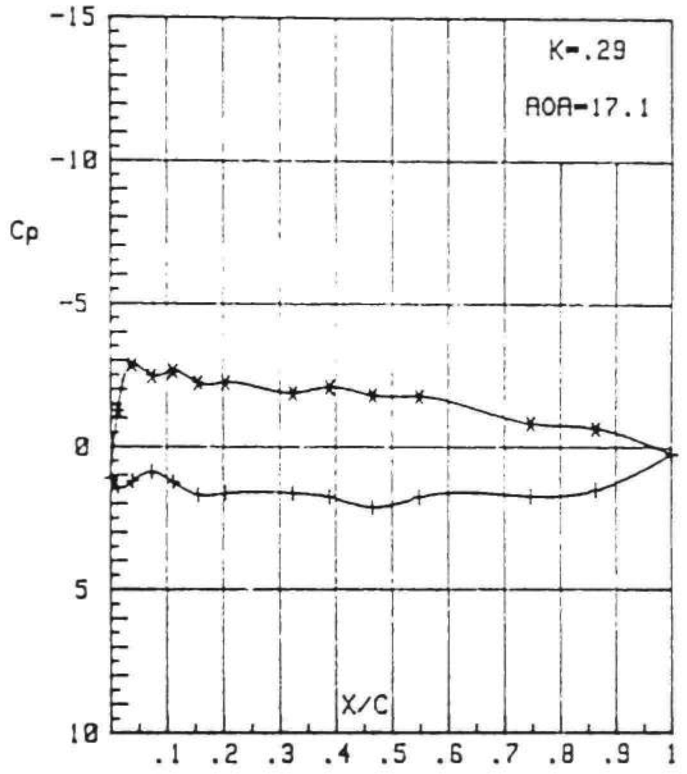
K=.29
AOA=17.1
-15
-10
Cp
-5
0
5
10
X/C
.1
.2
.3
.4
.5
.6
.7
.8
.9
1

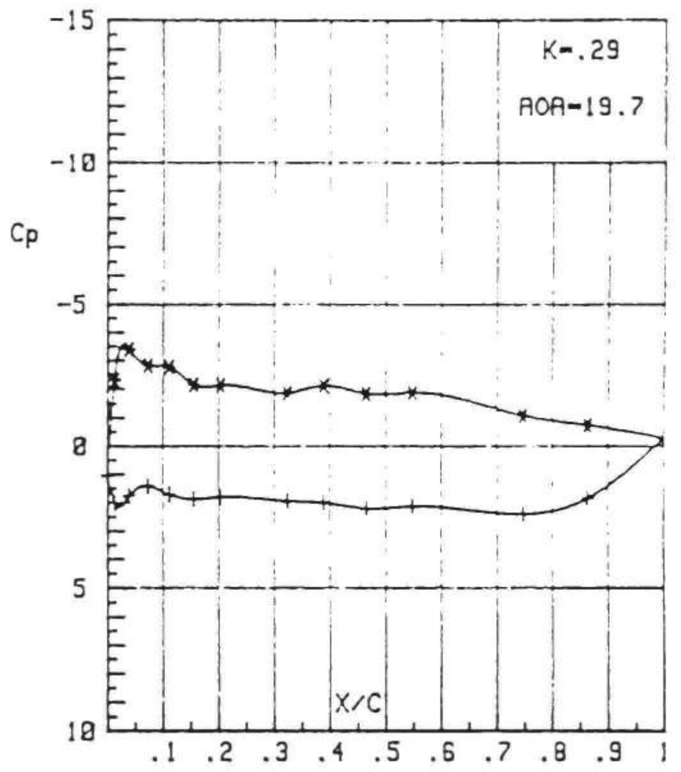
K=.29
AOA=19.7
-15
-10
Cp
-5
0
5
10
X/C
.1
.2
.3
.4
.5
.6
.7
.8
.9
1

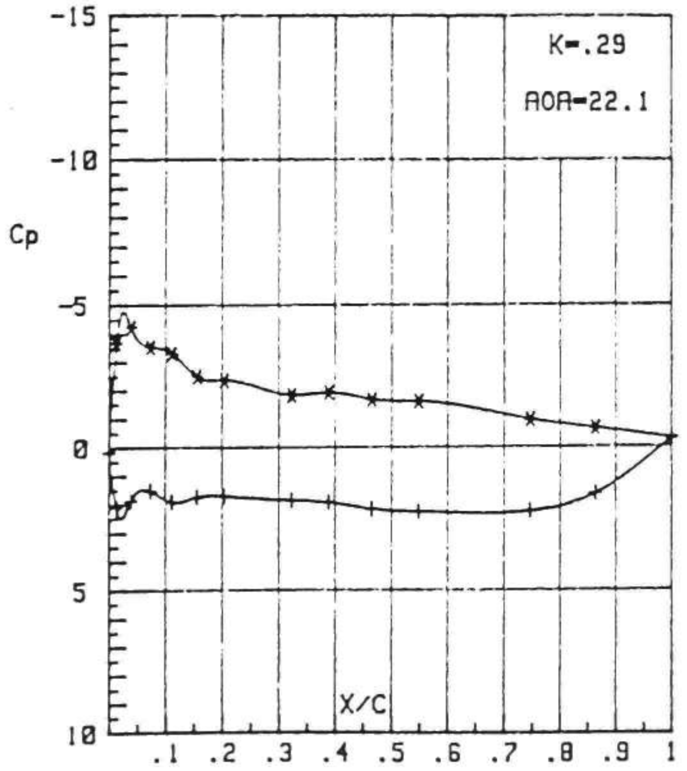
K=.29
AOA=22.1
-15
-10
Cp
-5
0
5
10
X/C
.1
.2
.3
.4
.5
.6
.7
.8
.9
1

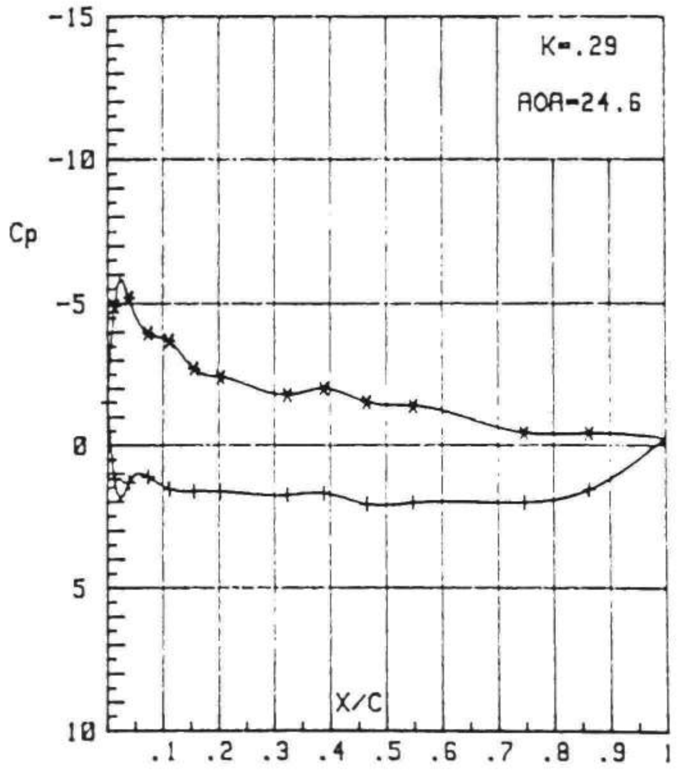
K=.29
AOA=24.6
-15
-10
Cp
-5
0
5
10
X/C
.1
.2
.3
.4
.5
.6
.7
.8
.9
1

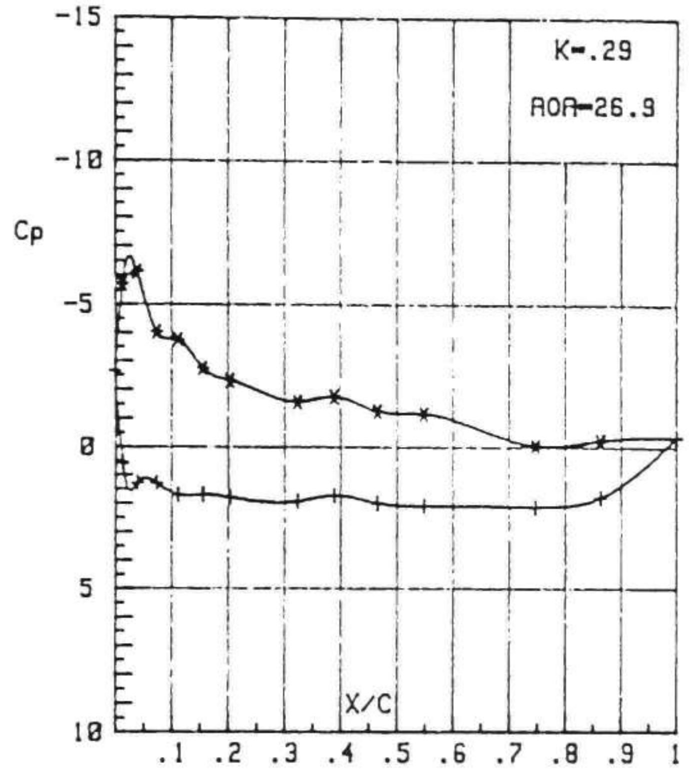
K=.29
AOA=26.9
Cp
-15
-10
-5
0
5
10
X/C
.1
.2
.3
.4
.5
.6
.7
.8
.9
1

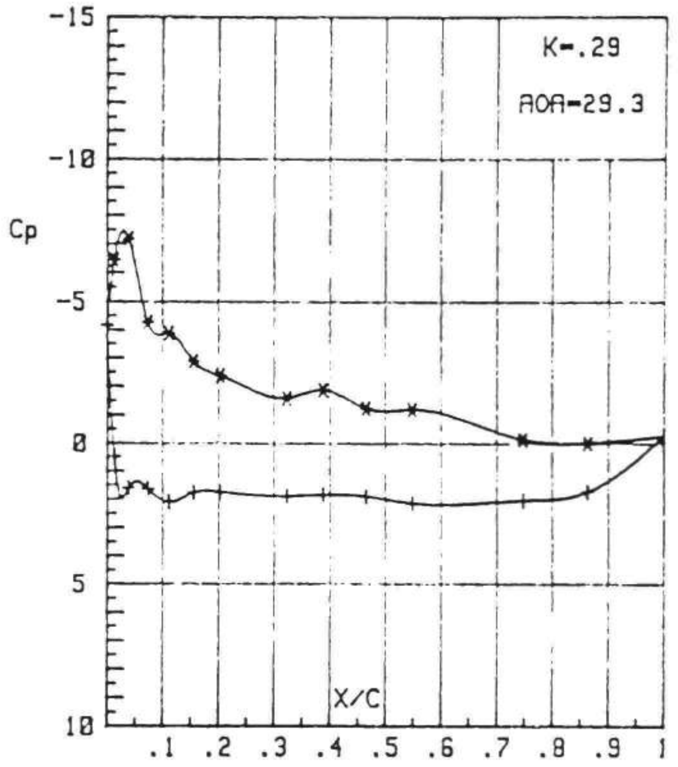
K=.29
AOA=29.3
Cp
-15
-10
-5
0
5
10
X/C
.1
.2
.3
.4
.5
.6
.7
.8
.9
1

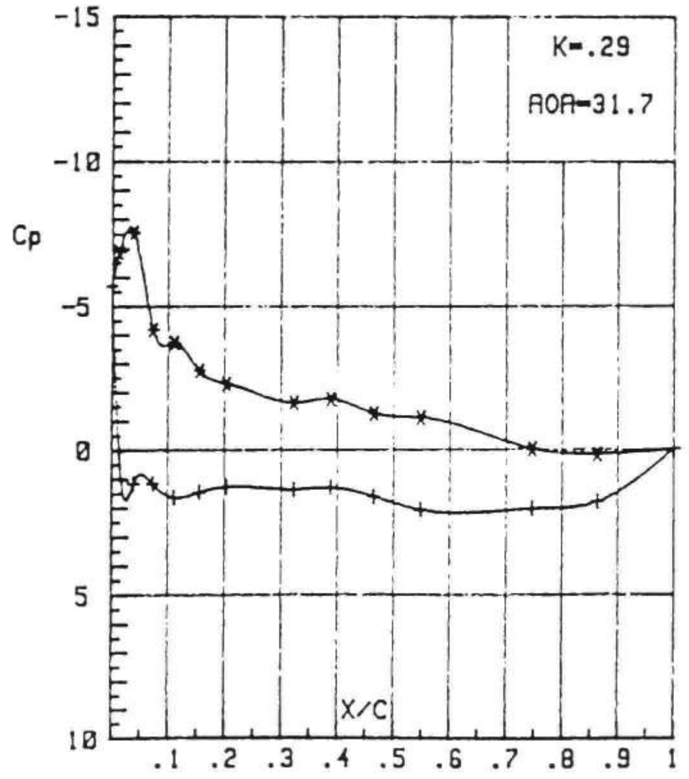
K=.29
AOA=31.7
Cp
-15
-10
-5
0
5
10
X/C
.1
.2
.3
.4
.5
.6
.7
.8
.9
1

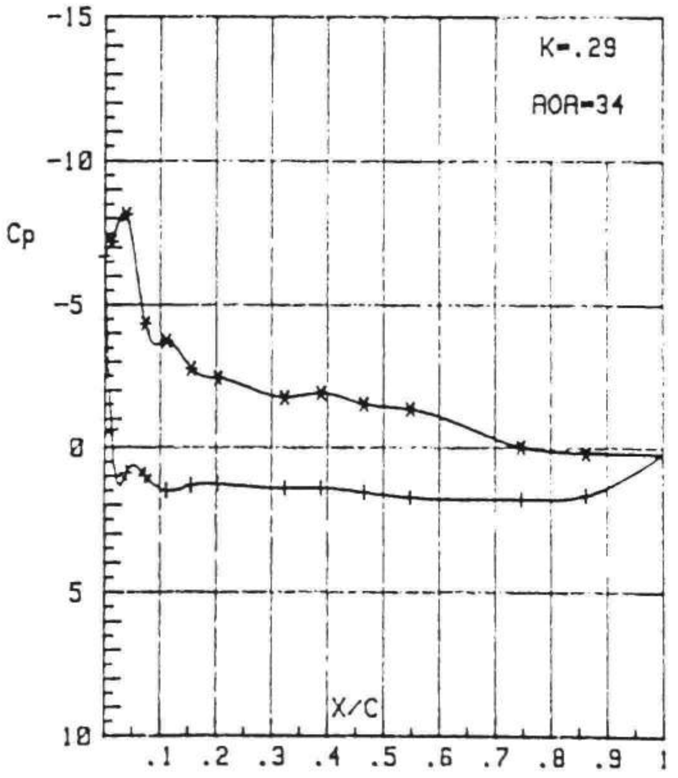
K=.29
AOA=34
Cp
-15
-10
-5
0
5
10
X/C
.1
.2
.3
.4
.5
.6
.7
.8
.9
1

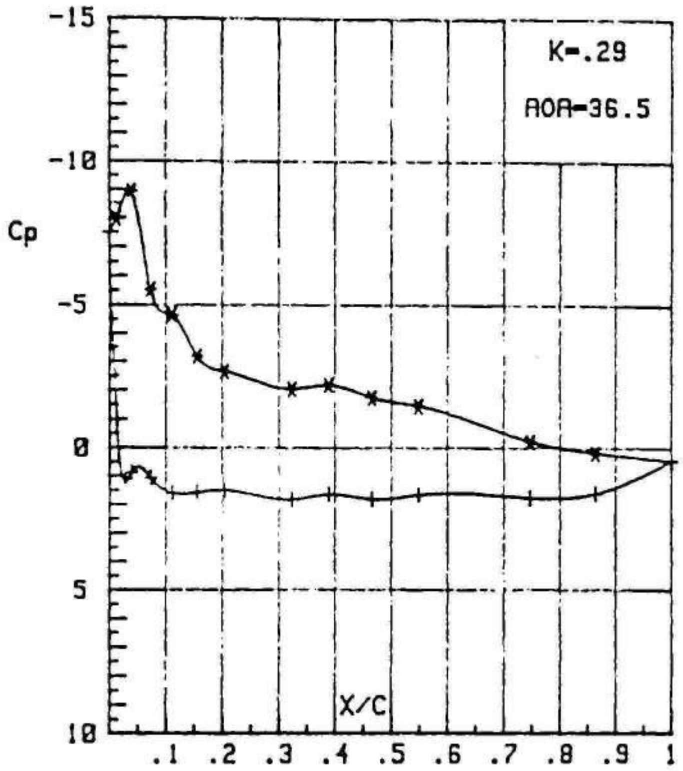
K=.29
AOA=36.5
Cp
X/C
-15
-10
-5
0
5
10
.1
.2
.3
.4
.5
.6
.7
.8
.9
1

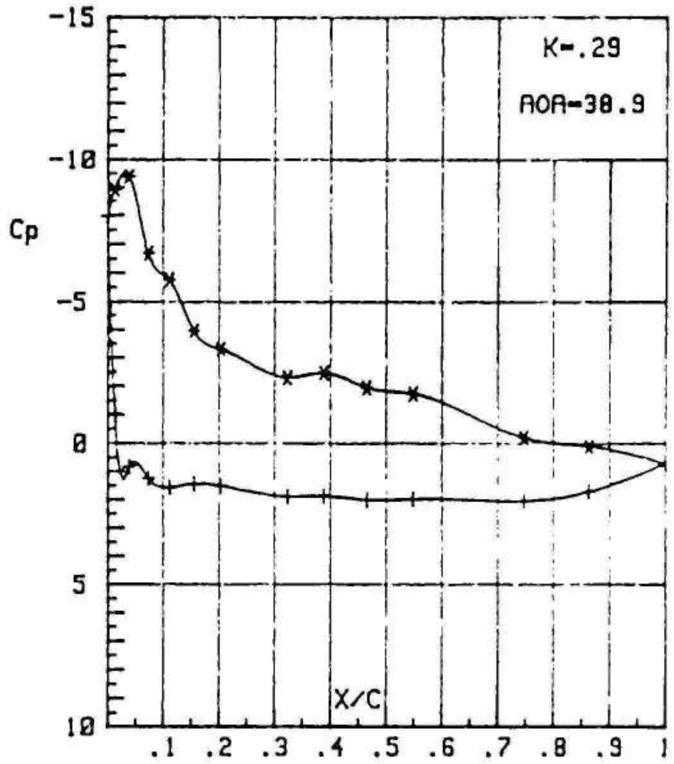
K=.29
AOA=38.9
Cp
X/C
-15
-10
-5
0
5
10
.1
.2
.3
.4
.5
.6
.7
.8
.9
1

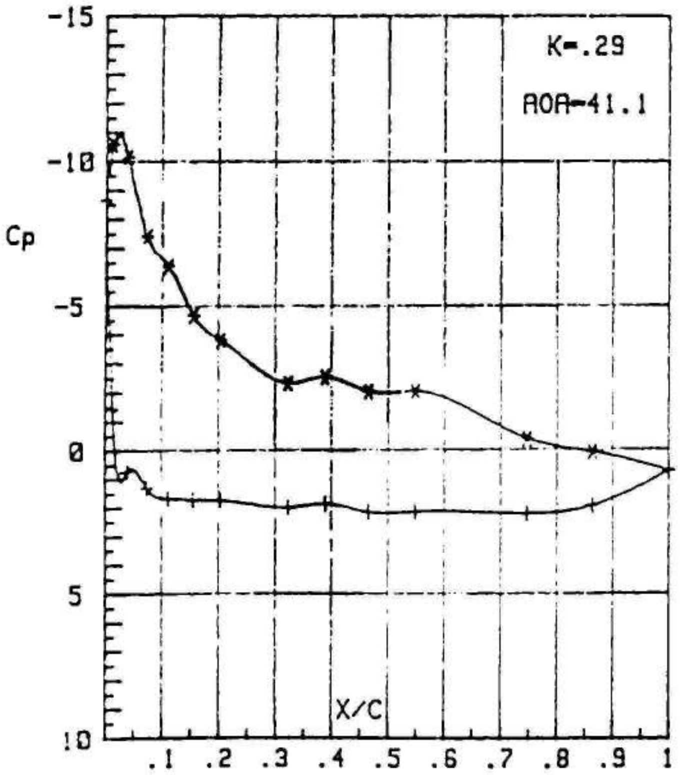
K=.29
AOA=41.1
Cp
X/C
-15
-10
-5
0
5
10
.1
.2
.3
.4
.5
.6
.7
.8
.9
1

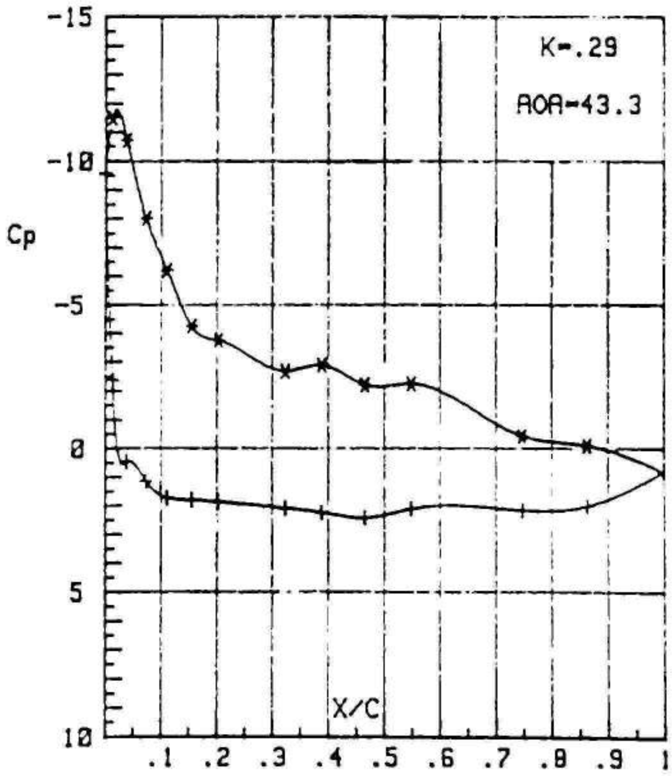
K=.29
AOA=43.3
Cp
X/C
-15
-10
-5
0
5
10
.1
.2
.3
.4
.5
.6
.7
.8
.9
1

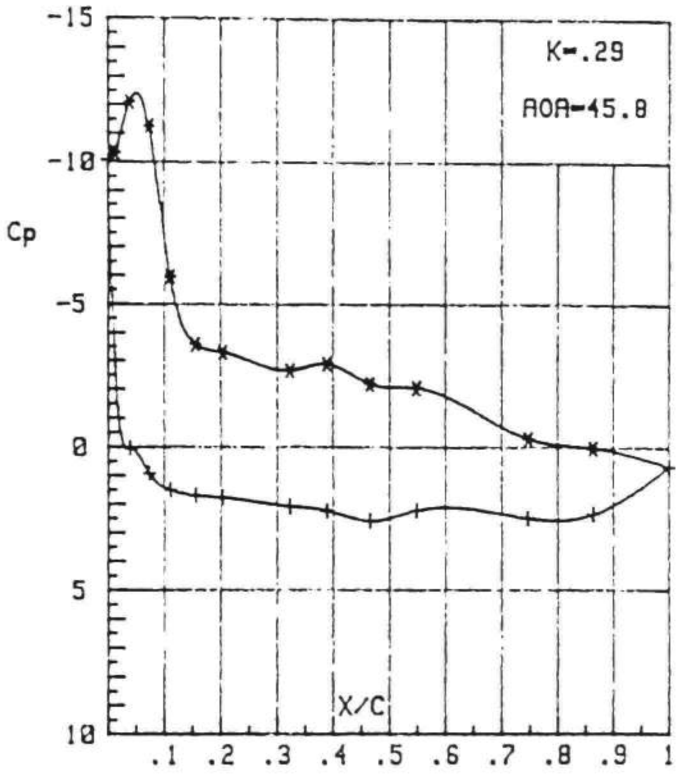
K=.29
AOA=45.8
Cp
-15
-10
-5
0
5
10
X/C
.1 .2 .3 .4 .5 .6 .7 .8 .9 1

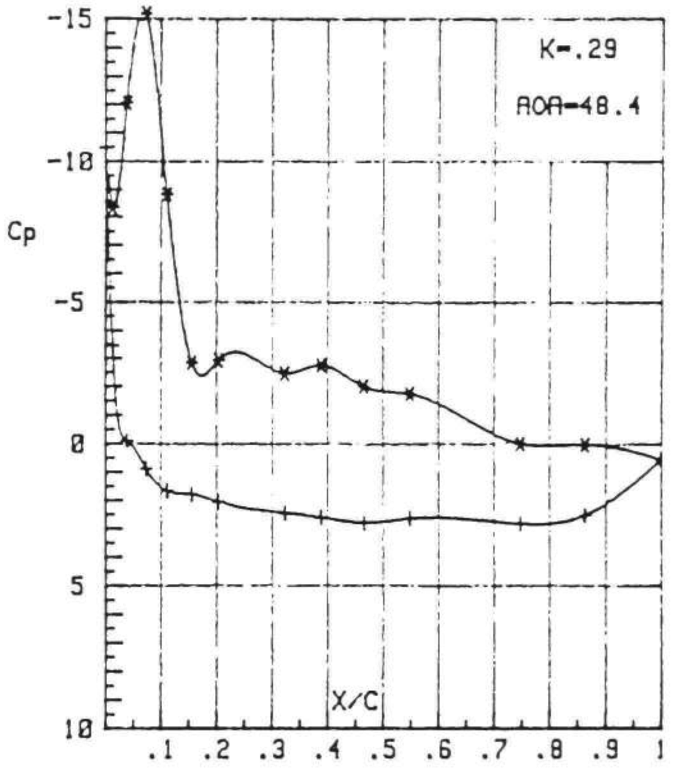
K=.29
AOA=48.4
Cp
-15
-10
-5
0
5
10
X/C
.1 .2 .3 .4 .5 .6 .7 .8 .9 1

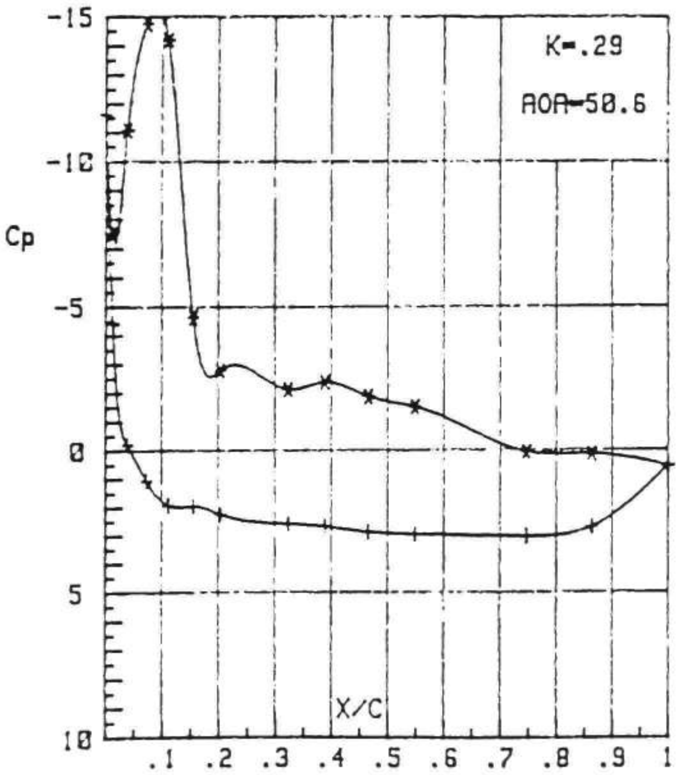
K=.29
AOA=50.6
Cp
-15
-10
-5
0
5
10
X/C
.1 .2 .3 .4 .5 .6 .7 .8 .9 1

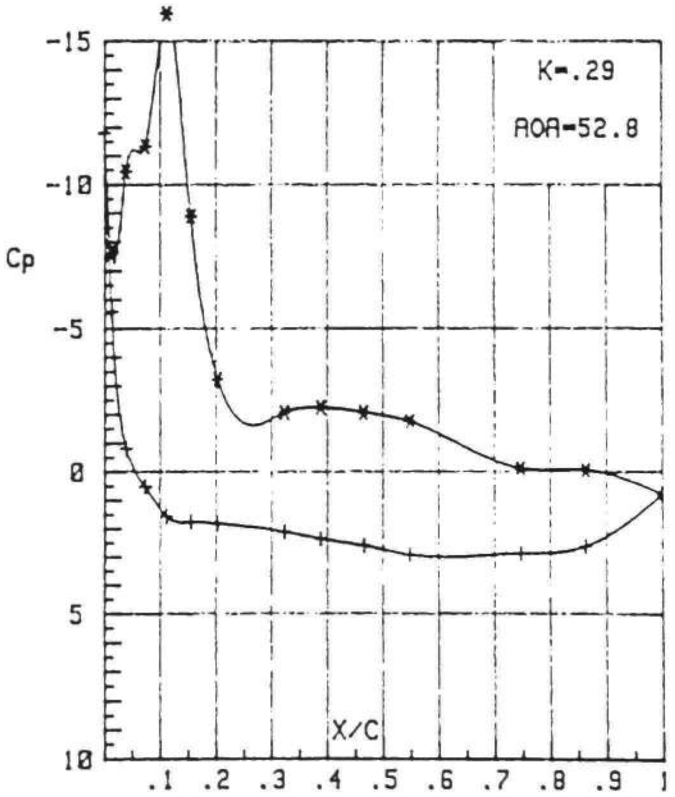
K=.29
AOA=52.8
Cp
-15
-10
-5
0
5
10
X/C
.1 .2 .3 .4 .5 .6 .7 .8 .9 1

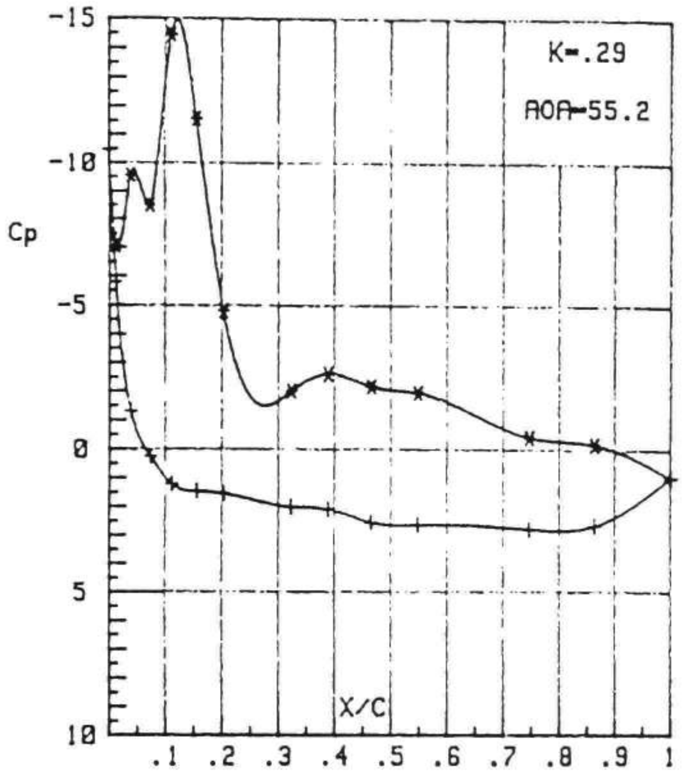
K=.29
AOA=55.2
Cp
-15
-10
-5
0
5
10
X/C
.1
.2
.3
.4
.5
.6
.7
.8
.9
1

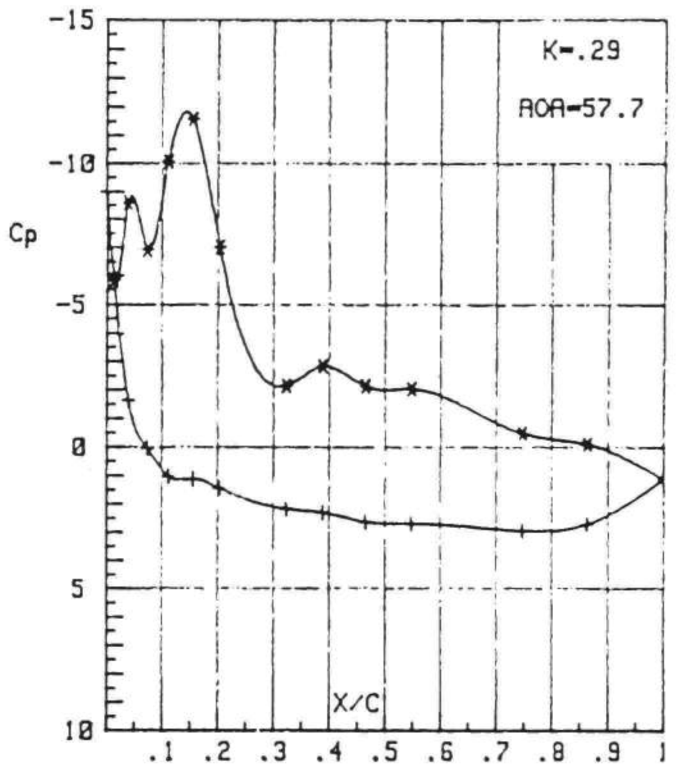
K=.29
AOA=57.7
Cp
-15
-10
-5
0
5
10
X/C
.1
.2
.3
.4
.5
.6
.7
.8
.9
1

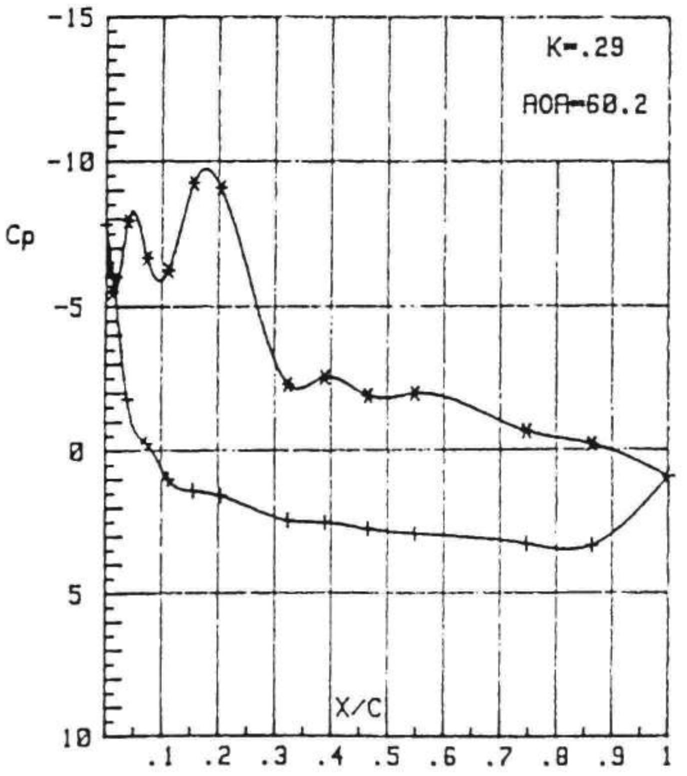
K=.29
AOA=60.2
Cp
-15
-10
-5
0
5
10
X/C
.1
.2
.3
.4
.5
.6
.7
.8
.9
1

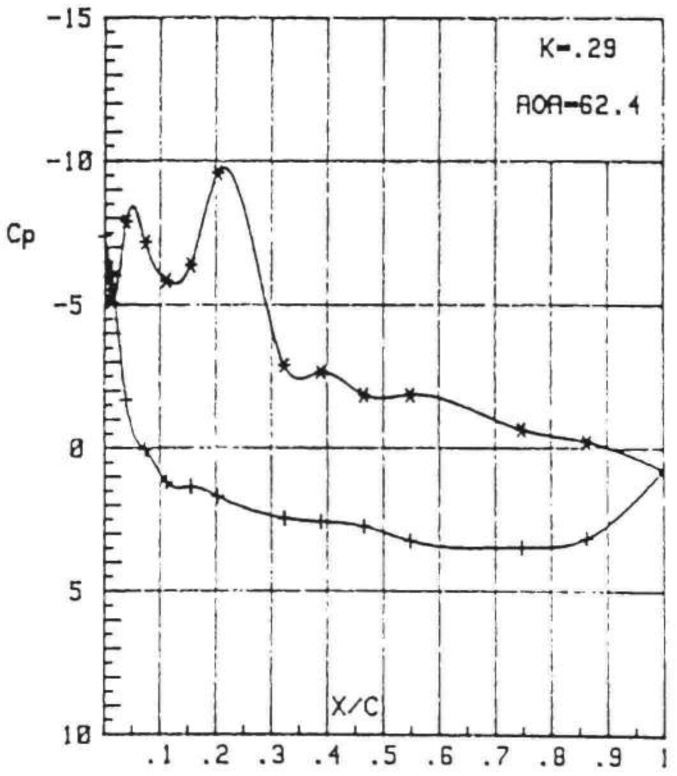
K=.29
AOA=62.4
Cp
-15
-10
-5
0
5
10
X/C
.1
.2
.3
.4
.5
.6
.7
.8
.9
1

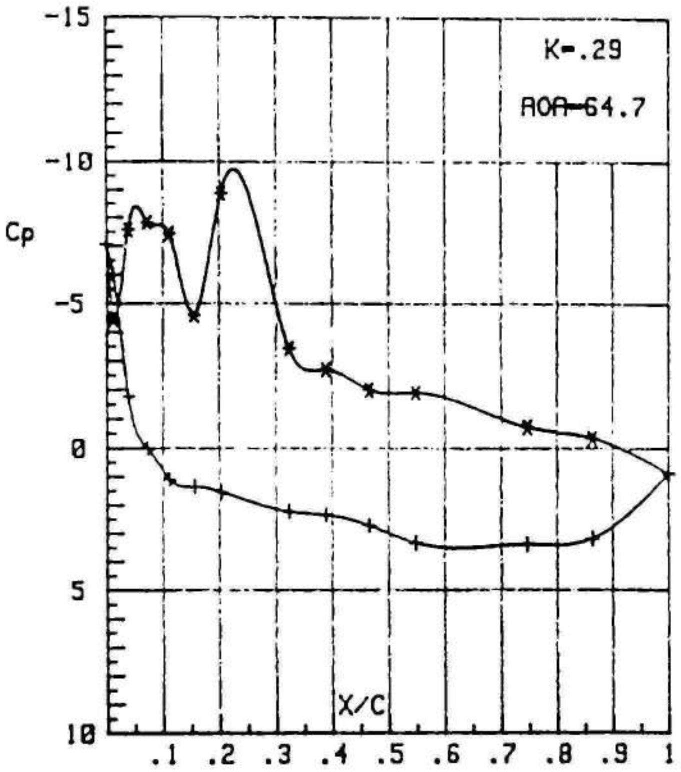
K=.29
AOA=64.7
Cp
-15
-10
-5
0
5
10
X/C
.1
.2
.3
.4
.5
.6
.7
.8
.9
1

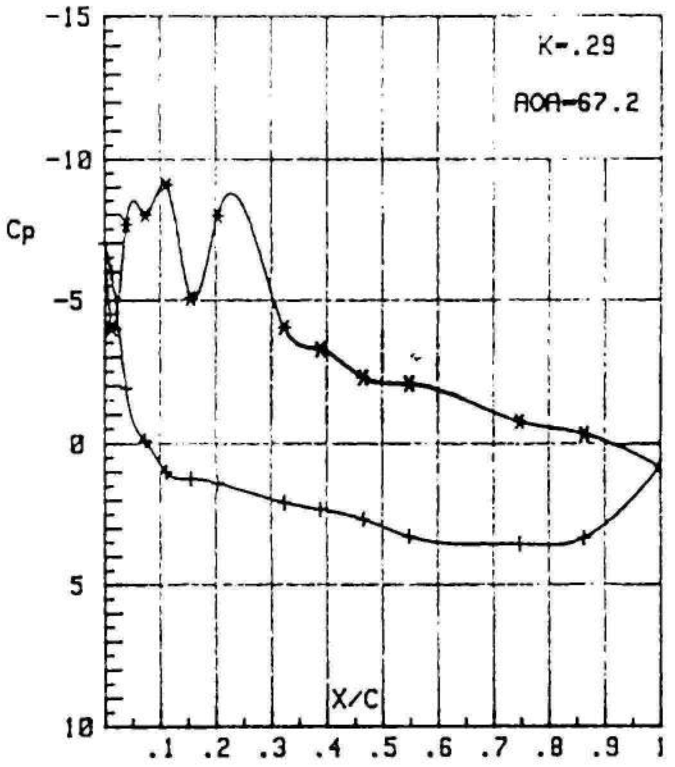
K=.29
AOA=67.2
Cp
-15
-10
-5
0
5
10
X/C
.1
.2
.3
.4
.5
.6
.7
.8
.9
1

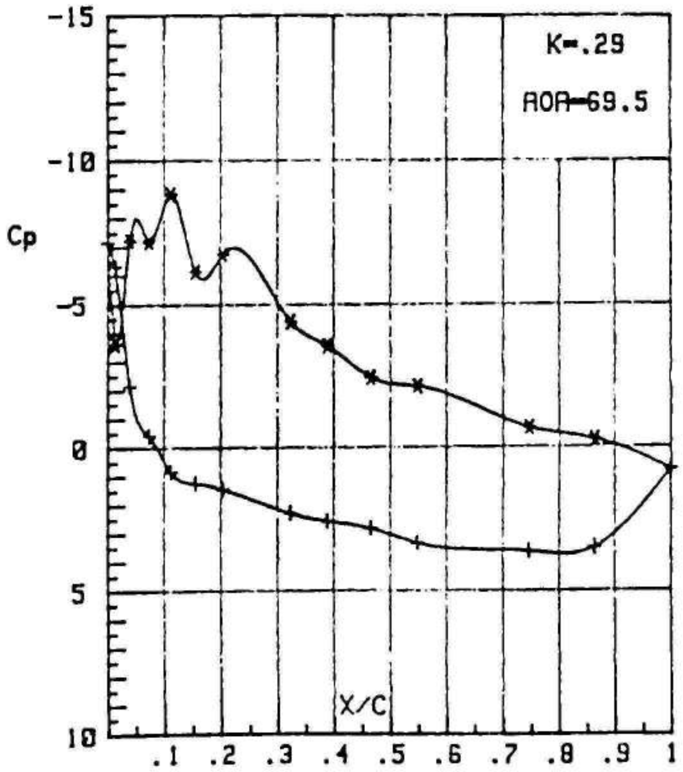
K=.29
AOA=69.5
Cp
-15
-10
-5
0
5
10
X/C
.1
.2
.3
.4
.5
.6
.7
.8
.9
1

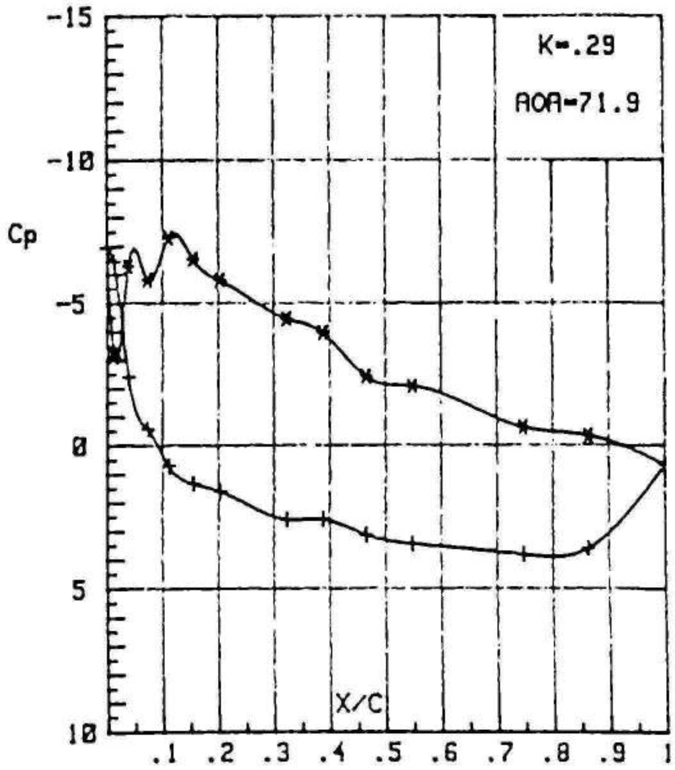
K=.29
AOA=71.9
Cp
-15
-10
-5
0
5
10
X/C
.1
.2
.3
.4
.5
.6
.7
.8
.9
1

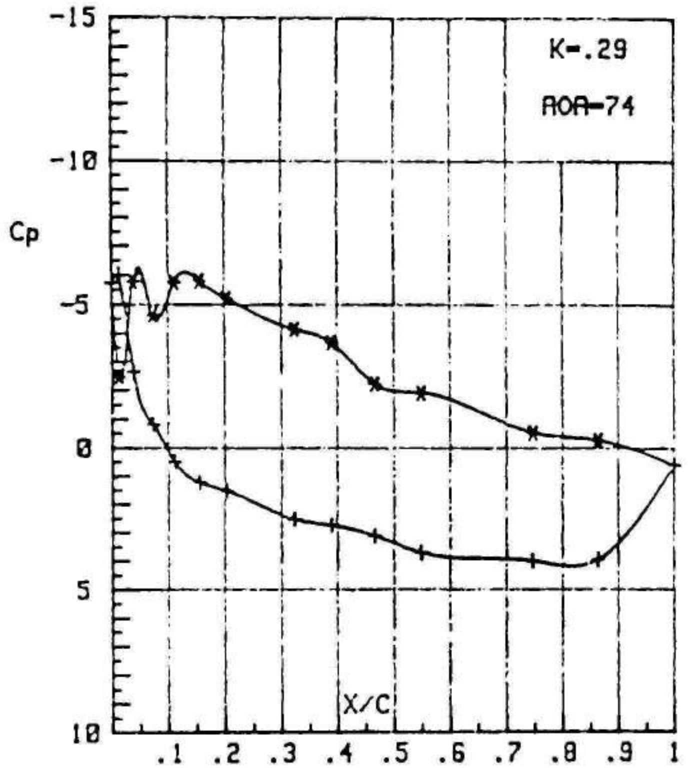
K=.29
AOA=74
Cp
-15
-10
-5
0
5
10
X/C
.1
.2
.3
.4
.5
.6
.7
.8
.9
1

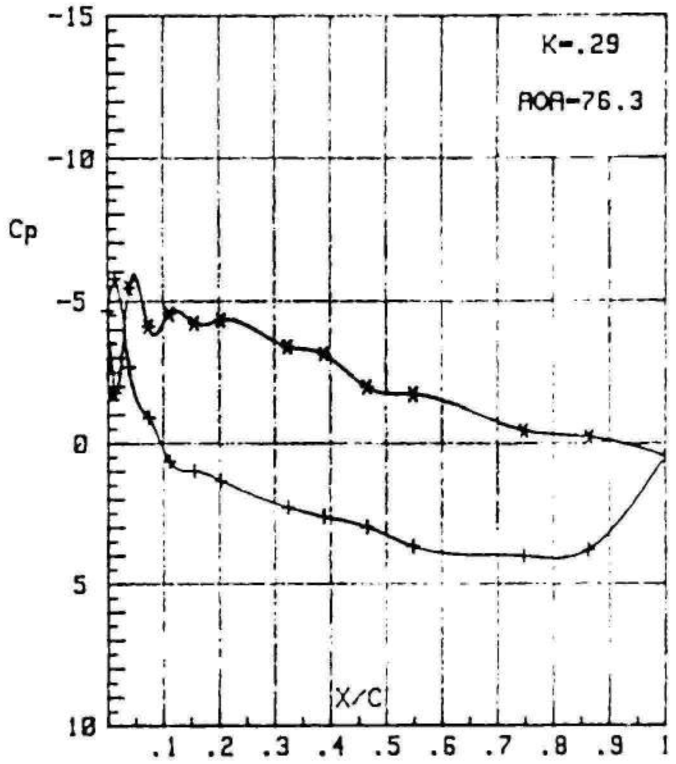
K=.29
AOA=76.3
Cp
-15
-10
-5
0
5
10
X/C
.1
.2
.3
.4
.5
.6
.7
.8
.9
1

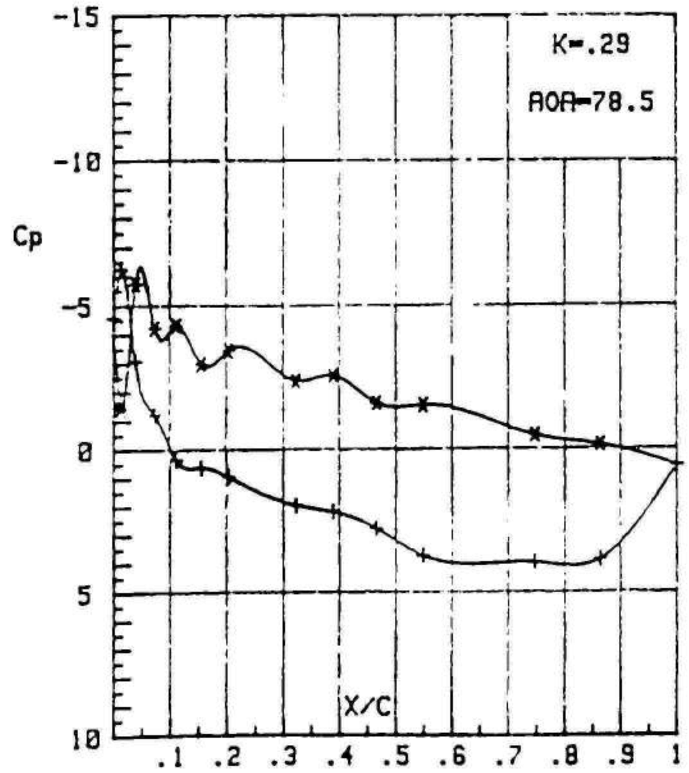
K=.29
AOA=78.5
Cp
-15
-10
-5
0
5
10
X/C
.1
.2
.3
.4
.5
.6
.7
.8
.9
1

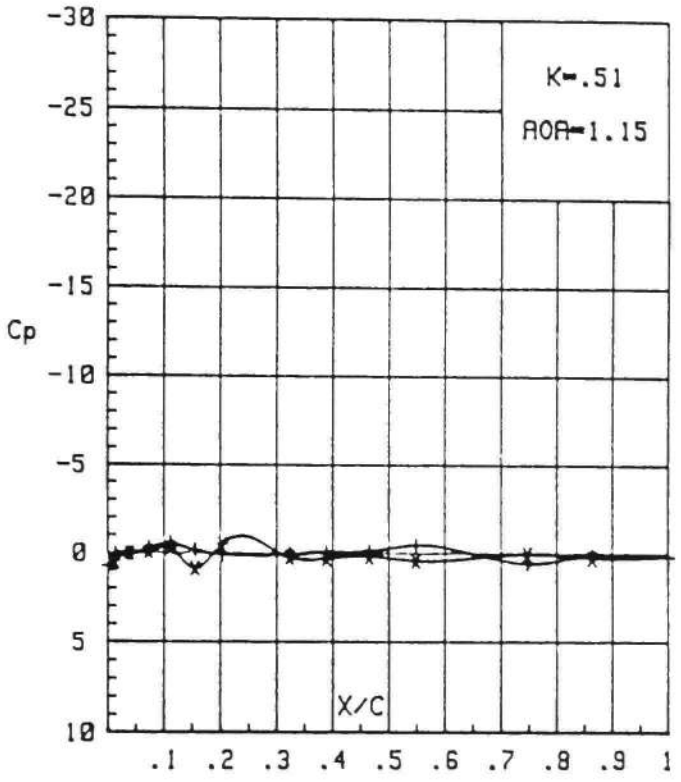
K=.51
AOA=1.15
Cp
X/C
-30
-25
-20
-15
-10
-5
0
5
10
.1 .2 .3 .4 .5 .6 .7 .8 .9 1

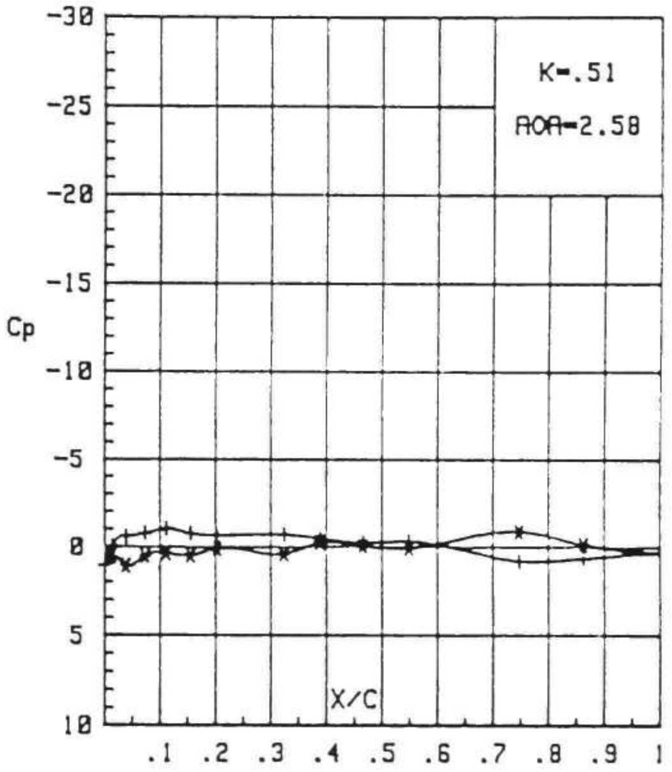
K=.51
AOA=2.58
Cp
X/C
-30
-25
-20
-15
-10
-5
0
5
10
.1 .2 .3 .4 .5 .6 .7 .8 .9 1

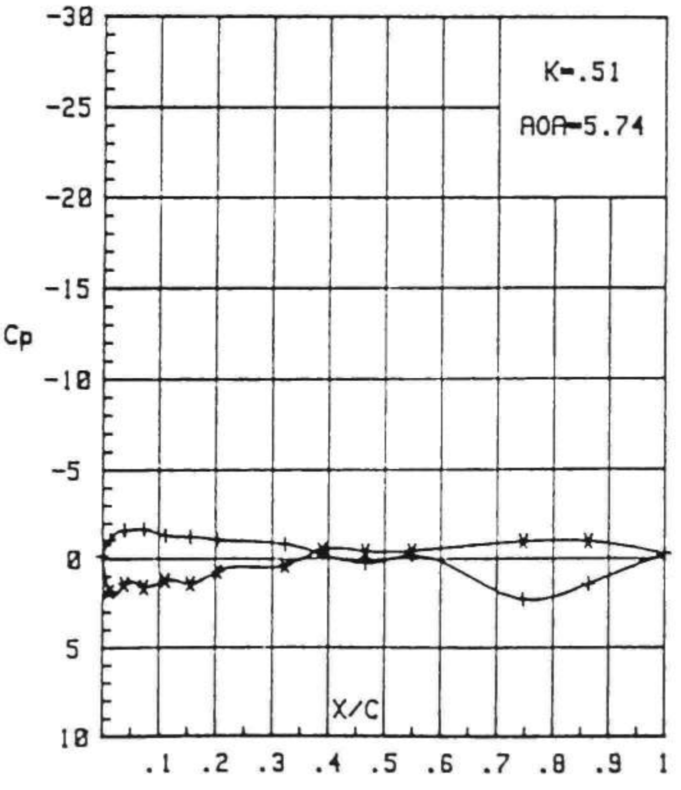
K=.51
AOA=5.74
Cp
X/C
-30
-25
-20
-15
-10
-5
0
5
10
.1 .2 .3 .4 .5 .6 .7 .8 .9 1

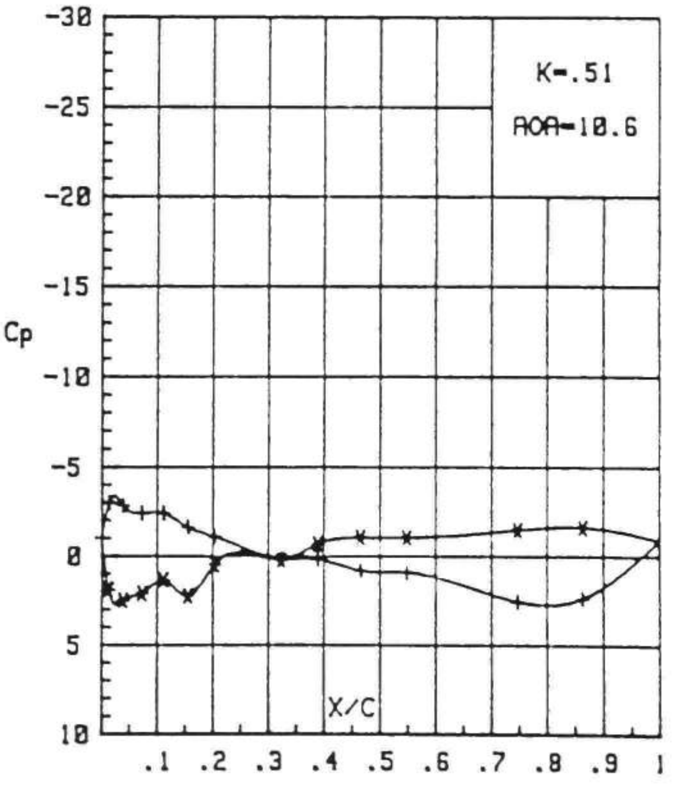
K=.51
AOA=10.6
Cp
X/C
-30
-25
-20
-15
-10
-5
0
5
10
.1 .2 .3 .4 .5 .6 .7 .8 .9 1

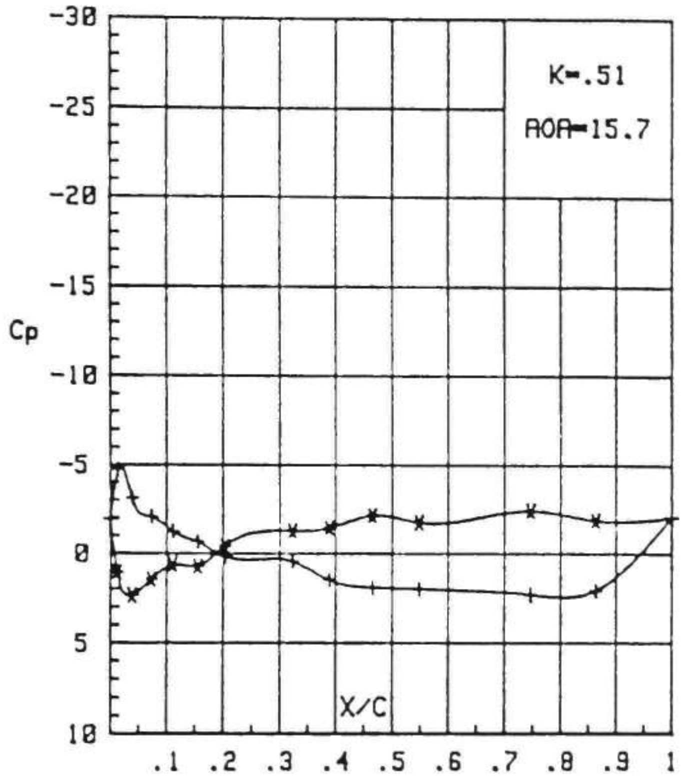
K=.51
AOA=15.7
Cp
-30
-25
-20
-15
-10
-5
0
5
10
X/C
.1
.2
.3
.4
.5
.6
.7
.8
.9
1

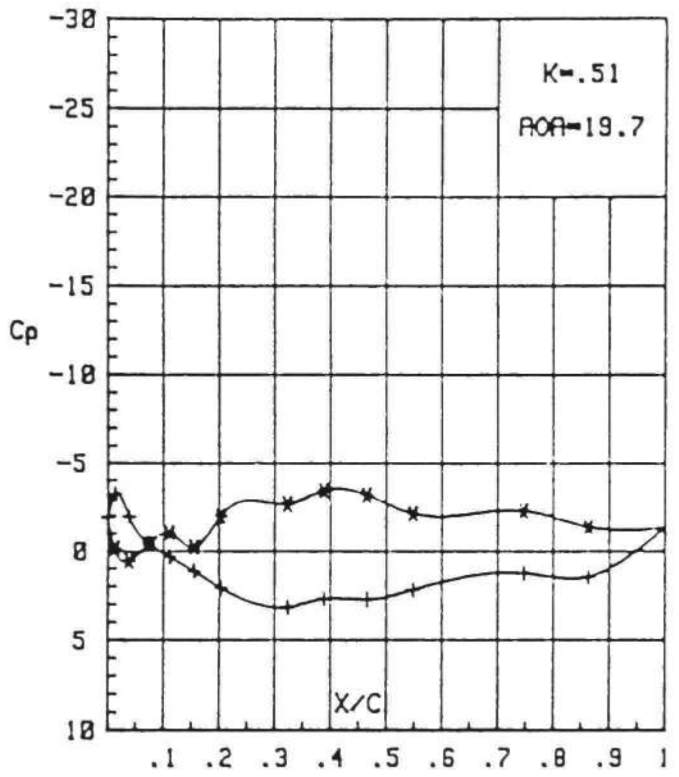
K=.51
AOA=19.7
Cp
-30
-25
-20
-15
-10
-5
0
5
10
X/C
.1
.2
.3
.4
.5
.6
.7
.8
.9
1

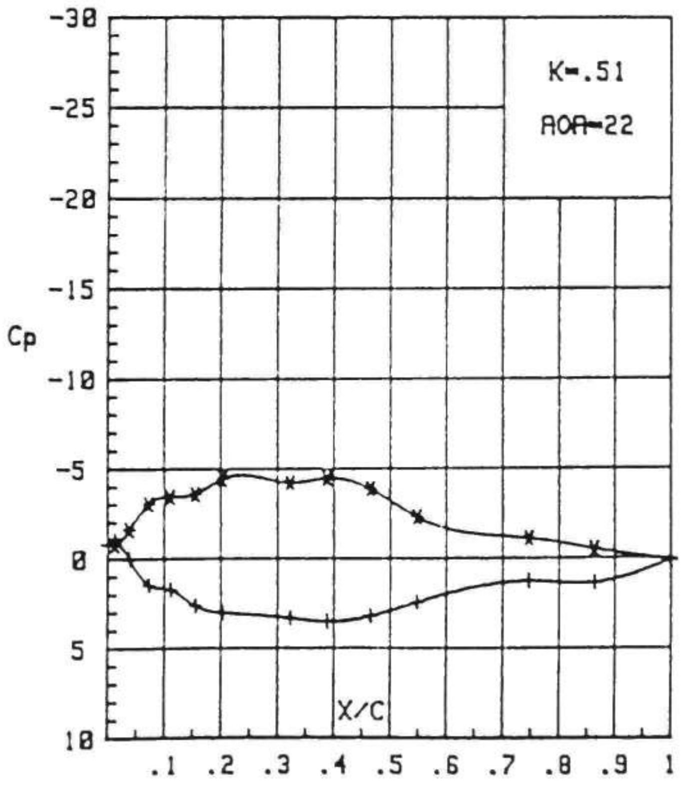
K=.51
AOA=22
Cp
-30
-25
-20
-15
-10
-5
0
5
10
X/C
.1
.2
.3
.4
.5
.6
.7
.8
.9
1

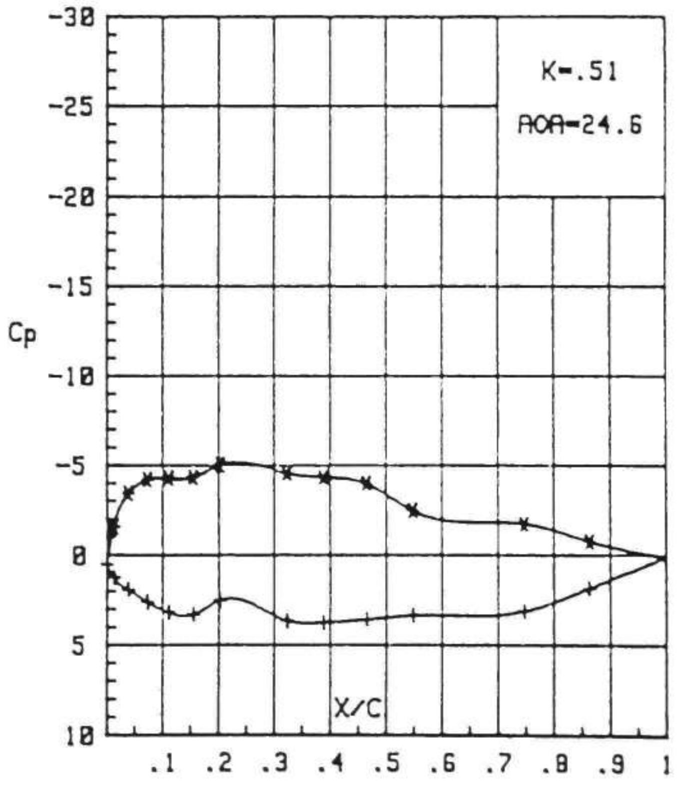
K=.51
AOA=24.6
Cp
-30
-25
-20
-15
-10
-5
0
5
10
X/C
.1
.2
.3
.4
.5
.6
.7
.8
.9
1

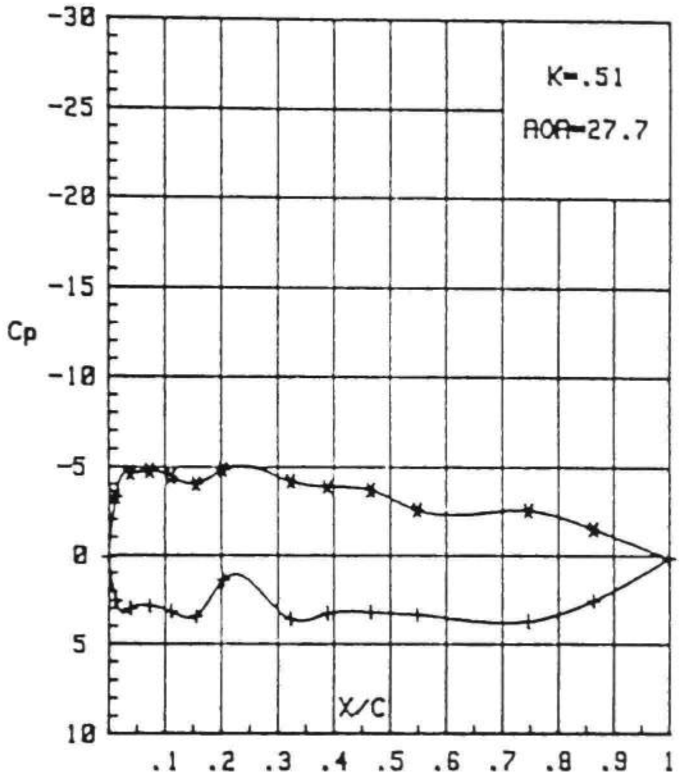
K=.51
AOA=27.7
Cp
X/C
-30
-25
-20
-15
-10
-5
0
5
10
.1 .2 .3 .4 .5 .6 .7 .8 .9 1

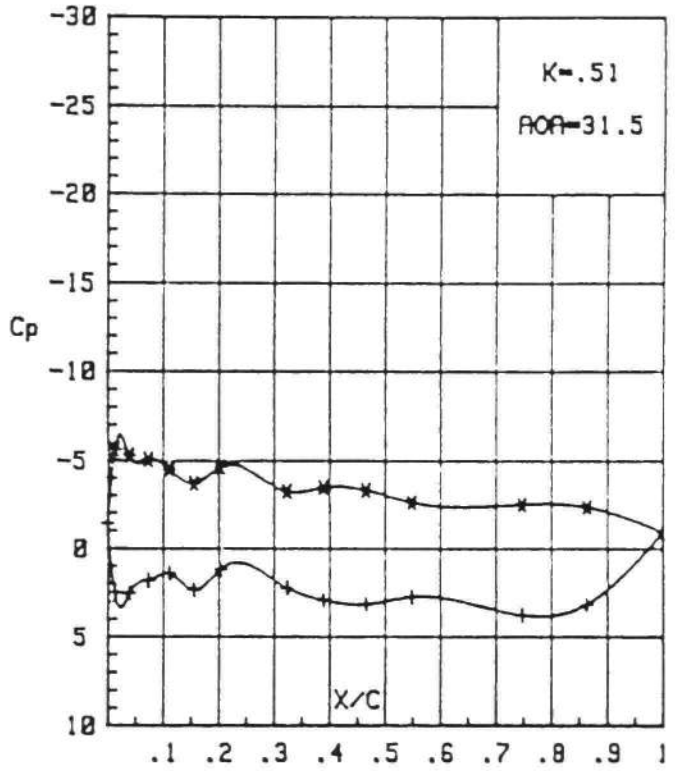
K=.51
AOA=31.5
Cp
X/C
-30
-25
-20
-15
-10
-5
0
5
10
.1 .2 .3 .4 .5 .6 .7 .8 .9 1

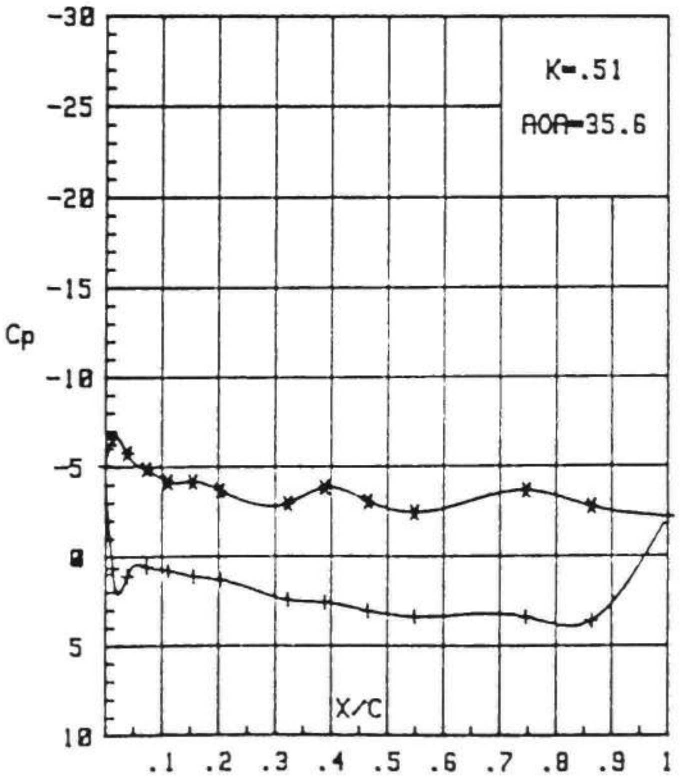
K=.51
AOA=35.6
Cp
X/C
-30
-25
-20
-15
-10
-5
0
5
10
.1 .2 .3 .4 .5 .6 .7 .8 .9 1

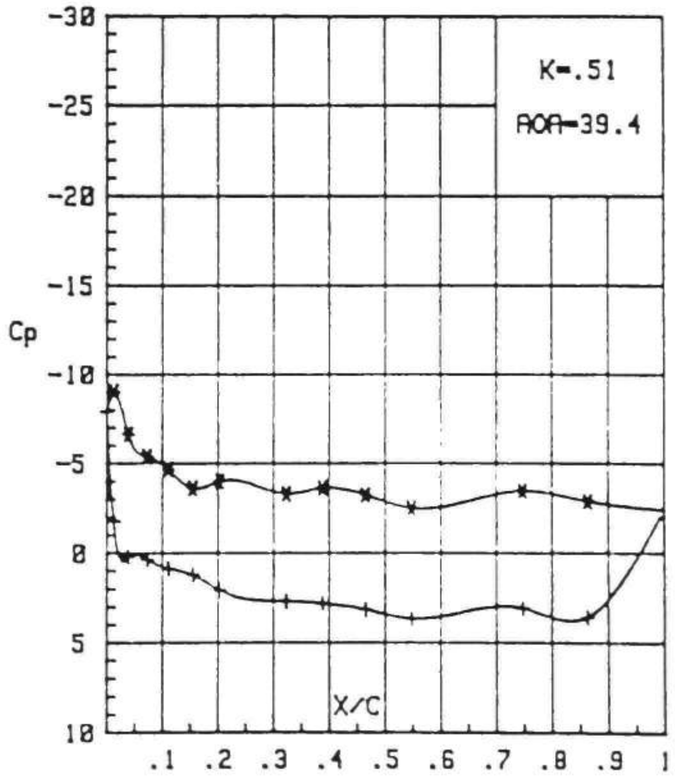
K=.51
AOA=39.4
Cp
X/C
-30
-25
-20
-15
-10
-5
0
5
10
.1 .2 .3 .4 .5 .6 .7 .8 .9 1

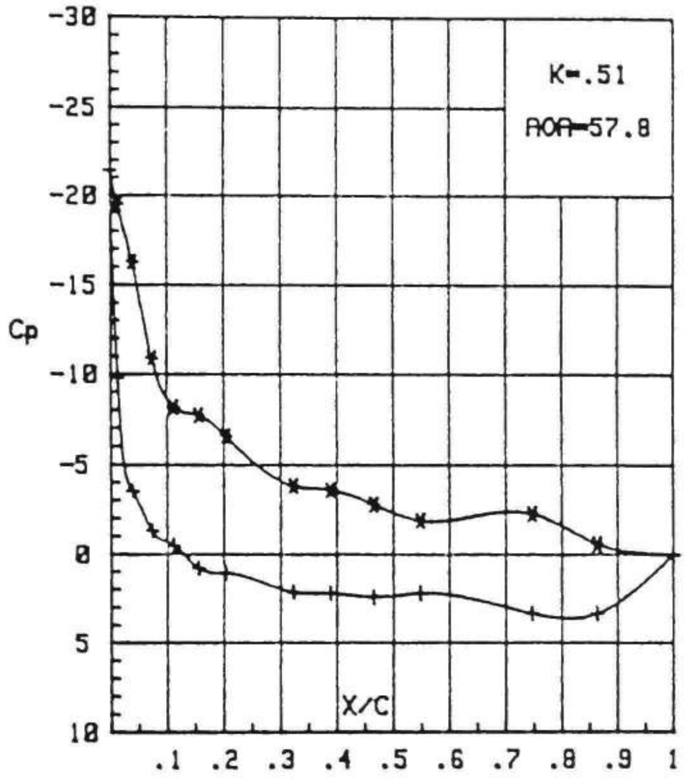
K=.51
AOA=57.8
Cp
X/C
-30
-25
-20
-15
-10
-5
0
5
10
.1
.2
.3
.4
.5
.6
.7
.8
.9
1

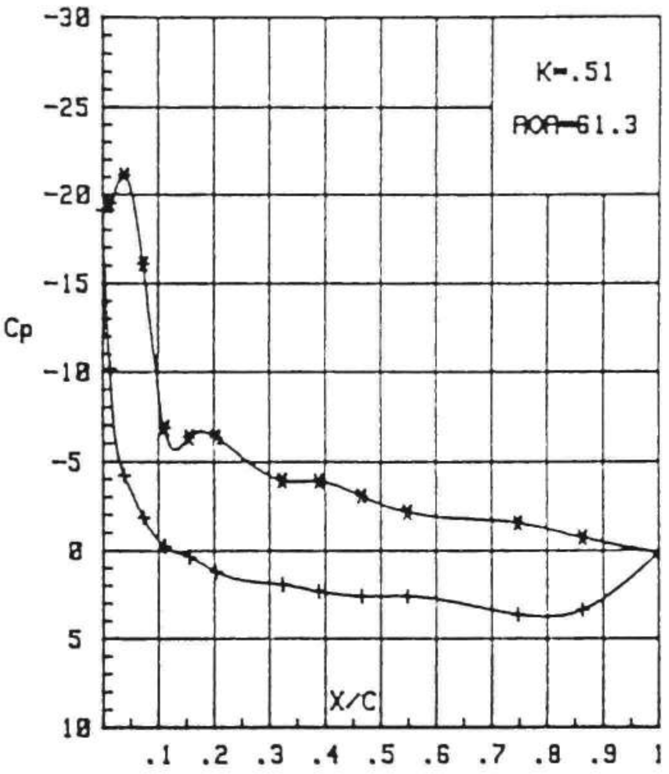
K=.51
AOA=61.3
Cp
X/C
-30
-25
-20
-15
-10
-5
0
5
10
.1
.2
.3
.4
.5
.6
.7
.8
.9
1

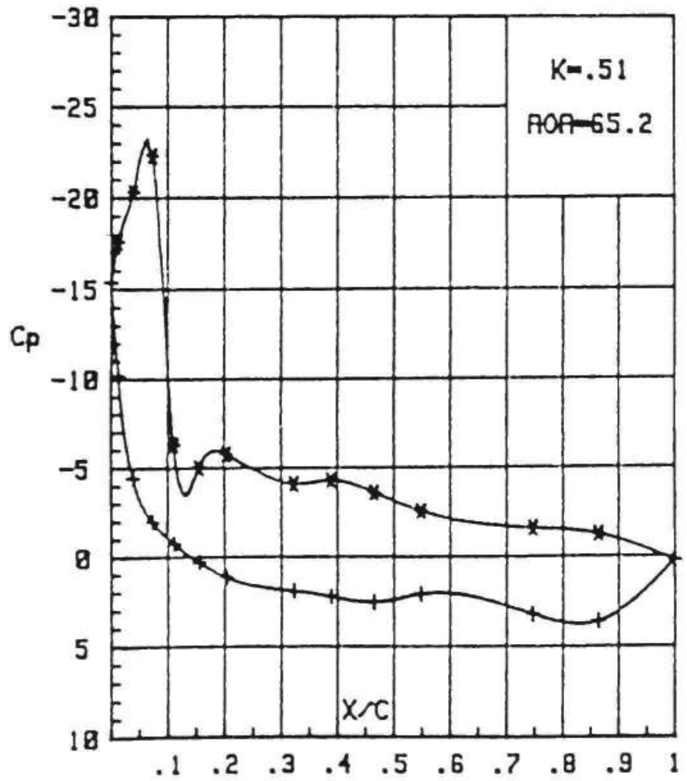
K=.51
AOA=65.2
Cp
X/C
-30
-25
-20
-15
-10
-5
0
5
10
.1
.2
.3
.4
.5
.6
.7
.8
.9
1

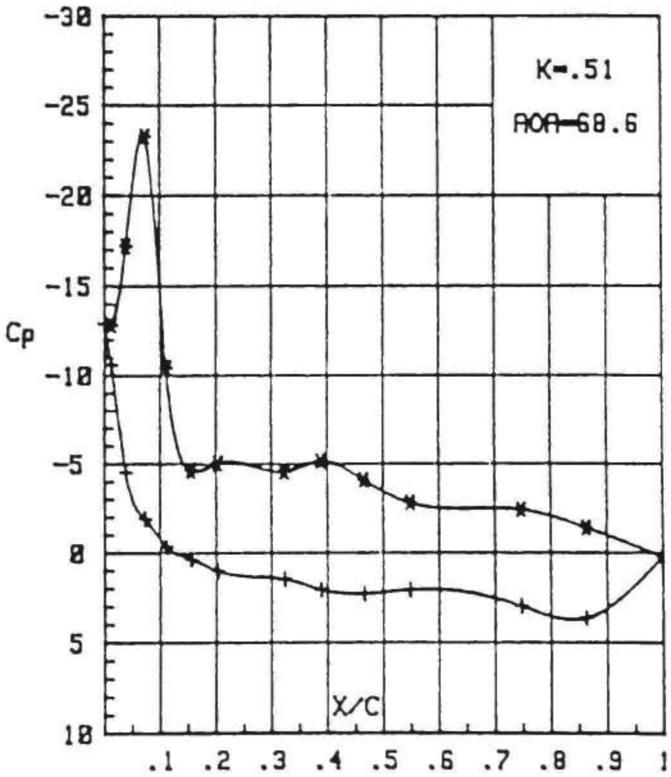
K=.51
AOA=68.6
Cp
X/C
-30
-25
-20
-15
-10
-5
0
5
10
.1
.2
.3
.4
.5
.6
.7
.8
.9
1

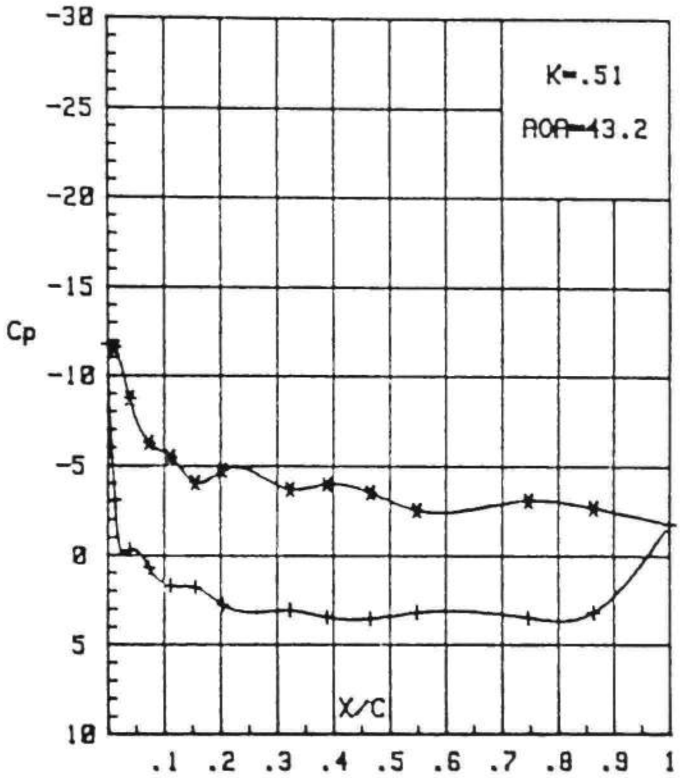
K=.51
AOA=43.2
Cp
X/C
-30
-25
-20
-15
-10
-5
0
5
10
.1
.2
.3
.4
.5
.6
.7
.8
.9
1

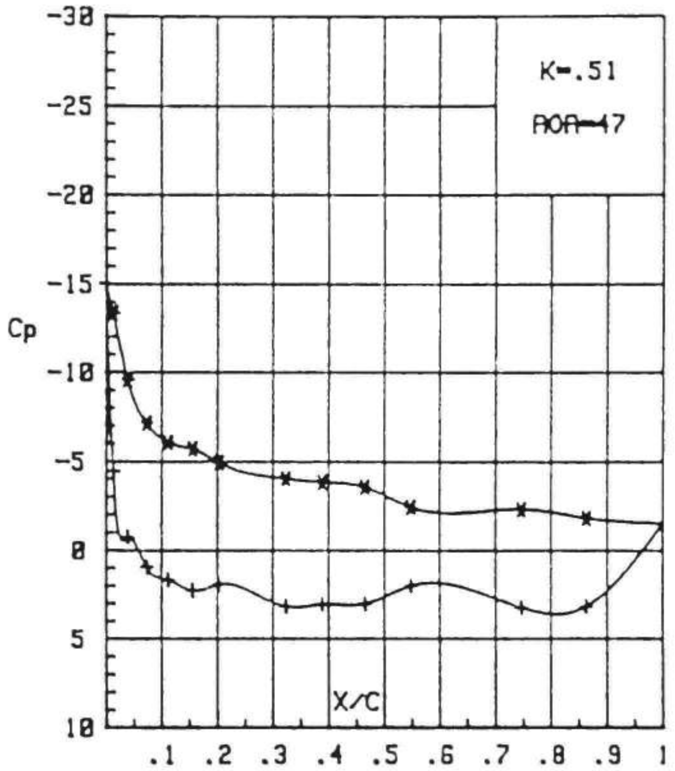
K=.51
AOA=47
Cp
X/C
-30
-25
-20
-15
-10
-5
0
5
10
.1
.2
.3
.4
.5
.6
.7
.8
.9
1

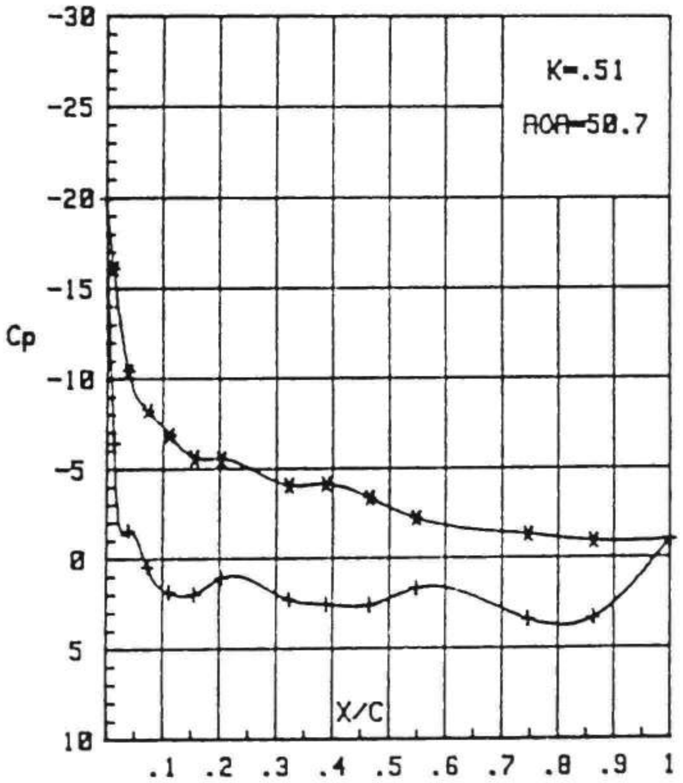
K=.51
AOA=50.7
Cp
X/C
-30
-25
-20
-15
-10
-5
0
5
10
.1
.2
.3
.4
.5
.6
.7
.8
.9
1

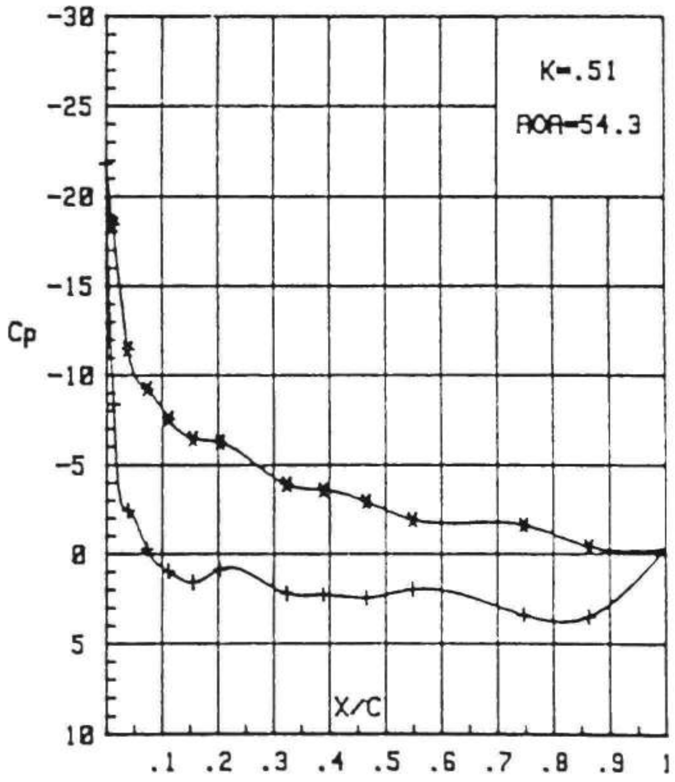
K=.51
AOA=54.3
Cp
X/C
-30
-25
-20
-15
-10
-5
0
5
10
.1
.2
.3
.4
.5
.6
.7
.8
.9
1

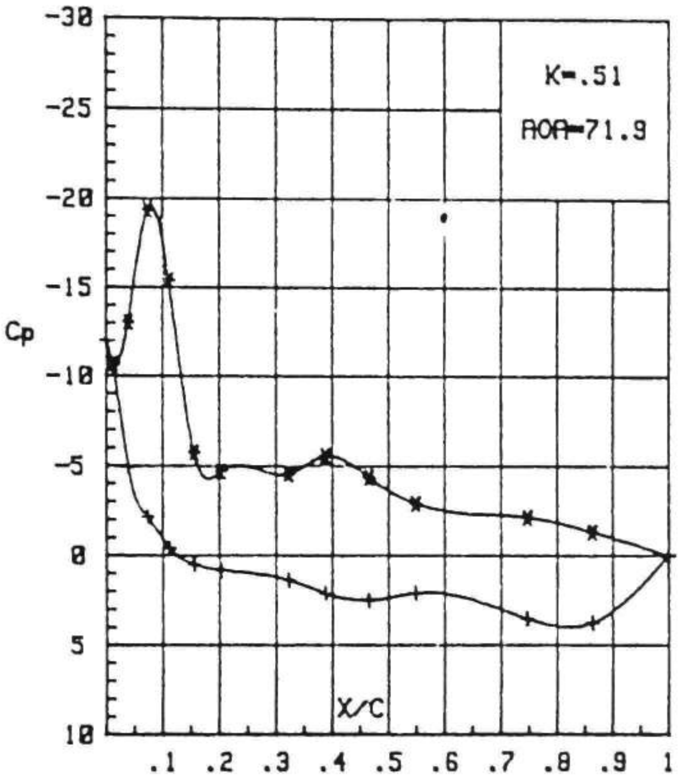
K=.51
AOA=71.9
Cp
X/C
-30
-25
-20
-15
-10
-5
0
5
10
.1
.2
.3
.4
.5
.6
.7
.8
.9
1

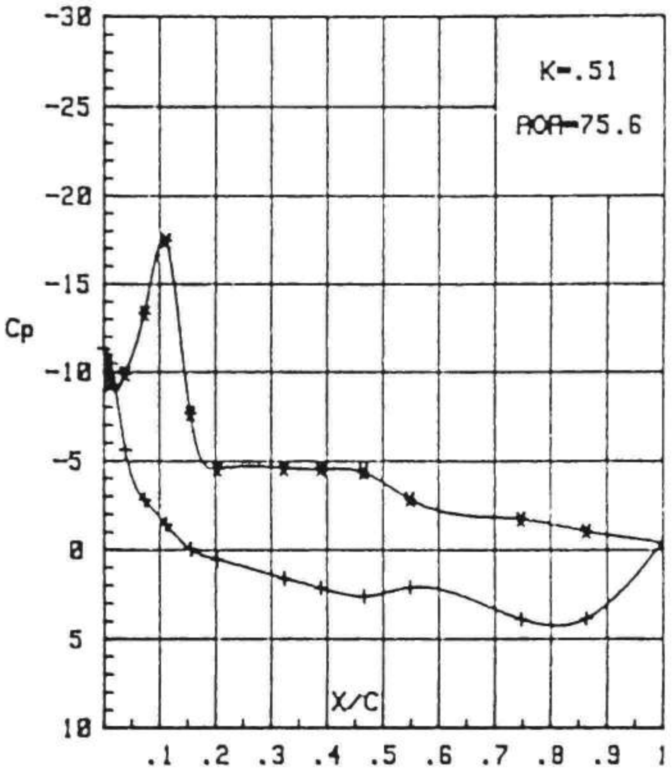
K=.51
AOA=75.6
Cp
X/C
-30
-25
-20
-15
-10
-5
0
5
10
.1
.2
.3
.4
.5
.6
.7
.8
.9
1

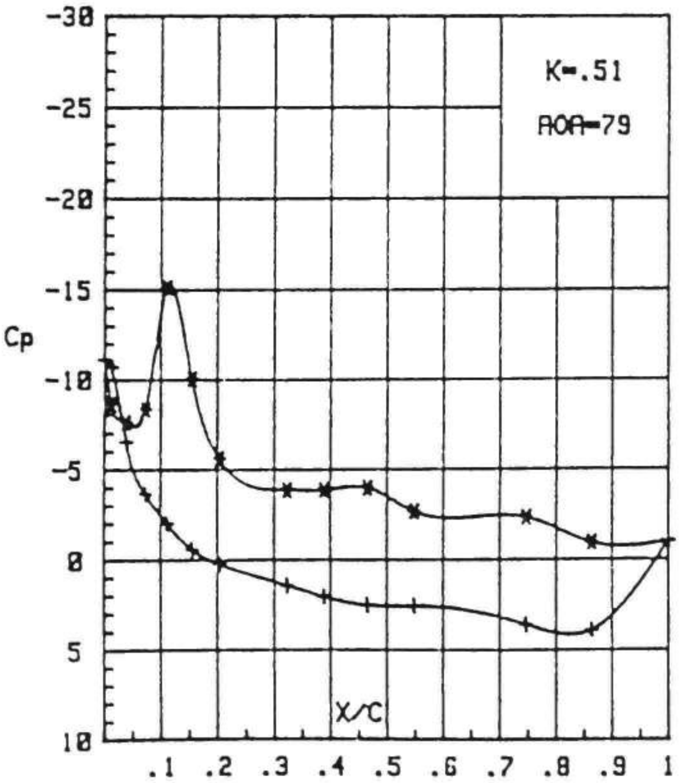
K=.51
AOA=79
Cp
X/C
-30
-25
-20
-15
-10
-5
0
5
10
.1
.2
.3
.4
.5
.6
.7
.8
.9
1

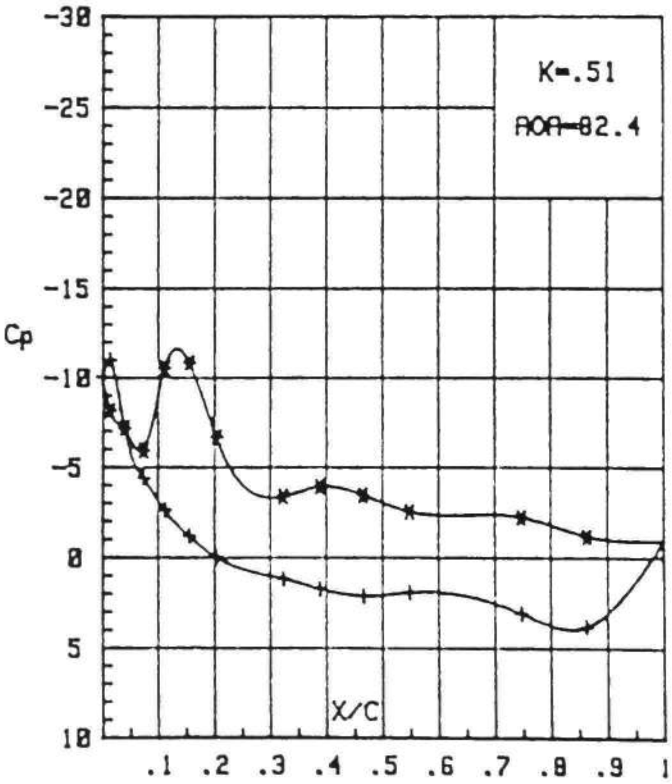
K=.51
AOA=82.4
Cp
X/C
-30
-25
-20
-15
-10
-5
0
5
10
.1
.2
.3
.4
.5
.6
.7
.8
.9
1

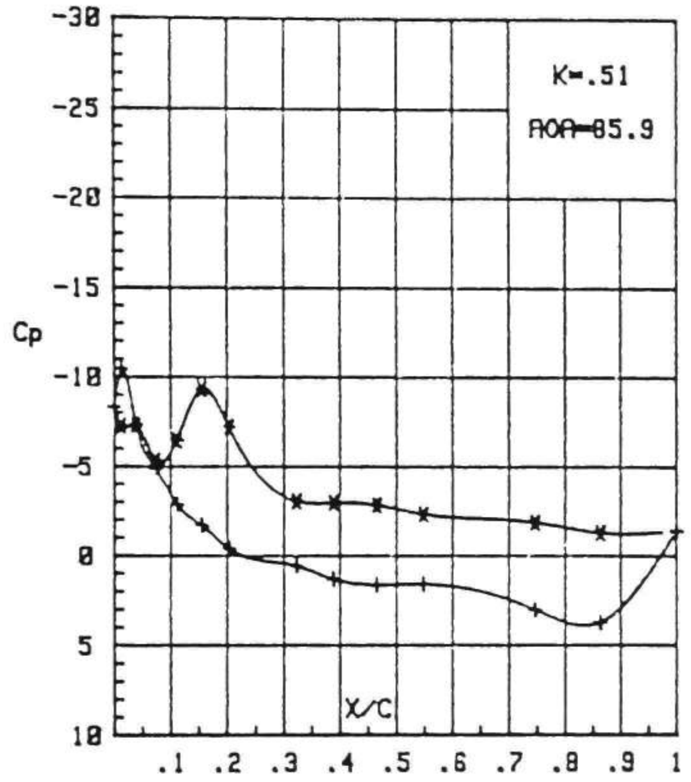
K=.51
AOA=85.9
Cp
-30
-25
-20
-15
-10
-5
0
5
10
X/C
.1
.2
.3
.4
.5
.6
.7
.8
.9
1

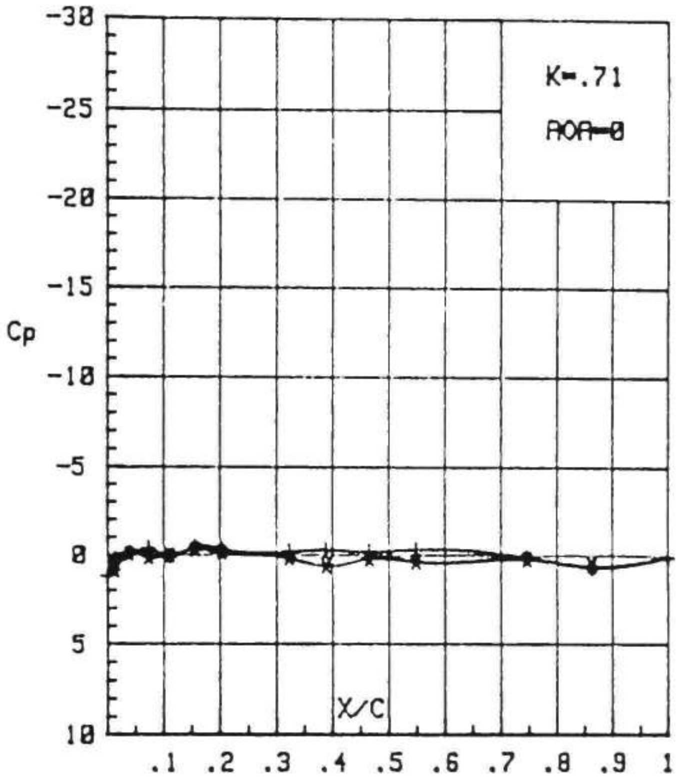
K=.71
AOA=0
Cp
-30
-25
-20
-15
-10
-5
0
5
10
X/C
.1
.2
.3
.4
.5
.6
.7
.8
.9
1

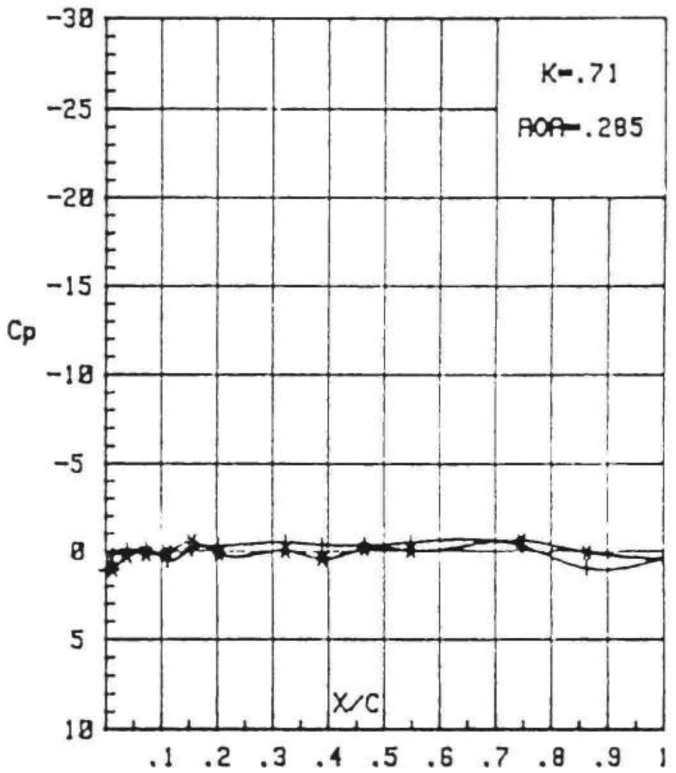
K=.71
AOA=.285
Cp
-30
-25
-20
-15
-10
-5
0
5
10
X/C
.1
.2
.3
.4
.5
.6
.7
.8
.9
1

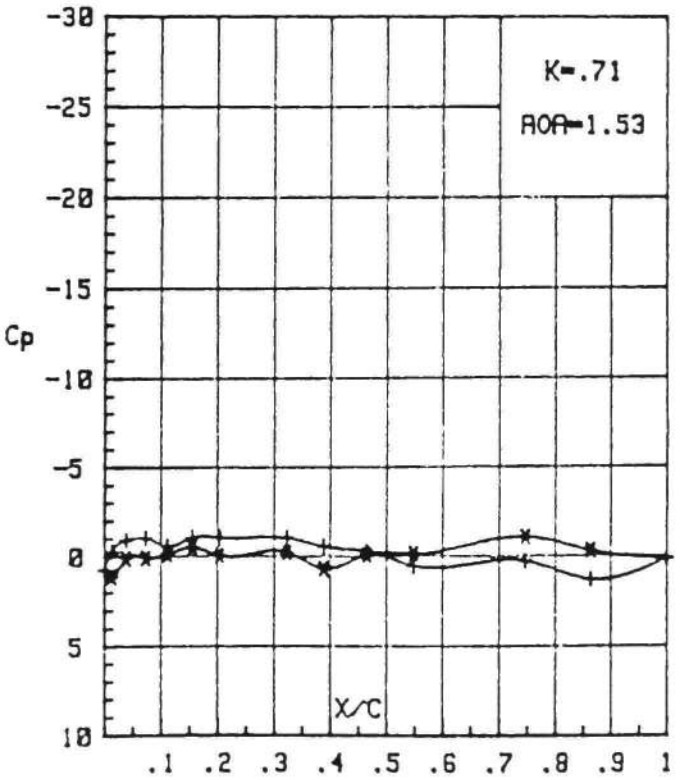
K=.71
AOA=1.53
Cp
-30
-25
-20
-15
-10
-5
0
5
10
X/C
.1
.2
.3
.4
.5
.6
.7
.8
.9
1

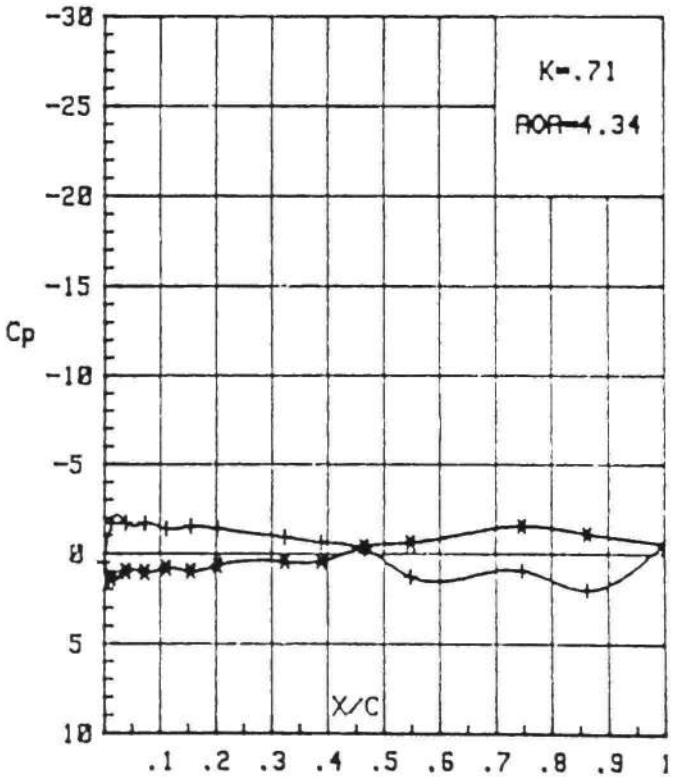
K=.71
AOA=4.34
Cp
-30
-25
-20
-15
-10
-5
0
5
10
X/C
.1
.2
.3
.4
.5
.6
.7
.8
.9
1

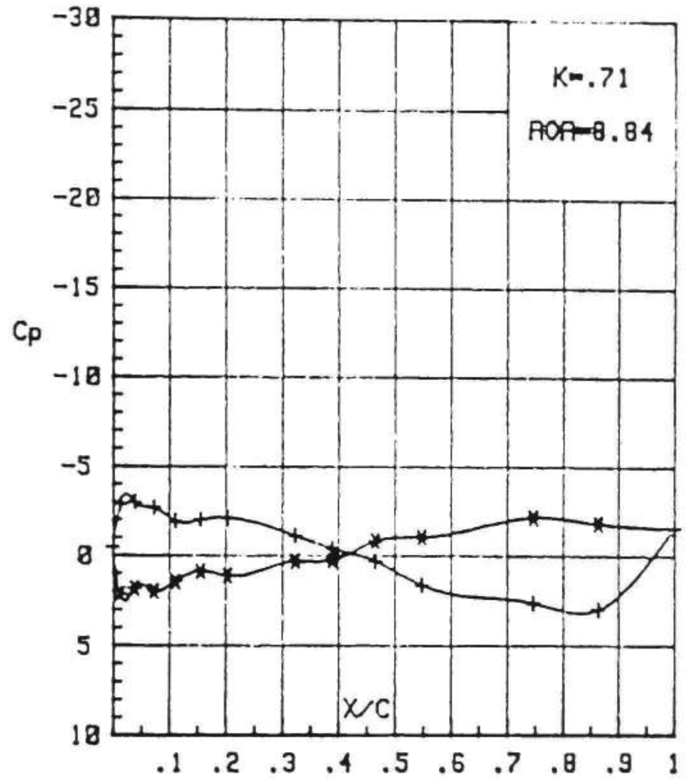
K=.71
AOA=8.84
Cp
-30
-25
-20
-15
-10
-5
0
5
10
X/C
.1
.2
.3
.4
.5
.6
.7
.8
.9
1

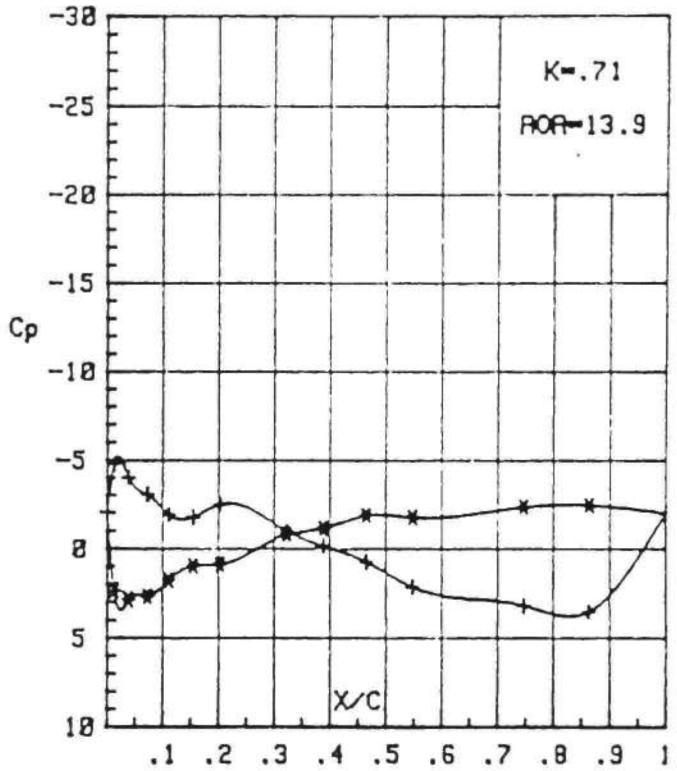
K=.71
AOA=13.9
Cp
-30
-25
-20
-15
-10
-5
0
5
10
X/C
.1
.2
.3
.4
.5
.6
.7
.8
.9
1

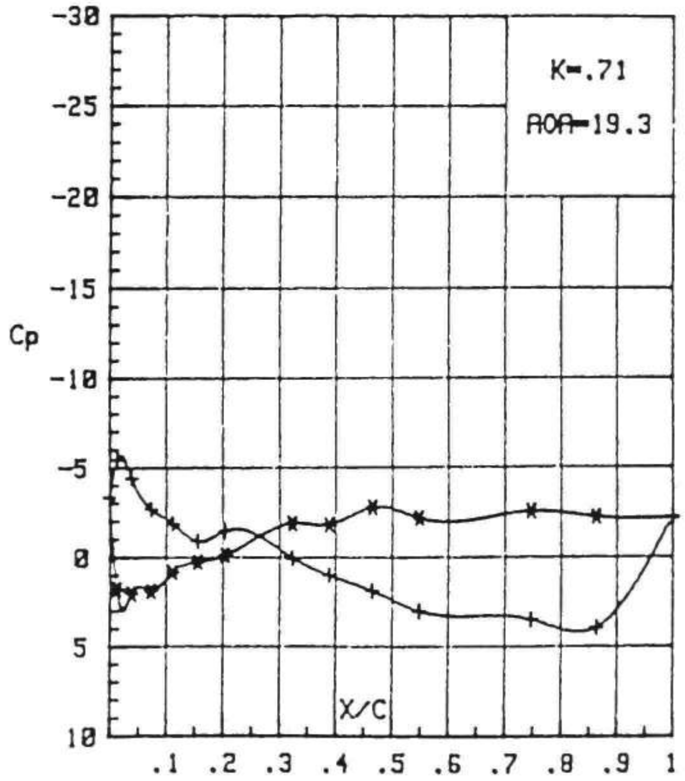
K=.71
AOA=19.3
Cp
-30
-25
-20
-15
-10
-5
0
5
10
X/C
.1
.2
.3
.4
.5
.6
.7
.8
.9
1

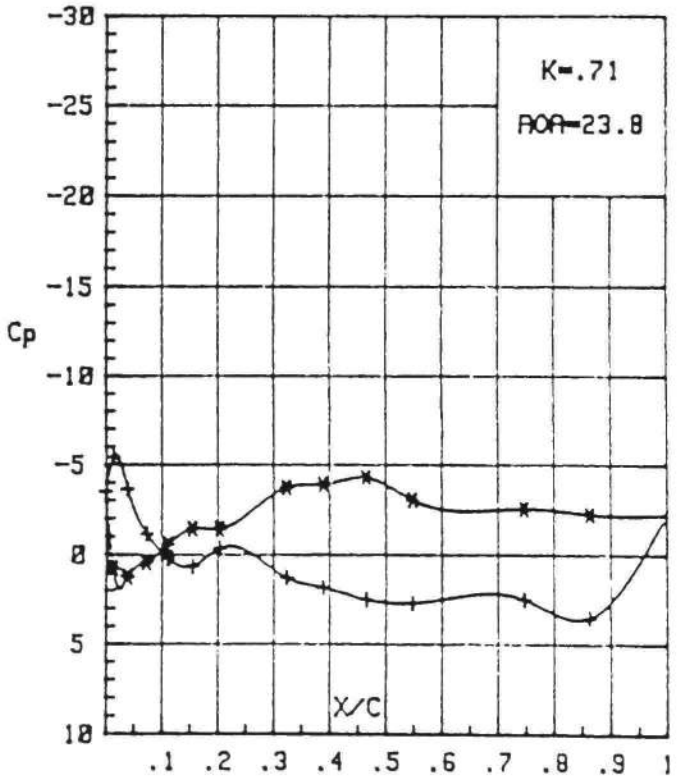
K=.71
AOA=23.8
Cp
-30
-25
-20
-15
-10
-5
0
5
10
X/C
.1
.2
.3
.4
.5
.6
.7
.8
.9
1

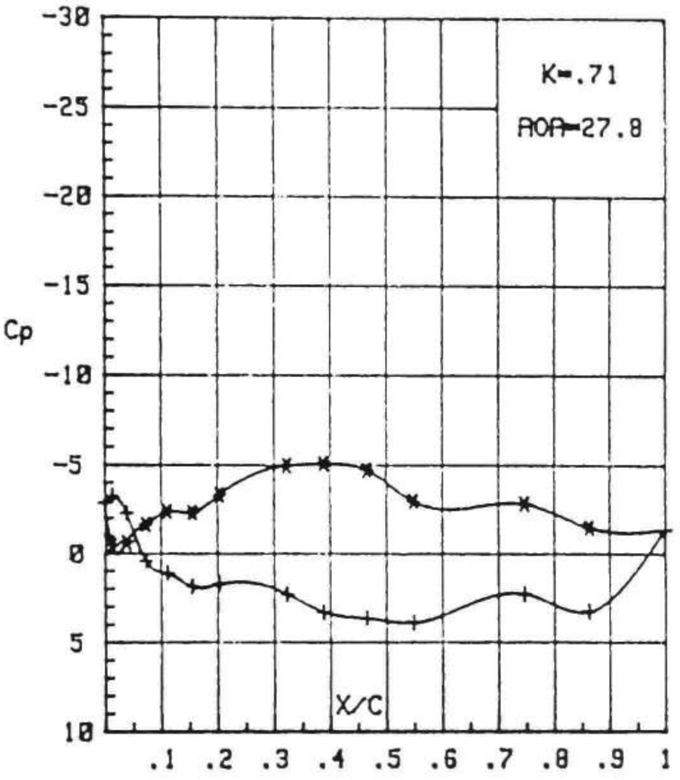
K=.71
AOA=27.8
Cp
-30
-25
-20
-15
-10
-5
0
5
10
X/C
.1
.2
.3
.4
.5
.6
.7
.8
.9
1

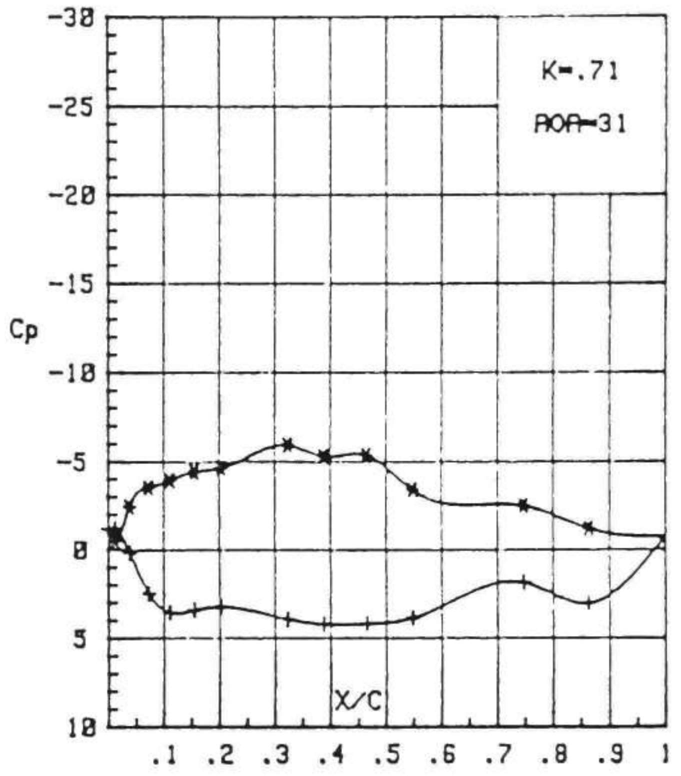
K=.71
AOA=31
Cp
-30
-25
-20
-15
-10
-5
0
5
10
X/C
.1
.2
.3
.4
.5
.6
.7
.8
.9
1

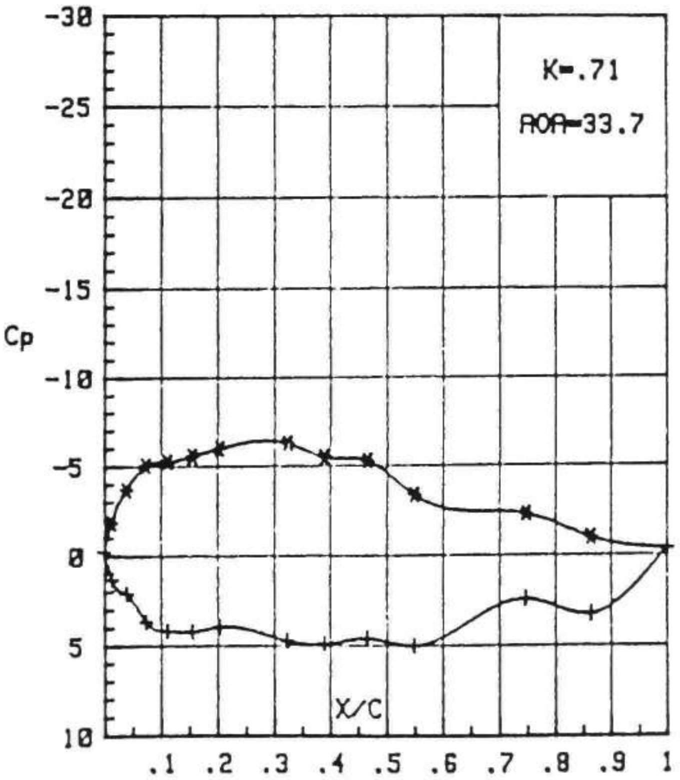
K=.71
AOA=33.7
Cp
-30
-25
-20
-15
-10
-5
0
5
10
X/C
.1
.2
.3
.4
.5
.6
.7
.8
.9
1

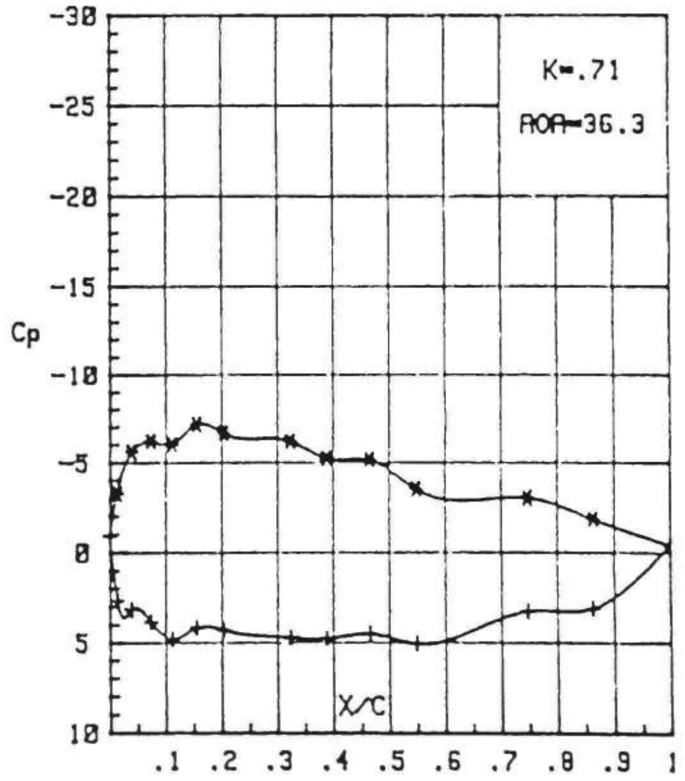
K=.71
AOA=36.3
Cp
-30
-25
-20
-15
-10
-5
0
5
10
X/C
.1
.2
.3
.4
.5
.6
.7
.8
.9
1

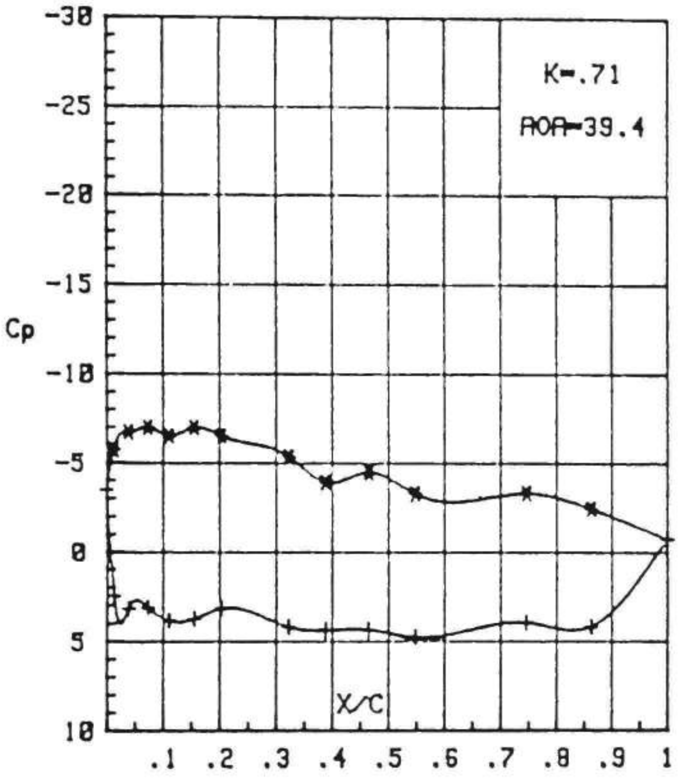
K=.71
AOA=39.4
Cp
-30
-25
-20
-15
-10
-5
0
5
10
X/C
.1
.2
.3
.4
.5
.6
.7
.8
.9
1

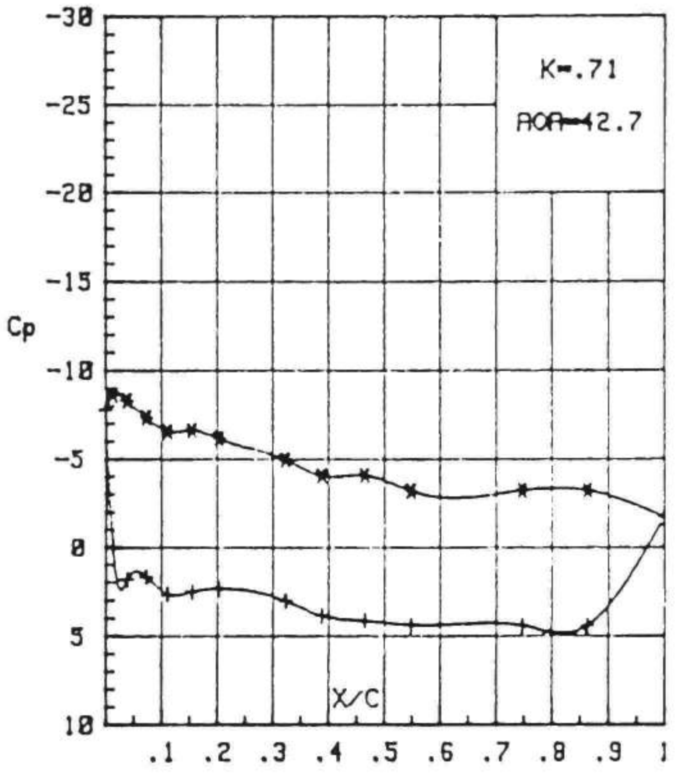
K=.71
AOA=42.7
Cp
-30
-25
-20
-15
-10
-5
0
5
10
X/C
.1
.2
.3
.4
.5
.6
.7
.8
.9
1

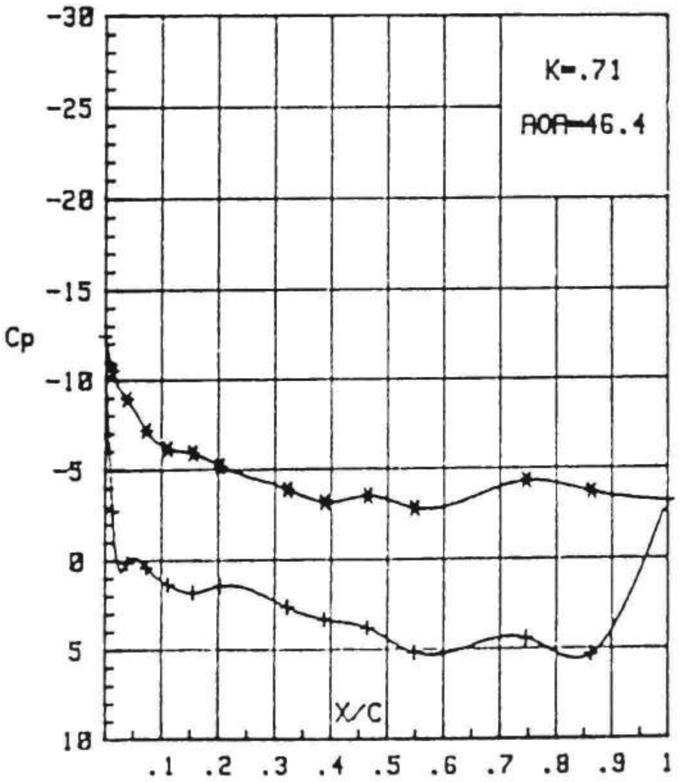
K=.71
AOA=46.4
Cp
-30
-25
-20
-15
-10
-5
0
5
10
X/C
.1
.2
.3
.4
.5
.6
.7
.8
.9
1

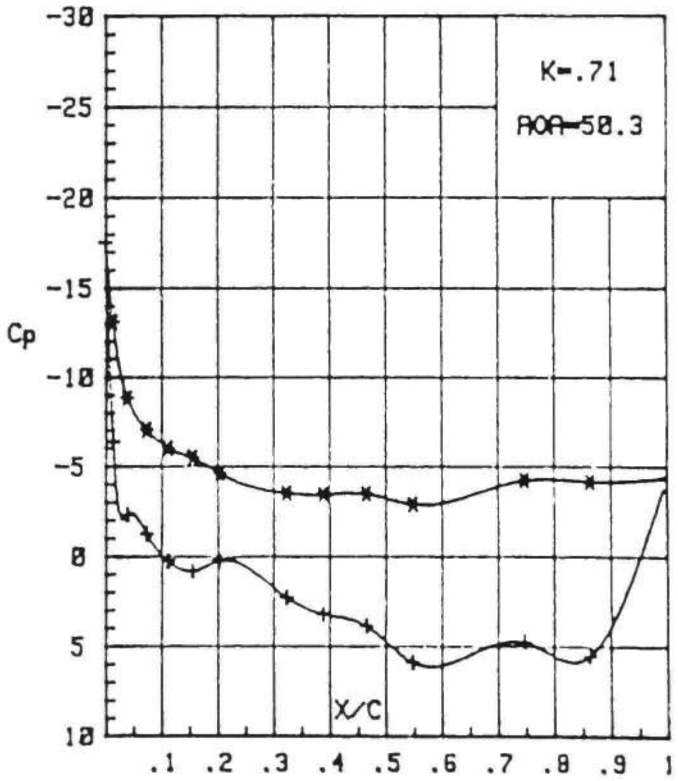
K=.71
AOA=50.3
Cp
-30
-25
-20
-15
-10
-5
0
5
10
X/C
.1
.2
.3
.4
.5
.6
.7
.8
.9
1

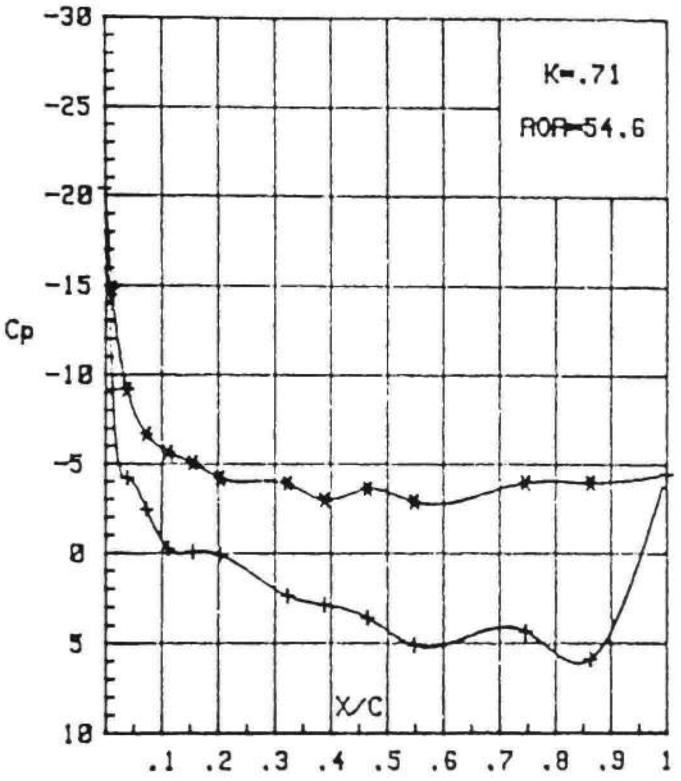
K=.71
AOA=54.6
Cp
-30
-25
-20
-15
-10
-5
0
5
10
X/C
.1
.2
.3
.4
.5
.6
.7
.8
.9
1

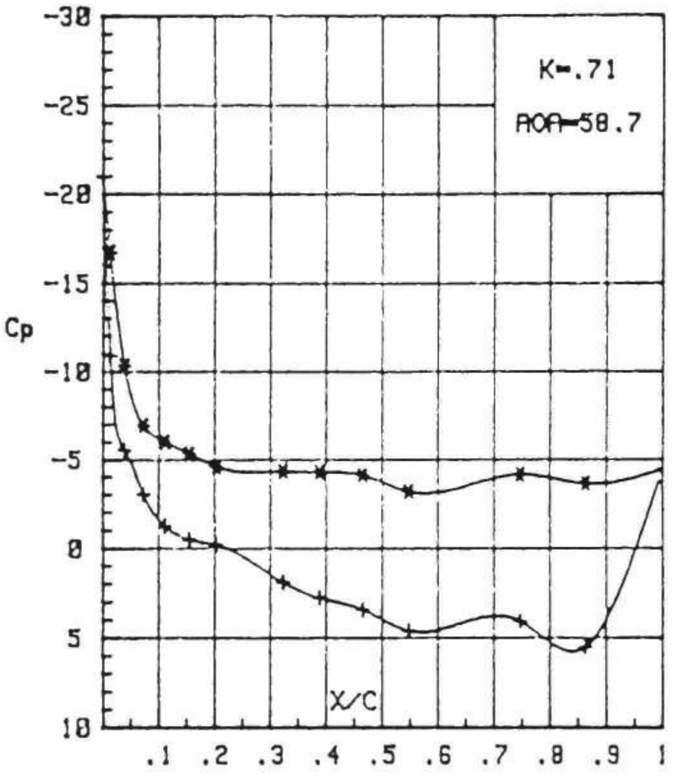
K=.71
AOA=58.7
Cp
-30
-25
-20
-15
-10
-5
0
5
10
X/C
.1
.2
.3
.4
.5
.6
.7
.8
.9
1

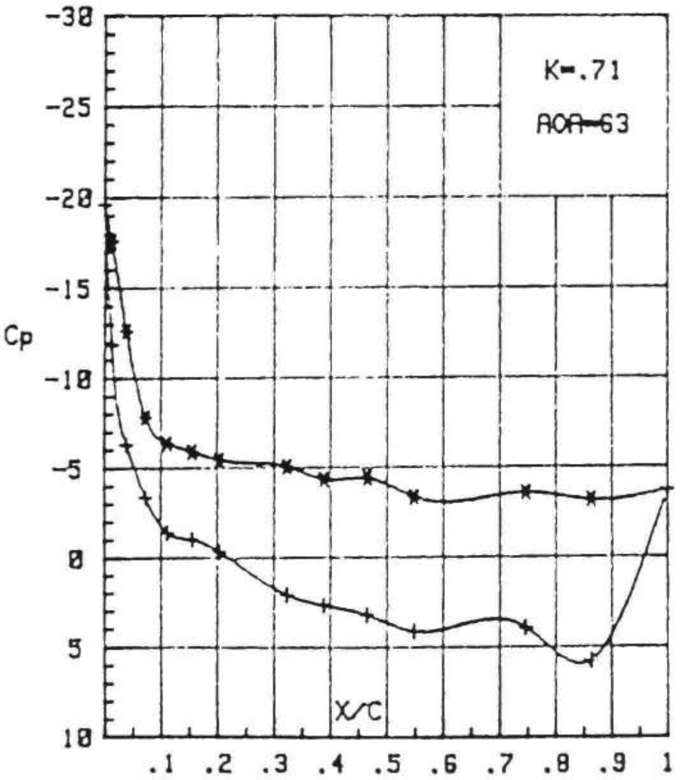
K=.71
AOA=63
Cp
-30
-25
-20
-15
-10
-5
0
5
10
X/C
.1
.2
.3
.4
.5
.6
.7
.8
.9
1

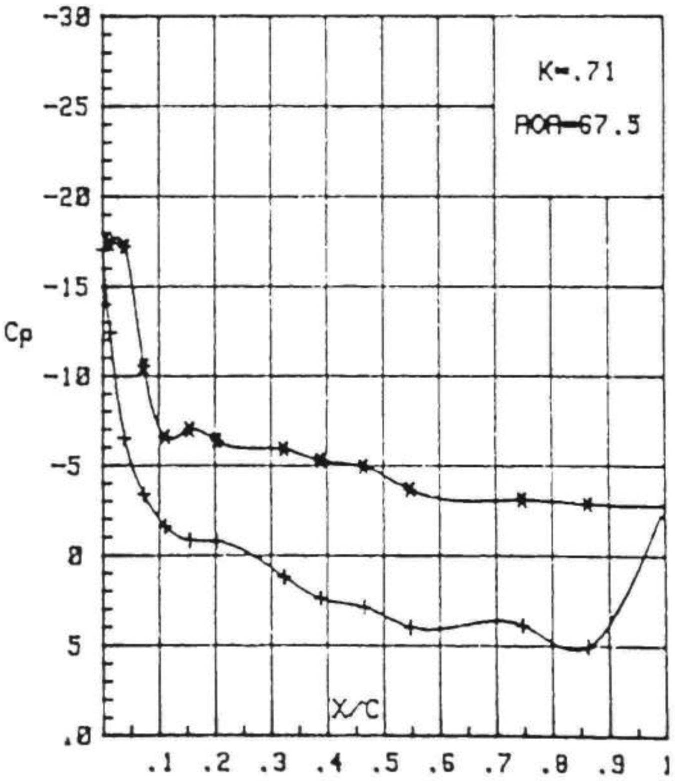
K=.71
AOA=67.5
Cp
-30
-25
-20
-15
-10
-5
0
5
.0
X/C
.1
.2
.3
.4
.5
.6
.7
.8
.9
1

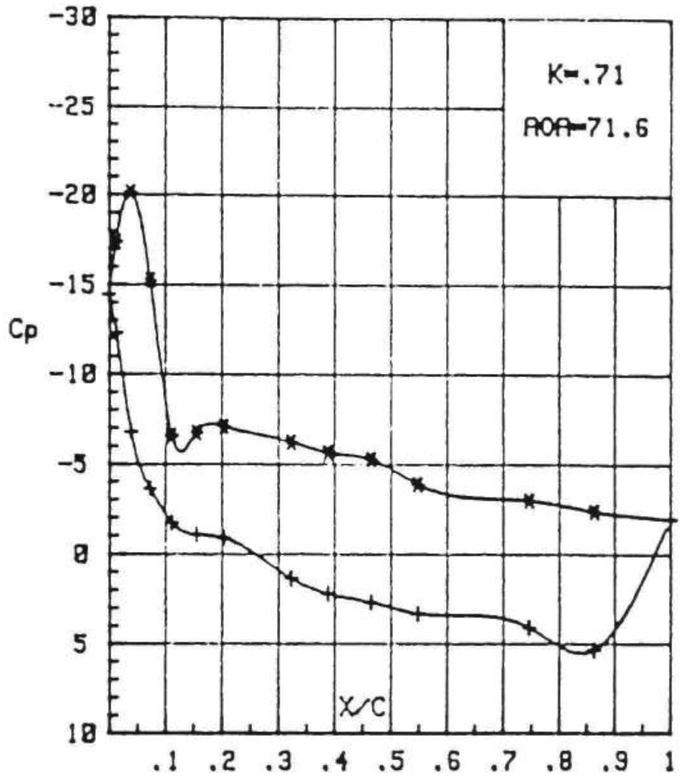
K=.71
AOA=71.6
Cp
X/C
-30
-25
-20
-15
-10
-5
0
5
10
.1
.2
.3
.4
.5
.6
.7
.8
.9
1

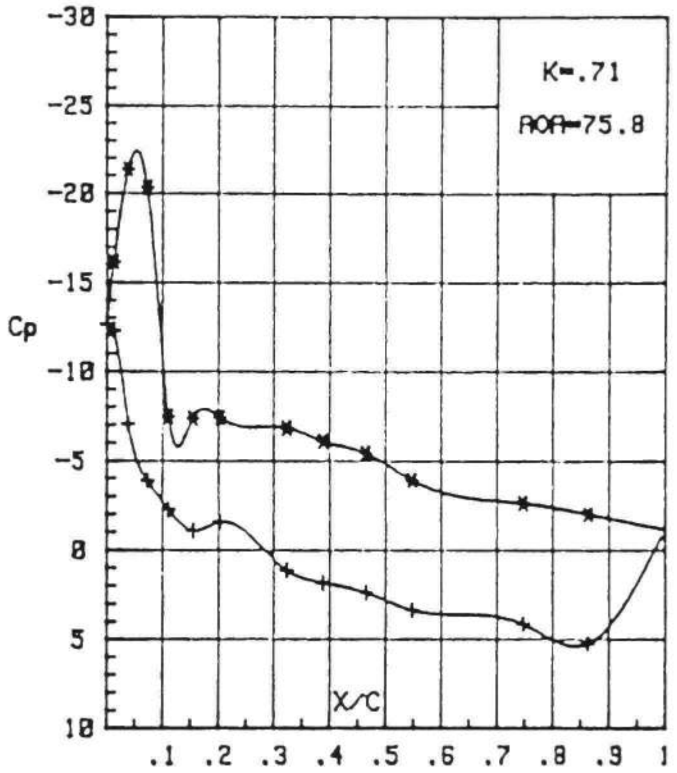
K=.71
AOA=75.8
Cp
X/C
-30
-25
-20
-15
-10
-5
0
5
10
.1
.2
.3
.4
.5
.6
.7
.8
.9
1

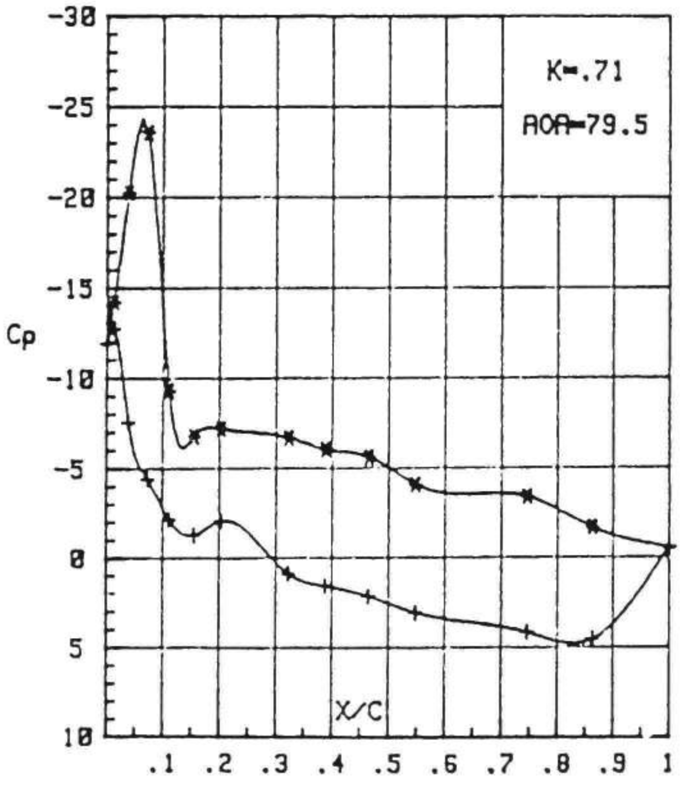
K=.71
AOA=79.5
Cp
X/C
-30
-25
-20
-15
-10
-5
0
5
10
.1
.2
.3
.4
.5
.6
.7
.8
.9
1

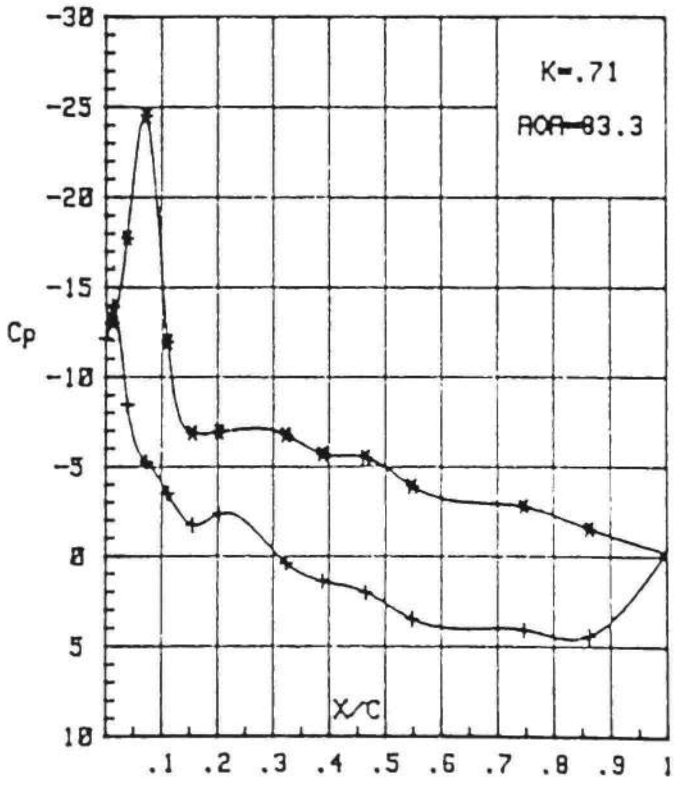
K=.71
AOA=83.3
Cp
X/C
-30
-25
-20
-15
-10
-5
0
5
10
.1
.2
.3
.4
.5
.6
.7
.8
.9
1

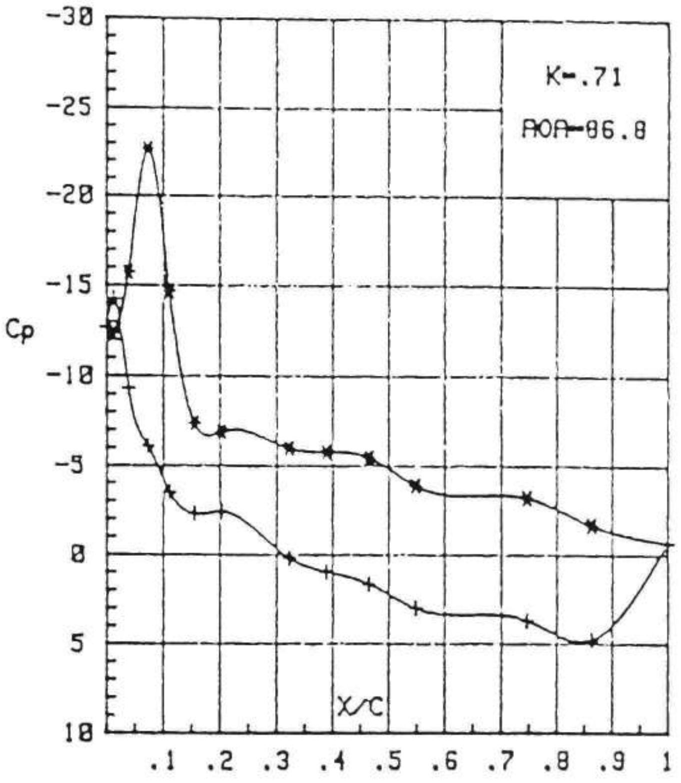
K=.71
AOA=06.8
Cp
-30
-25
-20
-15
-10
-5
0
5
10
X/C
.1
.2
.3
.4
.5
.6
.7
.8
.9
1

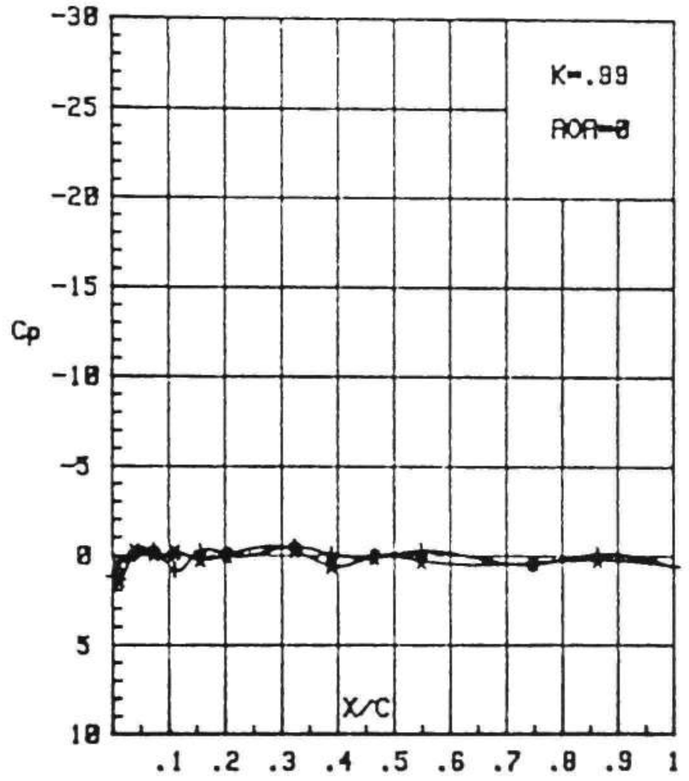
K=.99
AOA=0
Cp
X/C
-30
-25
-20
-15
-10
-5
0
5
10
.1
.2
.3
.4
.5
.6
.7
.8
.9
1

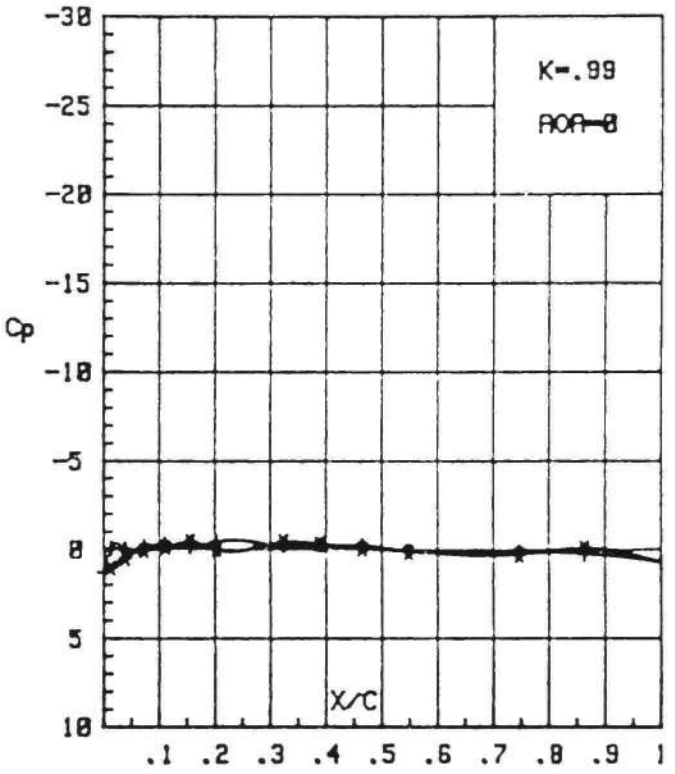
K=.99
AOA=0
Cp
X/C
-30
-25
-20
-15
-10
-5
0
5
10
.1
.2
.3
.4
.5
.6
.7
.8
.9
1

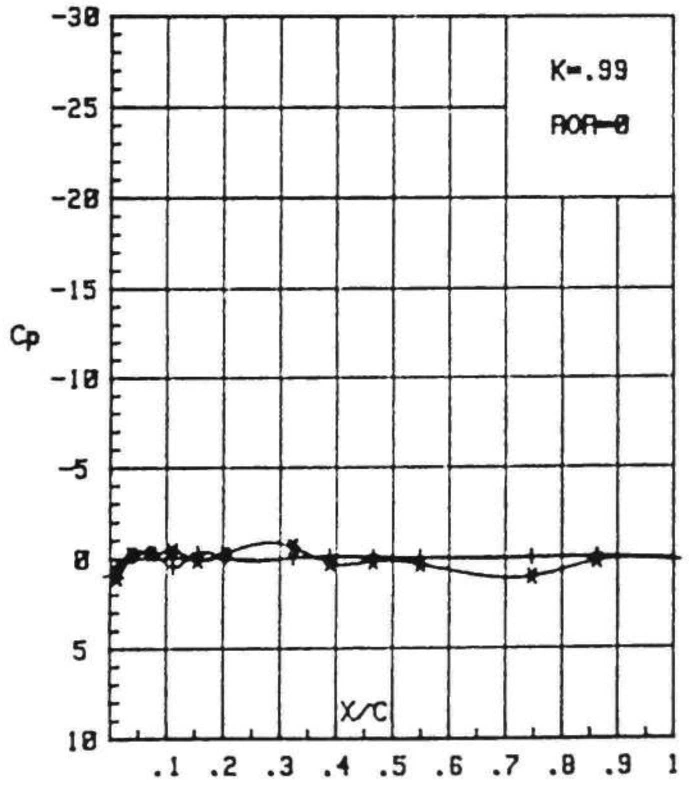
K=.99
AOA=0
Cp
X/C
-30
-25
-20
-15
-10
-5
0
5
10
.1
.2
.3
.4
.5
.6
.7
.8
.9
1

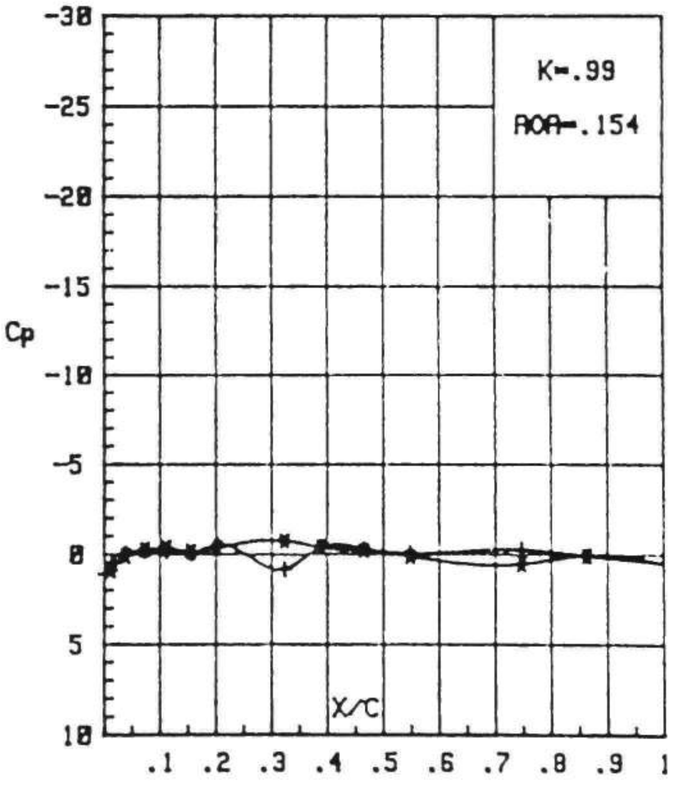
K=.99
AOA=.154
Cp
X/C
-30
-25
-20
-15
-10
-5
0
5
10
.1
.2
.3
.4
.5
.6
.7
.8
.9
1

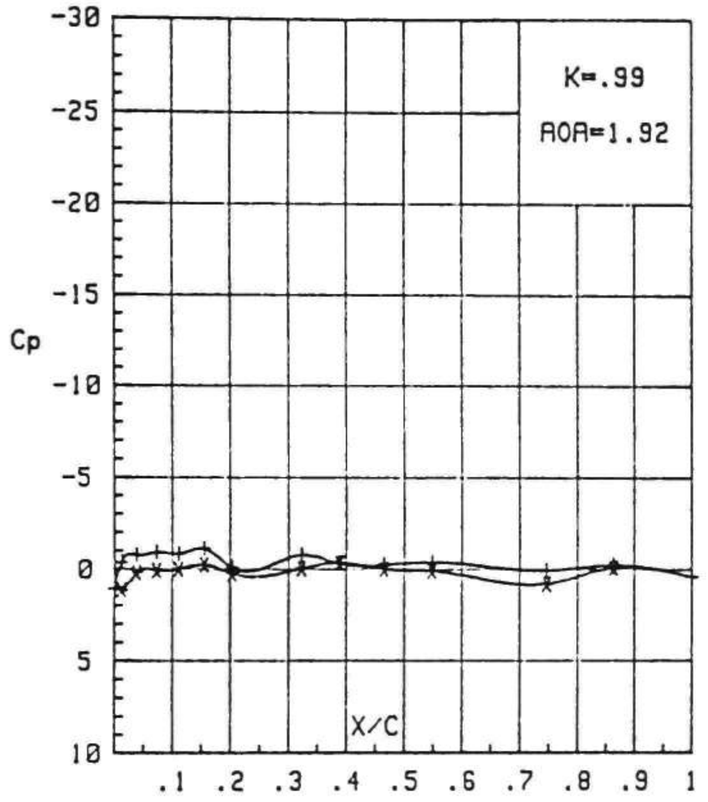
K=.99
AOA=1.92
Cp
-30
-25
-20
-15
-10
-5
0
5
10
X/C
.1
.2
.3
.4
.5
.6
.7
.8
.9
1

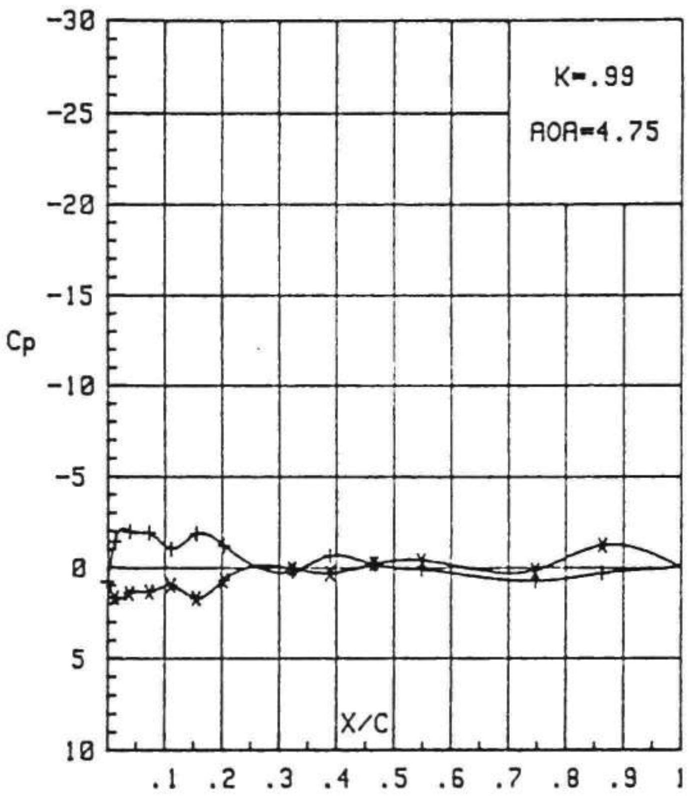
K=.99
AOA=4.75
Cp
-30
-25
-20
-15
-10
-5
0
5
10
X/C
.1
.2
.3
.4
.5
.6
.7
.8
.9
1

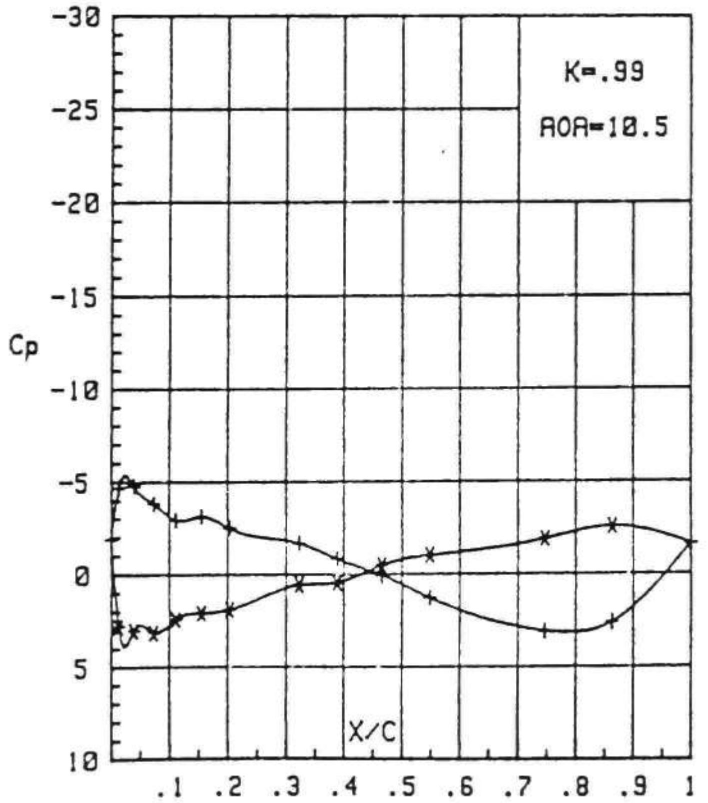
K=.99
AOA=10.5
Cp
-30
-25
-20
-15
-10
-5
0
5
10
X/C
.1
.2
.3
.4
.5
.6
.7
.8
.9
1

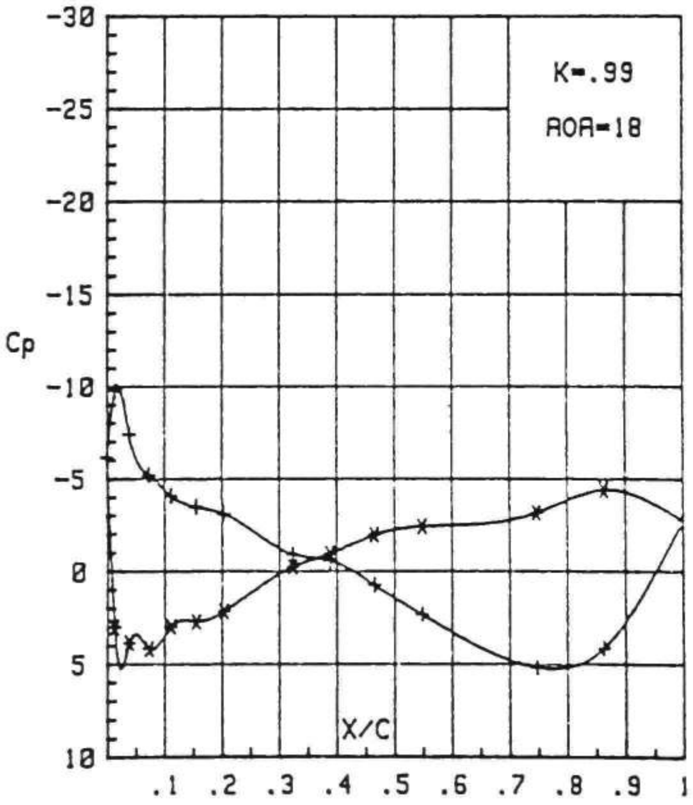
K=.99
AOA=18
Cp
-30
-25
-20
-15
-10
-5
0
5
10
X/C
.1
.2
.3
.4
.5
.6
.7
.8
.9
1

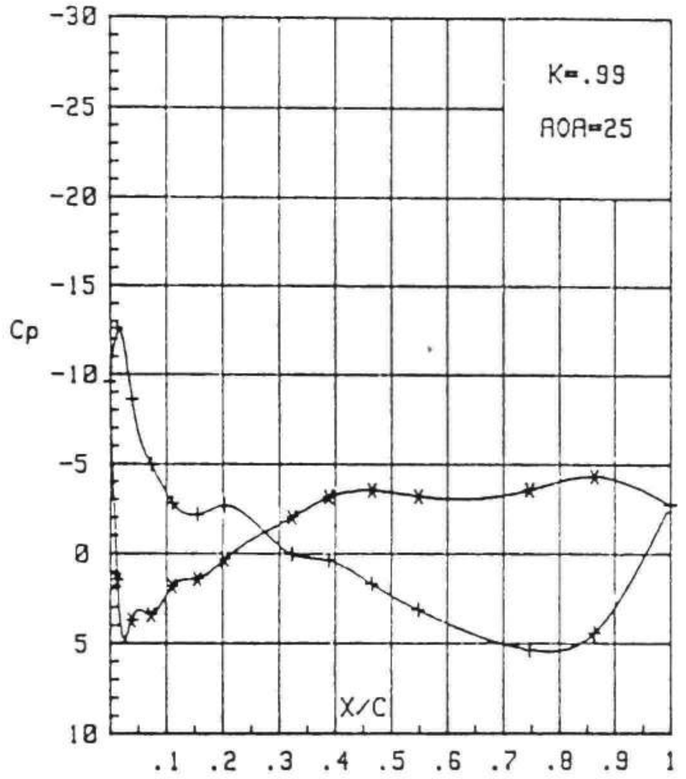
K=.99
AOA=25
Cp
-30
-25
-20
-15
-10
-5
0
5
10
X/C
.1
.2
.3
.4
.5
.6
.7
.8
.9
1

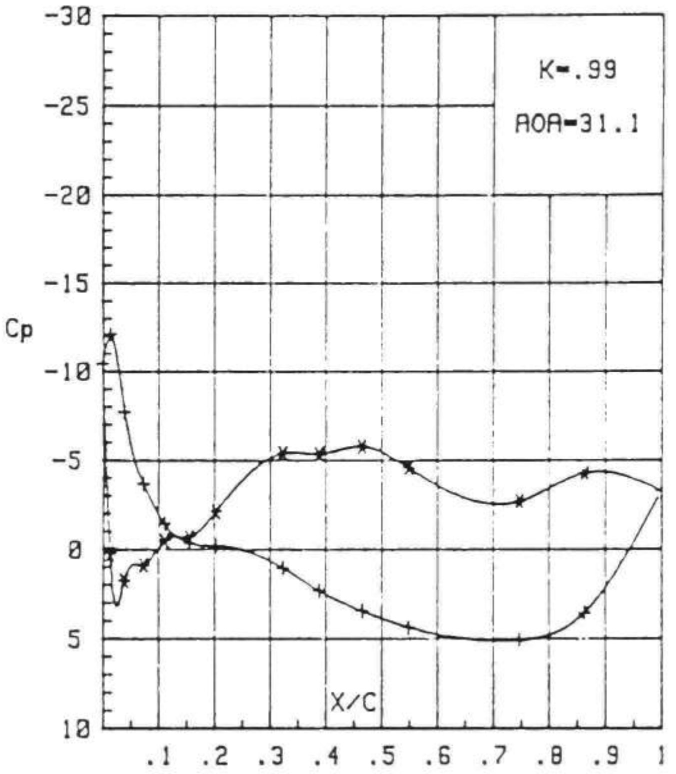
K=.99
AOA=31.1
Cp
-30
-25
-20
-15
-10
-5
0
5
10
X/C
.1
.2
.3
.4
.5
.6
.7
.8
.9
1

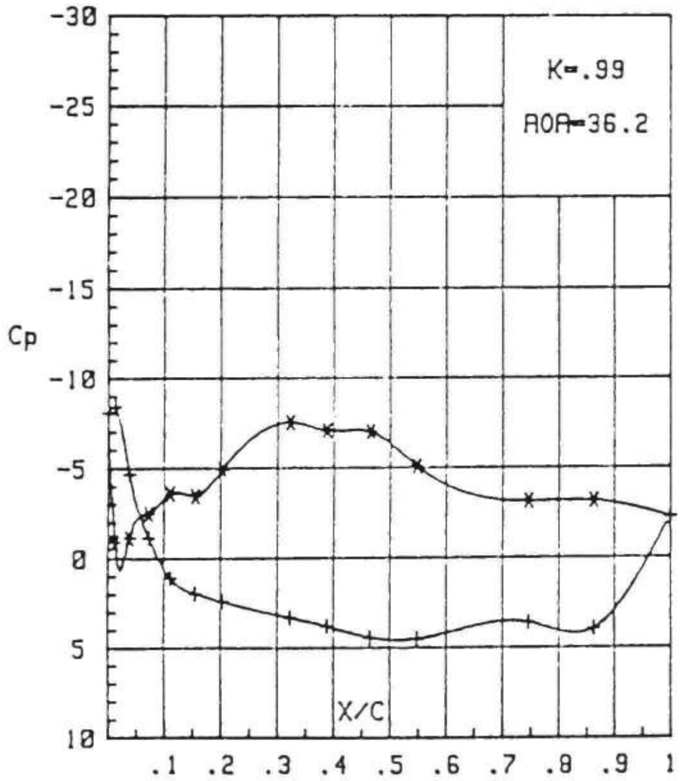
K=.99
AOA=36.2
Cp
-30
-25
-20
-15
-10
-5
0
5
10
X/C
.1
.2
.3
.4
.5
.6
.7
.8
.9
1

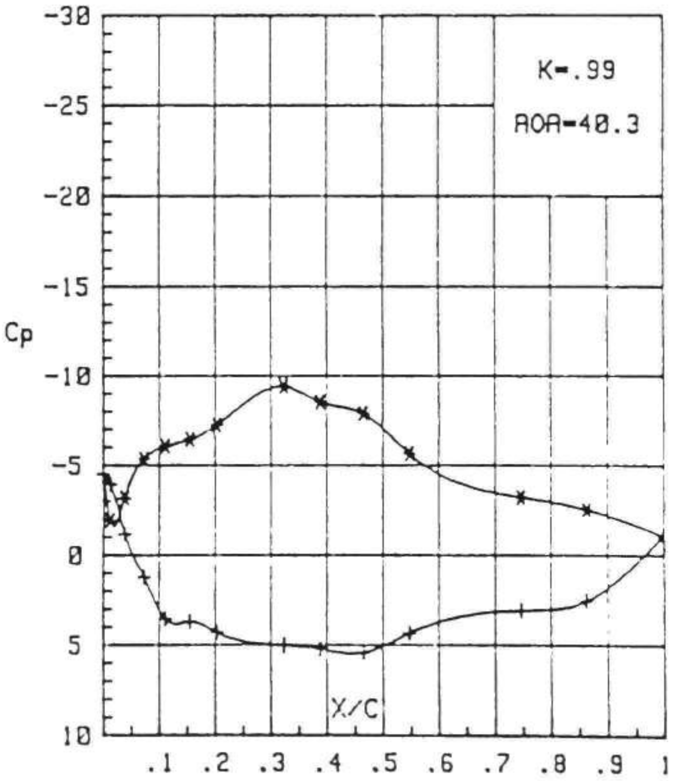
K=.99
AOA=40.3
Cp
-30
-25
-20
-15
-10
-5
0
5
10
X/C
.1
.2
.3
.4
.5
.6
.7
.8
.9
1

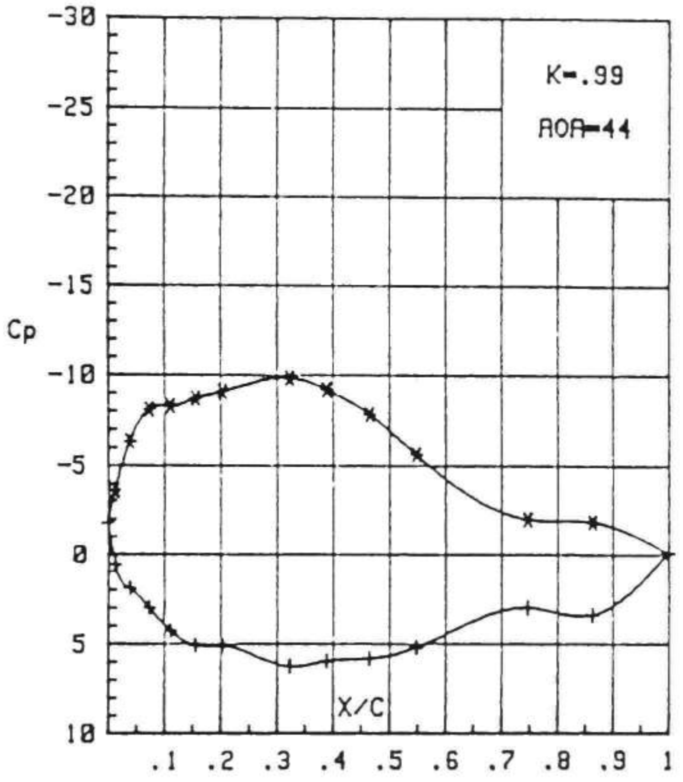
K=.99
AOA=44
Cp
-30
-25
-20
-15
-10
-5
0
5
10
X/C
.1
.2
.3
.4
.5
.6
.7
.8
.9
1

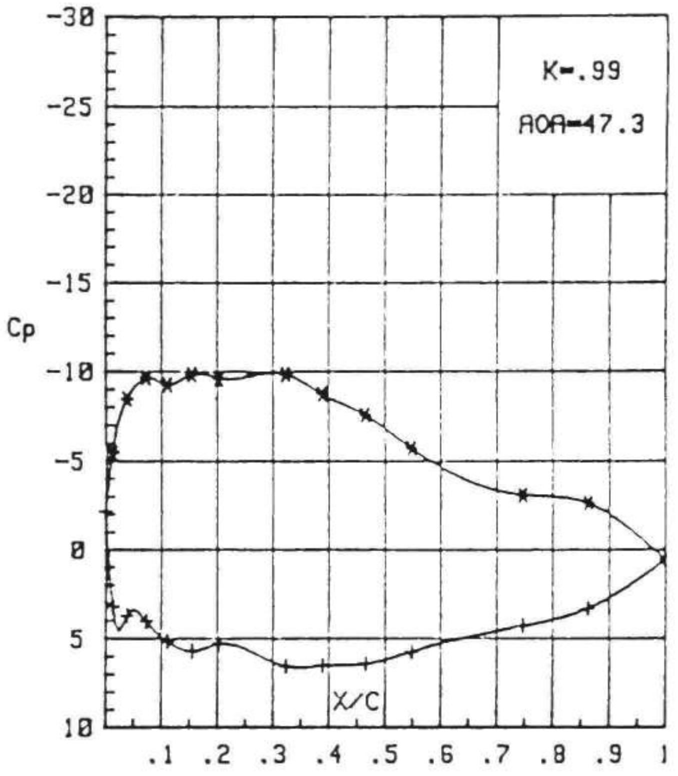
K=.99
AOA=47.3
Cp
-30
-25
-20
-15
-10
-5
0
5
10
X/C
.1
.2
.3
.4
.5
.6
.7
.8
.9
1

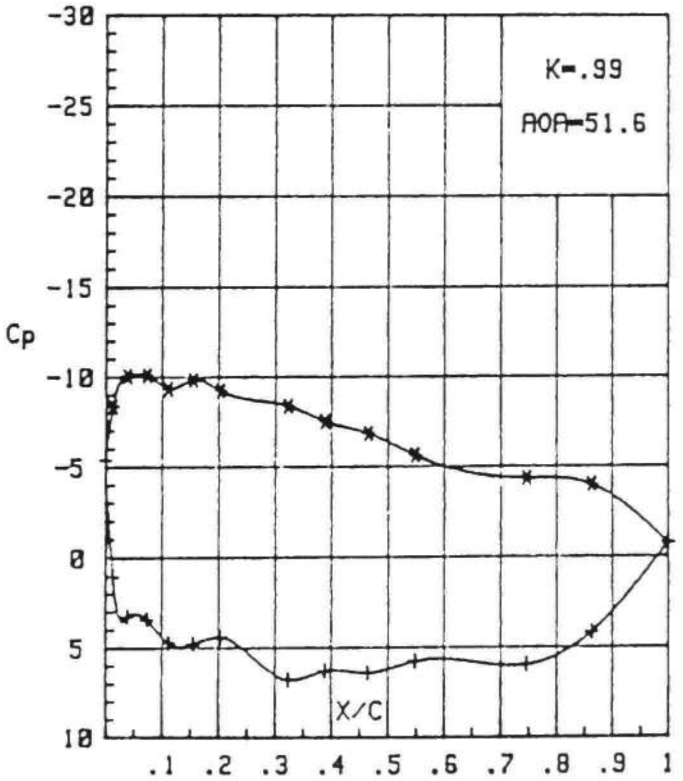
K=.99
AOA=51.6
Cp
-30
-25
-20
-15
-10
-5
0
5
10
X/C
.1
.2
.3
.4
.5
.6
.7
.8
.9
1

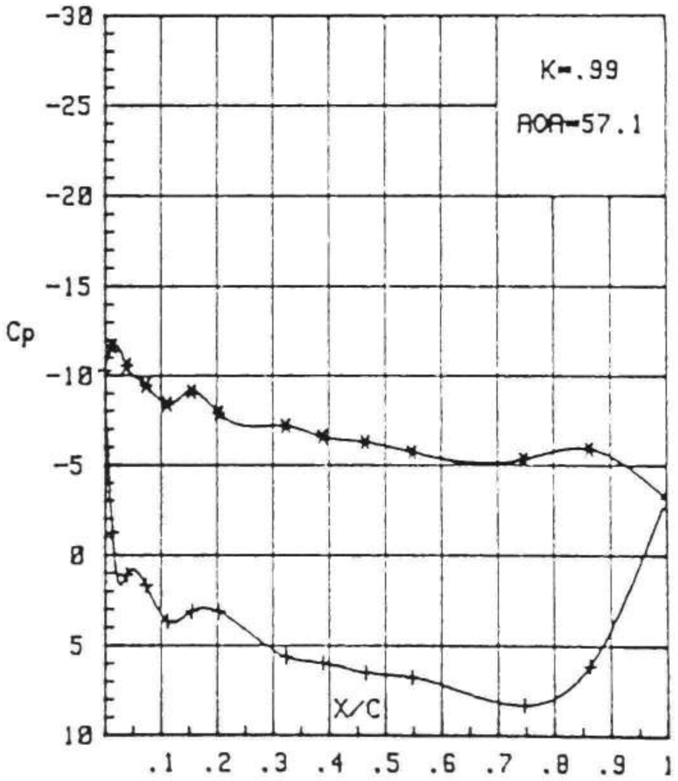
K=.99
AOA=57.1
Cp
-30
-25
-20
-15
-10
-5
0
5
10
X/C
.1
.2
.3
.4
.5
.6
.7
.8
.9
1

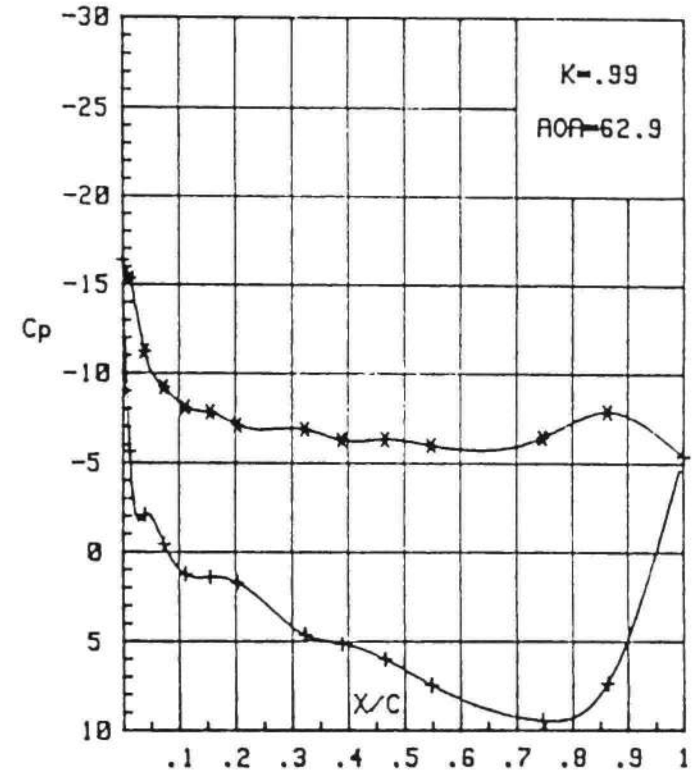
K=.99
AOA=62.9
Cp
-30
-25
-20
-15
-10
-5
0
5
10
X/C
.1
.2
.3
.4
.5
.6
.7
.8
.9
1

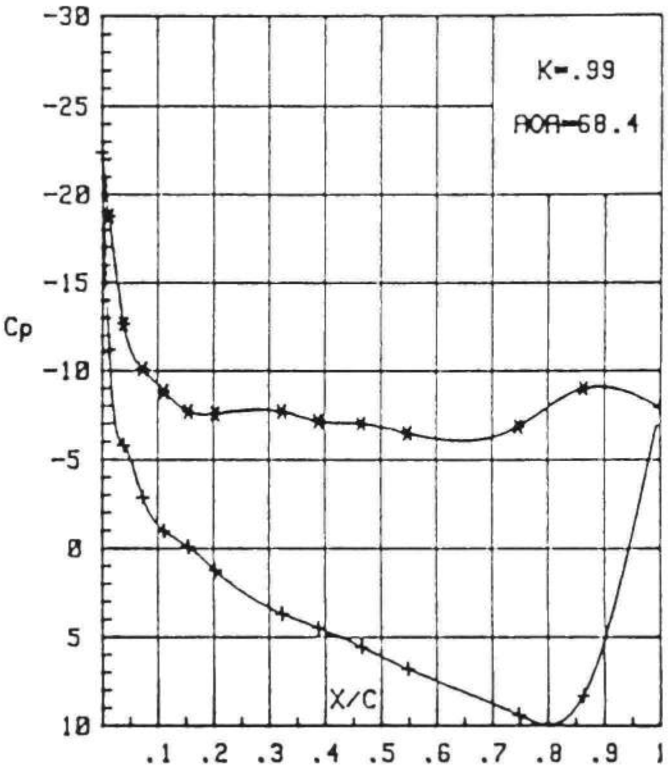
K=.99
AOA=68.4
Cp
-30
-25
-20
-15
-10
-5
0
5
10
X/C
.1
.2
.3
.4
.5
.6
.7
.8
.9
1

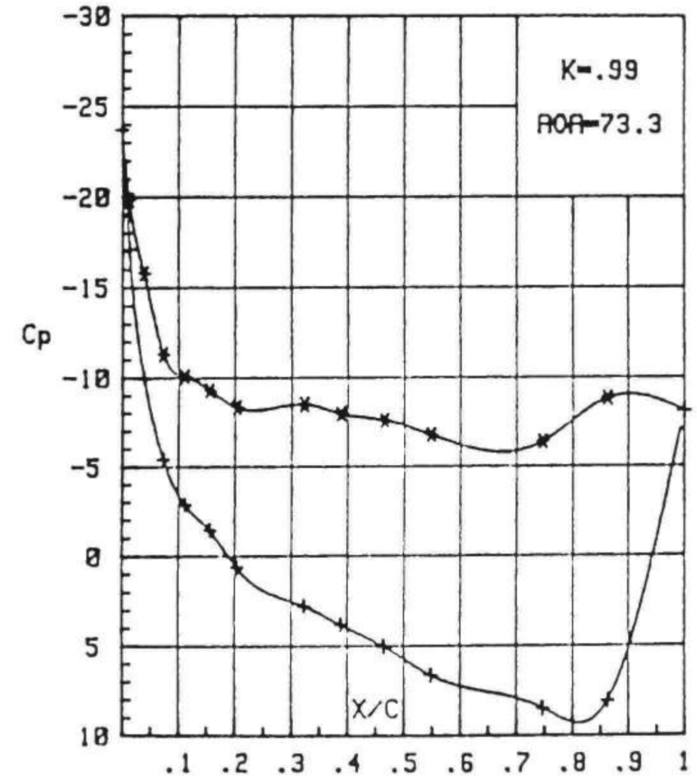
K=.99
AOA=73.3
Cp
-30
-25
-20
-15
-10
-5
0
5
10
X/C
.1
.2
.3
.4
.5
.6
.7
.8
.9
1

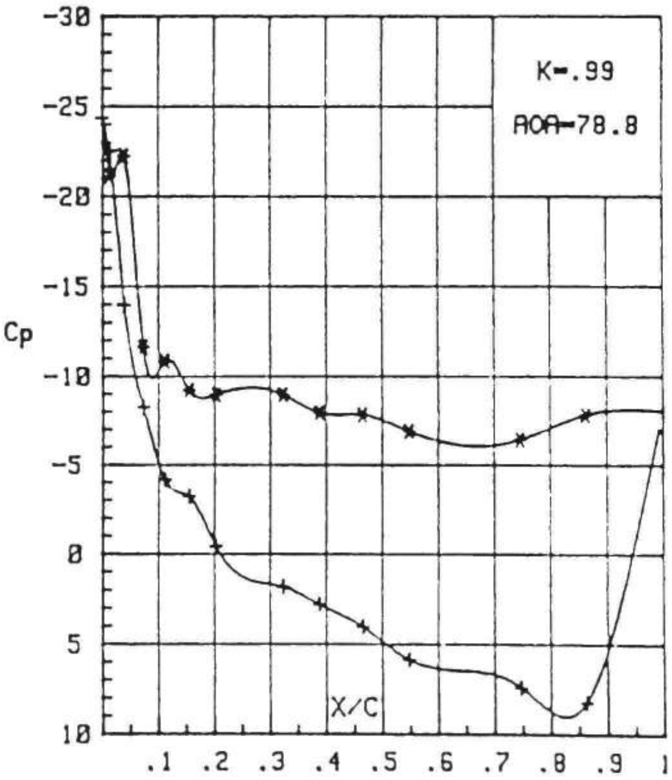
K=.99
AOA=78.8
Cp
-30
-25
-20
-15
-10
-5
0
5
10
X/C
.1
.2
.3
.4
.5
.6
.7
.8
.9
1

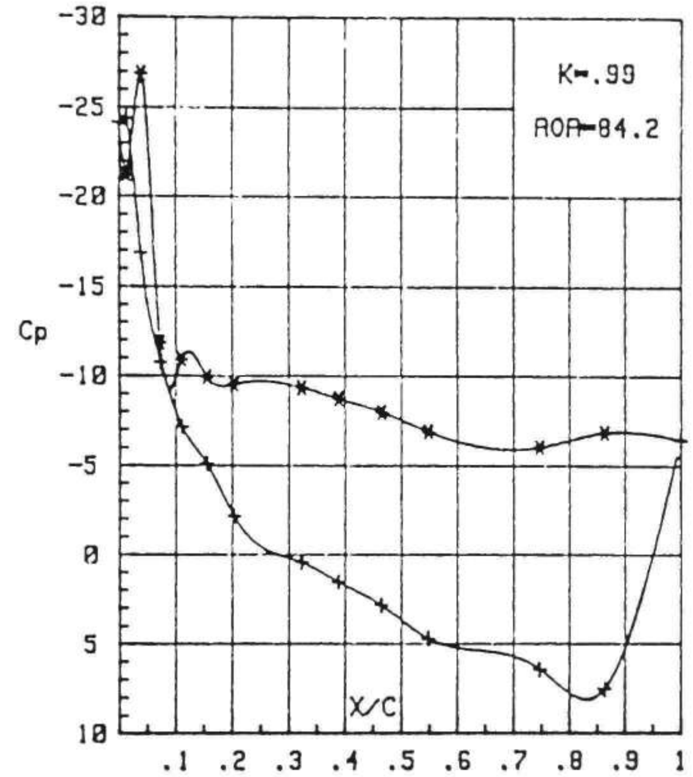
K=.99
AOA=84.2
Cp
X/C
-30
-25
-20
-15
-10
-5
0
5
10
.1
.2
.3
.4
.5
.6
.7
.8
.9
1

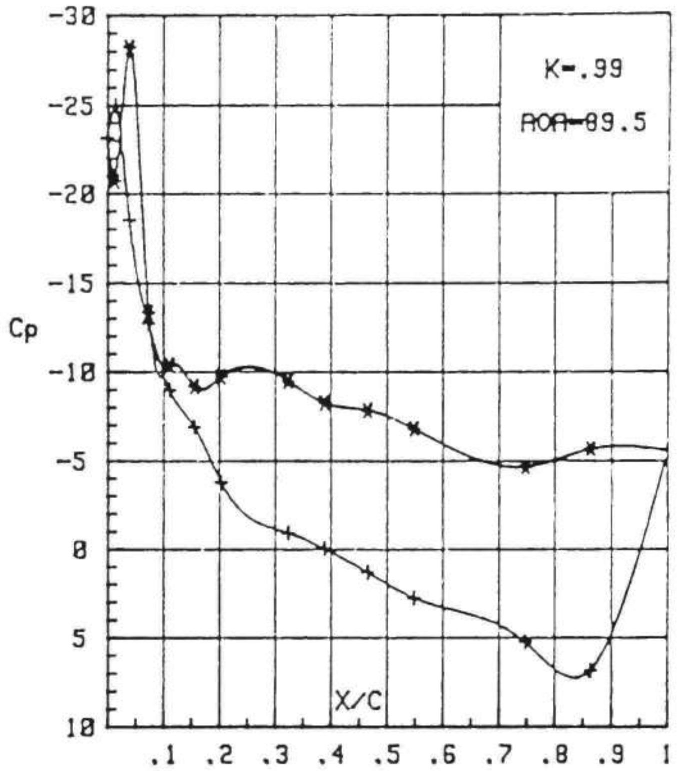
K=.99
AOA=89.5
Cp
X/C
-30
-25
-20
-15
-10
-5
0
5
10
.1
.2
.3
.4
.5
.6
.7
.8
.9
1

APPENDIX C

AERODYNAMIC FORCES

This appendix contains aerodynamic force data for non-dimensional pitching rates of .088, .19, .29, .51, .71, and .99 at a Reynolds number of 1×10^5. The following data key applies:

— - Filtered strain gage
〰 - Unfiltered strain gage
+ - Integrated Forces

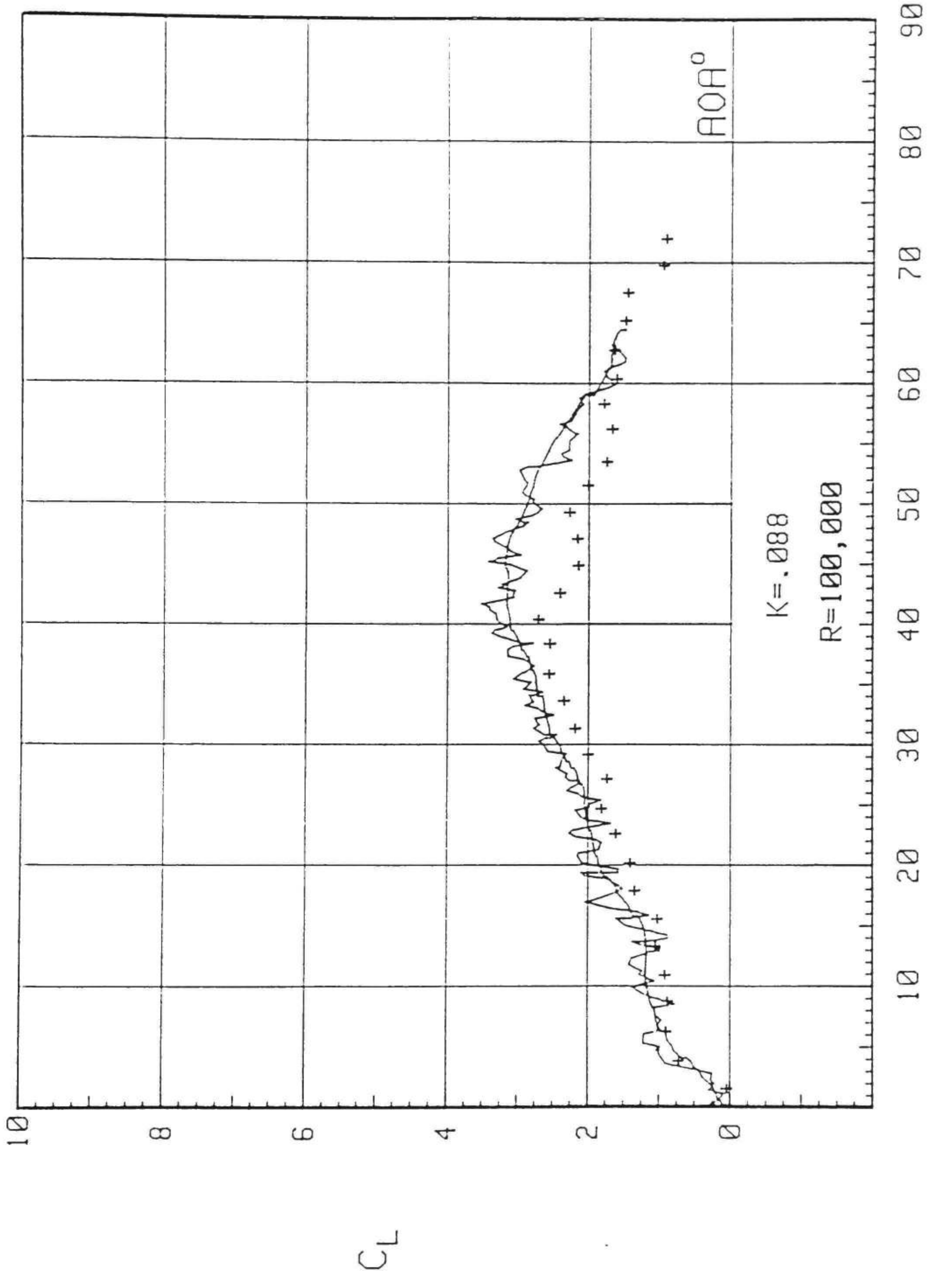
C_L
10
8
6
4
2
0
0
10
20
30
40
50
60
70
80
90
AOA°
K=.088
R=100,000

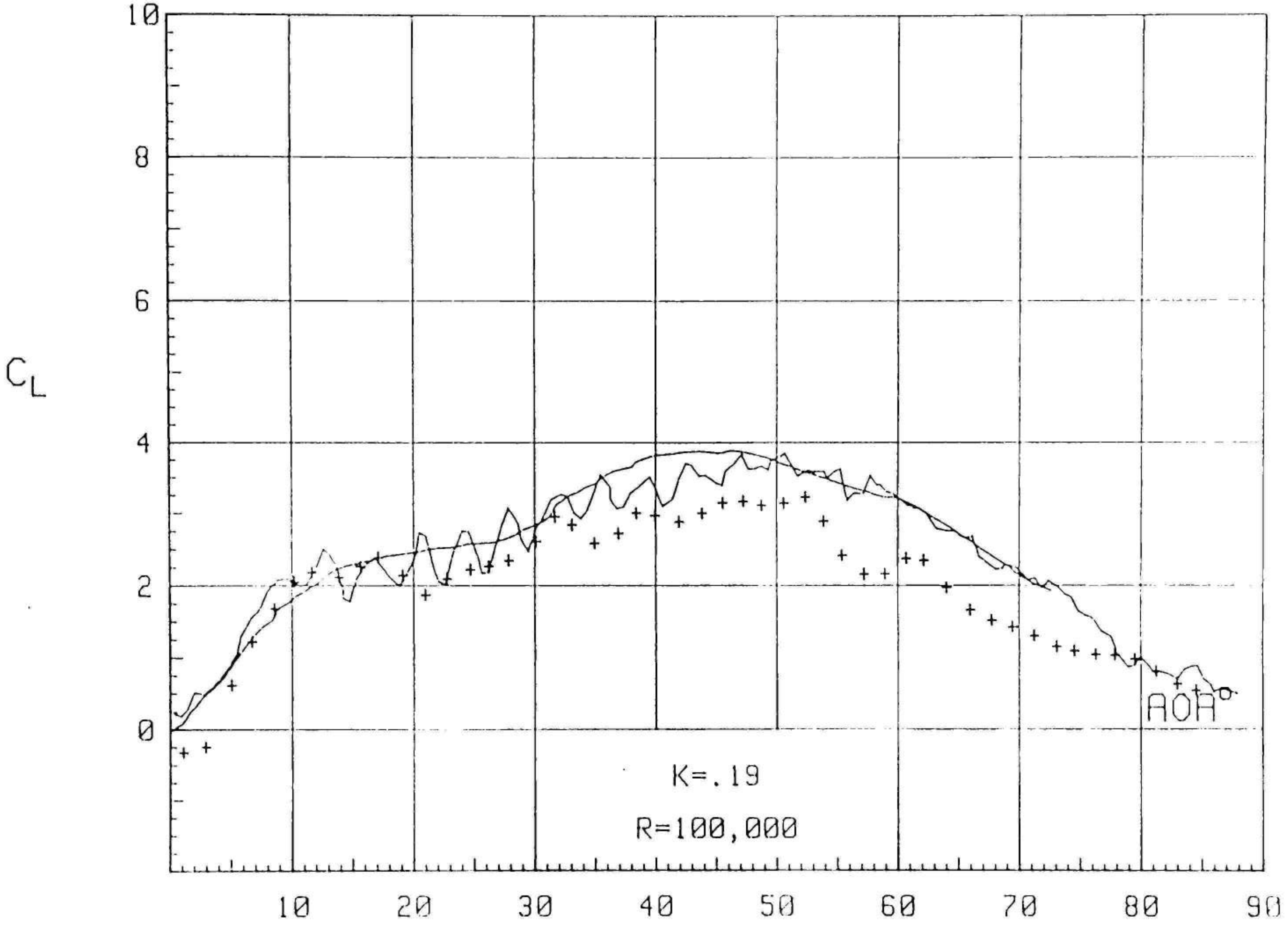
C$_L$
10
8
6
4
2
0
10
20
30
40
50
60
70
80
90
AOA°
K=.19
R=100,000

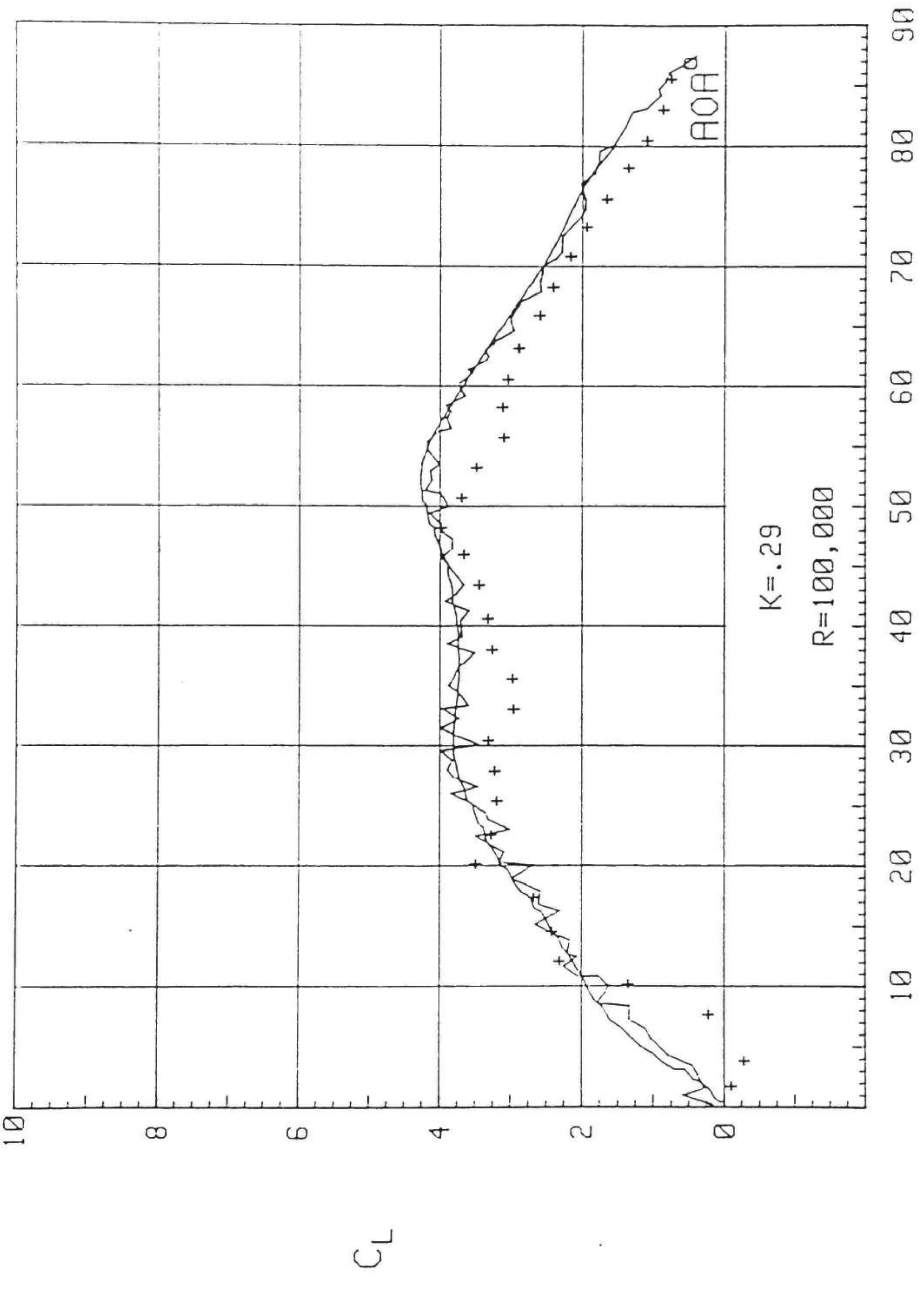
C_L
0
2
4
6
8
10
10
20
30
40
50
60
70
80
90
AOA
K=.29
R=100,000

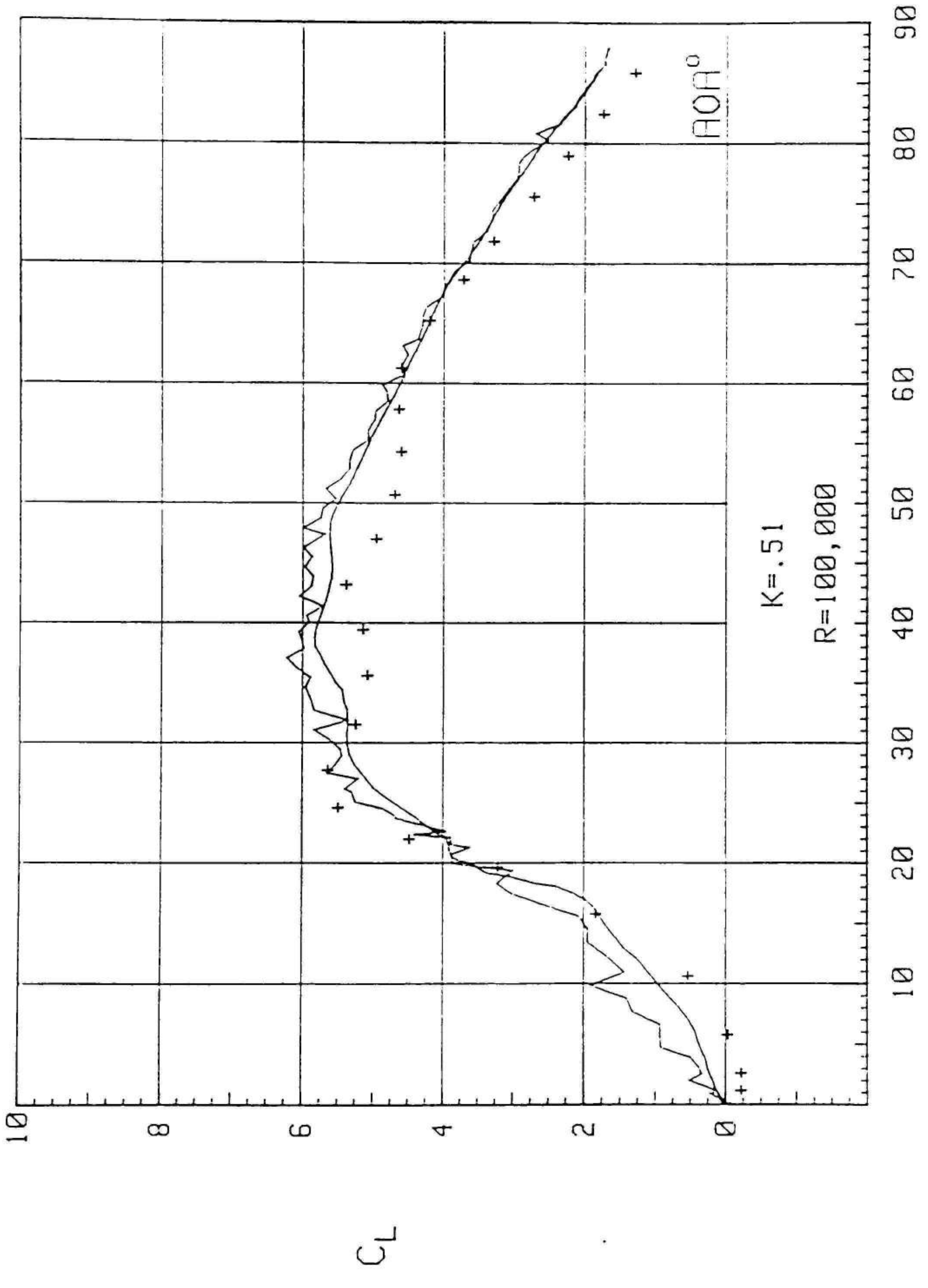
C$_L$
0
2
4
6
8
10
AOA°
10
20
30
40
50
60
70
80
90
K=.51
R=100,000

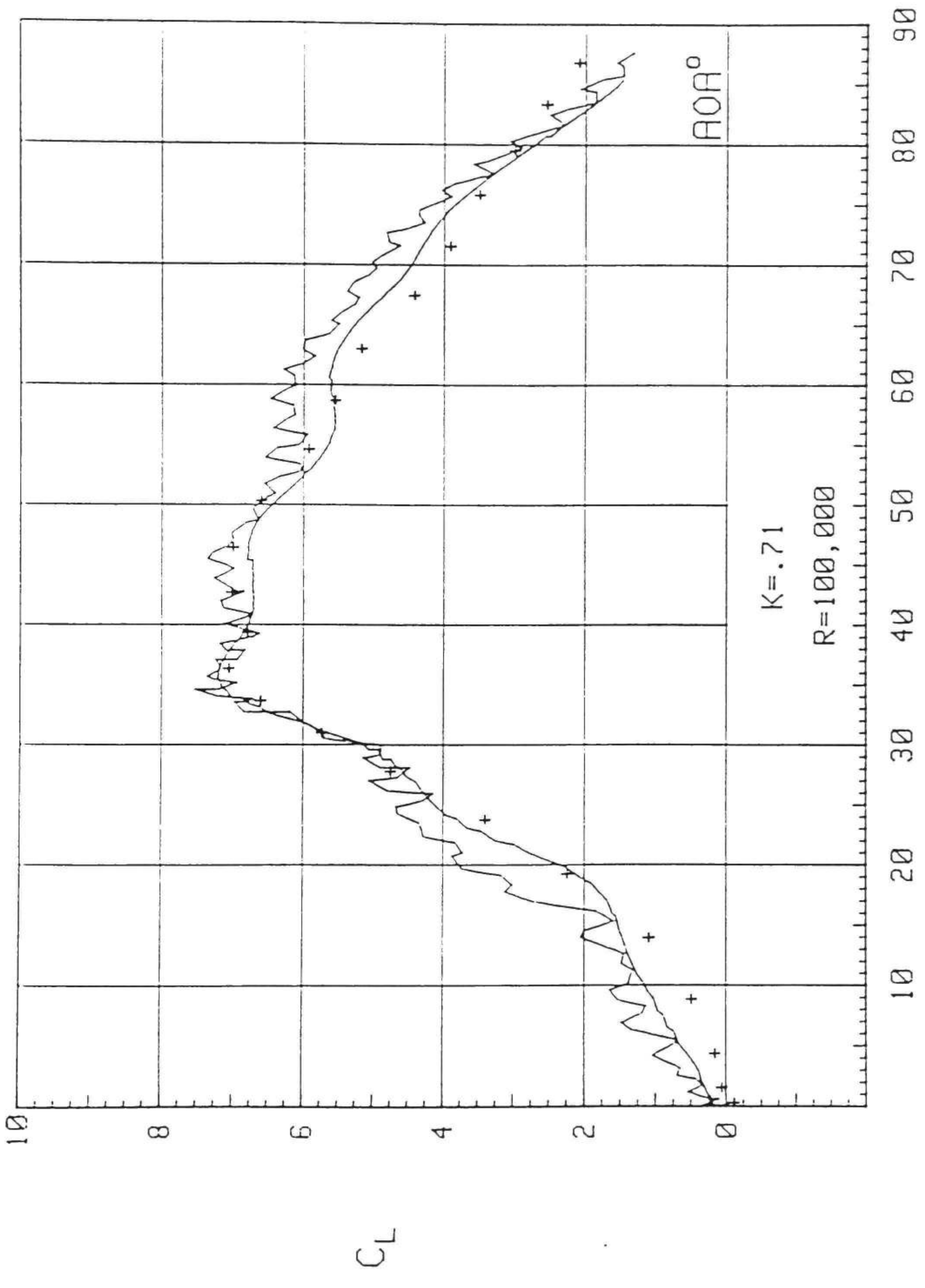
C_L
10
8
6
4
2
0
10
20
30
40
50
60
70
80
90
AOA°
K=.71
R=100,000

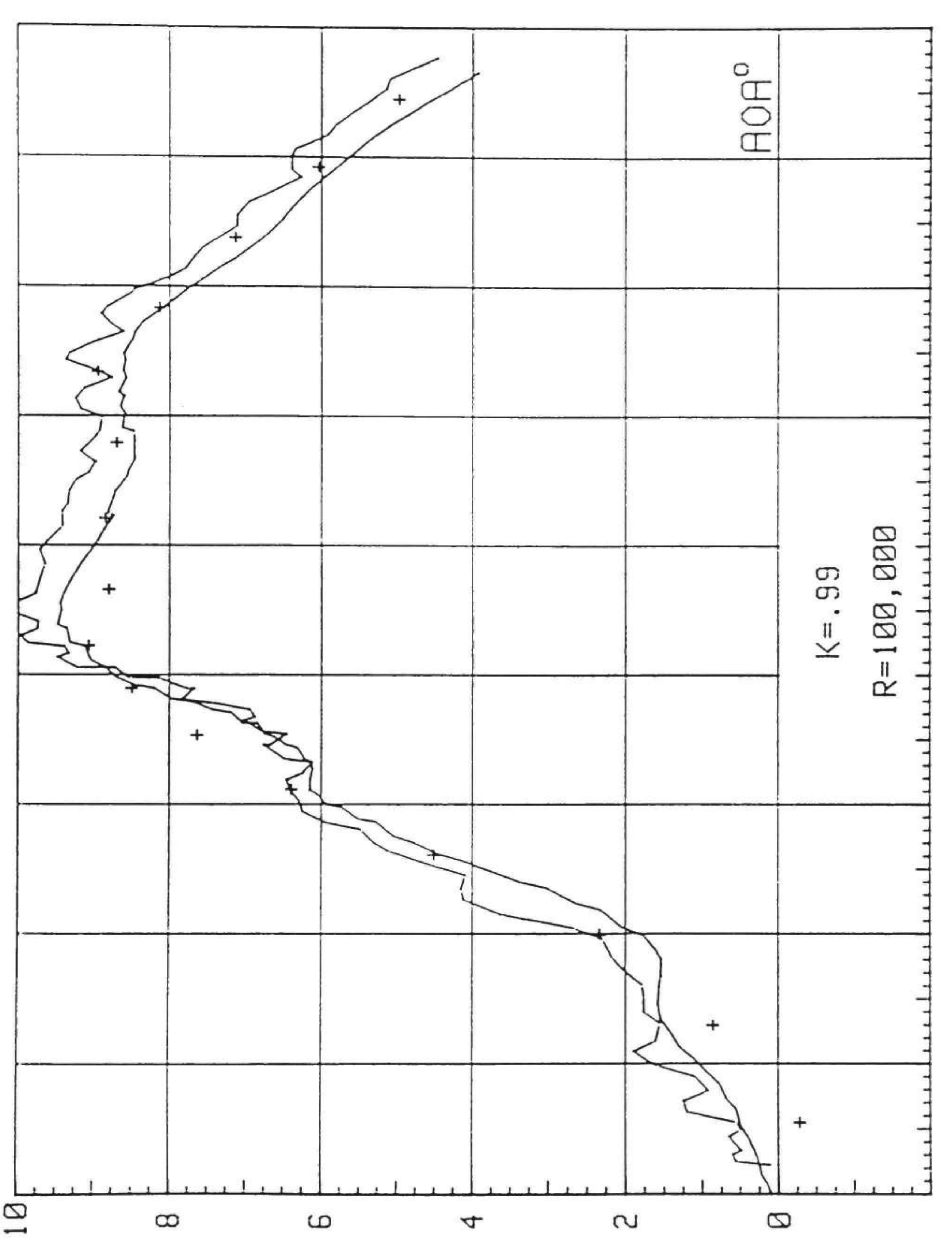
C_L
0
2
4
6
8
10
10
20
30
40
50
60
70
80
90
AOA°
K=.99
R=100,000

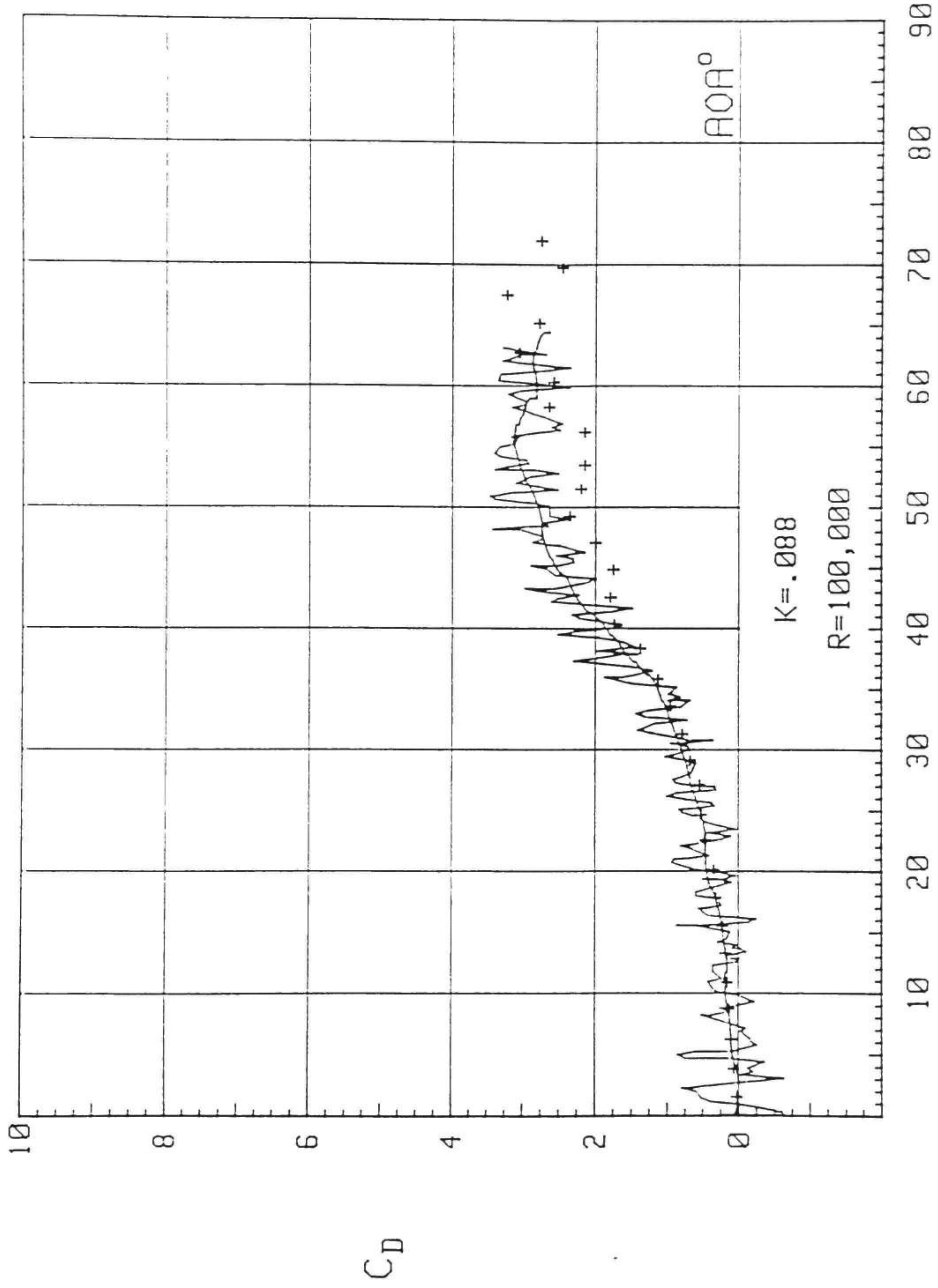
C_D
0
2
4
6
8
10
10
20
30
40
50
60
70
80
90
AOA°
K=.088
R=100,000

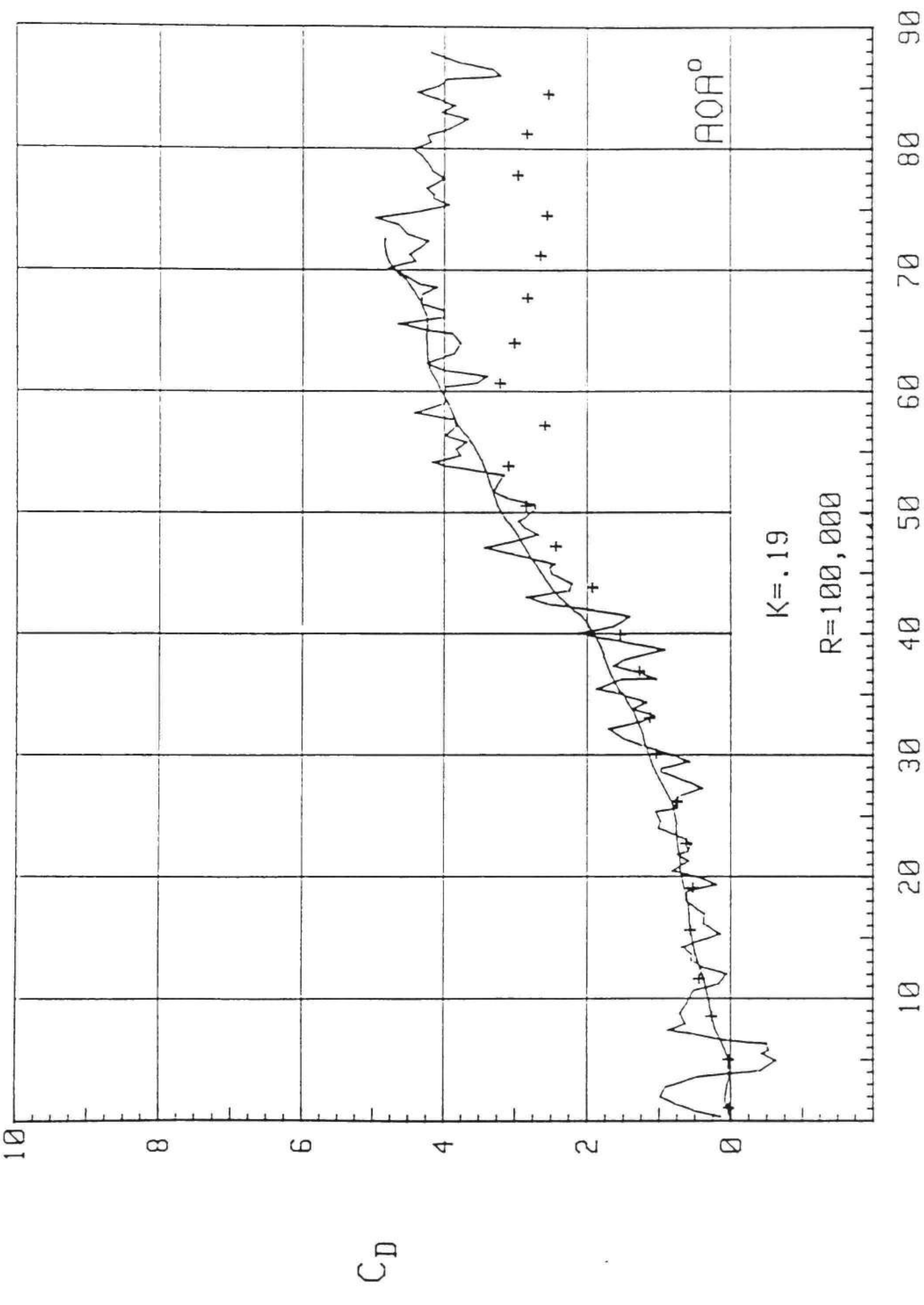
C_D
10
8
6
4
2
0
10
20
30
40
50
60
70
80
90
AOA°
K=.19
R=100,000

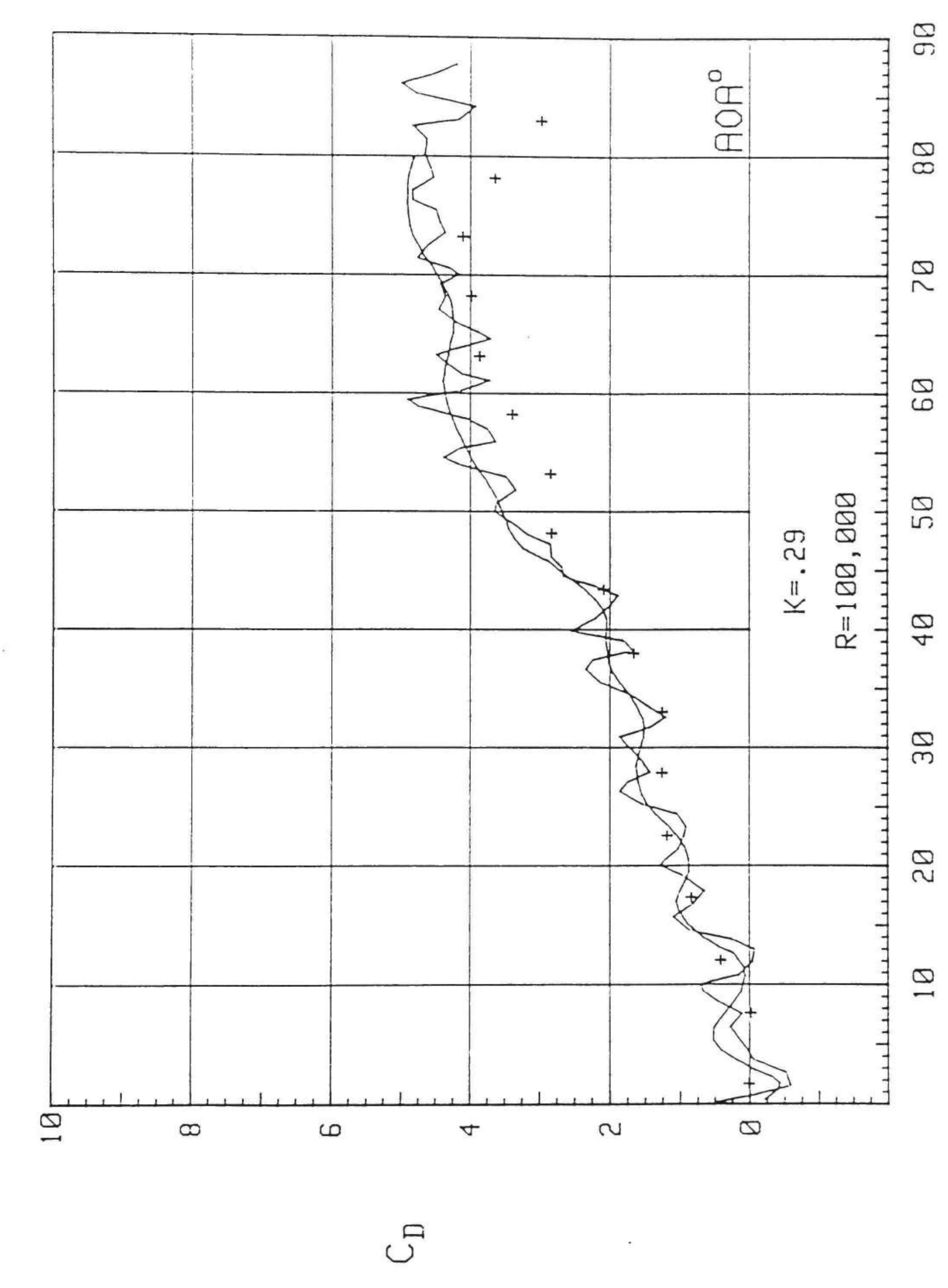

C_D
10
8
6
4
2
0
10
20
30
40
50
60
70
80
90
AOA°
K=.29
R=100,000

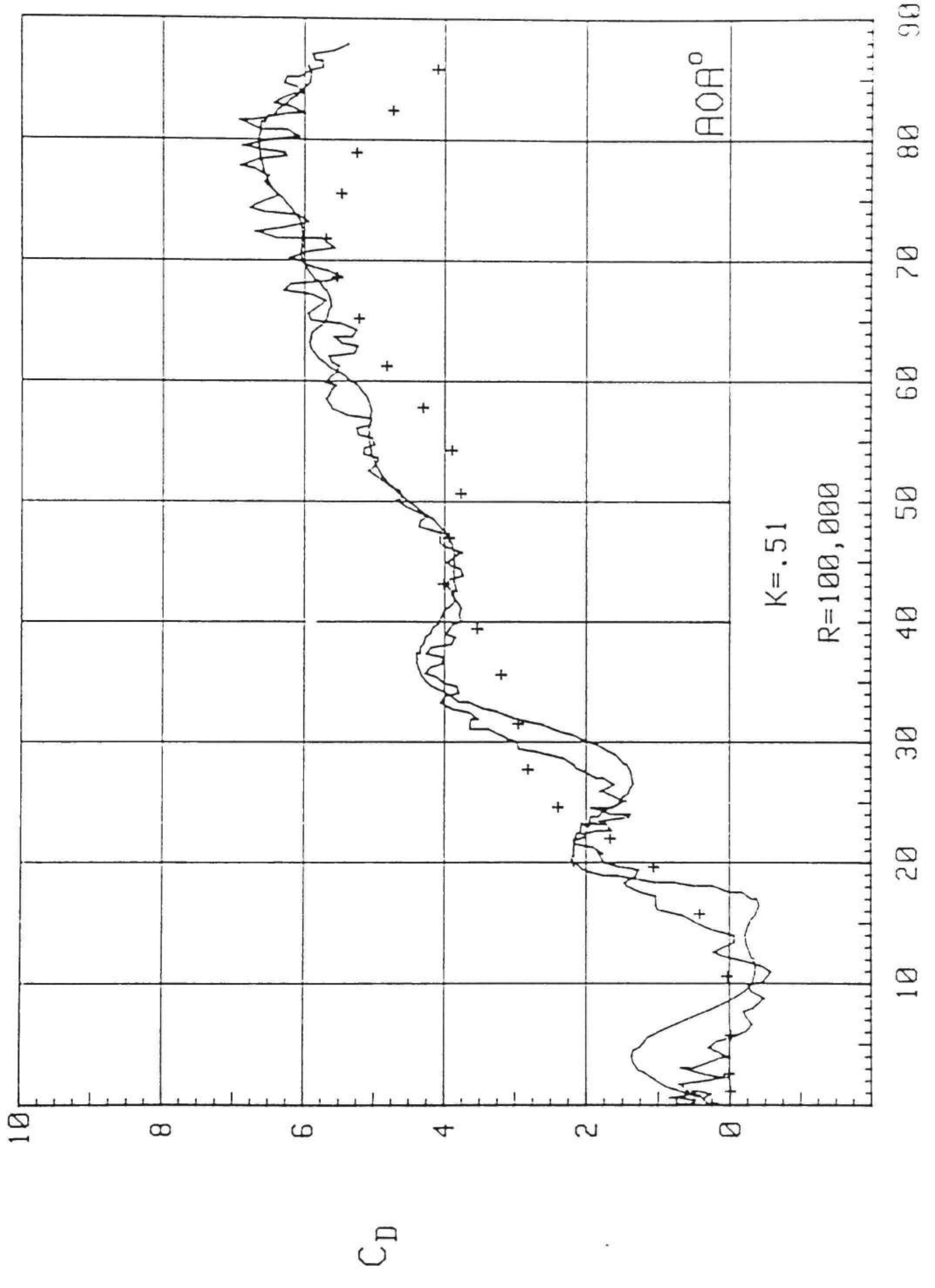
C_D
10
8
6
4
2
0
0
10
20
30
40
50
60
70
80
90
AOA°
K=.51
R=100,000

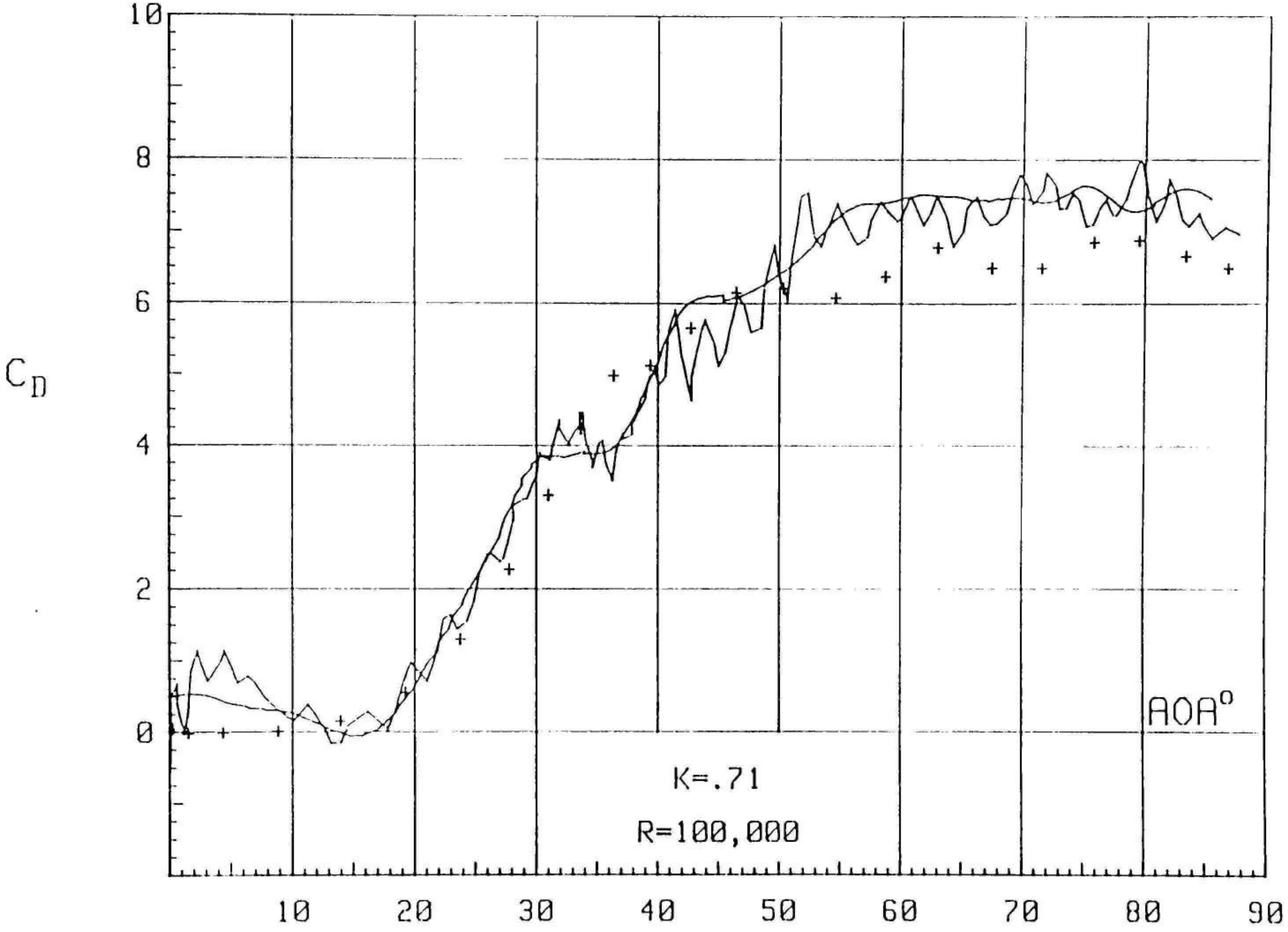
C_D
10
8
6
4
2
0
10
20
30
40
50
60
70
80
90
AOA°
K=.71
R=100,000

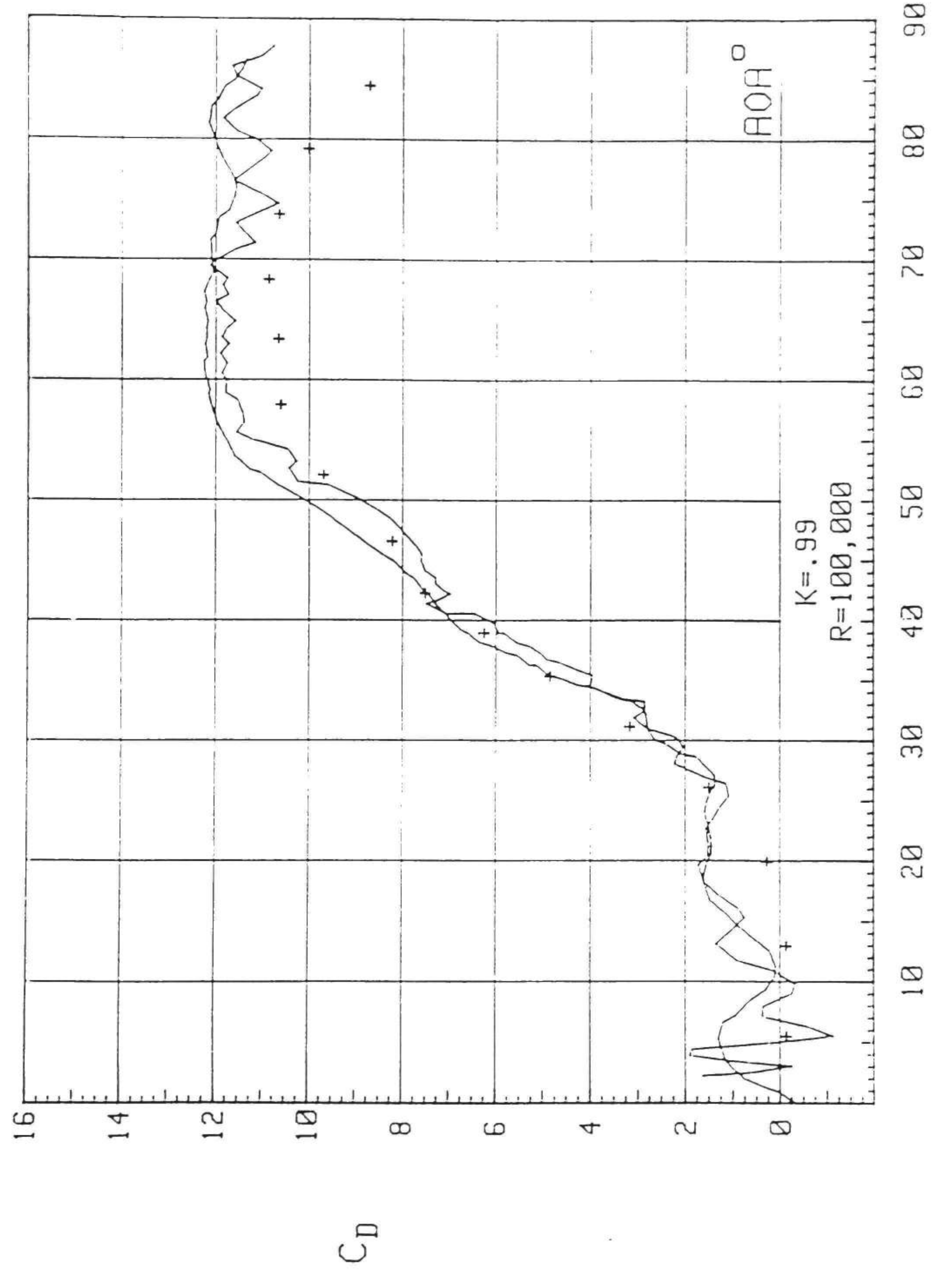
C_D
16
14
12
10
8
6
4
2
0
10
20
30
40
50
60
70
80
90
AOA°
K=.99
R=100,000

APPENDIX D

SOFTWARE LISTINGS

This appendix contains a software listing of the analytical model discussed in Chapter IV of this dissertation. The program is for a four-panel body.

```
      COMMON/NVOR/NBV,NTV,NNV
      COMMON/GAM/GS(3,400),GB(4),OGB(4),DNGAM,CPHI
      COMMON/LOC/X(3,400),Z(3,400)
      DIMENSION DL(50,2),TN(50,2),TME(50)
      DIMENSION XN(35),ZN(35,1),XT(35),ZT(35,1)
      PRINT 10
      DELT=0.06
      NWAK=35
      NTP=0
      NBV=4
      RC=0.075
      DO 1 N=1,NBV
      OGB(N)=0.0
    1 CONTINUE
      TTOT=5.0
      XNTTOT=50.0
      NTTOT=IFIX(XNTTOT)
      CALL INFLU(RC)
      DO 20 NT=1,NTTOT
      TIME=(NT)*DELT
      CALL MOTION(NT,DELT,XPIV,ZPIV,XAP,UPIV,WPIV,ALPR,ADOT,ASTAL)
      NTV=NT
      NNV=NT
      CALL ARVEL(NT,DELT,XPIV,ZPIV,XAP,UPIV,WPIV,ALPR,ADOT,RC)
      CALL GAMMA(NT,DELT,ADOT,RC,ALPR,ASTAL)
      CALL FORCE(NT,ALPR,CN,CT,CL,CD,DELT,ADOT)
      CALL WIVEL(NT,DELT,UPIV,WPIV,XAP,ALPR,RC)
      CALL DPRNT(NT,DELT,XPIV,ZPIV,UPIV,WPIV,ALPR,ADOT,CN,CT,CL,CD)
      CALL CONWA(ALPR,NT,DELT)
      TN(NT,1)=CN
      TN(NT,2)=CT
      DL(NT,1)=CL
      DL(NT,2)=CD
      TME(NT)=ALPR*57.296
      IF(NT.EQ.NWAK) GO TO 30
      GO TO 20
   30 DO 40 I=1,NWAK
      XN(I)=X(3,I)-XPIV
      ZN(I,1)=-Z(3,I)
      XT(I)=X(2,I)-XPIV
      ZT(I,1)=-Z(2,I)
   40 CONTINUE
      ALPW=ALPR*57.296
   20 CONTINUE
   21 WRITE(6,41) ALPW
   41 FORMAT(///,10X,'ANGLE OF ATTACK FOR WAKE GEOMETRY PLOTS ='
     $,F10.3,//)
      CALL UGETIO(3,5,6)
      CALL USPLO(XN,ZN,NWAK,NWAK,1,1,'L.E. WAKE GEOMETRY',18,'X',1
     $,'Y',1,RANGE,'*',0,IER)
      CALL UGETIO(3,5,6)
      CALL USPLO(XT,ZT,NWAK,NWAK,1,1,'T.E. WAKE GEOMETRY',18,'X',1
     $,'Y',1,RANGE,'*',0,IER)
```

```
      CALL UGETIO(3,5,6)
      CALL USPLO(TME,DL,NT,NT,2,1,'LIFT AND DRAG FORCE CALCULATIONS'
     $,32,'A-O-A',5,'L$D',0,RANGE,'LD',1,IER)
      CALL UGETIO(3,5,6)
      CALL USPLO(TME,TN,NT,NT,2,1,'NORM. AND TANG. FORCE CALCULATIONS'
     $,34,'A-O-A',5,'N$T',0,RANGE,'NT',1,IER)
   10 FORMAT(10X,
     $'**********************************',/10X,
     $'* USTAR2S UNSTEADY AIRFOIL CODE *',/10X,
     $'**********************************',////)
      END
C
```

```
C
      SUBROUTINE INFLU(RC)
      COMMON/NVOR/NBV,NTV,NNV
      COMMON/ALOC/XS(7),ZS(7),XA(7),ZA(7),XB(7),ZB(7),XBS(7),ZBS(7)
      COMMON/GAM/GS(3,400),GB(3),OGB(3),DNGAM,CPHI
      COMMON/INFL/C(7,7),CI(7,7),D(7)
      PI=3.14159
      NB2=NBV+2
      NB3=NBV+3
      XA(1)=0.0
      ZA(1)=0.0
      XA(NB2)=1.0
      ZA(NB2)=0.0
      XA(NB3)=.25
      ZA(NB3)=0.0
      DO 10 J=1,NBV
      JP=J+1
      XA(JP)=(FLOAT(J)-.25)/FLOAT(NBV)
      ZA(JP)=0.0
   10 CONTINUE
      DO 20 J=1,NBV
      XB(J)=(FLOAT(J)-.75)/FLOAT(NBV)
      ZB(J)=0.0
   20 CONTINUE
      DO 30 I=1,NBV
      DO 40 J=1,NBV
      S=1.0
      JP=J+1
      DX=XA(JP)-XB(I)
      DY=ZA(JP)-ZB(I)
      R=SQRT(DX**2+DY**2)
      IF(R.LT.RC) R=RC
      RT=1.0-XA(JP)
      IF(RT.LT.RC) RT=RC
      CIT=1.0/(2.0*PI*RT)
      IF(DX.GT.0.0) S=-1.0
      C(J,I)=S/(2.0*PI*R)-CIT
   40 CONTINUE
   30 CONTINUE
      DO 50 I=1,NBV
      DO 60 J=1,NBV
      D(J)=0.0
      IF(I.EQ.J) D(J)=1.0
   60 CONTINUE
      CALL SOLVE
      DO 70 J=1,NBV
      CI(J,I)=GB(J)
   70 CONTINUE
   50 CONTINUE
      DO 80 I=1,NBV
      DO 90 J=1,NBV
      JP=J+1
      RT=1.0-XA(JP)
      IF(RT.LT.RC) RT=RC
      CIT=1.0/(2.0*PI*RT)
      C(J,I)=C(J,I)+CIT
   90 CONTINUE
   80 CONTINUE
      WRITE(6,41)
   41 FORMAT(///,15X,'INFLUENCE MATRIX',//)
      WRITE(6,42)((C(I,J),J=1,NBV),I=1,NBV)
   42 FORMAT(10X,3F10.3)
      WRITE(6,43)
   43 FORMAT(///,13X,'INVERSE INFLU MATRIX',//)
      WRITE(6,42)((CI(I,J),J=1,NBV),I=1,NBV)
      WRITE(6,44)
   44 FORMAT(///)
      RETURN
      END
C
```

```
C
      SUBROUTINE  MOTION(NT,DELT,XPIV,ZPIV,XAP,UPIV,WPIV,ALPR,ADOT,
     $ASTAL)
C     CONSTANT PITCH RATE FROM ALPRO
      XAP=0.25
      UPIV=-1.0
      IF(NT.EQ.1) UPIV=-.001
      WPIV=0.0
      ADOT=0.0
      NPIT=3
      IF(NT.GT.NPIT) ADOT=.58
      ASTAL=54.0/57.296
      ALPDO=0.0
      ALPRO=ALPDO/57.29578
      XPIV=UPIV*(NT-1)*DELT
      ZPIV=WPIV*(NT-1)*DELT
      DNP=FLOAT(NT-NPIT)
      IF(DNP.LT.0.0) GO TO 6
      ALPR=ADOT*DNP*DELT+ALPRO
    6 IF(NT.GT.1) GO TO 5
      PRINT 10,XAP,ALPDO,DELT,ADOT
   10 FORMAT(10X,'CONSTANT PITCH RATE MOTION',///15X,'PIVOT=',
     $F7.3,2X,'FROM NOSE',/15X,'INITIAL ANGLE=',F7.3,'DEGREES',/15X,
     $'TIME STEP=',F7.3,/15X,'PITCH RATE=',F7.3//)
    5 CONTINUE
      RETURN
      END
C
```

```
C
      SUBROUTINE ARVEL(NT,DELT,XPIV,ZPIV,XAP,UPIV,WPIV,ALPR,ADOT,RC)
      COMMON/LOC/X(3,400),Z(3,400)
      COMMON/ALOC/XS(7),ZS(7),XA(7),ZA(7),XB(7),ZB(7),XBS(7),ZBS(7)
      COMMON/AVEL/UA(7),WA(7),UAS(7),WAS(7),US(7),WS(7),UST(7),
     $WST(7),ALD(7),AL(7),UBAS(7),WBAS(7)
      COMMON/NVOR/NBV,NTV,NNV
      NB2=NBV+2
      DO 5 I=1,NB2
      XS(I)=XPIV+COS(ALPR)*(XA(I)-XAP)-SIN(ALPR)*ZA(I)
      ZS(I)=ZPIV+SIN(ALPR)*(XA(I)-XAP)+COS(ALPR)*ZA(I)
    5 CONTINUE
      DO 7 I=1,NBV
      XBS(I)=XPIV+COS(ALPR)*(XB(I)-XAP)-SIN(ALPR)*ZB(I)
      ZBS(I)=ZPIV+SIN(ALPR)*(XB(I)-XAP)+COS(ALPR)*ZB(I)
    7 CONTINUE
      DO 6 J=1,NBV
      X(1,J)=XBS(J)
      Z(1,J)=ZBS(J)
    6 CONTINUE
      X(2,NTV)=XS(NB2)
      Z(2,NTV)=ZS(NB2)
      X(3,NNV)=XS(1)
      Z(3,NNV)=ZS(1)
      DO 20 I=1,NB2
      UAS(I)=-UPIV*COS(ALPR)-WPIV*SIN(ALPR)
      WAS(I)= UPIV*SIN(ALPR)-WPIV*COS(ALPR)-(XA(I)-XAP)*ADOT
      IF(NT.EQ.1) GO TO 10
      CALL PIVEL(NBV,NTV-1,NNV-1,XS(I),ZS(I),US(I),WS(I),DELT,RC)
      GO TO 15
   10 US(I)=0.0
      WS(I)=0.0
   15 CONTINUE
      UA(I)=US(I)*COS(ALPR)+WS(I)*SIN(ALPR)
      WA(I)=-US(I)*SIN(ALPR)+WS(I)*COS(ALPR)
   20 CONTINUE
      DO 30 I=1,NBV
      UBAS(I)=-UPIV*COS(ALPR)-WPIV*SIN(ALPR)
      WBAS(I)= UPIV*SIN(ALPR)-WPIV*COS(ALPR)-(XB(I)-XAP)*ADOT
   30 CONTINUE
      RETURN
      END
C
```

```
C
      SUBROUTINE GAMMA(NT,DELT,ADOT,RC,ALPR,ASTAL)
      COMMON/GAM/GS(3,400),GB(4),OGB(4),DNGAM,CPHI
      COMMON/NVOR/NBV,NTV,NNV
      COMMON/ALOC/XS(7),ZS(7),XA(7),ZA(7),XB(7),ZB(7),XBS(7),ZBS(7)
      COMMON/AVEL/UA(7),WA(7),UAS(7),WAS(7),US(7),WS(7),UST(7),
     $WST(7),ALD(7),AL(7),UBAS(7),WBAS(7)
      COMMON/INFL/C(7,7),CI(7,7),D(7)
      DIMENSION F(7)
      PI=3.14159
      NB2=NBV+2
      DO 10 I1=1,NBV
      I=I1+1
      SUM=0.0
      DO 5 J=1,NBV
      SUM=SUM+C(I1,J)*OGB(J)
    5 CONTINUE
      F(I)=SUM
   10 CONTINUE
      SUM1=0.0
      SUM2=0.0
      DO 11 I=1,NBV
      RN=XB(I)
      RT=1.0-XB(I)
      IF(RT.LT.RC) RT=RC
      IF(RN.LT.RC) RN=RC
      SUM1=SUM1+OGB(I)/(2.0*PI*RN)
      SUM2=SUM2-OGB(I)/(2.0*PI*(1.0-RT))
   11 CONTINUE
      F(1)=SUM1
      F(NB2)=SUM2
      DO 15 I=1,NB2
      WST(I)=WA(I)+WAS(I)-F(I)
      UST(I)=UA(I)+UAS(I)
      WSTN=-WST(I)
      USTP=+UST(I)
      AL(I)=ATAN2(WSTN,USTP)
      ALD(I)=AL(I)*180.0/PI
   15 CONTINUE
      CALL NGAM(AL(3),DNGAM,CPHI,ALPR)
      IF(NT.EQ.1) DNGAM=0.0
      GN=-DNGAM*DELT
      IF(ALPR.LT.ASTAL) GN=0.0
      GS(3,NNV)=GN
      DO 50 J=1,NBV
      JP=J+1
      RN=XA(JP)
      RT=1.0-XA(JP)
      IF(RN.LT.RC) RN=RC
      IF(RT.LT.RC) RT=RC
      CIT=1.0/(2.0*PI*RT)
      CIN=-1.0/(2.0*PI*RN)
      SUM=0.0
      DO 16 I=1,NBV
      SUM=SUM+OGB(I)
   16 CONTINUE
      D(J)=-WST(JP)+(CIT-CIN)*GN-CIT*SUM
   50 CONTINUE
      DO 51 I=1,NBV
      SUM=0.0
      DO 52 J=1,NBV
      SUM=SUM+CI(I,J)*D(J)
   52 CONTINUE
      GB(I)=SUM
   51 CONTINUE
      SUM=0.0
      DO 60 J=1,NBV
      SUM=SUM+GB(J)-OGB(J)
   60 CONTINUE
      GT=-(GN+SUM)
      GS(2,NT)=GT
      DO 62 J=1,NBV
      GS(1,J)=GB(J)
      OGB(J)=GB(J)
   62 CONTINUE
C
      RETURN
      END
C
```

```
C
      SUBROUTINE SOLVE
      COMMON/NVOR/NBV,NTV,NNV
      COMMON/GAM/GS(3,400),GB(4),OGB(4),DNGAM,CPHI
      COMMON/INFL/C(7,7),CI(7,7),D(7)
      DIMENSION A(4,5),U(4,4),Z(4),SUM(4)
      REAL L(4,4)
      DO 10 I1=1,NBV
      DO 20 I2=1,NBV
      A(I1,I2)=C(I1,I2)
   20 CONTINUE
   10 CONTINUE
      NB1=NBV+1
      DO 30 I=1,NBV
      A(I,NB1)=D(I)
   30 CONTINUE
      K=1
      DO 40 I=2,NBV
      C1=ABS(A(K,1))
      C2=ABS(A(I,1))
      IF(C1.GT.C2) GO TO 40
      K=I
   40 CONTINUE
      DO 50 I=1,NB1
      C1=A(1,I)
      A(1,I)=A(K,I)
      A(K,I)=C1
   50 CONTINUE
      L(1,1)=1.0
      U(1,1)=A(1,1)
      DO 60 I=2,NBV
      L(I,1)=A(I,1)/U(1,1)
      U(1,I)=A(1,I)
   60 CONTINUE
      K1=2
   65 K1M=K1-1
      DO 70 I1=K1,NBV
      SUM(I1)=0.0
      DO 80 I2=1,K1M
      SUM(I1)=SUM(I1)+L(I1,I2)*U(I2,K1)
   80 CONTINUE
   70 CONTINUE
      K=K1
      K1P=K1+1
      DO 90 I=K1P,NBV
      C1=ABS(A(K,K1)-SUM(K))
      C2=ABS(A(I,K1)-SUM(I))
      IF(C1.GT.C2) GO TO 90
      K=I
   90 CONTINUE
      DO 100 I=1,NB1
      C1=A(K1,I)
      A(K1,I)=A(K,I)
      A(K,I)=C1
```

```
  100 CONTINUE
      DO 110I=1,NBV
      C1=L(K1,I)
      L(K1,I)=L(K,I)
      L(K,I)=C1
  110 CONTINUE
      L(K1,K1)=1.0
      U(K1,K1)=A(K1,K1)-SUM(K1)
      IF(K1.EQ.NBV) GO TO 120
      K=K1+1
      DO 130 I=K,NBV
      L(I,K1)=(A(I,K1)-SUM(I))/U(K1,K1)
  130 CONTINUE
      DO 140 I1=K,NBV
      SUM(I1)=0.0
      DO 150 I2=1,K1M
      SUM(I1)=SUM(I1)+L(K1,I2)*U(I2,I1)
  150 CONTINUE
      U(K1,I1)=A(K1,I1)-SUM(I1)
  140 CONTINUE
      K1=K1+1
      GO TO 65
  120 Z(1)=A(1,NB1)
      DO 160 I1=2,NBV
      SUM(I1)=0.0
      I1M=I1-1
      DO 170 I2=1,I1M
      SUM(I1)=SUM(I1)+L(I1,I2)*Z(I2)
  170 CONTINUE
      Z(I1)=A(I1,NB1)-SUM(I1)
  160 CONTINUE
      GB(NBV)=Z(NBV)/U(NBV,NBV)
      NBM=NBV-1
      DO 180 I1=1,NBM
      I1M=NBV-I1
      I1P=I1M+1
      SUM(I1M)=0.0
      DO 190 I2=I1P,NBV
      SUM(I1M)=SUM(I1M)+U(I1M,I2)*GB(I2)
  190 CONTINUE
      GB(I1M)=(Z(I1M)-SUM(I1M))/U(I1M,I1M)
  180 CONTINUE
      RETURN
      END
C
```

```
C
      SUBROUTINE NGAM(ALGAM,DNGAM,CPHI,ALPR)
      DNGAM=4.35*SIN(ALPR)
      CPHI=1.00
      RETURN
      END
C
```

```
C
      SUBROUTINE FORCE(NT,ALPR,CN,CT,CL,CD,DELT,ADOT)
      COMMON/LOC/X(3,400),Z(3,400)
      COMMON/NVOR/NBV,NTV,NNV
      COMMON/GAM/GS(3,400),GB(4),OGB(4),DNGAM,CPHI
      COMMON/AVEL/UA(7),WA(7),UAS(7),WAS(7),US(7),WS(7),UST(7),
     $WST(7),ALD(6),AL(7),UBAS(7),WBAS(7)
      XIMP=0.0
      ZIMP=0.0
      DO 10 I=1,NBV
      XIMP=XIMP+Z(1,I)*GS(1,I)
      ZIMP=ZIMP+X(1,I)*GS(1,I)
   10 CONTINUE
      DO 20 I=1,NTV
      XIMP=XIMP+Z(2,I)*GS(2,I)
      ZIMP=ZIMP+X(2,I)*GS(2,I)
   20 CONTINUE
      DO 30 I=1,NNV
      XIMP=XIMP+Z(3,I)*GS(3,I)
      ZIMP=ZIMP+X(3,I)*GS(3,I)
   30 CONTINUE
      IF(NT.EQ.1) GO TO 50
      CL=2.0*(ZIMP-OZIMP)/DELT
      CD=2.0*(XIMP-OXIMP)/DELT
   40 GO TO 60
   50 CONTINUE
      GBL=0.0
      GBD=0.0
      DO 51 I=1,NBV
      UB=UBAS(I)*COS(ALPR)-WBAS(I)*SIN(ALPR)
      WB=WBAS(I)*COS(ALPR)+UBAS(I)*SIN(ALPR)
      GBL=GBL-GB(I)*UB
      GBD=GBD+GB(I)*WB
   51 CONTINUE
      CL=2.0*GBL
      CD=2.0*GBD
   60 CONTINUE
      CT=CL*SIN(ALPR)-CD*COS(ALPR)
      CN=CD*SIN(ALPR)+CL*COS(ALPR)
      OXIMP=XIMP
      OZIMP=ZIMP
      RETURN
      END
C
```

```
C
      SUBROUTINE WIVEL(NT,DELT,UPIV,WPIV,XAP,ALPR,RC)
      COMMON/NVOR/NBV,NTV,NNV
      COMMON/LOC/X(3,400),Z(3,400)
      COMMON/VEL/U(3,400),W(3,400)
      COMMON/VEO/UO(3,400),WO(3,400)
      COMMON/GAM/GS(3,400),GB(4),OGB(4),DNGAM,CPHI
      COMMON/AVEL/UA(7),WA(7),UAS(7),WAS(7),US(7),WS(7),UST(7),
     $WST(7),ALD(7),AL(7),UBAS(7),WBAS(7)
      COMMON/ALOC/XS(7),ZS(7),XA(7),ZA(7),XB(7),ZB(7),XBS(7),ZBS(7)
      DO 10 L=1,NBV
      CALL PIVEL(NBV,NTV,NNV,X(1,L),Z(1,L),U(1,L),W(1,L),DELT,RC)
      U(1,L)=U(1,L)-UPIV+ADOT*(XB(L)-XAP)*SIN(ALPR)
      W(1,L)=W(1,L)-WPIV-ADOT*(XB(L)-XAP)*COS(ALPR)
   10 CONTINUE
      DO 20 L=1,NTV
      UO(2,L)=U(2,L)
      WO(2,L)=W(2,L)
      CALL PIVEL(NBV,NTV,NNV,X(2,L),Z(2,L),U(2,L),W(2,L),DELT,RC)
   20 CONTINUE
      DO 30 L=1,NNV
      UO(3,L)=U(3,L)
      WO(3,L)=W(3,L)
      CALL PIVEL(NBV,NTV,NNV,X(3,L),Z(3,L),U(3,L),W(3,L),DELT,RC)
   30 CONTINUE
      RETURN
      END
C
```

```
C
      SUBROUTINE CONWA(ALPR,NT,DELT)
      COMMON/AVEL/UA(7),WA(7),UAS(7),WAS(7),US(7),WS(7),UST(7),
     $WST(7),ALD(7),AL(7),UBAS(7),WBAS(7)
      COMMON/NVOR/NBV,NTV,NNV
      COMMON/LOC/X(3,400),Z(3,400)
      COMMON/VEL/U(3,400),W(3,400)
      COMMON/VEO/UO(3,400),WO(3,400)
      NNV1=NNV-1
      NTV1=NTV-1
      IF(NNV.EQ.1) GO TO 11
      DO 10 L=1,NNV1
      X(3,L)=X(3,L)+(3.0*U(3,L)-UO(3,L))*DELT/2.0
      Z(3,L)=Z(3,L)+(3.0*W(3,L)-WO(3,L))*DELT/2.0
   10 CONTINUE
   11 CONTINUE
      U1=-(UAS(1)*COS(ALPR)-WAS(1)*SIN(ALPR))
      W1=-(WAS(1)*COS(ALPR)+UAS(1)*SIN(ALPR))
      X(3,NNV)=X(3,NNV)+(U(3,NNV)+U1)*DELT/2.0
      Z(3,NNV)=Z(3,NNV)+(W(3,NNV)+W1)*DELT/2.0
      IF(NTV.EQ.1) GO TO 21
      DO 20 L=1,NTV1
      X(2,L)=X(2,L)+(3.0*U(2,L)-UO(2,L))*DELT/2.0
      Z(2,L)=Z(2,L)+(3.0*W(2,L)-WO(2,L))*DELT/2.0
   20 CONTINUE
   21 CONTINUE
      U6=-(UAS(6)*COS(ALPR)-WAS(6)*SIN(ALPR))
      W6=-(WAS(6)*COS(ALPR)+UAS(6)*SIN(ALPR))
      X(2,NTV)=X(2,NTV)+(U(2,NTV)+U6)*DELT/2.0
      Z(2,NTV)=Z(2,NTV)+(W(2,NTV)+W6)*DELT/2.0
      RETURN
      END
C
```

```
C
      SUBROUTINE PIVEL(NBV,NTV,NNV,XP,ZP,UP,WP,DELT,RC)
      COMMON/LOC/X(3,400),Z(3,400)
      COMMON/GAM/GS(3,400),GB(4),OGB(4),DNGAM,CPHI
      USUM=0.0
      WSUM=0.0
      DO 20 L=1,NBV
      CALL FIVEL(X(1,L),XP,Z(1,L),ZP,GS(1,L),UU,WW,RC)
      USUM=USUM+UU
      WSUM=WSUM+WW
   20 CONTINUE
      DO 30 L=1,NTV
      RC=.07*SQRT(FLOAT(NTV-L+1))
      CALL FIVEL(X(2,L),XP,Z(2,L),ZP,GS(2,L),UU,WW,RC)
      USUM=USUM+UU
      WSUM=WSUM+WW
   30 CONTINUE
      DO 40 L=1,NNV
      RC=.07*SQRT(FLOAT(NNV-L+1))
      CALL FIVEL(X(3,L),XP,Z(3,L),ZP,GS(3,L),UU,WW,RC)
      USUM=USUM+UU
      WSUM=WSUM+WW
   40 CONTINUE
      UP=USUM
      WP=WSUM
      RETURN
      END
C
```

```
C
      SUBROUTINE FIVEL(XV,XP,ZV,ZP,GAMMA,UU,WW,RC)
      PI=3.14159
      CX=XV-XP
      CZ=ZV-ZP
      R2=CX*CX+CZ*CZ
      RC2=RC*RC
      IF(R2.LT.RC2) GO TO 10
      VF=GAMMA/(6.283185*R2)
      GO TO 11
   10 VF=GAMMA/(6.283185*RC2)
   11 UU=-CZ*VF
      WW= CX*VF
      RETURN
      END
C
```

```
C
      SUBROUTINE DPRNT(NT,DELT,XPIV,ZPIV,UPIV,WPIV,ALPR,ADOT
     $,CN,CT,CL,CD)
      COMMON/NVOR/NBV,NTV,NNV
      COMMON/AVEL/UA(7),WA(7),UAS(7),WAS(7),US(7),WS(7),UST(7),
     $WST(7),ALD(7),AL(7),UBAS(7),WBAS(7)
      COMMON/VEL/U(3,400),W(3,400)
      COMMON/LOC/X(3,400),Z(3,400)
      COMMON/ALOC/XS(7),ZS(7),XA(7),ZA(7),XB(7),ZB(7),XBS(7),ZBS(7)
      COMMON/GAM/GS(3,400),GB(4),OGB(4),DNGAM,CPHI
      COMMON/INFL/C(7,7),CI(7,7),D(7)
      TIME=(NT-1)*DELT
      ALPD=57.296*ALPR
      PRINT 10,NT,TIME,ALPD,XPIV,ZPIV,UPIV,WPIV
   10 FORMAT(10X,'DATA FOR TIME STEP',I3,' (TIME=',F6.2,')',
     $///15X,'ANGLE OF ATTACK=',F7.3,'DEGREES',/15X,
     $'PIVOT POSITION,X=',F7.3,',Z=',F7.3,/15X,
     $'PIVOT VELOCITY,U=',F7.3,',W=',F7.3,//)
      PRINT 20
   20 FORMAT(15X,'SURFACE VELOCITY DATA',//15X,'POINT',
     $6X,'SURFACE',11X,'FLUID',7X,'AERO ALPHA',/23X,
     $'U',7X,'W',9X,'U',7X,'W',7X,'(DEGREES)',/)
      DO 30 I=1,6
      PRINT 40,I,UAS(I),WAS(I),UA(I),WA(I),ALD(I)
   40 FORMAT(15X,I3,2F8.3,F10.3,F8.3,F9.2)
   30 CONTINUE
      PRINT 50
   50 FORMAT(//15X,'VORTEX DATA',//17X,'IDENT',
     $6X,'POSITION',8X,'VELOCITY',5X,'GAMMA',/15X,
     $'TYPE',1X,'TIME',4X,'X',7X,'Z',7X,'U',7X,'W')
      DO 60 I=1,NBV
      NTYPE=1
      PRINT 70,NTYPE,I,X(1,I),Z(1,I),U(1,I),W(1,I),GS(1,I)
   70 FORMAT(15X,I2,I5,F9.3,4F8.3)
   60 CONTINUE
      DO 80 I=1,NTV
      NTYPE=2
      PRINT 70,NTYPE,I,X(2,I),Z(2,I),U(2,I),W(2,I),GS(2,I)
   80 CONTINUE
      DO 90 I=1,NNV
      NTYPE=3
      PRINT 70,NTYPE,I,X(3,I),Z(3,I),U(3,I),W(3,I),GS(3,I)
   90 CONTINUE
      PRINT 100,CN,CT,CL,CD
  100 FORMAT(//15X,'FORCE DATA',//17X,'CN=',F7.3,4X,
     $'CT=',F7.3,/17X,'CL=',F7.3,4X,'CD=',F7.3,/////)
      RETURN
      END
```